CZECH TECHNICAL UNIVERSITY IN PRAGUE

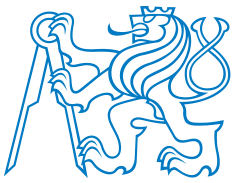

Faculty of Nuclear Sciences and Physical Engineering

DISSERTATION

Analysis of Air Showers with respect to Primary Composition of Cosmic Rays

Prague, 2015 Jakub Vícha

Bibliografický záznam

Autor	Ing. Jakub Vícha České vysoké učení technické v Praze Fakulta jaderná a fyzikálně inženýrská Katedra fyziky

Název práce	Analýza spršek kosmického záření vzhledem ke složení primárních částic
Studijní program	Aplikace přírodních věd
Studijní obor	Jaderné inženýrství
Školitel	RNDr. Petr Trávníček, PhD. Fyzikální ústav Akademie věd České republiky, v. v. i.
Akademický rok	2015/2016
Počet stran	145
Klíčová slova	Kosmické záření, ultra–vysoké energie, hmotové složení, CIC metoda, hloubka maxima spršky, mionová složka, rozptyl hmot, hadronické interakce, komora rezistivních desek.

Bibliographic Entry

Author	Ing. Jakub Vícha Czech Technical University in Prague Faculty of Nuclear Sciences and Physical Engineering Department of Physics
Title of Dissertation	Analysis of Air Showers with respect to Primary Composition of Cosmic Rays
Degree Programme	Application of Natural Sciences
Field of Study	Nuclear Engineering
Supervisor	RNDr. Petr Trávníček, PhD. Institute of Physics of the Academy of Sciences of the Czech Republic
Academic year	2015/2016
Number of Pages	145
Keywords	Cosmic Rays, Ultra–high Energy, Mass Composition, CIC Method, Depth of Shower Maximum, Muon Shower Size, Spread of Primary Masses, Hadronic Interactions, Resistive Plate Chamber.

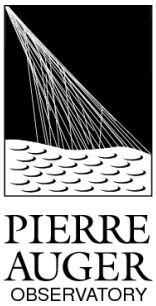

Acknowledgements

Foremost I want to express my gratitude to my supervisor Dr. Petr Trávníček for his guidance, expertise, support and all the help he provided me during all these years. I am also very grateful to Dr. Dalibor Nosek for his unique and valuable advices and constructive criticism that he provided me all the time. I can not imagine to accomplish the thesis in its shape without them.

I want to thank Jiří Blažek for his feedback on the manuscript. My thanks go also to Jan Ebr, Vladimír Novotný and Stanislav Štefánik for stimulating discussions about various cosmic–ray topics; including the content of the thesis.

I am also very grateful to the Czech group of the Pierre Auger Collaboration and to the Institute of Physics of the Academy of Sciences for giving me the opportunity to participate in such a wonderfully mysterious branch of astroparticle physics, as cosmic rays are. I want to also thank my other colleagues from the Pierre Auger Collaboration for fruitful discussions and comments on my research. Especially I want to thank Dr. Bernardo Tomé for his help and advices regarding the MARTA simulations.

Last but not least, I would like to thank my family and friends, especially to Petra Boháčová, for their continuous support throughout my studies and life.

Remark

In the dissertation, the natural system of units that is common for the field of particle physics is used ($\hbar = c = 1$), if not specified otherwise. The astrophysical distances are expressed in parsec units (1 pc $\cong$ 3.26 light years) and the intensities of magnetic field in gauss units (1 G = 10^{-4} T). The decimal logarithm is denoted as $\log \equiv \log_{10}$ and the natural logarithm as $\ln \equiv \log_{e}$. The theoretical introduction in the dissertation was written rather concisely referring to other sources, where the topics are elaborated in more details, instead of encyclopedic description of the wide field of cosmic-ray physics.

Declaration

I hereby certify that I am the sole author of this thesis. I certify that, to the best of my knowledge, my thesis does not infringe upon anyone's copyright nor violate any proprietary rights and that any ideas, techniques, quotations, or any other material from the work of other people included in my thesis, published or otherwise, are fully acknowledged in accordance with the standard referencing practices.

14. 12. 2015 Jakub Vícha

Abstrakt

Kosmické záření o energiích vyšších než ~10^{18} eV (UHECR) je stále neznámého původu a nejistého složení obvzláště na těch nejvyšších energiích. Disertační práce se zabývá určením složení primárních částic pomocí detekce rozsáhlých atmosférických spršek sekundárních částic. V práci byly zavedeny metody, jejichž potenciál byl zkoumán pomocí Monte Carlo (MC) simulací. V jednom případě byla navržená metoda použita na data Observatoře Pierra Augera. Původní výzkum se zaměřením na složení primárních částic byl rozdělen do třech částí podle svého obsahu.

V první části byl studován útlum signálu povrchových detektorů se zenitovým úhlem v závislosti na složení primárních částic. V rámci MC simulací byly uvažovány odezvy povrchových detektorů současných a rovněž i budoucích observatoří UHECR. Byly porovnány dva různé způsoby korekce detekovaného signálu na zenitový úhel, které jsou používané na dvou největších experimentech pozorujících kosmické záření. Použití metody, která je založena na MC přístupu a která se používá na experimentu Telescope Array, vnáší do energetické rekonstrukce zenitovou závislost v případě smíšeného složení UHECR, která by mohla být pozorovatelná v poměru energií rekonstruovaných v povrchových a flurescenčních detektorech. Metoda řezu konstantní intenzity (CIC) používaná na Observatoři Pierra Augera, která vychází pouze z naměřených dat, nevnáší ze své definice žádnou zenitovou závislost do energetické rekonstrukce při neznámém složení kosmického záření. Bylo rovněž ukázáno, že dokonce i přítomnost prominentního zdroje UHECR na nejvyšších energiích by měla zanedbatelný vliv na rekonstrukci energie v povrchovém detektoru. Dále byla zavedena nová metoda určení rozptylu hmot primárních částic. Tato metoda byla demonstrována pro hypotetickou observatoř složenou ze dvou typů povrchových detektorů citlivých zvlášť na elektromagnetickou a mionovou komponentu spršky. Přitom se využívalo principu CIC použitého zároveň na signály z obou povrchových detektorů. Výsledky vykazovaly malou citlivost k detailům hadronických interakcí.

Ve druhé části byla zavedena metoda kombinující měření počtu mionů a hloubky maxima spršky (X_{max}) s cílem zesílit znalost o složení kosmického záření. Metoda byla demonstrována a testována pomocí MC simulací a poté rovněž předběžně aplikována na data Observatoře Pierra Augera. Z interpretace těchto naměřených dat pomocí MC simulací vyplývá, že UHECR je s vysokou pravděpodobností smíšeného složení jader atomů s variancí logaritmu nukleonového čísla $\sigma^2(\ln A) \in \langle 1,\ 3\rangle$ v rozsahu energií $10^{17.8-19.0}$ eV. Výsledky získané s pomocí modelů hadronických interakcí QGSJet II–04 a Sibyll 2.1 byly v rozporu s interpretacemi nezávislých analýz měření X_{max}, zatímco výsledky pro model EPOS–LHC byly s těmito analýzami kompatibilní. Přebytek počtu mionů v naměřených datech vzhledem k předpovědím MC simulací byl odhadnut na ~10-20% pro EPOS–LHC, ~25-35% pro QGSJet II–04 a ~55-70% pro Sibyll 2.1.

Ve třetí části byla vyhodnocena schopnost rozlišit jednotlivé primární částice pomocí případné detekce mionů s komorami rezistivních desek (RPC) umístěnými pod vodními Čerenkovskými detektory na Observatoři Pierra Augera. Pokud by se RPC umístily pod všechny stanice povrchového detektoru observatoře, separabilita primárních částic na nejvyšších energiích by byla srovnatelná se separabilitou dosaženou měřením X_{max} pomocí fluorescenční detekce.

Abstract

The ultra–high energy cosmic rays (UHECR) of energy above $\sim 10^{18}$ eV are still of unknown origin and uncertain mass composition; especially at the highest energies. The thesis was devoted to the problem of resolving the mass composition of these primary particles using the detection of induced extensive air showers. The potential of original methods was investigated using Monte Carlo (MC) simulations. In one case, the method was also applied to the data of the Pierre Auger Observatory. The original research with emphasis on the mass composition of primary particles was divided into three general objectives.

At first, the attenuation of the signal in surface detectors with zenith angle was studied wrt. the mass composition of primary particles using MC simulations. The current and also future observatories of UHECR were considered in MC simulations. The two different approaches applied by the two largest cosmic–ray experiments were compared. It was found that the MC–based method applied by the Telescope Array can bring into the energy reconstruction zenith angle bias in case of a mixed composition of UHECR. This bias should show up in the ratio of energies reconstructed in the surface detectors and in the fluorescence detectors. The data–driven Constant Intensity Cut (CIC) method that is used at the Pierre Auger Observatory does not introduce the zenith angle bias in case of unknown primary composition from its definition. It was also shown that even a presence of a prominent source of UHECR at the highest energies would have a negligible impact on the energy reconstruction based on the CIC method. Further, a novel method to obtain the spread of primary masses was introduced for a hypothetical observatory composed of two types of surface detectors sensitive to the electromagnetic and muon component of shower, respectively. In that, the CIC approach applied simultaneously to the signals of both detectors was utilized. The results showed small dependence on details of hadronic interactions.

Secondly, the original method combining the measurement of the muon shower size and the depth of shower maximum (X_{max}) with the aim to strengthen the information about the cosmic–ray composition was introduced. The method was demonstrated and tested with MC simulations and then also preliminarily applied to the data of the Pierre Auger Observatory. It was found with these measured data that the mass composition of UHECR is most probably mixed with the variance of the logarithmic mass $\sigma^2(\ln A) \in \langle 1,\ 3\rangle$ in a range of energies $10^{17.8-19.0}$ eV. The results obtained for models of hadronic interactions QGSJet II–04 and Sibyll 2.1 were found to be inconsistent with interpretations of independent X_{max} analyses, whereas the results for the model EPOS–LHC were compatible with these analyses. The lack of muons produced in MC simulations wrt. the measured data was estimated to be ~10-20%, ~25-35% and ~55-70% for EPOS–LHC, QGSJet II–04 and Sibyll 2.1, respectively.

Finally, the possible detection of muons with Resistive Plate Chambers (RPCs) placed under the water Cherenkov detectors at the Pierre Auger Observatory and its impact on the separation between the primary–mass species was evaluated using detailed MC simulations. Considering the deployment of RPCs under all water Cherenkov stations, the separability of primaries at the highest energies was estimated to be comparable with the measurement of X_{max} with fluorescence detectors.

Contents

1 Introduction **17**

2 Extensive Air Showers **19**

2.1 Primary Particles 19

2.1.1 Origin 20

2.1.2 Mass Composition 23

2.1.3 Propagation Effects 24

2.2 Extended Heitler Model of Shower Cascade 27

2.2.1 Photon–Induced Showers 27

2.2.2 Proton–Induced Showers 29

2.2.3 Nucleus–Induced Showers 32

2.3 Sensitivity of Detectors to Mass Composition of UHECR 32

3 Pierre Auger Observatory **37**

3.1 Surface Detector 38

3.2 Fluorescence Detector 39

3.3 Shower Energy 41

3.3.1 FD Energy 41

3.3.2 SD Energy 43

3.4 Selected Physics Results of the Pierre Auger Observatory 45

3.4.1 Energy Spectrum 46

3.4.2 Mass Composition 47

3.4.3 Searches for Anisotropy 54

3.4.4 Discussion of Measurements 59

4 Sensitivity of Attenuated Signals in Surface Detectors to Primary Masses **63**

4.1 Attenuation Curves obtained with Different Observatories 63

4.1.1 CORSIKA simulations 65

4.1.2 Toy MC 66

4.1.3 Energy reconstruction 67

4.1.4 CIC Method with a Source . . . 70
4.2 Dispersion of Primary Masses applying CIC Approach . . . 71
4.2.1 Simulated Detector Signals Corresponding to UHECR Showers . . . 72
4.2.2 Sensitivity to Mass Composition . . . 77
4.3 Summary . . . 80

5 Combined Analysis of Ground Signal and Depth of Shower Maximum 83
5.1 Combined Analysis of Muon Shower Size and Depth of Shower Maximum . . . 83
5.1.1 Simulated Showers . . . 85
5.1.2 Method . . . 85
5.1.3 Tests of Method . . . 87
5.2 Application to the Data of the Pierre Auger Observatory . . . 90
5.2.1 Ground Signal and Depth of Shower Maximum . . . 90
5.2.2 Breaks in Dependence of Mean Ground Signal on X_{max} . . . 93
5.2.3 Interpretation of Measured Data based on Simulated Showers . . . 102
5.3 Summary . . . 114

6 Number of Muons with Resistive Plate Chambers 115
6.1 Description of Surface Array Equipped with RPC Detectors . . . 116
6.2 Simulated Showers and Detector Responses . . . 119
6.3 Parametrization of LDF Slope . . . 119
6.3.1 Stability of Parametrized LDF Slope . . . 122
6.4 Separability of Primaries using MARTA . . . 124
6.4.1 Selection Efficiency . . . 124
6.4.2 Resolution . . . 125
6.4.3 EM Bias . . . 127
6.4.4 Merit Factor . . . 128
6.5 Discussion of MARTA Potential . . . 131

7 Conclusions 133

References 137

Chapter 1

Introduction

Cosmic rays of ultra–high energy (above 10^{18} eV) are a mind–burdening mystery for almost fifty years. The first giant–array experiment Volcano Range observed a cosmic–ray shower of energy above 10^{20} eV already in 1962 [1]. However in 1966, just one year after the discovery of the cosmic microwave background, Greisen [2] and Zatsepin with Kuzmin [3] calculated that there should be almost no cosmic–ray protons above the energy $\sim 6 \cdot 10^{19}$ eV originating outside the near universe (~100 Mpc). Thenceforth, nobody was able to satisfactorily explain how such particles could be produced in agreement with the data of various experiments observing the ultra–high energy cosmic rays (UHECR).

The main obstacles in investigations of UHECR are the very low flux of cosmic rays that steeply decreases with energy (E), approximately as $E^{-2.7}$, and the fact that all experiments measuring UHECR actually detect only a small part of the extensive air shower of secondary particles without a direct observation of the primary particle inducing the shower. Moreover, the intervening magnetic fields between the source and the Earth atmosphere deviate the directions of primary particles differently according to their different charge. Unlike the situation in accelerator physics, where the beam energy and the types of colliding particles are known, it is needed to understand the UHECR shower physics very well to draw back any conclusion about the primary particles. To challenge all these obstacles, experiments with giant aperture and great precision of reconstructed shower parameters together with a good reliability of hadronic interaction models extrapolated from accelerator energies are needed to reveal the basic characteristics of UHECR; including their mass composition.

On the other hand, these particles of energies more than 10^6 times higher than the mankind has ever achieved, provide also a unique opportunity to study hadronic interactions of energy in center–mass system more than one order of magnitude higher than the energy of collisions in the Large Hadron Collider (LHC) at CERN, Geneva. Besides the unprecedented astrophysical implications, the Pierre Auger Observatory with its possibility of simultaneous detection of longitudinal and lateral profiles of UHECR showers provides a great opportunity to study the basic properties of UHECR and to investigate the hadronic interactions responsible for the development of extensive air showers.

The content of the thesis is organized as follows:

- The Chapter 2 introduces the topic of extensive air showers induced by UHECR with emphasis on the shower properties that are relevant for the author's original research.
- The Chapter 3 describes the Pierre Auger Observatory as a hybrid instrument that provides unique data of fluorescence and ground detectors. The most important scientific results achieved with the Pierre Auger Observatory data are briefly discussed.

The following three chapters include author's original research using MC simulations and the Pierre Auger Observatory data.

- The attenuation of the signals in different ground detectors with zenith angle and its relation to the mass composition of UHECR is elaborated in more details in Chapter 4 with emphasis on the Constant Intensity Cut method.
- In Chapter 5, a combined analysis of ground and fluorescence measurements with respect to the mass composition of UHECR is presented using MC simulations and also preliminarily applied to the Pierre Auger Observatory data.
- In Chapter 6, a novel option to detect muons of extensive air showers deploying resistive plate chambers under the water Cherenkov stations at the Pierre Auger Observatory is discussed using detailed MC simulations.
- The thesis is summarized in Chapter 7.

Chapter 2

Extensive Air Showers

The flux of cosmic rays of energy beyond 10^{15} eV is already so low that an ideal full–efficient detector of collecting area 1 m^2 placed at the Earth's orbit (observing 1 steradian of space angle) would detect directly only few particles of such a high energy during its lifetime. Nevertheless, the secondary particles (created by cascade interactions of the primary particle in the atmosphere) penetrate deeper in the atmosphere as the primary energy increases. Therefore, above this energy, it starts to be convenient to build large arrays of coincident particle detectors on ground observing extensive air showers (EAS) of secondary particles induced by primary particles of very high energies. The Earth's atmosphere is actually utilized as a huge inhomogeneous (varying air density) calorimeter. The interesting history of air–shower detection and the development of various detection techniques is summarized e.g. in [4, 5].

In this chapter, basic properties of EAS are briefly described with an emphasis on the indirect detection of primary particles inducing these showers. A model of the description of shower development is also included in the chapter to shed light on the level of theoretical understanding of the measured properties of EAS. Finally, few shower parameters relevant for the discrimination of showers according to the mass of primary particle are discussed. To avoid exhaustive encyclopedic description of all the shower properties, the reader is referred to [6, 7, 8] where further detailed information can be found.

2.1 Primary Particles

Unlike to particle–physics experiments at man–made accelerators where the energy and types of colliding particles are known, in case of EAS measurements the properties of primary particles can be derived only indirectly from the shower properties and with limited precision. For this purpose, astrophysics scenarios and hadronic interactions at energies far beyond accelerators' abilities need to be assumed. Under "primaries" all kinds of particles inducing EAS are understood. In this thesis, primaries are distinguished as cosmic rays (charged particles[1]) and neutral particles (neutrons, photons

[1] According to common definition: cosmic rays are charged particles originating outside the Earth's atmosphere.

and neutrinos).

All experiments observing particles of ultra–high energies indicate a dominance of charged particles as it is discussed in Section 3.4.3. However, the possible detection of a neutral particle needs to be kept in mind as the arrival directions of neutral particles would point directly to their sources.

2.1.1 Origin

UHECR can gain such a high energy either by a gradual acceleration mechanism ("bottom–up" process) or by the so–called "top–down" process. In the latter case, UHECR can be produced by a decay of some unknown super–massive particles (rest mass $\sim 10^{21}$ eV) or by interactions of extremely energetic particles (energy higher than 10^{20} eV). Naturally, the neutral particles of ultra–high energy can be produced only by the top–down processes or by interactions of UHECR.

Energy Spectrum

A very important aspect of cosmic rays that can shed light on their origin is their energy spectrum that decreases with energy E as $E^{-\gamma}$ where $\gamma \equiv \gamma(E)$ is the spectral index. The energy at which the spectral index is suddenly changed is usually called the spectral break. It may indicate an energy limit of particles of the same type or origin contributing to the all–particle spectrum, or an energy limit for the magnetic field of our Galaxy to confine the charged particles. However, it might also indicate a threshold energy for interaction processes during their propagation in the Universe.

In Fig. 2.1, the energy spectrum measured by KASCADE and KASCADE–Grande experiments is shown together with data of other experiments as an example. The all–particle spectra for energies between 10^{15} eV and 10^{18} eV are consistent among all the experiments. KASCADE and KASCADE–Grande experiments were able to distinguish three mass groups of particles using a simultaneous measurement of the electromagnetic and the muon components. Estimated value of the spectral break for proton–like particles (blue) is observed at ~4 PeV, for medium–heavy particles (green) at ~8 PeV and for heavy particles (red) at ~80 PeV. Note that the latter spectral break was observed by KASCADE–Grande and the other two by KASCADE, thus a systematic uncertainty in the energy scale needs to be kept in mind. Nevertheless, the energies of these three breaks increase approximately linearly with the increasing average charge $\langle Z \rangle$ of the selected particles (light $\langle Z \rangle$: ~1, medium $\langle Z \rangle$: ~2–14, heavy $\langle Z \rangle$: ~26). This rigidity scaling of spectral breaks indicates a gradual acceleration of particles in a one type of sources up to the energy which is a limit of particle confinement in the region of acceleration, as predicted in [9].

The spectral break in the all–particle spectrum at ~4 PeV, which is consistent with the spectral break of light particles, is called "the knee" in the literature. Similarly, the less significant spectral break at energy ~80 PeV is usually denoted as "the second knee" or "the Fe–like knee". The all–particle spectrum of UHECR with its features (so–called ankle around ~5 EeV and a steep suppression of the flux at energies above ~30 EeV) is described in Section 3.4.1.

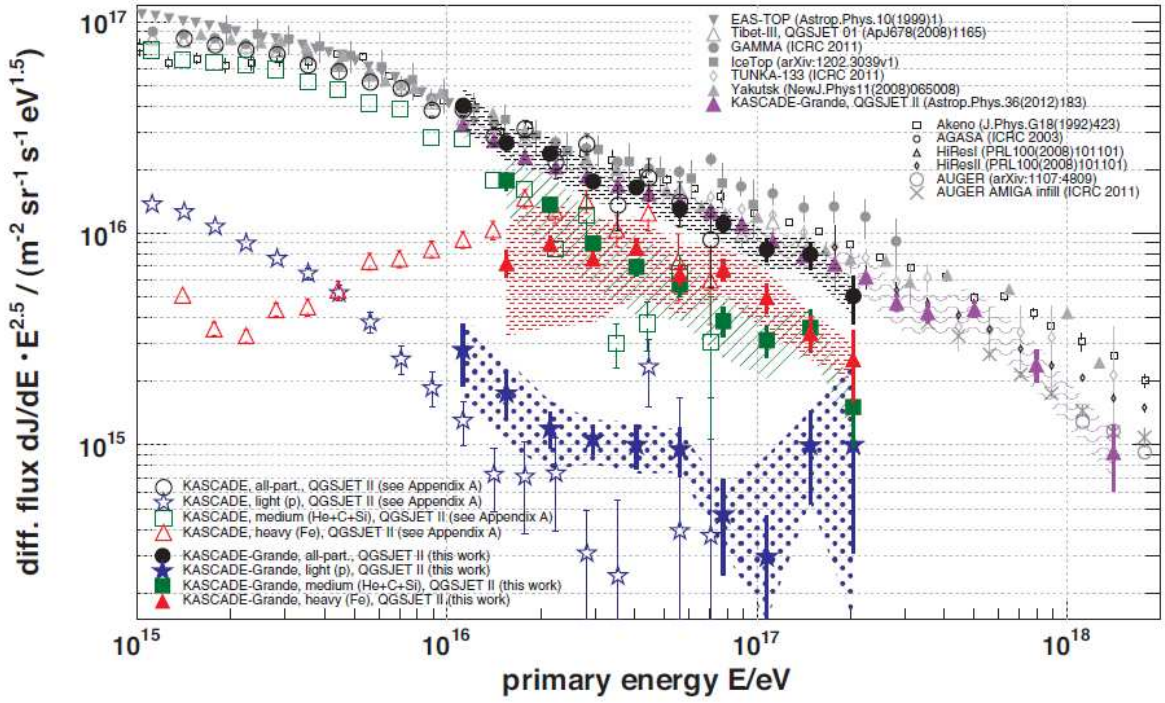

Figure 2.1: Energy spectrum measured by KASCADE and KASCADE–Grande experiments compared with other experiments. Different groups of primaries are distinguished by colors (protons in blue, medium heavy nuclei in green and iron nuclei in red). Note that the spectral break for protons occurs at ~4 EeV, for medium heavy nuclei at ~8 EeV and for iron nuclei at ~80 EeV. The systematic uncertainty of the KASCADE–Grande experiment is indicated by shaded regions. Picture comes from [10].

Acceleration Mechanisms

Up to ~10^{18} eV the so–called Fermi acceleration of the first order [11] seems to be a plausible mechanism to produce cosmic rays in our Galaxy. It could be carried out during the propagation of Supernova shock wave in the interstellar region. The power released into the cosmic rays from Supernova explosions with an observed rate ~1 per century per galaxy should be sufficient to describe the cosmic–ray flux. Furthermore, the spectral index would be similar to the observed one. Nevertheless, only the spectral tail of heavier elements is usually considered to be present as the remaining Galactic component in UHECR. Most of UHECR, especially at the highest energies, originate probably outside our Galaxy as no sufficiently "violent" object has been observed in the Milky Way.

There is still a comprehensive acceleration model missing that would describe the detected UHECR of energies around 10^{20} eV. The well–known Hillas plot (Fig. 2.2) nicely visualizes possible sources according to their characteristic size and their characteristic strength of magnetic field. According to this plot, only few known types of astrophysical objects seem to be capable to accelerate particles up to 10^{20} eV. Active galactic nuclei (AGN), magnetars and galaxy clusters are mentioned here in some details together with the Top–down models.

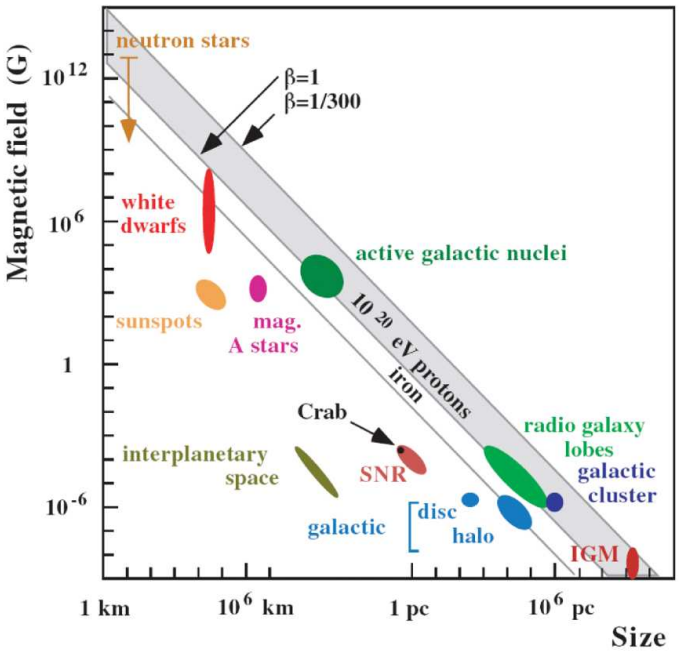

Figure 2.2: Hillas plot. The magnetic field intensity of astrophysical objects is plotted vs. their characteristic size. Objects situated below the marked line are not able to accelerate iron nuclei, or protons to the energy 10^{20} eV. The relativistic velocity β corresponds to the velocity of a shock wave or to the object velocity. Picture comes from [12].

AGNs are Active Galactic Nuclei in the center of galaxies with higher than normal luminosity. Such a galaxy contains a super–massive ($\sim 10^{6-9}$ mass of Sun) black hole in the center and it is accompanied with a long–ranged jets of particles with a jet size comparable to the size of the entire galaxy. They are very luminous objects in the most of the electromagnetic spectrum. The source of this radiation is assumed to come from the accretion of mass into the black hole. UHECR can be accelerated along the jets or hot spots [13]. As an example, the closest AGN is Cen A located ~4 Mpc from the Earth in the Centaurus constellation visible from the southern hemisphere.

Magnetars are neutron stars with a magnetic field of extremely high intensity ($\sim 10^{11}$ T). Although at a small region, the extremely strong magnetic field can confine the charged particles inside this region during the acceleration process for a sufficiently long period of time to produce even UHECR, e.g. [14]. The spatial distribution of magnetars is naturally similar to the distribution of luminous matter at the cosmological scale.

Galactic Clusters contain many galaxies in a cosmologically small region, but they are large enough to be capable to accelerate particles during the large–scale shocks, e.g. [15]. One such a cluster is located ~50 Mpc near the direction of Cen A.

Top–down Models

These "exotic" models require a presence of relict super–heavy particles of masses exceeding $\sim 10^{21}$ eV with a lifetime greater than the age of the Universe (UHECR as the decay products) or a presence of only weakly interacting particles of extremely high energies. For instance, neutrinos (rest mass m_ν) of energy greater than $M_{Z0}^2/m_\nu \sim 10^{22}$ eV interacting with background relict neutrino of temperature 1.8 K would produce Z^0 boson (rest mass M_{Z0}) that decays into hadrons (70%), photons and neutrinos. This would imply an isotropic distribution of arrival directions of protons and photons; with a substantial contribution of photons to the all–particle flux. Neutrinos are generally hard to observe because of their low cross–section and neutrons do not propagate far because of their short lifetime (~880 s). This so–called Z–burst model is in tension with the current data as it is described in Section 3.4.3.

In case of decays of relict super heavy particles (possible cold Dark matter candidates) a correlation with the Galactic center or Galactic plane would be expected. Nowadays, the experimental data practically rule out the Top–down scenarios to be the dominant source of UHECR as it will be discussed in Section 3.4.3. More information about Top–down models as possible UHECR sources can be found e.g. in [16].

Creation of Neutral Particles

Neutral particles of ultra–high energy can be created as direct products in aforementioned Top–down models, or they might be also produced by interactions of UHECR with matter or cosmic microwave background. Collisions of UHECR with matter surrounding their source can produce charged and neutral pions of very high energy ($\sim 10^{16-19}$ eV). They decay very fast (still inside the region of the source) and their decay products, neutrinos of PeV energies and photons of TeV energies[2] can be detected by suitable experiments, e.g. IceCube [17], KM3NeT [18] (neutrino experiments) and H.E.S.S. [19], HAWC [20], CTA [21] (gamma experiments), as indications of UHECR acceleration sites (so–called "smoking guns").

2.1.2 Mass Composition

Stable nuclei of elements with charge Z ranging from 1 (protons) to 26 (iron nuclei) are considered to be the dominant representatives of primary particles with ultra–high energy due to astrophysical reasons (abundance of elements in the Universe, distances of sources higher than ~Mpc) and observed data (very small fraction of neutral particles).

The deviations of arrival directions of UHECR from the directions of their sources are dependent on the UHECR charges (masses). The type of the primary particle influences cross–section, multiplicity and elasticity of the first few interactions in the atmosphere and consequently the whole evolution

[2]The opacity of the Universe for photons steeply increases above the threshold energy for pair production ~300 TeV. However, the opacity of photons at EeV energies is again comparable with the opacity at 100 TeV.

of the induced EAS. Therefore, the knowledge of the mass composition of primary particles is crucial not only for astrophysical analyses, but also for studies of high–energy hadronic interactions.

However, the differences in the measured properties of showers induced by protons and iron nuclei are suppressed by shower–to–shower fluctuations, detector resolution and also by uncertainties coming from the models of hadronic interactions. Therefore the estimation of the mass composition of UHECR is extremely hard to be achieved on event–by–event basis and very hard on statistical basis. The perfect knowledge of detector response and the reliable extrapolation of hadronic interactions up to the highest energies taking place in the shower development are crucial to estimate the mass composition of UHECR.

2.1.3 Propagation Effects

Unlike to neutral particles, the charged particles are deflected in galactic and extragalactic magnetic fields and therefore the information about the directions of their sources can be lost. Deflection of UHECR of energy E and charge Z in the magnetic field of constant intensity B can be described by the so–called Larmor radius (R_{L}) as

$$R_{\mathrm{L}}[\mathrm{kpc}] = \frac{E[\mathrm{EeV}]}{Z \cdot B[\mu\mathrm{G}]}. \tag{2.1}$$

Considering the mean intensity of magnetic field in our Galaxy to be ∼3 μG and the thickness of the Galactic disc 0.3 kpc, the estimated energy above which the arrival directions of UHECR can provide information about their extragalactic origin has to be above ∼1 EeV for protons and ∼26 EeV for iron nuclei. Otherwise, they would become isotropic in the magnetic field of our Galaxy; or a large–scale signature at few % level would occur at most. This is in accordance with the results of two largest UHECR experiments: the Pierre Auger Observatory [22] and the Telescope Array [23]. None of the two experiments observes any significant small–scale anisotropic signal in the arrival directions of EAS below ∼40 EeV as it is shown in Section 3.17.

The intensity of extragalactic magnetic fields is mostly estimated to be of the order of ∼nG and therefore of a negligible intensity compared to the intensity of the Galactic magnetic field. But it is worth to note that the extragalactic magnetic fields are only very roughly estimated (weaker than 1 nG [24, 25]) and they could have a larger impact on the deviations of UHECR during their propagation in the Universe. In fact, the trajectories of UHECR particles in the extragalactic space are several orders of magnitude longer than their paths inside our Galaxy. Thus, the cumulative effect of extragalactic magnetic fields on the deviations of UHECR can be very significant, if the sources of UHECR are distant $\gtrsim$ 100 Mpc.

An UHECR particle of charge Z and energy E should, in the first approximation, move along the same path (the same Larmor radius) as the particle of charge z and energy $z/Z \cdot E$ originating from the same source. Then, for a source of UHECR nuclei with charges z and Z some correlation of the most energetic heavy nuclei with the light nuclei at the corresponding lower energies could be observed

on the sky map, when no lensing effects of magnetic fields between the source and our Galaxy are present. This effect was first considered in [26] and it can be utilized to study or constrain the mass composition of UHECR at their source.

The above-mentioned propagation of UHECR particles was considered for stable and noninteracting particles only. In reality, also the lifetime and interactions of primaries with photons and hadronic matter needs to be taken into account. The extragalactic space is empty of hadronic matter (less than 1 hadron per m^3 in average) but quite rich for Cosmic Microwave Background (CMB) photons (~400 photons per cm^3) and it contains also a non-negligible amount of optical, infra–red and ultra–violet (OPT/IR/UV) photons. Protons and nuclei are influenced by different processes at different energies. For more detailed information see [27], from which only several aspects are mentioned here.

Protons propagating in the extragalactic space interact mainly with CMB and IR/OPT/UV photons and lose energy by adiabatic losses (due to the expansion of the Universe) that are dominant at lower energies (below $\sim 10^{18}$ eV). Interactions with CMB photons become relevant at $\sim 10^{18}$ eV through the pair production process

$$\mathrm{p} + \gamma_{\mathrm{CMB}} \longrightarrow \mathrm{p} + \mathrm{e}^+ + \mathrm{e}^-. \tag{2.2}$$

At energy $\sim 7 \cdot 10^{19}$ eV the pion production via Δ^+ resonance (rest mass 1232 MeV)

$$\mathrm{p} + \gamma_{\mathrm{CMB}} \longrightarrow \Delta^+ \longrightarrow \mathrm{p} + \pi^0, \tag{2.3}$$

$$\mathrm{p} + \gamma_{\mathrm{CMB}} \longrightarrow \Delta^+ \longrightarrow \mathrm{n} + \pi^+ \tag{2.4}$$

starts to take over as the cross–section of these processes steeply increases around this energy. This is also known as the GZK effect (named according to Greisen [2] and Zatsepin with Kuzmin [3]) restricting the region of sources to the astronomically close universe (within ~100 Mpc for protons of energy above 10^{20} eV). The neutrinos decayed from the produced charged pions and photons decayed from the produced neutral pions are called GZK neutrinos and GZK photons, respectively. Interactions of protons with IR/OPT/UV photons are sub-dominant in the whole energy range.

In case of nuclei A with nucleon number *A*, the interactions with background photons are different. The background photons (IR and CMB) are boosted in the UHECR nucleus rest–frame to 10–20 MeV energies. The most relevant process is the Giant Dipole Resonance (GDR) emitting one, or two nucleons (n), or α particles:

$$\mathrm{A} + \gamma_{\mathrm{CMB}} \longrightarrow \mathrm{GDR} \longrightarrow (\mathrm{A}-1) + \mathrm{n}\,, \tag{2.5}$$

$$\mathrm{A} + \gamma_{\mathrm{CMB}} \longrightarrow \mathrm{GDR} \longrightarrow (\mathrm{A}-2) + 2\mathrm{n}, \tag{2.6}$$

$$\mathrm{A} + \gamma_{\mathrm{CMB}} \longrightarrow \mathrm{GDR} \longrightarrow (\mathrm{A}-4) + \alpha\ . \tag{2.7}$$

The GDR process becomes very efficient for nucleus energies ~$3{\cdot}10^{20}$ eV. The GZK effect for nuclei takes place at approximately A-times higher energies than for protons.

Fig. 2.3 shows that the attenuation lengths of medium–mass nuclei (He, O, Si) are smaller than those of protons and heavy nuclei above ~10^{19} eV. Furthermore, iron nuclei have the attenuation length larger or comparable to the attenuation length of protons up to ~$3{\cdot}10^{20}$ eV. It has a consequence that medium–heavy nuclei ($1 < A < 56$) should not contribute significantly to the end of UHECR spectrum, if their sources are not close (~Mpc) to the Earth[3].

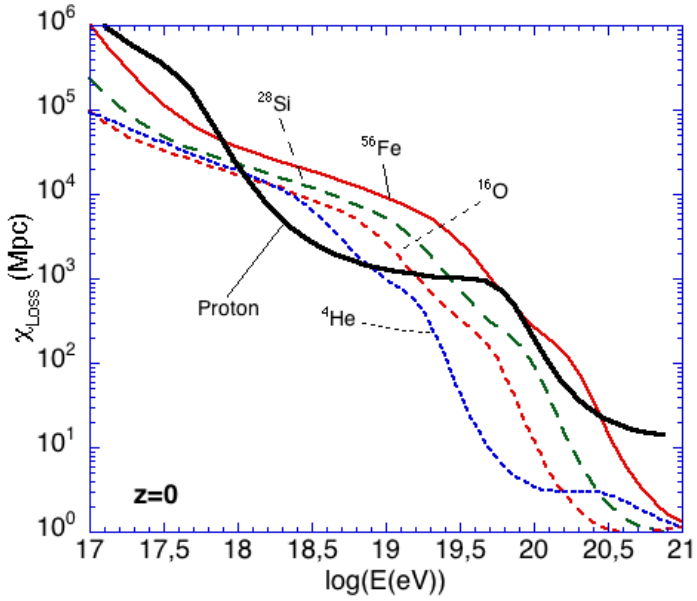

Figure 2.3: Attenuation length depending on energy for different nuclei considering the redshift $z = 0$. Picture comes from [27].

UHECR nucleus can also be spallated during its propagation through matter, or most probably directly in the surrounding medium at their sources. During the spallation of nucleus the emitted nucleons have the same Lorentz factor as the origin nucleus. This has a consequence that the emitted protons propagate with a half Larmor radius compared to the original nucleus. Considering such protons (rest mass m_p, energy E_p) spallated from a nucleus of charge Z, mass number A and energy E_A propagating through the magnetic field of intensity B, the nucleus is bended according to the Larmor radius R_L^A:

$$R_\mathrm{L}^\mathrm{A} = \frac{E_\mathrm{A}}{Z \cdot B} \simeq \frac{A \cdot m_\mathrm{p} \cdot \gamma}{Z \cdot B} \simeq 2 \cdot R_\mathrm{L}^\mathrm{p} \tag{2.8}$$

[3]To have a clearer notion about the relevant orders of distances, the Galactic center is distant ~10 kpc, the galaxy in Andromeda (M42) around 0.3 Mpc, the closest galaxy with active nucleus (Centaurus A) ~4 Mpc, Virgo cluster of galaxies ~20 Mpc and the size of the Universe is several Gpc.

as the spallated protons are bended according to the Larmor radius $R_{\rm L}^{\rm p}$:

$$R_{\rm L}^{\rm p} = \frac{E_{\rm p}}{B} = \frac{m_{\rm p}\gamma}{B}. \tag{2.9}$$

The deflection angle α of a particle coming from the distance d can be approximated as $\alpha \sim d \times R_{\rm L}$. If there is an anisotropy observed on the sky within a radius $\alpha_{\rm A}$ at energy $E_{\rm A}$ caused by heavier nuclei with mass number A, the consequent anisotropy can be expected at energy $\sim E_{\rm A}/A$ within an angle $2 \cdot \alpha_{\rm A}$ caused by protons spallated in the surrounding material of the source.

The neutral particles propagate, naturally, unaffected by magnetic fields. Neutrons, photons and neutrinos of ultra–high energies can be produced during the GZK effect of UHECR protons or by interactions with matter in the acceleration region. Neutrons can also come from the photo-disintegration and spallation of UHECR nuclei. Neutrinos can propagate throughout the space without almost any limitation because of their low cross–section. Photons above EeV energies have the attenuation length about several Mpc [28], so photons only from the closest sources could be detected at these energies. Neutrons have the mean lifetime $\tau_{\rm n} \approx 10^3$ s, so at EeV energies they can propagate up to a distance $\approx \gamma \cdot c \cdot \tau_{\rm n} = 10$ kpc. This distance is comparable with the distance between the Earth and the center of our Galaxy. At higher energies than EeV, the propagation distances of neutrons and photons increases, however, the rate of such energetic particles steeply decreases.

2.2 Extended Heitler Model of Shower Cascade

Typical vertical UHECR shower contains around 10^{10} particles at its maximum covering an area on ground of tens of km^2. Three shower components are distinguished in this thesis. The electromagnetic (EM) component contains $e^{\pm}$ and γ. The hard component consists of muons and neutrinos, but mostly only the muon part will be considered in the following. The hadronic component is composed of nuclear fragments and other hadrons near the shower axis. First qualitative description of the development of shower cascade, so–called Heitler model, was given in [29] considering the EM component only. Further extensions of the Heitler model (so–called Extended Heitler model or Heitler–Matthews model) followed [30], [31] incorporating the hadronic cascade and improving the consistency with detailed transport MC simulations.

2.2.1 Photon–Induced Showers

Considering just the EM component of a hadron–induced shower (carrying ~90% of the shower energy) or the shower induced by a photon, the subsequent cascade of interactions can be described in the first approximation as in the left panel of Fig. 2.4. A photon after one splitting length[4] $X_0 \cdot \ln 2$ splits into a pair of electron and positron of equal energies. Electrons and positrons are assumed to

[4]Radiation length X_0 is the amount of matter traversed in material by a charged particle before decreasing its energy to the 1/e of the original energy by radiation losses. Half of energy is then reached after $X_0 \cdot \ln 2$. In case of $e^{\pm}$ in the air $X_0 \approx 37$ g/cm^2. Note that the mean free path for conversion of γ to $e^{\pm}$ is very similar ($\sim 9/7 X_0$) to the radiation length of $e^{\pm}$.

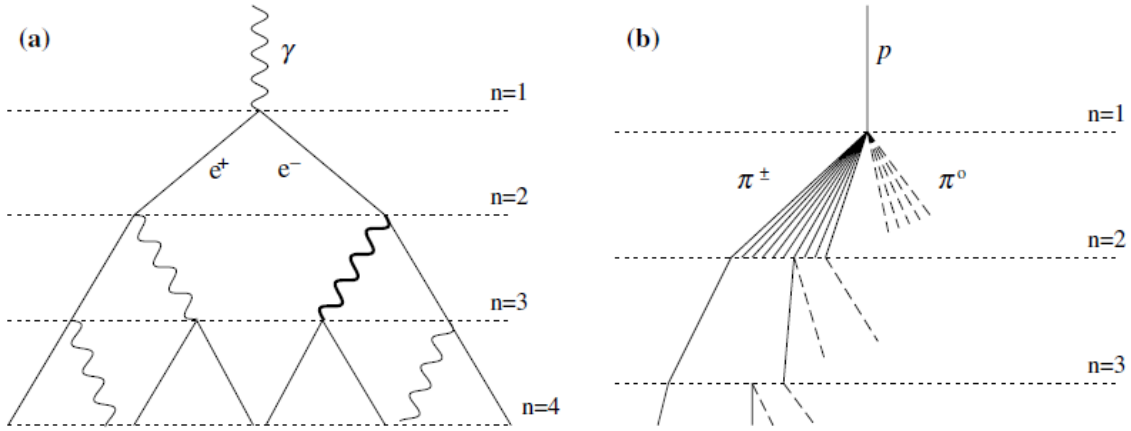

Figure 2.4: Schematic description of the EM cascade (**left**) and of the hadronic cascade (**right**). The number of generation is denoted by n. Pictures come from [30].

radiate a photon (bremsstrahlung) of half of the electron (positron) energy, again after passing $X_0 \cdot \ln 2$. In all cases, two daughter particles are created from one mother particle. The daughter particles have the same energies equal to one half of the energy of mother particle after one splitting length. This process stops when the energies fall below $\xi_c^e \approx 85$ MeV, which is the critical energy[5] of electron in air. Then, after n radiation lengths the number of particles equals to 2^n. The shower reaches its maximum when all particles have energy $\sim\xi_c^e$, thus the shower energy E_0 can be expressed as

$$E_0 = 2^{n_{\max}} \cdot \xi_c^e \tag{2.10}$$

where $n_{\max}$ is the generation number of shower stage at its maximum. Assuming that an electron has half of its energy after passing $X_0 \cdot \ln 2$, the depth[6] $X_{\max}^{\gamma}$ at which the EM component reaches its maximum is

$$X_{\max}^{\gamma} = n_{\max} \cdot X_0 \cdot \ln 2 = X_0 \cdot \ln\left(\frac{E_0}{\xi_c^e}\right). \tag{2.12}$$

The important aspect of the Heitler model of EM cascade is the fact that the depth of shower maximum increases linearly with the logarithm of the primary energy and that the corresponding elongation rate value D is

$$D = \frac{\mathrm{d}\left(X_{\max}^{\gamma}\right)}{\mathrm{d}\left(\log E_0\right)} \simeq 2.3 \cdot X_0 = 85 \text{ g/cm}^2. \tag{2.13}$$

However, the elongation rate of photons using showers generated with the transport MC program CONEX 4.37 [32, 33] without the so–called preshowering effect [34, 35] (creation of $e^{\pm}$ pairs in the

[5] At the critical energy of a particle in a given medium, its ionization and radiation losses are equal.

[6] The atmospheric depth X at the altitude h is defined as

$$X = \int_{\infty}^{h} \frac{l \cdot \rho(l)}{\cos(\Theta)} \mathrm{d}l \tag{2.11}$$

where $\rho(l)$ is the air density at the altitude l and Θ is the zenith angle of primary particle.

magnetic field of the Earth relevant for energies above $\sim 10^{19.5}$) gives value around 110 g/cm^2 for the hadronic interaction model QGSJet II–04 [36]. This difference is mainly caused by the fact that the Heitler model neglects losses of particles during their propagation and it overestimates the actual ratio of electrons to photons. The number of electrons and positrons at maximum is predicted to be $2/3 \cdot 2^{n_{\max}}$, but multiple photons are often radiated during bremsstrahlung and many $e^{\pm}$ that range out are not further considered within this model. Actually, the number of electrons (N_e) is predicted to be $\sim$1/10 of $2^{n_{\max}}$ according to detailed MC simulations in [30].

2.2.2 Proton–Induced Showers

In case of air showers induced by hadrons, the cascade of secondary particles is modeled similarly as the EM cascade, but now in steps of interaction length[7] of pions λ_i (right panel of Fig. 2.4). After traversing one λ_i a hadron produces N_{ch} charged pions and $1/2$ N_{ch} neutral pions. The latter are assumed to immediately decay (lifetime $\sim 10^{-17}$s) to photons inducing EM showers. Charged pions continue with interactions after every λ_i until their energy equals the critical energy of pions ξ_c^{π}. All charged pions of energy below ξ_c^{π} are assumed to decay into muons which is a fair approximation (branching ratio 99.99%, mean lifetime 26 ns):

$$\pi^{\pm} \longrightarrow \mu^{\pm} + \nu_{\mu} \left(\overline{\nu}_{\mu}\right). \tag{2.14}$$

The multiplicity N_{ch} in π–nucleon collisions is assumed to be constant, $N_{ch} = 10$, and $\xi_c^{\pi} = 20$ GeV being reasonable estimates of the values measured at lower energies [30].

The immediate decay of π^0 and the value of ξ_c^{π} are fair approximations as it can be seen in Fig. 2.5. The energy evolutions of the interaction length (λ_i) and of the decay length (λ_d) are shown for charged and neutral pions. The interaction length was assumed to be the same for charged and neutral pions. It was calculated as

$$\lambda_i(E) = \frac{m_{\text{air}}}{N_{\text{Av}}\, \sigma_{\text{inel}}^{\pi-\text{air}}(E)} \tag{2.15}$$

with $N_{\text{Av}} = 6.022 \cdot 10^{23}$ mol^{-1} and $m_{\text{air}} = 14.54$ g/mol being the Avogadro constant and average atomic weight of air, respectively. The energy dependence of inelastic pion–air cross section $\sigma_{\text{inel}}^{\pi-\text{air}}(E)$ was taken from [38]. The distance traversed before the decay of pions was calculated as

$$l_d = c \cdot \tau \cdot \gamma \tag{2.16}$$

where c is the speed of light, τ the mean lifetime and $\gamma = E_{\pi}/m_{\pi}$ the Lorentz factor of pion with energy E_{π} and rest mass m_{π} (135 MeV for π^0 and 139.6 MeV for $\pi^{\pm}$). Integrating over the air density according to the U.S. standard atmosphere model [38] the decay length λ_d in mass–overburden units was obtained. Three production depths of pions (corresponding to vertical atmospheric depth at altitudes 4, 16 and 32 km a.s.l.) were considered in the plot shown in Fig. 2.5. The decay length λ_d

[7] Fairly good approximation in the range of 10–1000 GeV is $\lambda_i = 120$ g/cm^2 [37].

depends also naturally on the zenith angle Θ of pion direction (≈ shower direction) because of different amount of atmosphere passed along the path. In the energy regions where λ_i and λ_d are similar, the nuclear interactions of π_0 can compete with its decay only for few first interactions of UHECR at the highest energies. The charged pions of energy below ~tens of GeV are more probable to decay before interaction feeding the muon component of the shower.

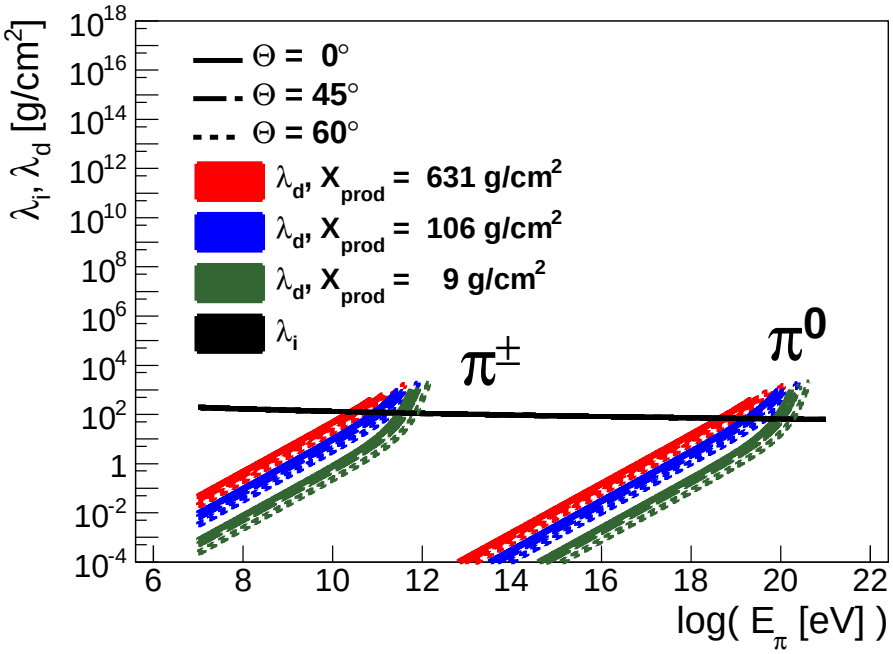

Figure 2.5: Energy evolutions of interaction (λ_i) and decay (λ_d) lengths for charged and neutral pions. Three production depths (X_{prod} = 631, 106 and 9 g/cm^2) of pions were assumed corresponding to vertical atmospheric depths at 4, 16 and 32 km a.s.l. Three zenith angles (Θ) of pions were considered. The U.S. standard atmosphere and the approximate energy evolution of inelastic π–air cross section were assumed according to [38].

The produced muons decay as

$$\mu^{\pm} \longrightarrow e^{\pm} + \nu_e(\overline{\nu_e}) + \overline{\nu_\mu}(\nu_\mu) \tag{2.17}$$

with the mean lifetime 2.2 μs and ~100% branching ratio. For instance, a muon with kinetic energy equal to its mass (105.7 MeV) traverses in average 1.3 km and 1 GeV muon over 6 km before it decays. Thus, only the least energetic muons (~hundreds of MeV) mostly decay before reaching the ground. Also note that the number of muons being equal to the number of pions is fair approximation.

Consider a proton of energy E_0 inducing an air shower. After n interactions, assuming again equal division of energy to produced particles, all charged pions carry energy $(2/3)^n E_0$. The energy of a single pion E_π is then

$$E_\pi = \frac{E_0}{(3/2 \cdot N_{ch})^n}. \tag{2.18}$$

The primary energy E_0 is finally divided at its maximum between $N_{\rm max}^{\rm EM}$ EM particles and $N_{\rm max}^{\pi}$ charged pions within this model. Then, denoting the number of muons $N_{\mu}^{\rm p} = N_{\rm max}^{\pi}$, it can be written

$$E_0 = \xi_{\rm c}^{e} \cdot N_{\rm max}^{\rm EM} + \xi_{\rm c}^{\pi} \cdot N_{\mu}^{\rm p}. \tag{2.19}$$

By scaling the number of electrons as before to be $N_{\rm e}^{\rm p} = N_{\rm max}^{\rm EM}/10$ the primary energy is

$$E_0 = 10 \cdot \xi_{\rm c}^{\rm e} \left(N_{\rm e}^{\rm p} + \frac{\xi_{\rm c}^{\pi}}{10 \cdot \xi_{\rm c}^{\rm e}} N_{\mu}^{\rm p} \right) \simeq 0.85 \text{ GeV}(N_{\rm e}^{\rm p} + 24 \cdot N_{\mu}^{\rm p}). \tag{2.20}$$

The important consequence of the last relation is that the primary energy is easy to calculate, when both $N_{\rm e}^{\rm p}$ and $N_{\mu}^{\rm p}$ are measured near the shower maximum.

The number of muons at maximum of a proton–induced shower can be expressed as

$$N_{\mu}^{\rm p} = N_{\rm max}^{\pi} = (N_{\rm ch})^{n_{\rm c}} = \left(\frac{E_0}{\xi_{\rm c}^{\pi}} \right)^{\beta} \tag{2.21}$$

where n_c is the number of generations at the shower maximum obtained from Eq. (2.18) and

$$\beta = \frac{\ln(N_{\rm ch})}{\ln(3/2 \cdot N_{\rm ch})} = 0.85. \tag{2.22}$$

The relation between $N_{\mu}^{\rm p}$ and primary energy is well justified by detailed MC simulations giving β values 0.85-0.92 [30]. Higher values of β than in Eq. (2.22) can be obtained within the model, if the interaction inelasticity is incorporated and the multiplicity increased [30].

Using Eq. (2.21) in Eq. (2.20)

$$N_{\rm e}^{\rm p} = \frac{E_0}{10 \cdot \xi_{\rm c}^{\rm e}} - \frac{\xi_{\rm c}^{\pi}}{10 \cdot \xi_{\rm c}^{\rm e}} \left(\frac{E_0}{\xi_{\rm c}^{\pi}} \right)^{\beta} \approx \frac{E_0}{10 \cdot \xi_{\rm c}^{\rm e}} \tag{2.23}$$

as the fraction of energy going to muons can be neglected at ultra–high energies.

The depth of shower maximum of proton–induced shower ($X_{\rm max}^{\rm p}$) can be estimated as

$$X_{\rm max}^{\rm p} = X_1 + X_0 \cdot \ln \left(\frac{E_0}{3 \cdot N_{\rm ch} \cdot \xi_{\rm c}^{\rm e}} \right) \tag{2.24}$$

with an EM shower starting after the depth X_1 of the first interaction. Using the parametrized p–air cross section and the multiplicity of charged particles, the elongation rate value 58·g/cm^2 is obtained (smaller than $X_{\rm max}^{\gamma}$), which is in good agreement with detailed MC simulations. However, the absolute value of $X_{\rm max}^{\rm p}$ is about 100·g/cm^2 below the values from the detailed MC simulations. It can be explained by the fact that the production of π^0 is neglected for subsequent interactions of the primary particle and also that the leading particle effects are not considered.

Although the depth of shower maximum and the energy evolution of the number of muons is quite well estimated just on basic assumptions about the shower development within the Heitler–Matthews

model, it can not be used for a reliable comparison with the measured data. For that, detailed MC simulations are more convenient as they include all the aforementioned features and other particle physics effects extrapolated from the accelerator data. Moreover, the detailed MC simulations can predict also the fluctuations in shower properties that can not be considered within the Extended Heitler model.

2.2.3 Nucleus–Induced Showers

The superposition model [31] describes the interactions of a nucleus in the atmosphere in a simplified way. The shower induced by a nucleus of mass number A and energy E_0 is treated as the sum of A independent proton showers with energy E_0/A. The nucleus of higher A has a larger cross section than a nucleus of lower A and interacts generally earlier in the atmosphere. Due to the higher multiplicity (A independent sub-showers) the shower induced by a nucleus evolves earlier in the atmosphere than the proton–induced shower and also more pions, and subsequently more muons, are produced with smaller shower–to–shower fluctuations.

The depth of shower maximum $X^{\mathrm{A}}_{\mathrm{max}}$, the number of electrons $N^{\mathrm{A}}_{\mathrm{e}}$ and the number of muons N^{A}_{μ} at maximum of a nucleus–induced shower are then related to the corresponding quantities of proton–induced shower of the same energy as

$$X^{\mathrm{A}}_{\mathrm{max}} = X^{\mathrm{p}}_{\mathrm{max}} - X_0 \cdot \ln(A), \tag{2.25}$$

$$N^{\mathrm{A}}_{\mu} = N^{\mathrm{p}}_{\mu} \cdot A^{1-\beta}, \tag{2.26}$$

$$N^{\mathrm{A}}_{\mathrm{e}} = A \cdot \frac{E_0/A}{10 \cdot \xi^{\mathrm{e}}_{\mathrm{c}}} = N^{\mathrm{p}}_{\mathrm{e}}. \tag{2.27}$$

2.3 Sensitivity of Detectors to Mass Composition of UHECR

The difference in the depth of shower maximum (measured by optical detectors) between showers induced by protons and iron nuclei is estimated as $X^{\mathrm{p}}_{\mathrm{max}} - X^{\mathrm{Fe}}_{\mathrm{max}} \simeq 150$ g/cm^2 using Eq. (2.25). Regarding the number of muons at the shower maximum, the relative difference is $(N^{\mathrm{Fe}}_{\mu} - N^{\mathrm{p}}_{\mu})/N^{\mathrm{p}}_{\mu} = 56^{1-\beta} - 1 \simeq 0.5 - 0.8$ from Eq. (2.26). Accordingly, the showers induced by iron nuclei contain approximately more than 50% more muons at the shower maximum than the proton–induced showers. It must be acknowledged that the number of muons is measured with particle detectors that are placed at certain observation level, usually, beyond the shower maximum. The attenuation length of secondary muons in air is about 800 g/cm^2, so a reasonable amount of muons can be still measured on the ground. But it needs to be also mentioned that the number of muons on ground (N_{μ}) of Fe showers is partly reduced wrt. proton showers because of the faster development of Fe showers. Altogether, the depth of shower maximum and the number of muons on ground have a good potential for mass composition studies. On the other hand, from Eq. (2.27), the number of electrons at the shower maximum can provide an unbiased estimation of the primary energy wrt. the primary composition.

Nevertheless, using the detailed MC simulations of showers induced by protons and iron nuclei the difference in case of the mean $X_{\max}$ is about 100 g/cm^2 and in case of the mean N_μ measured on ground (~1400 m a.s.l.) about 40%. Naturally, the resolutions of detector instruments, $\delta(X_{\max})$ for $X_{\max}$ and $\delta(N_\mu)$ for N_μ measurements, play the decisive role in the potential of any experiment to discriminate between primary species. Current experimental abilities are $\delta(X_{\max}) \approx 20$ g/cm^2 and $\delta(N_\mu)/N_\mu \approx 10 - 20\%$.

For ground detectors located at an altitude with vertical atmospheric depth X_{ground} ($> X_{\max}$), the number of electrons (N_{e}) is attenuated after its maximum ($N_{\text{e}}^{\max}$) as

$$N_{\text{e}} = N_{\text{e}}^{\max} \cdot e^{-\frac{X_{\text{ground}}/\cos(\Theta) - X_{\max}}{\lambda_{\text{e}}}} \tag{2.28}$$

where $\lambda_{\text{e}} \approx 60$ g/cm^2 is the attenuation length of the number of electrons after the shower maximum. The number of electrons on the ground is then expected to be smaller for showers induced by iron nuclei than by protons of the same energy since the Fe showers reach their maximum higher in the atmosphere. Therefore a combination of N_{e} and N_μ measured by ground detectors can be very beneficial to study the mass composition.

As an illustration of separability of different primaries using $X_{\max}$ and N_μ at altitude of 1400 m a.s.l., distributions of these two quantities are shown in Fig. 2.6. For each of three primary particles (p, Fe and γ) 500 showers were produced with the transport MC program CONEX. High–energy hadronic interactions were modeled with QGSJet II–04 and the primary energies were set to 10^{19} eV and $\Theta = 38°$. Note that the detector resolution was not incorporated. The distribution of $X_{\max}$ for proton–induced showers is so wide that it overlaps over the $X_{\max}$ distribution of Fe–induced showers. Therefore an event–by–event study of the mass composition of primary particles using only the $X_{\max}$ quantity is actually impossible due to the shower–to–shower fluctuations; even without considering the effect of the detector resolution.

To quantify the separability of two primaries, the Merit Factor $MF(\text{i, j})$ of two distributions H_{i} and H_{j}, i≠j, is introduced (e.g. in [39]) as

$$MF(\text{i, j}) = \frac{|\langle H_{\text{i}}\rangle - \langle H_{\text{j}}\rangle|}{\sqrt{\sigma^2(H_{\text{i}}) + \sigma^2(H_{\text{j}})}} \tag{2.29}$$

expressing the difference between the means $\langle H_{\text{i}}\rangle$ and $\langle H_{\text{j}}\rangle$ of two considered distributions in units of the "average standard deviation" calculated from the variances $\sigma^2(H_{\text{i}})$, $\sigma^2(H_{\text{j}})$ of these two distributions. Higher value of $MF(\text{i, j})$ indicates better separability of primaries.

From Fig. 2.6, better separation of primaries seems to be achievable using the total N_μ measured by surface detectors, $MF(\text{p, Fe}) = 2.2$, than in the case of $X_{\max}$, $MF(\text{p, Fe}) = 1.5$. However, the total N_μ is quite hard to be measured precisely. Ground detectors of limited collecting areas sample only parts of the whole muon component. These particle detectors are usually utilizing the ionization or the Cherenkov effect that makes them sensitive also to the EM component ($e^{\pm}$ and photons via pair

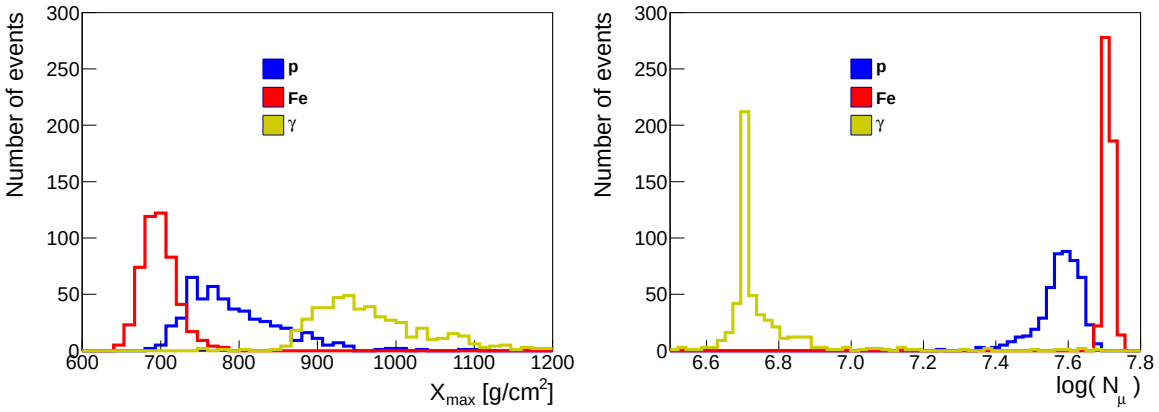

Figure 2.6: Illustration of the potential to separate showers induced by protons, iron nuclei and photons using the distributions of $X_{\rm max}$ (**left panel**) and of the number of muons with energy $\geqq$ 1 GeV at 1400 m a.s.l. (**right panel**). Simulation program CONEX was used for production of 500 proton (p), 500 iron (Fe) and 500 photon (γ) showers of energy 10 EeV and $\Theta = 38°$ applying the hadronic interaction model QGSJet II–04.

production in the medium). Therefore a shielding of the EM component with some mass overburden is a necessary complement of the muon detectors[8]. Produced muons lose in matter ~2 MeV of their energy per g/cm^2 (minimum ionizing particles). For instance, the mass overburden of 250 g/cm^2 (~1.3 m of soil) creates an energy threshold 500 MeV for muons and a suppression of $N_{\rm e}$ down to ~2% according to Eq. (2.28). Consequently, only the harder muons can reach the detectors as the softer muons are absorbed together with the most of the EM component.

The scatter plots in the left panel of Fig. 2.7 illustrate that the combined measurement of N_μ and $X_{\rm max}$ of individual showers, neglecting the detector resolutions, increases the separability of primary particles. However, when the detector resolutions $\delta(X_{\rm max}) = 20$ g/cm^2 and $\delta(N_\mu)/N_\mu = 20\%$ are considered in the right panel of Fig. 2.7, the separability of primaries gets substantially worse wrt. to the ideal case shown in the left panel.

From the experimental point of view, it is more convenient to study the first two central moments of the measured distributions of $X_{\rm max}$ and N_μ than to fit these distributions as a priori the number and types of primaries is unknown. The mean value (the first central moment), $\langle X_{\rm max}\rangle$, of a set of N primary nuclei with mass number A_i ($i = 1, \ ..., \ N$), mean depth of shower maximum $X_{\rm max}^{\rm A_i}$ and relative fractions $f_i \in \langle 0, \ 1\rangle$, where $\sum_{i=1}^{N} f_i = 1$, can be expressed using Eq. (2.25) as

$$\langle X_{\rm max}\rangle \approx \sum_{i=1}^{N} f_i \cdot \langle X_{\rm max}^{\rm A_i}\rangle = \langle X_{\rm max}^{\rm p}\rangle - X_0\langle \ln A\rangle. \tag{2.30}$$

[8] An alternative to measure the muon component from the μ+EM signal would be to measure independently the EM component with thin detectors and then to subtract it from the μ+EM signal.

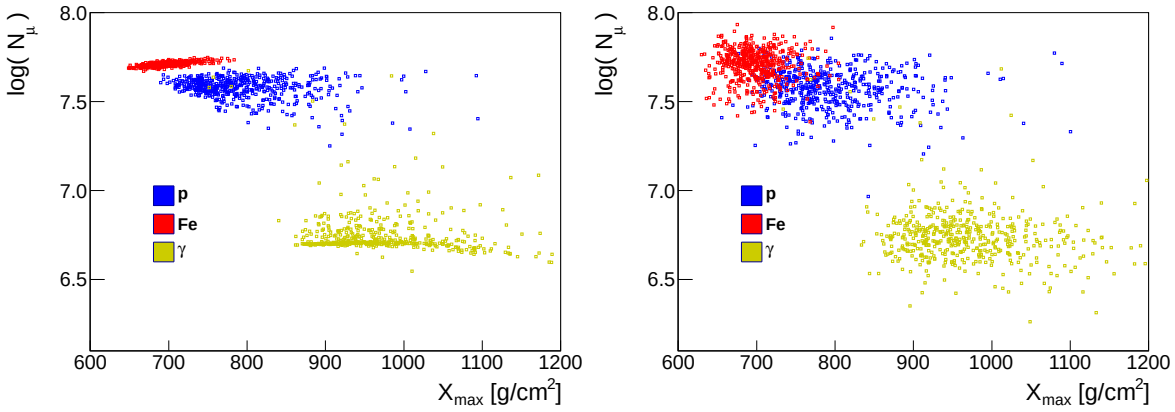

Figure 2.7: Illustration of the potential to separate primary particles using the combined measurement of N_μ and $X_{\max}$. **Left panel** shows the scatter plots obtained directly from simulations and **right panel** contains the showers with $X_{\max}$ smeared by Gaussian with the variance 20 g/cm^2 and N_μ with the relative variance 20%. Simulation program CONEX was used for the production of 500 proton (p), 500 iron (Fe) and 500 photon (γ) showers of energy 10 EeV and $\Theta = 38°$ applying the hadronic interaction model QGSJet II–04.

The last equation means that the mean logarithmic mass, $\langle \ln A \rangle$, can be inferred from the measurement of the mean $X_{\max}$. Furthermore, the second central moment of the distribution of the logarithmic mass (spread of primary masses), $\sigma^2(\ln A)$, can be deduced [40] from the measurement of the second central moment of the $X_{\max}$ distribution. The two central moments of the logarithmic mass in the primary beam are defined by

$$\langle \ln A \rangle = \sum_{i=1}^{N} f_i \cdot \ln A_i, \qquad \sigma^2(\ln A) = \sum_{i=1}^{N} f_i \cdot (\ln A_i - \langle \ln A \rangle)^2. \tag{2.31}$$

From Figs. 2.6, 2.7 it can be also deduced that showers induced by iron nuclei have smaller shower–to–shower fluctuations than showers induced by protons of the same energy. This can be roughly understood using the superposition model, where the density of secondary particles of the Fe shower is averaged over 56 proton–like sub-showers with 56–times smaller energy than the energy of the Fe shower.

As studies of higher central moments generally require higher precision of the measured distributions and naturally also good reliability of MC predictions, only the first two central moments of the $X_{\max}$ distribution are typically used to analyze the current UHECR data. As the relation between the measured quantities and the central moments of $\ln A$ has to be obtained using assumptions about the details of hadronic interactions [40], the experimentally inferred $\langle \ln A \rangle$ and $\sigma^2(\ln A)$ suffer with relatively high systematic uncertainties coming from different predictions of different hadronic interaction models.

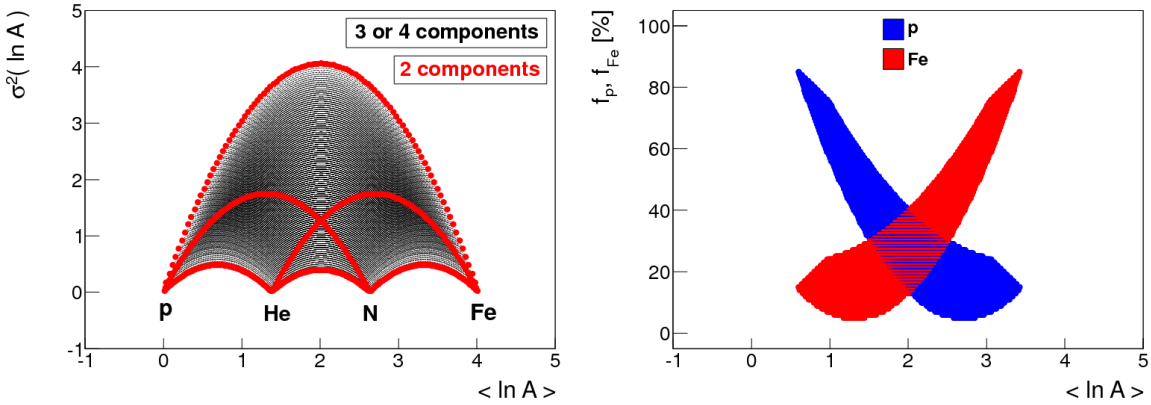

Figure 2.8: **Left panel:** Umbrella plot. Relation between the variance of the logarithmic mass, $\sigma^2(\ln A)$, and the mean logarithmic mass, $\langle \ln A \rangle$, is illustrated for two components in red, for three and four components in black. All possible compositions of p, He, N and Fe with relative abundances in steps of 1% were considered. **Right panel:** Possible fractions of primary protons (f_{p} in blue) and possible fractions of iron nuclei (f_{Fe} in red) for all four component scenarios with primary fractions in steps of 1% satisfying $2 < \sigma^2(\ln A) < 3$ as a function of $\langle \ln A \rangle$.

The importance of the measurement of $\sigma^2(\ln A)$ can be seen in the left panel of Fig. 2.8 where the "phase space" of $\sigma^2(\ln A)$ and $\langle \ln A \rangle$ is depicted for all mass composition scenarios of p, He, N and Fe with relative abundances in steps of 1%. The combinations of only two primaries are shown in red. For instance, measuring the value of $\sigma^2(\ln A)$ between 2 and 3 would suggest the presence of protons and iron nuclei in the studied sample of showers. Then, the possible fractions of protons and the possible fractions of iron nuclei can be estimated from the right panel of Fig. 2.8 for any measured value of $\langle \ln A \rangle$. In this plot, these possible fractions are depicted for any combination of the four primaries in steps of 1% satisfying $2 < \sigma^2(\ln A) < 3$.

Of course, every such a deduction can be made only by the assumption that the measured quantities after the transformation to $\langle \ln A \rangle$ and $\sigma^2(\ln A)$ lie inside the region indicated in the left panel of Fig. 2.8. In other words, this "umbrella" plot restricts also the measurable values of quantities that can be transformed to $\langle \ln A \rangle$ and $\sigma^2(\ln A)$ for certain hadronic interaction model. This provides the opportunity for testing the predictions of hadronic interaction models.

Chapter 3

Pierre Auger Observatory

The largest experiment ever built that measures extensive air showers induced by UHECR, the Pierre Auger Observatory, is briefly described in this chapter. The instrument is described in more detail in [22]. The physics results achieved at the observatory that are relevant for the content of this thesis are emphasized at the end of this chapter.

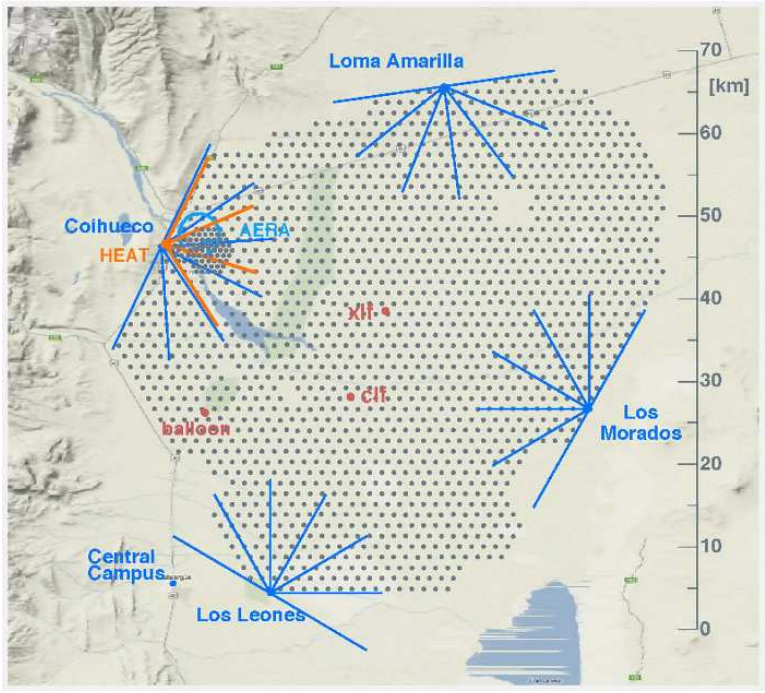

Figure 3.1: Schematic view of the Pierre Auger Observatory. The array of gray points represents the positions of stations of the surface detector. The names of 4 fluorescence detector buildings are shown in blue together with the illustration of azimuthal field of view of the individual fluorescence telescopes. Positions of stations for atmospheric monitoring are marked in red. The location of additional radio detection stations (AERA) and of the enhancement of the fluorescence detector (HEAT) are also shown together with the position of the Central Campus. Picture comes from [41].

The observatory was built in Argentinian Pampa at altitude about 1 400 m a.s.l. in the province Mendoza, near the city Malargüe, to observe UHECR arriving dominantly from the southern sky. The ground detection of secondary particles with water Cherenkov detectors covering an area of 3 000 km^2 is combined with the optical observation of the emission light produced in the atmosphere using fluorescence telescopes. The fluorescence detector buildings surround the array of surface detectors at 4 sites (see Fig. 3.1). The construction of the observatory started in 2001 and after the era of the Engineering Array [42] the observatory started to collect scientific data in 2004. The deployment of the designed observatory with 1 600 tanks and 24 fluorescence telescopes was finished in April 2008. Nowadays, including additional enhancements to extend the energy coverage down to $\sim 10^{17}$ eV, more than 1 660 water Cherenkov stations and 27 fluorescence telescopes are installed in total. The Pierre Auger Collaboration is a community of more than 500 members from 17 countries.

Besides a huge aperture (volume of atmosphere available for shower detection), the uniqueness of the Pierre Auger Observatory lies in the simultaneous observation of cosmic–ray showers with two different detection techniques. In the so–called hybrid measurement, the arrival time of shower to the ground registered by at least one station of the surface detector is used to constrain the longitudinal profile of shower that is reconstructed with the fluorescence telescopes. Such longitudinal profile provides a very precise measurement of the EM component as a function of atmospheric depth and consequently a precise measurement of the shower energy. Moreover, the events reconstructed simultaneously with surface and fluorescence detectors (so–called Golden events) are used to calibrate the surface detector signal by the energy measured with the fluorescence detector. The previous giant–array experiments (e.g. AGASA [43]) relied on the MC predictions for the energy calibration of the surface detector signal. This was shown to be very questionable because of the persisting incapability of MC simulations to reproduce the signals of ground arrays as it will be further discussed in this thesis.

3.1 Surface Detector

The Surface Detector (SD) at the Pierre Auger Observatory consists of 1 600 water Cherenkov stations. These particle detectors are aligned in the regular triangular grid with 1 500 m spacing representing the main detector covering 3 000 km^2. Since September 2011, there are also more than 60 stations deployed in the denser grid with spacing 750 m – Infill, near the FD site Coihueco, allowing to observe showers with energies down to $\sim 10^{17}$ eV at area 23.5 km^2.

In each station, 12 m^3 of purified water (1.2 m deep cylinder placed on area 10 m^2) form the radiative medium for Cherenkov photons. These photons are produced by charged particles traversing the medium with velocity higher than c/n where n is the refractive index of water $\sim$1.33 and c is the speed of light in vacuum. For muons the energy threshold for production of Cherenkov photons equals to 160 MeV. The produced photons are reflected from the inner walls of the tank and, in the end, they are collected by 3 photomultipliers (PMTs) of 9 inch diameter placed at the top of the station. The

schematic description of the instrument of one water Cherenkov station is shown in Fig. 3.2. The signal in the SD station is sensitive to electrons, gammas (creation of $e^{\pm}$ pairs) and muons as well. The induced signal is measured in VEM (Vertical Equivalent Muon) units, which is the signal induced by a single muon of energy 250 MeV penetrating the detector in vertical direction.

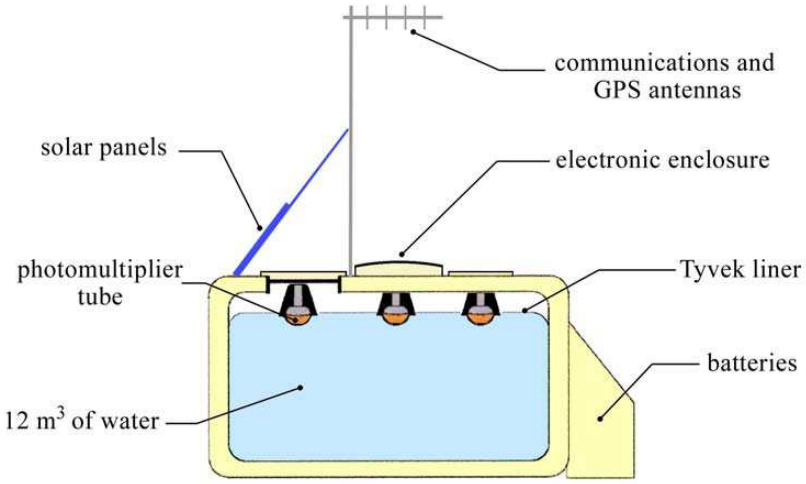

Figure 3.2: Description of the water Cherenkov station deployed at the Pierre Auger Observatory. Cross–section of the cylindrical tank with accessories is depicted. Picture is obtained from [42].

The direction of the shower axis and the position of the shower core[1] are obtained from the recorded signals and trigger times at each of the triggered stations. The direction of the shower axis is then reconstructed with a resolution better than 1° at 10 EeV [44] (depending on the number of hit stations). The main SD has an equal probability ($\geqq 0.95$) to trigger showers induced by protons and iron nuclei for energies above $10^{18.5}$ eV. Analogously, in case of the Infill array the trigger reaches almost the full efficiency above $10^{17.5}$ eV. The zenith angle is covered from 0 to 60° in case of the main array and from 0 to 55° in case of the Infill. More detailed description of the SD and its trigger conditions can be found in [45].

There is also a possibility to reconstruct horizontal ($62° \leq \Theta \leq 80°$) events [46]. For such high zenith angles the signal in the SD is induced dominantly by muons as the EM component is already too much absorbed in such atmospheric depths (> 1870 g/cm^2).

3.2 Fluorescence Detector

The Fluorescence Detector (FD) collects the emitted fluorescence light of nitrogen molecules (300–400 nm) that were excited and ionized by charged secondary particles. The amount of emitted light is actually proportional to the energy deposit of secondary electrons. The emission induced by muons is at 1% level wrt. total amount of fluorescence emission because of their very low ionization losses. The

[1]Position where the shower axis intersects the ground.

fluorescence emission is isotropic compared to the collimated Cherenkov light that is also produced during the propagation of secondary particles in the atmosphere. Therefore, the produced fluorescence light can be observed from wide observation angles and far distances. Together with the background noise, the direct and the scattered Cherenkov light needs to be subtracted from the total signals in the FD; especially for showers hitting the ground in direction towards the aperture of a fluorescence telescope. The fluorescence light is very weak and therefore the data taking is limited to nights with the moon fraction below ~60%. It has a consequence that the duty cycle of the total time is only about 13 % on the contrary to the almost fully efficient SD.

Each of 4 fluorescence detector buildings is composed of 6 fluorescence telescopes. These buildings are situated at top of 4 small hills to observe the atmospheric volume above the SD array by each telescope 30° in the horizontal direction and 1.4–30° in the elevation. The schematic illustration of one FD building (left) and one fluorescence telescope (right) is shown in Fig. 3.3. The light after passing the UV filter is reflected from the segmented mirrors of total area ~13 m^2 to the array of 440 hexagonal PMTs, each covering a region of 1.5° × 1.5° of the sky. A pixel triggered by EAS provides information about the number of detected photons (the deposited energy) and the time of detection at certain longitudinal direction of the shower. More detailed description of the FD and the trigger hierarchy is given in [47].

Another 3 fluorescence telescopes, denoted as High Elevation Auger Telescopes (HEAT) [48], were installed at Coihueco site with a possibility to tilt them upwards observing higher parts of the shower development. This is important for low energy showers with the shower maximum outside the standard field of view of the telescopes and it improves the reliability of reconstructed shower properties.

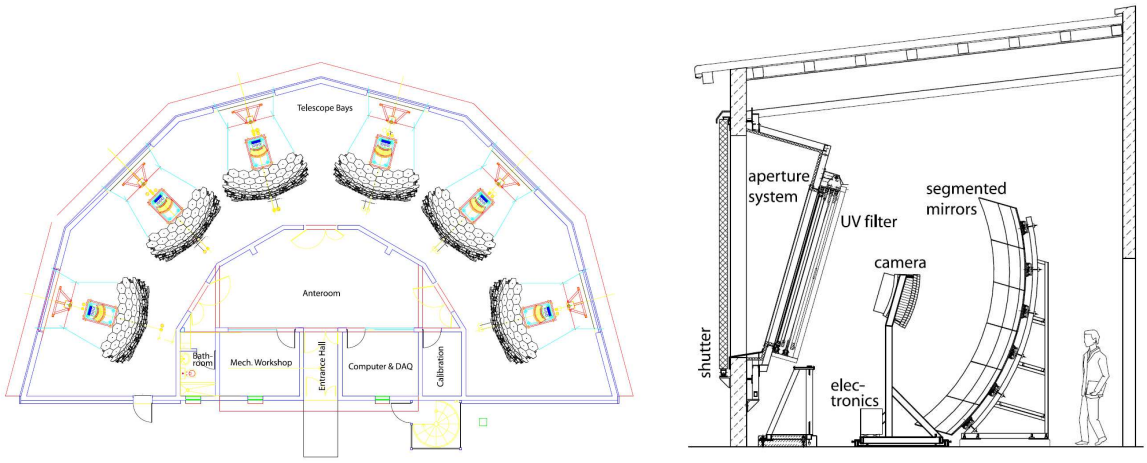

Figure 3.3: **Left panel:** Schematic top view of the fluorescence detector building with 6 bays containing fluorescence telescopes. **Right panel:** Schematic side view of the fluorescence telescope with major parts of the instrument described. Pictures are obtained from [47].

As the Pierre Auger Observatory utilizes the atmosphere as a huge calorimeter, it is necessary to monitor the atmosphere accordingly. Vertical Aerosol Optical Depth (VAOD) reflects the content of aerosols in the atmosphere that can dilute the observed longitudinal profile of shower substantially. VAOD is measured on an hourly basis using two central laser facilities (CLF, XLF) and cross–checked by lidars that operate at each FD site. Clouds can suppress the FD signal or increase the background due to the light scattering in the cloud. Therefore the clouds are monitored with infra cameras and with background–light cameras of fish–eye shape at each FD site. The cloud coverage is furthermore checked by the Geostationary Operational Environmental Satellites. The atmospheric properties, such as the air density or the air humidity, are obtained from Global Data Assimilation System every three hours. The atmospheric parameters monitored by these instruments are taken into account in the shower reconstruction. More information about the atmospheric monitoring at the Pierre Auger Observatory can be found in [49].

Using the hybrid reconstruction, the direction of the shower axis is reconstructed with a precision typically well below 1° and the core location within 100 m depending on the observation conditions (atmosphere, shower geometry wrt. telescope aperture etc.). The depth of shower maximum can be obtained with a precision ∼20 g/cm^2 applying the quality cuts.

3.3 Shower Energy

The energy of EAS is one of the most important information about the primary particle inducing the shower. Determination of the shower energy has impact on various aspects of UHECR study (energy spectrum, elongation rate, energy threshold for anisotropy searches etc.) and therefore its precise measurement is of a crucial importance.

3.3.1 FD Energy

The detection method based on the emission of fluorescence light from nitrogen molecules is not only an interesting and elegant detection technique, but it is also a very accurate mean of estimation of the shower energy. The knowledge of the fluorescence yield[2] as a function of air pressure, air temperature and air humidity allows to convert the signal induced in the FD photomultiplier (colored pixels in left panel of Fig. 3.4) to the deposited energy at certain depth along the shower axis. The calorimetric energy of EAS is then inferred integrating the longitudinal profile of the deposited energy. The longitudinal profile (energy losses dE/dX as a function of the atmospheric depth X) is approximated by the so–called Gaisser–Hillas function [51] (see right panel of Fig. 3.4) as

$$\frac{\mathrm{d}E}{\mathrm{d}X}(X) = \frac{\mathrm{d}E}{\mathrm{d}X}(X_{\max}) \cdot \left(\frac{X - X_0}{X_{\max} - X_0}\right)^{\frac{X_{\max}-X_0}{\lambda}} \cdot \mathrm{e}^{\frac{X_{\max}-X}{\lambda}} \tag{3.1}$$

[2]The fluorescence yield is the number of photons of given wavelength (usually 337 nm) emitted by 1 MeV of the deposited energy in the air of normal conditions (1013 hPa, 293 K). The most precise measurement so far [50] gives the value $5.61 \pm 0.06_{\mathrm{stat}} \pm 0.21_{\mathrm{syst}}$ photons/MeV.

where $X_{\max}$ corresponds to the depth of shower maximum and X_0, λ are other fitting parameters[3].

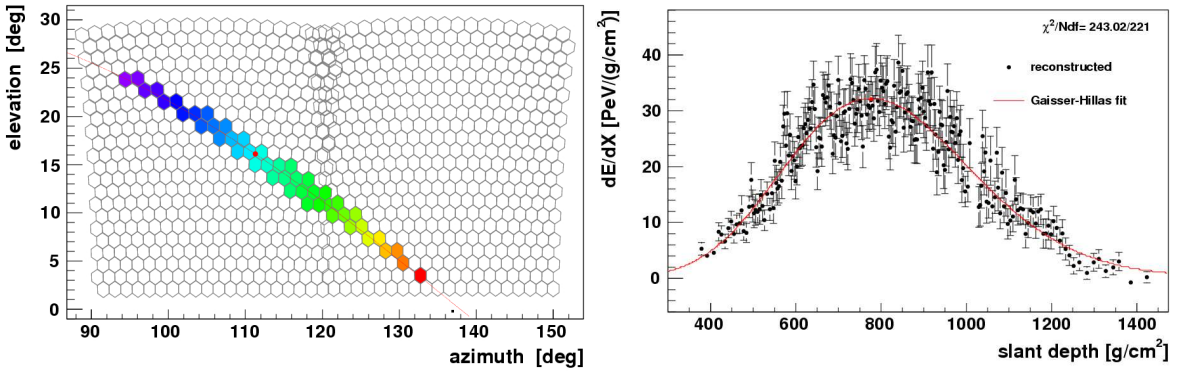

Figure 3.4: **Left panel:** An example of EAS reconstructed with two fluorescence telescopes at the Pierre Auger Observatory. Color of pixels denotes the time sequence of detection (from purple to red). Red point corresponds to the position of the shower maximum along the shower axis (red line). **Right panel:** The reconstructed longitudinal profile fitted with the Gaisser–Hillas function. The pictures were obtained using the code EventBrowser provided in the package Advanced Data Summary Tree (ADST) [52].

Because of low ionization losses of muons, the size of the calorimetric energy is actually the size of the electromagnetic component only. Therefore it is needed to correct the calorimetric energy for the part of energy that is carried away by muons, neutrinos and hadrons (so–called missing energy or invisible energy) to obtain the energy of the whole shower $E_{\rm FD}$ measured by the FD. The missing energy at the Pierre Auger Observatory is inferred using Golden events. It is assumed to be proportional to the muon shower size [53], which is estimated using the SD signal [54]. This method is illustrated in Fig. 3.5. Note that the missing energy inferred using the measured data is higher than the MC predictions by ∼30%.

The systematic uncertainty of $E_{\rm FD}$ due to the correction for missing energy is 3 % at 10^{18} eV and 2% at 10^{19} eV [54]. The total systematic uncertainty of the FD energy reconstructed at the Pierre Auger Observatory is estimated to be 14 % [55] and it is dominated by the uncertainty of the absolute calibration of the PMT responses[4]. The resolution of $E_{\rm FD}$ is estimated to be 7–8% [55]. The reconstructed energy has very small bias wrt. the mass composition of primary particles since the calorimetric energy is formed dominantly by the EM component; see also Eq. (2.27).

The weak point of the fluorescence detection lies in the fact that the fluorescence light is not very bright and can be easily overwhelmed by the background light. Attention is thus paid to a continuous monitoring of the background light intensity. Since the light can be also lost in clouds or scattered on aerosols the atmospheric monitoring plays a very important role at the observatory.

[3] X_0 is usually referred to as the position of the first interaction, but in the Gaisser–Hillas fit it may become even unphysical negative values. The parameter λ reflects the steepness of increase and decrease of dE/dX with X.

[4] Note that the systematic uncertainty improved considerably (from 22 %) in 2013 mainly due to the precise measurement of the fluorescence yield [55].

Another important issue is the stability of the FD response to a shower and its absolute sensitivity. Therefore the relative calibrations of PMT responses are performed every night before and after the data taking to reflect the actual conditions for the FD measurement. These relative calibrations are related to the absolute calibration which is performed using the homogeneous source of light of known intensity; approximately once per year.

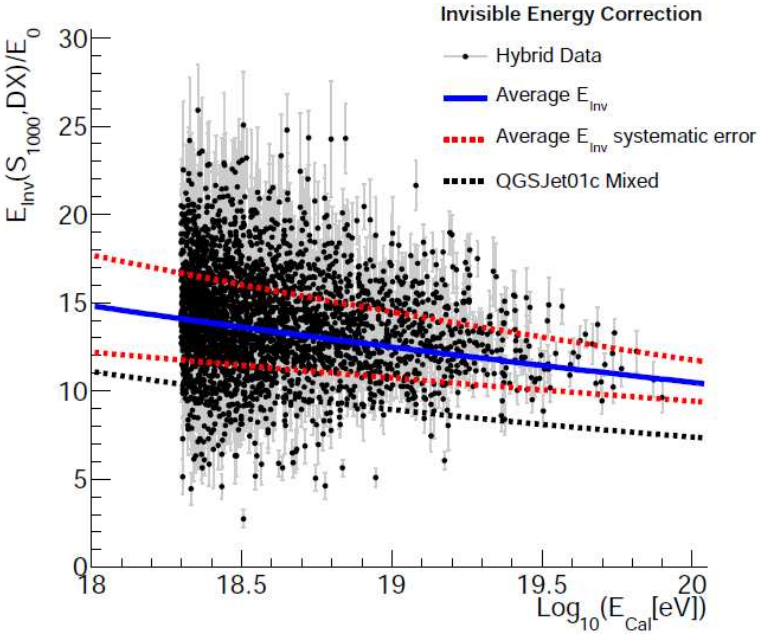

Figure 3.5: The correction factor of the missing energy relative to the shower energy E_0 depending on the logarithm of the calorimetric energy E_{Cal}. The Golden events in a bin of the ground signal and in a bin of $DX = X_{\mathrm{ground}} - X_{\mathrm{max}}$ were used. The picture comes from [54].

3.3.2 SD Energy

The dependence of the signal (S) measured in the SD station at the perpendicular distance (r) to the shower axis is called the Lateral Distribution Function (LDF). It can be described by the modified NKG type function [56, 57] of general form as

$$S(r) = k \cdot \left(\frac{r}{r_s}\right)^{-\beta} \cdot \left(1 + \frac{r}{r_s}\right)^{-\beta} \tag{3.2}$$

where the parameter k reflects the shower size, the parameter β is the LDF slope and r_s was set to 700 m for the array spacing (1500 m) of the Pierre Auger Observatory. The geometry of the SD alignment has a consequence that the optimal distance from the shower core where the uncertainty in the signal estimation due to a lack of knowledge of the LDF is minimized approaches about 1000 m. Illustration of this statement with a simulated shower is shown in Fig. 3.6 for different LDF shapes.

Therefore $S(1000\text{ m})$, denoted as $S(1000)$, is used as the shower signal in the SD that is directly related to the shower energy at the Pierre Auger Observatory.

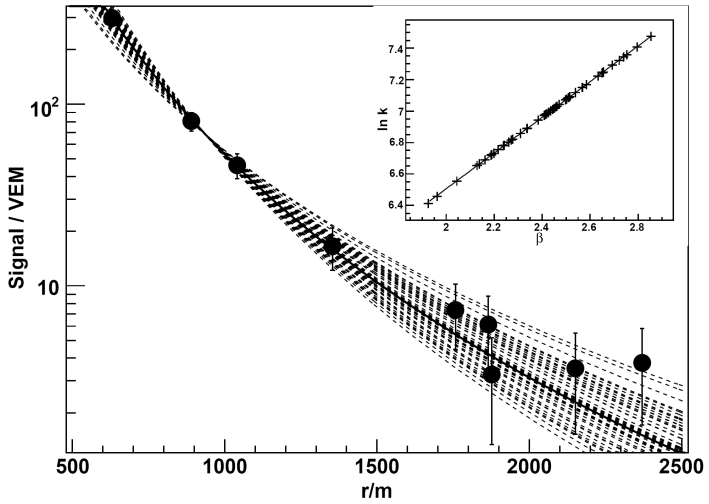

Figure 3.6: Reconstructed LDF of NKG type for 50 different values of the LDF slope for a single MC shower. The inset plot shows the relationship between the shower size and the LDF slope, from which the optimum distance can be derived analytically. Picture is obtained from [58].

Nevertheless, showers of the same energy but of different zenith angles induce different signals in the SD due to the different amount of atmosphere passed before reaching the ground. This effect is corrected using the Constant Intensity Cut (CIC) method [59]. The method is applied to the measured data only. It utilizes the fact that cosmic rays are isotropic at lower energies and therefore also the integral intensity of cosmic rays above a certain low energy is isotropic. At first, all events are ordered in bins of $\cos^2(\Theta)$ according to the value of $S(1000)$. Then, every n^{th} value (arbitrary cut corresponding to a flux above a certain energy) of $S(1000)$ is selected for every bin in $\cos^2(\Theta)$ to satisfy the isotropic assumption. The obtained dependence of $S(1000)$ on the zenith angle (attenuation curve) is shown in the left panel of Fig. 3.7. This dependence is usually fitted with quadratic or cubic function in $\cos^2(\Theta)$. Assuming that the shape of the attenuation curve does not depend much on the shower energy (within few % [60]) only a single shape of the attenuation curve (so–called CIC curve) is needed to correct the SD signals of all the detected showers. The median of the distribution of the zenith angle of UHECR with energy above 3 EeV ($\Theta = 38^\circ$) was chosen as the reference angle to convert the corrected $S(1000)$ to the shower energy. This parameter, S_{38}, is actually the parameter $S(1000)$ induced by the shower of the same energy, but with the zenith angle 38°.

In case of the Infill, where the spacing of stations is smaller (750 m), the optimal distance and the reference angle are 600 m and 35°, respectively. The parameter used for the estimation of the shower energy is denoted S_{35}. For the inclined showers the parameter N_{19} is obtained applying muon maps to incorporate the geomagnetic effects on the propagation of muons [46].

The hybrid structure of the Pierre Auger Observatory provides a great opportunity to calibrate the

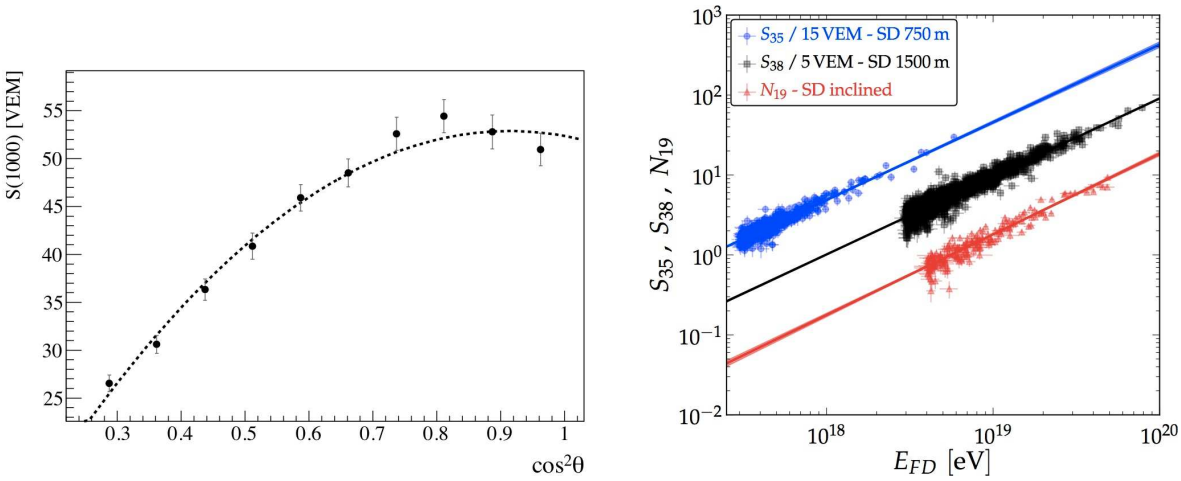

Figure 3.7: **Left panel:** The attenuation curve (quadratic fit) of the SD signal with zenith angle inferred at ∼7 EeV. Picture comes from [61]. **Right panel:** Signals in the SD (S_{38} for the main array within 60°, N_{19} for the main array with $62° \leq \Theta \leq 80°$ and S_{35} for the Infill within 55°) calibrated with the FD energy (E_{FD}) for high quality Golden events. The Maximum Likelihood fits are also shown. Picture comes from [44].

SD signal by the precisely measured FD energy. This calibration procedure assumes the relation

$$E_{\mathrm{FD}} = a \cdot (S_{38})^b \tag{3.3}$$

where $a = (0.190 \pm 0.005)$ EeV and $b = 1.025 \pm 0.007$ [44] are the calibration coefficients for the main array inferred from the Maximum Likelihood fit. High quality Golden events were selected for the calibration procedure and they are plotted in the right panel of Fig. 3.7 for the main array (black), Infill (blue) and inclined showers (red) together with the Maximum Likelihood fits. The value of the fitted parameter b in Eq. (3.3) for corresponding reference signals was around 1 in all three cases. Threshold energies to trigger showers induced by protons and iron nuclei with the same probabilities are 3 EeV, 0.3 EeV and 4 EeV for the main array, Infill and inclined showers, respectively. The importance of this calibration procedure lies in the independence on MC simulations. The energy resolution of the E_{SD} for the main array is estimated to be 17–12% improving with energy [55].

3.4 Selected Physics Results of the Pierre Auger Observatory

The measurements of the Pierre Auger Observatory that are relevant for the content of the thesis are shown and briefly discussed in this section. The processing of measured and simulated data is concisely described e.g. in [62].

3.4.1 Energy Spectrum

The spectrum of cosmic rays measured by the Pierre Auger Observatory span over almost three orders of magnitude in energy. The low energy part (above $10^{17.5}$ eV) is obtained by the Infill, followed by the hybrid spectrum (above $10^{18.0}$ eV) and the spectrum collected by the main array (above $10^{18.5}$ eV) and it is complemented with the spectrum of inclined events (above $10^{18.6}$ eV). The individual spectra of these four measurements are shown in the left panel and their overall combination in the right panel of Fig. 3.8.

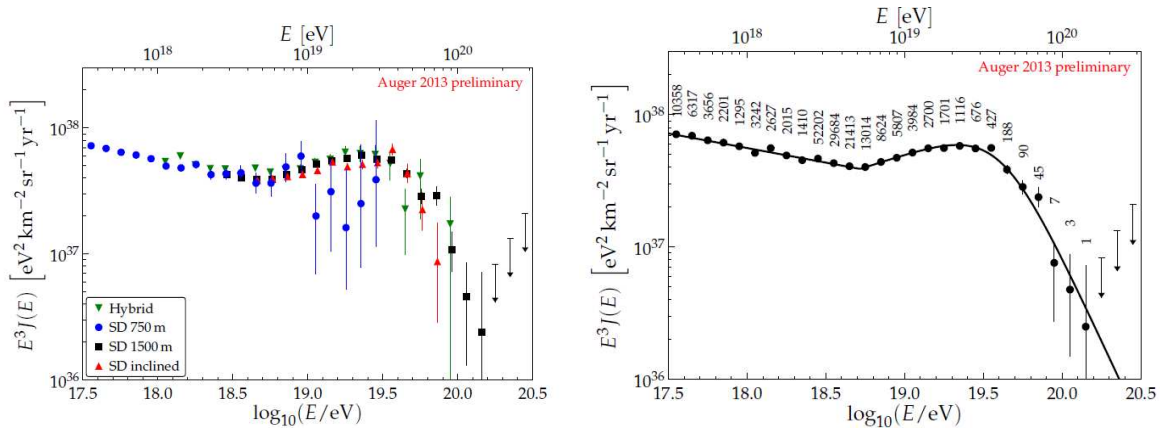

Figure 3.8: **Left panel:** Spectra of cosmic rays measured by the Pierre Auger Observatory using SD and hybrid data. **Right panel:** The combined spectrum of the Pierre Auger Observatory together with indicated number of detected events. Note that the flux is multiplied by E^3 to better visualize the change of the spectral index. Pictures come from [44].

The spectra of all four independent data samples are consistent and two main features are clearly visible: the so–called ankle at energy ~$10^{18.7}$ eV (~5 EeV) and the steep decrease of the flux above ~$10^{19.5}$ eV (~30 EeV). The ankle is formed by hardening of the spectrum at energies above $10^{18.7}$ eV. In case of pure proton primaries, this spectral feature could be explained by the so–called dip model [63] where such a "dip" in the spectrum is a consequence of $e^{\pm}$ pair creations on the cosmic microwave background. An alternative explanation [64] of the ankle is the transition from the Galactic component of cosmic rays (below the ankle energy) to the Extragalactic component of cosmic rays (above the ankle energy) with a smaller spectral index. The latter explanation of the ankle does not need any assumptions about the UHECR composition. The origin of the ankle can be also explained by a photo-disintegration of ultra–high energy nuclei in the region surrounding the UHECR accelerator [65].

The steep decrease above ~$10^{19.5}$ eV is confirmed at a more than 20 σ c.l. [66]. Two alternative explanations are discussed in the literature most frequently. The first one describes this steep decrease as the consequence of the GZK effect of protons described in Section 2.1.3. The other alternative interprets this spectral feature as the consequence of limited energies to which the UHECR sources can accelerate UHECR nuclei.

3.4.2 Mass Composition

Studies of the mass composition of primary particles using the measurement of $X_{\max}$ (EM component from FD) and the measurement of the maximum of muon production depth $X^{\mu}_{\max}$ (muon component from SD) are presented in the following text together with the study of correlation between the ground signal and $X_{\max}$. Moreover, an excess of muons observed with the Pierre Auger Observatory data wrt. MC predictions is also discussed.

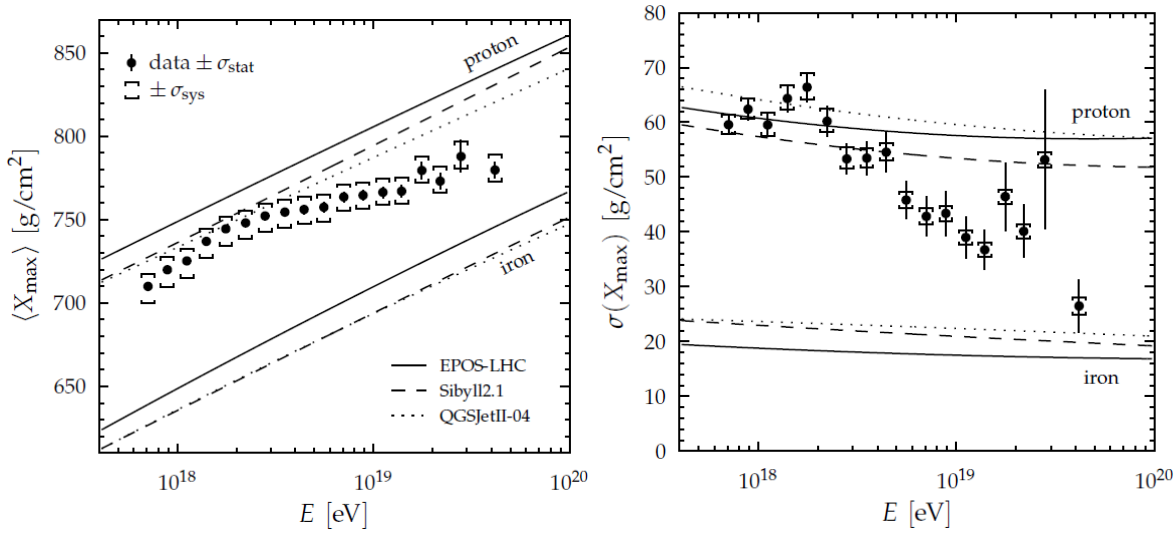

Figure 3.9: Energy evolution of the mean of the $X_{\max}$ distribution (**left panel**) and the squared root of the variance of the $X_{\max}$ distribution (**right panel**). MC predictions for showers induced by protons and iron nuclei are shown for three models of hadronic interactions. Pictures come from [67].

Depth of Shower Maximum

It was shown in Sec. 2.2 that $X_{\max}$ is sensitive to the mass composition of primary particles. In Fig. 3.9, the first two central moments of the measured distributions of $X_{\max}$ for hybrid showers measured at the Pierre Auger Observatory are plotted as a function of energy. Comparing with MC predictions of three models of hadronic interactions (QGSJet II–04 and EPOS–LHC [68, 69] are tuned with the LHC data (run I), whereas Sibyll 2.1 [70] is not), it seems that the mass composition of UHECR is getting lighter up to energy ~2 EeV where UHECR could be dominated by proton primaries. For energies above ~2 EeV, the mass composition is getting steadily heavier with increasing energy up to ~40 EeV. The cuts removing the effect of the limited field of view of the fluorescence telescopes with respect to various shower geometries were applied together with selection cuts ensuring high quality of the reconstructed $X_{\max}$ and no bias in $X_{\max}$ wrt. the mass composition of primary particles [67]. The systematic uncertainty in case of $\langle X_{\max} \rangle$ is estimated to be below 10 g/cm^2 for all energy bins and in case of $\sigma(X_{\max})$ about few g/cm^2 which is even smaller than the statistical uncertainty. Thorough

tests of the presented systematic uncertainties were performed in [67]. The resolution of the $X_{\max}$ measurement improves with energy and was estimated to be below 20 g/cm^2 above the ankle energy.

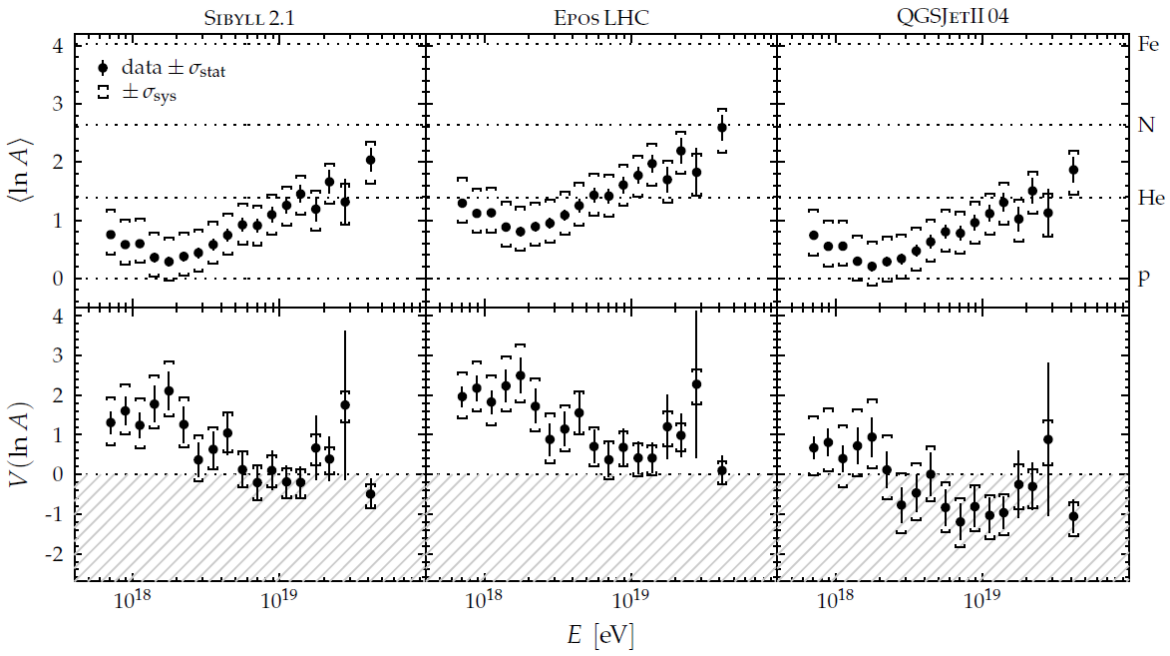

Figure 3.10: Energy evolution of $\langle \ln A \rangle$ (**top panels**) and $\sigma^2(\ln A)$ (**bottom panels**) for three models of hadronic interactions. Picture comes from [67].

The interpretation of the $X_{\max}$ measurement using the first two central moments of $\ln A$ was presented in [40]. Their dependence on the shower energy for three models of hadronic interaction models is shown in Fig. 3.10.

The plots of $\langle \ln A \rangle$ in upper panels of Fig. 3.10 visualize, what was already evident in Fig. 3.9, that the mass composition of cosmic rays is in average lightest around the energy 2 EeV. Approximately (considering all the three models), $\langle \ln A \rangle$ decreases from the value in the range of $0.5 < \langle \ln A \rangle < 1.5$ to the minimal value in the range of $0 < \langle \ln A \rangle < 1$ at the energy 2 EeV. Beyond this energy, the value of $\langle \ln A \rangle$ increases steadily up to the value in the range of $1.5 < \langle \ln A \rangle < 3$.

The variances of $\ln A$ (bottom panels in Fig. 3.10) suffer naturally with higher statistical errors than the means of $\ln A$. Note that the variances of $\ln A$ for QGSJet II–04 even become negative which are unphysical solutions. Thus, an arbitrary systematic shift of $\sigma^2(\ln A)$ by +1.0 at all energies for QGSJet II–04 can be considered to obtain physically reasonable values with $\sigma^2(\ln A) > 0$. Then, when only the statistical uncertainties are considered, all three models together constrain $\langle \ln A \rangle$ and $\sigma^2(\ln A)$ as

- $\log(E_{\rm FD}) = 17.8 - 17.9$: $0.5 < \langle \ln A \rangle < 1.5$ and $1.0 < \sigma^2(\ln A) < 2.0$,
- $\log(E_{\rm FD}) = 18.2 - 18.3$: $0.0 < \langle \ln A \rangle < 1.0$ and $1.5 < \sigma^2(\ln A) < 3.0$,
- $\log(E_{\rm FD}) \approx 19.6$: $1.5 < \langle \ln A \rangle < 3.0$ and $0.0 < \sigma^2(\ln A) < 1.0$.

Note that $\log(E_{\mathrm{FD}}) = 18.2 - 18.3$ corresponds to energies around 2 EeV where $\langle \ln A \rangle$ reaches its minimum. These three ranges of $\sigma^2(\ln A)$ are used in Fig. 3.11 to plot the corresponding possible fractions of protons and iron nuclei as it was demonstrated at the end of Section 2.3.

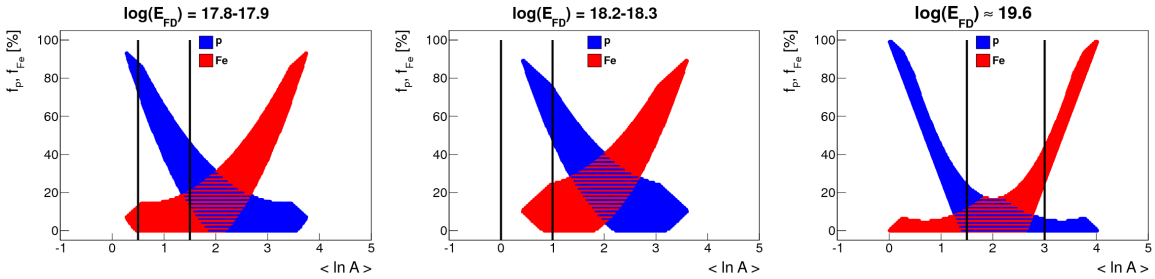

Figure 3.11: Possible fractions of protons (f_{p} in blue) and possible fractions of iron nuclei (f_{Fe} in red) for all combinations of four primaries (p, He, N and Fe) in steps of 1% depending on $\langle \ln A \rangle$. These possible fractions are depicted only for combinations of primaries satisfying $1 < \sigma^2(\ln A) < 2$ (**left panel**), $1.5 < \sigma^2(\ln A) < 3$ (**middle panel**) and $0 < \sigma^2(\ln A) < 1$ (**right panel**). The ranges of $\langle \ln A \rangle$ estimated from Fig. 3.10 are indicated by black lines.

Analogously to the left panel of Fig. 2.8, all combinations of four primaries (p, He, N, Fe) in steps of 1% were considered to fill the region in the $(\sigma^2(\ln A), \langle \ln A \rangle)$ plane. Then, from the measured ranges of $\sigma^2(\ln A)$ and $\langle \ln A \rangle$, the possible fraction of protons is estimated to increase from 15–85% at ~0.7 EeV to 50–90% at the energy ~2 EeV. Beyond this energy, it decreases down to a value below 20% at the energy ~40 EeV. Similarly, the possible fraction of iron nuclei is estimated to be below 20% at ~0.7 EeV and below 25% at the energy ~2 EeV. At the energy ~40 EeV, the fraction of iron nuclei can be 40% at most.

Following the X_{max} distributions published in [67], the most probable fractions of the assumed primaries were inferred in [71]. For each energy bin, the measured X_{max} distribution was compared with combinations of simulated X_{max} distributions of four different primaries (p, He, N, Fe) to find the most probable combination of these primaries that describes the measured X_{max} distribution. The results are shown in Fig. 3.12 for three models of hadronic interactions together with the p-value of the Maximum Likelihood fits. Note that up to the energy $\sim 10^{19}$ eV all three models of hadronic interactions estimate the proton plus helium fraction to be above 50%.

Maximum of Muon Production Depth

For showers with the zenith angle around 60° the signal reconstructed in the SD is dominated by the muon component as the EM component is highly absorbed in the atmosphere. The secondary muons propagate through the atmosphere approximately along straight lines with the speed of light. Since these muons come from decays of charged pions and kaons, their production carries information about the high energy interactions of hadrons and therefore also some information about the type of the primary particle.

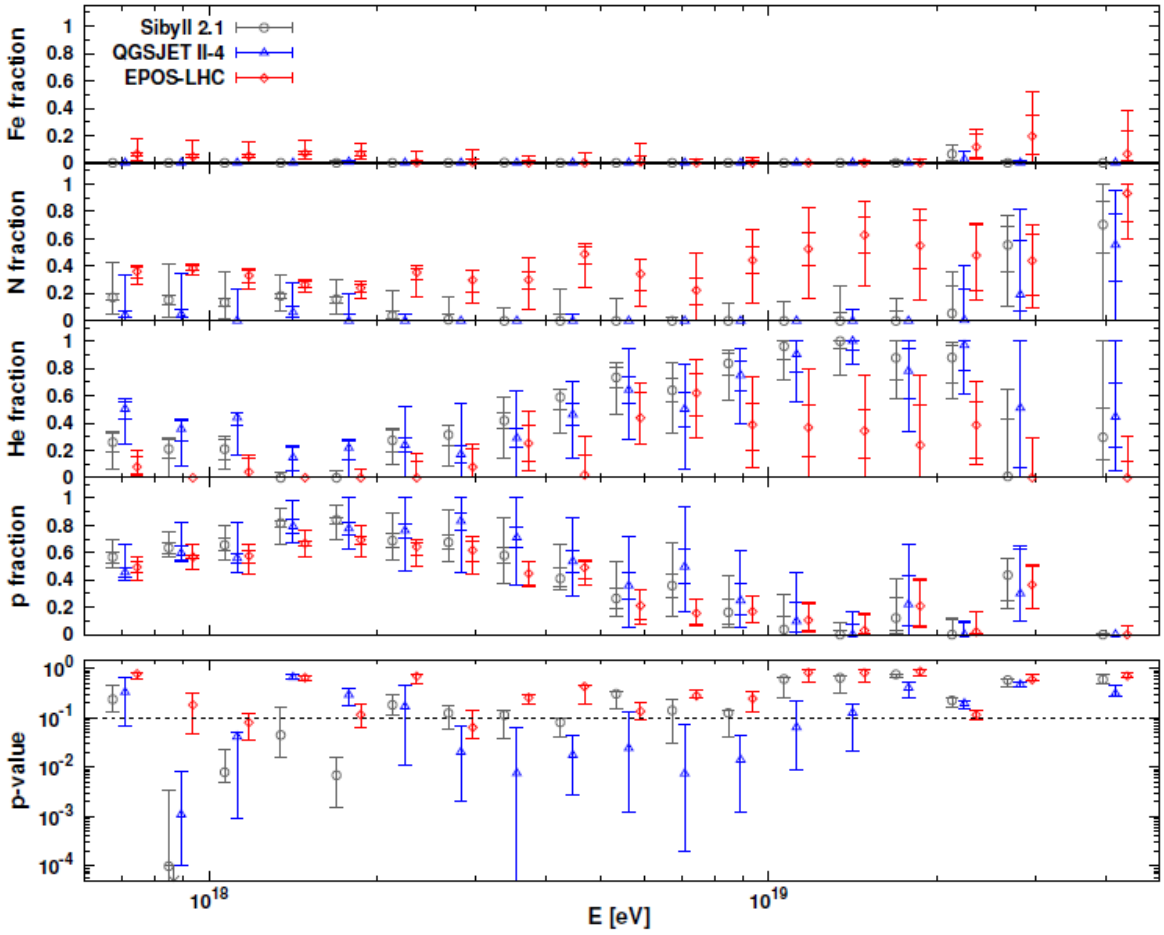

Figure 3.12: Energy evolution of the primary fractions inferred from the comparison of measured and simulated X_{max} distributions for four primary particles (p, He, N, Fe). The p-value corresponding to the Maximum Likelihood fit is shown in the undermost panel. For each energy bin the points of the three models were slightly shifted for better visibility. Picture comes from [71].

A geometric reconstruction (see the schematic drawing in the left panel of Fig. 3.13) of the muon production depth (dependence of the number of produced muons on the shower depth) is possible at higher energies ($\gtrsim 10^{19}$ eV). At such energies, the muon density on ground is sufficiently high even for distances far from the shower core. When the shower axis is obtained from the standard SD reconstruction, the distance Δ can be derived from the time difference between the arrival of the shower front and of the individual muons. It provides information about the position of the production of muons along the shower axis. Single muons induce sharp spikes in the signal trace whereas the response of the shower front including also the EM component from the decayed muons is much broader in the signal trace. Therefore, the selection of spikes in the SD signal trace provides the opportunity how to select signals of the individual muons.

Events with $55° \leq \Theta \leq 65°$ and energy higher than 20 EeV were selected for the study of the muon production depth by the Pierre Auger Observatory [72]. For about 500 events, the signal traces

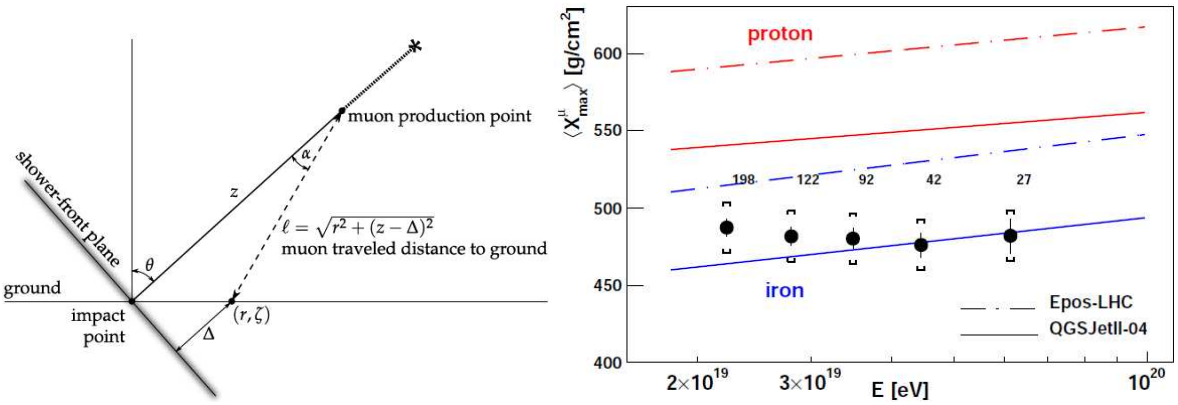

Figure 3.13: **Left panel:** Schematic drawing of geometric reconstruction of the muon production depth. **Right panel:** Energy evolution of the mean maximum of the muon production depth for data of the Pierre Auger Observatory. Number of events in energy bins are indicated. The MC predictions for two primaries and two models of hadronic interactions are depicted as well. Pictures come from [72].

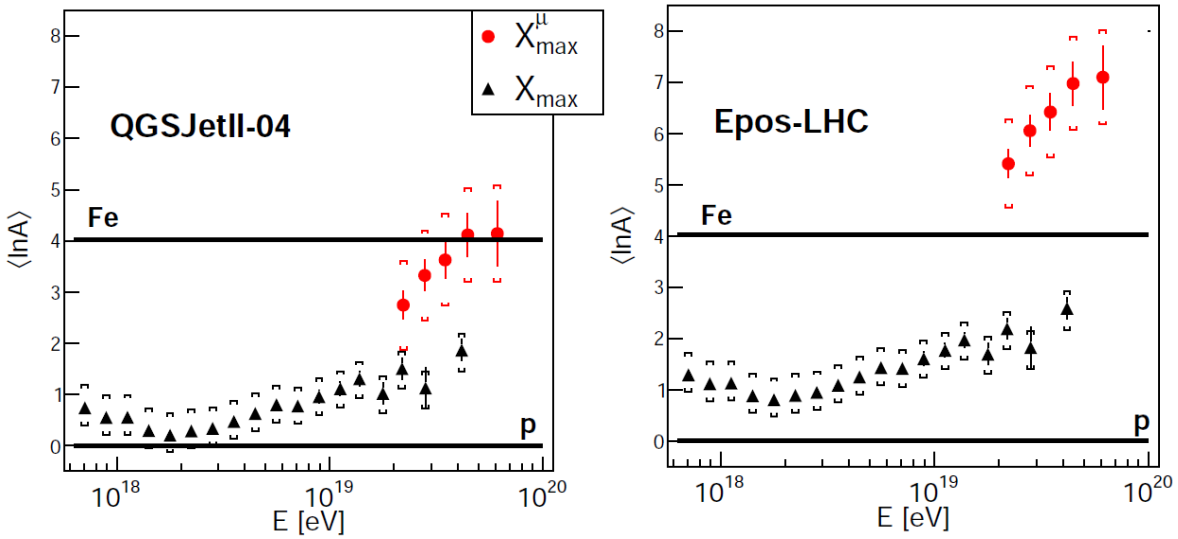

Figure 3.14: Energy evolution of the mean $\ln A$ inferred from $\langle X_{\mathrm{max}} \rangle$ and $\langle X^{\mu}_{\mathrm{max}} \rangle$ measurements using QGSJet II–04 (**left**) and EPOS–LHC (**right**). Values of $\langle \ln A \rangle$ for showers induced by protons and iron nuclei are indicated by thick horizontal lines. Pictures come from [72].

collected by stations farther than 1700 m from the shower core were used to reconstruct the muon production depths. The depth, at which the maximum of produced muons (X^{μ}_{max}) is measured, is sensitive to the type of the primary particle. A comparison of the measured data with MC predictions is shown in the right panel of Fig. 3.13. Note that for the model EPOS–LHC the data points lie outside the region between the predictions for showers induced by protons and iron nuclei. However, this inconsistency can be explained [73] by tuning of the pion diffraction for which only indirect

measurements of old experiments are available. This modification does not substantially affect other shower observables as X_{max} or particle densities on ground.

The mean $\ln A$ obtained from $\langle X_{\mathrm{max}} \rangle$ and $\langle X^{\mu}_{\mathrm{max}} \rangle$ measurements is plotted as a function of energy in Fig. 3.14 for the two models of hadronic interactions tuned to the LHC data. The interpretations of the SD and the FD measurements are inconsistent for both these models. A smaller tension between these interpretations is obtained in case of QGSJet II–04 than in case of EPOS–LHC. The results indicate that further tuning of models of hadronic interactions is still needed at accelerators to draw conclusions about the mass composition of cosmic rays from the X^{μ}_{max} measurement. On the other hand, measurements of X^{μ}_{max} can be used to test the models of hadronic interactions.

Correlation between Ground Signal and Depth of Shower Maximum

The mass composition of primaries can be addressed also using the combined measurement of the ground signal ($S\,1000$) and X_{max} of Golden events. The variance of the mass number can be inferred from the correlation coefficient (r_{G}) between these two quantities according to [74] when the muon shower size and X_{max} were considered. The application to the data of the Pierre Auger Observatory was performed in [75] for energies $10^{18.5-19.0}$ eV and zenith angles $0° - 65°$. The ground signal was corrected for the dependence on zenith angle and energy, denoted as $S^{*}(1000)$, and X_{max} was corrected for the energy dependence (X^{*}_{max}). Fig. 3.15 shows the comparison of the measured r_{G} with MC predictions of $\sigma(\ln A) = \sqrt{\langle \ln^2 A \rangle - \langle \ln A \rangle^2}$ for two models of hadronic interactions. The MC predictions were considered for all possible relative fractions of four primaries (p, He, O, Fe) in steps of 10%. For the single–mass composition of primary particles, r_{G} is positive or close to zero, whereas for the mixed composition scenarios r_{G} becomes negative. The data of the Pierre Auger Observatory indicate a mixed composition of nearby masses and excludes the pure proton composition with more than $5\,\sigma$.

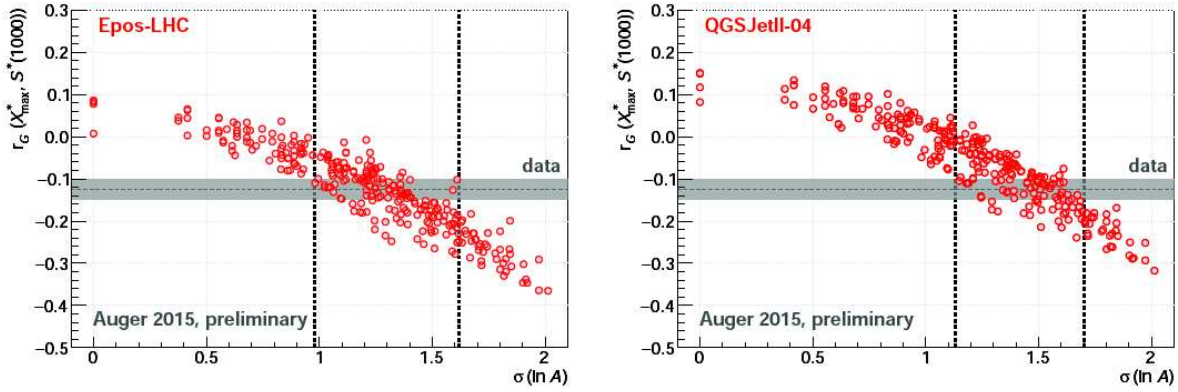

Figure 3.15: The correlation coefficient between the ground signal and the depth of shower maximum for energies $10^{18.5}$–$10^{19.0}$ eV compared with MC predictions for EPOS–LHC (**left**) and for QGSJet II–04 (**right**). All possible relative fractions of four primaries (p, He, O, Fe) in steps of 10% were considered. Pictures come from [75].

Excess of Muons

As already indicated, on one hand, the mass composition of UHECR can be inferred by assuming the validity of certain model of hadronic interactions. On the other hand, UHECR data provide an opportunity to test the reliability of these models. When the measured data lie outside a region restricted by MC predictions for showers induced by protons and iron nuclei with certain model of hadronic interactions, there is a strong indication that something is wrong with this model (e.g. $\sigma^2(\ln A)$ for QGSJet II–04 in Fig. 3.10 and $\langle \ln A \rangle$ from $\langle X^{\mu}_{\rm max} \rangle$ for EPOS–LHC in Fig. 3.14). Whereas the longitudinal profiles of the EM component (FD data) seem to be described by MC quite well [76], there are significant discrepancies in the predictions for densities of ground particles (SD data) at the Pierre Auger Observatory that are attributed to the lack of muons in MC simulations. These discrepancies are observed for vertical ($\Theta < 60°$) as well as for inclined ($\Theta > 60°$) Golden events.

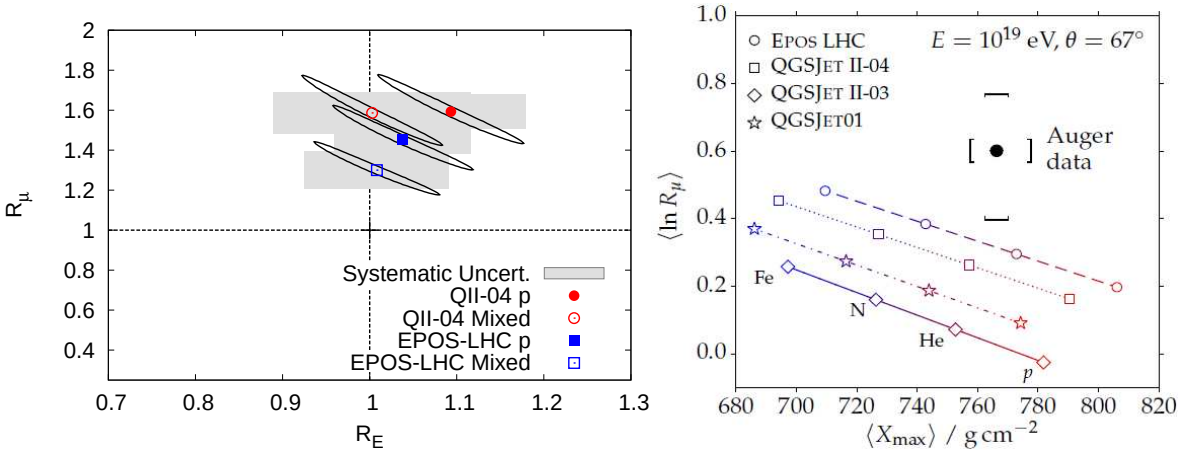

Figure 3.16: **Left panel:** Rescaling of the number of muons (R_μ) depending on the rescaling of the energy scale ($R_{\rm E}$) needed to describe the Golden events of the Pierre Auger Observatory at energy 10^{19} eV for $\Theta < 60°$. Picture comes from [77]. The mixed composition corresponds to the best–fit combination of p, He, N and Fe primaries describing the longitudinal profiles. **Right panel:** The mean logarithm of the rescaling of the number of muons vs. the mean depth of shower maximum inferred from inclined Golden events at energy 10^{19} eV. Picture comes from [78].

In case of the vertical Golden events, MC showers with the longitudinal profile very similar to the longitudinal profile of the measured FD data around 10^{19} eV were used for the comparison of corresponding simulated and measured signals in the SD [77]. In the left panel of Fig. 3.16, the necessary rescaling of the number of muons (R_μ) in MC is plotted vs. the rescaling of the energy scale ($R_{\rm E}$) needed to describe the measured data. Including the systematic uncertainties, ~10-50% higher number of muons is needed in case of EPOS–LHC and 30-80% in case of QGSJet II–04.

For the inclined Golden events, the shower energy is obtained from the FD and the muon content from the SD as the EM component is highly absorbed in the atmosphere. In the right panel of Fig. 3.16, the mean logarithm of the rescaling of the number of muons is plotted vs. the mean depth of shower

maximum for showers at 10^{19} eV. Note that the measured data lie above the MC predictions, even if the systematic uncertainty is considered. Including the systematic uncertainty, ~5-50% higher number of muons is observed compared to EPOS–LHC and 15-65% to QGSJet II–04.

To summarize, in any analysis concerning the number of muons that was performed at the Pierre Auger Observatory so far, a significant deficit of muons is observed in current models of hadronic interactions.

3.4.3 Searches for Anisotropy

Clustering of events on the sky could reveal directions of their sources. It can be caused by neutral particles (neutrons, photons or neutrinos) or by light particles at the highest energies. Three types of anisotropy are usually distinguished according to the angular scale at which the search is performed: small–scale within few degrees, medium–scale at around tens of degrees and large–scale at more than about 40 degrees.

Searches with Neutral Particles

The neutral particles are not deflected in magnetic fields and thus their arrival directions point directly to their sources. Identification of EAS induced by a neutral particle is therefore of high scientific importance.

Showers induced by photons could be distinguished from the showers induced by protons according to the deeper X_{max} or much smaller muon signal. The SD measurement at the Pierre Auger Observatory provides a large exposure to search for photons. Photon candidates are identified according to the curvature of the shower front and rise-time of the signals in water Cherenkov stations [79] indicating young showers deep in the atmosphere (substantial portion of the EM component on the ground). Hybrid measurement has a lower exposure because of the lower duty cycle, but it has a lower energy threshold than the main SD. Most importantly, it observes X_{max} that can separate well between a shower initiated by photon, or hadron (left panel of Fig. 2.6).

No clear photon candidates have been observed by the Pierre Auger Observatory [79]. Limits on the photon fluxes from the both mentioned types of measurements are shown in the left panel of Fig. 3.17. Even a multivariate analysis [80] combining the SD and the FD observables with a higher separation power between the photon– and hadron–induced showers ranging in energy from $10^{17.3}$ eV to $10^{18.5}$ eV did not find any clear photon candidate. Nevertheless, this result is very interesting, since the limits set by the Pierre Auger Observatory are strict enough to actually rule out most of the so–called Top–down models as the dominant source of the UHECR origin.

Showers induced by neutrinos can be distinguished from the hadron– and photon–induced showers only for inclined events since the neutrinos can induce showers much deeper in the atmosphere than the showers induced by hadrons and photons due to their weakly–interacting nature. In [81] two types of neutrino detection were considered according to the zenith angle. Downward–going showers include showers with $60^\circ \leq \Theta \leq 90^\circ$ induced by neutrinos of all flavors with charged–current and

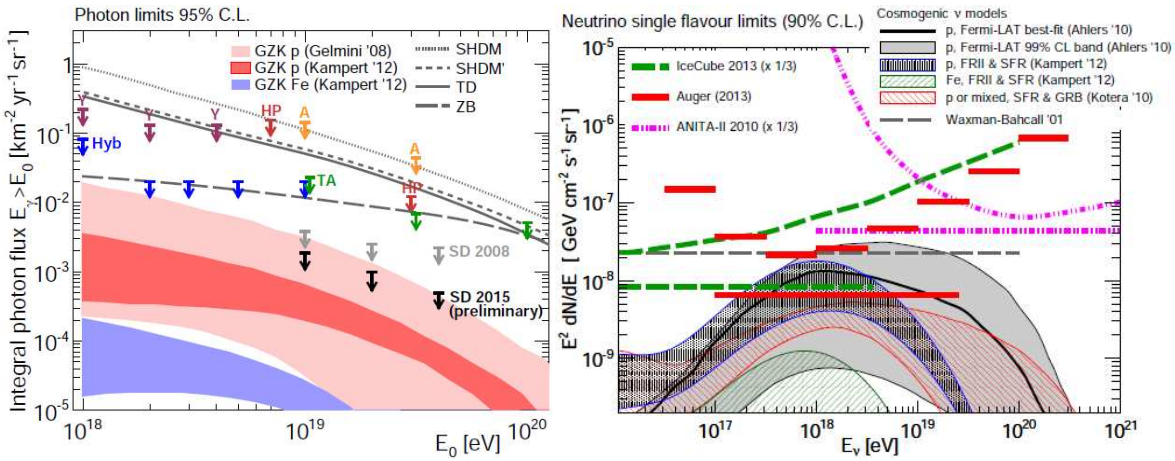

Figure 3.17: **Left panel:** Upper limits on the photon flux measured by various experiments. The latest results from the SD and hybrid measurements of the Pierre Auger Observatory are shown with black and blue arrows, respectively. **Right panel:** Differential and integral upper limits on the neutrino flux measured by various experiments. The upper limits set by the Pierre Auger Collaboration are depicted in red. Pictures come from [79] where detailed explanation can be found.

neutral–current interactions and also ν_τ interacting in the Andes mountains. In the latter case, the air shower is initiated by the decay products of τ (~10 km range of τ produced by interaction of ν_τ of energy ~EeV). Neutrino showers with $90^\circ \leq \Theta \leq 95^\circ$ are denoted as Earth–skimming and they are produced by the decays of τ. In both cases the SD measurements are used to search for young showers with broad SD traces indicating a high amount of the EM component.

No such neutrino–induced shower has been observed at the Pierre Auger Observatory so far. In the right panel of Fig. 3.17 the upper limits on the ν flux inferred by the Pierre Auger Observatory are shown together with the results of other experiments. These limits could have greater impact on various mass composition scenarios when a higher exposure is collected since the ν fluxes originating from UHECR composed of protons, or iron nuclei are one order of magnitude different.

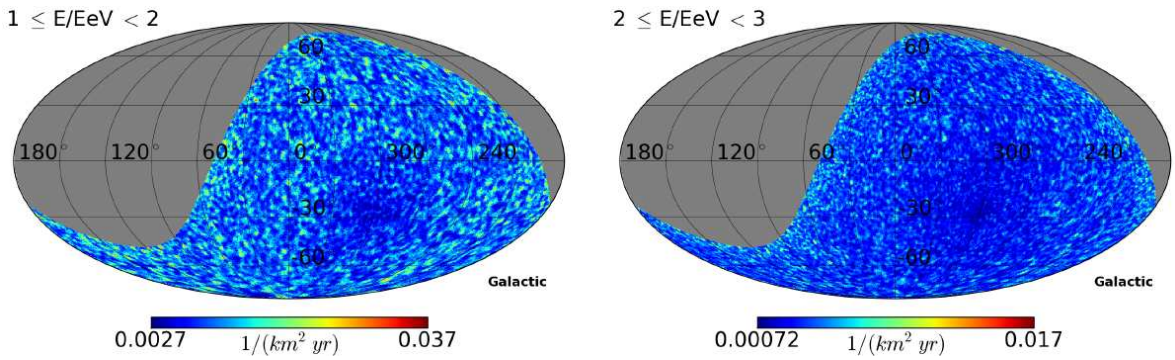

Figure 3.18: Limits on the neutron flux plotted in galactic coordinates for energy in the range ⟨1, 2) EeV (**left**) and ⟨2, 3) EeV (**right**). Pictures come from [82].

As it was indicated in Section 2.1.3, a search for neutrons coming from our Galaxy can be performed at EeV energies. The showers induced by protons and neutrons are indistinguishable. However, protons are strongly isotropized in the Galactic magnetic field at EeV energies. Therefore, a small–scale anisotropy of arrival directions near the Galactic plane would suggest a production of neutrons in the Galactic sources. The search performed in [82] did not find any indication about the small–scale anisotropy at EeV energies and therefore the upper limits on the neutron flux were calculated. They are drawn in galactic coordinates in Fig. 3.18 for two energy ranges.

Clustering of UHECR at the Highest Energies

Protons at energies higher than ∼50 EeV could be already so little distorted in the Galactic and extragalactic magnetic fields that a small–scale anisotropic pattern around the positions of their sources on the sky could emerge in the observed data. The first attempt of the Pierre Auger Observatory to reveal the sources of UHECR was in [83] when a correlation test of arrival directions with the nearby AGNs was performed. For the first time an isotropic distribution of UHECR at the highest energies was rejected at a 99% confidence level. However, the level of this correlation (with the nearby AGNs from one particular catalog) decreased with time [84]. Moreover, the correlation did not improve with increasing energy as one would expect for the correlation caused only by protons. The sky map of 231 events of energy above 52 EeV is shown in Fig. 3.19. The only anisotropic pattern at the highest energies that did not vanish with time is a $\sim 3\sigma$ excess in the $\sim 20^\circ$ vicinity of the Cen A (marked with the red cross) with respect to the isotropic expectation [84] which is illustrated in Fig. 3.20.

Such observations are difficult to explain, but the medium–scale excess in the Cen A region could constrain the local extragalactic magnetic field. According to three models of the Galactic magnetic field that are commonly used, the events with energy ∼50 EeV coming from the direction of Cen A are distorted by the magnetic field in our Galaxy at a level of few degrees for protons and helium nuclei. For C, N, O and heavier nuclei, the deflections are predicted to be much larger than 20° [85, 86]. Therefore, if the current models of the Galactic magnetic field are reliable and if the medium–scale excess of events comes from events originating in Cen A, this excess of events should be caused by protons or nuclei lighter than the CNO group distorted predominantly in the extragalactic magnetic field. Nuclei with the mass number between helium and nitrogen are not probable to propagate up to several Mpc distances without their decay or interaction with background photons at these energies [27] (see also Fig. 2.3). Assume in the following that the excess of events with respect to the background expectation around the position of Cen A within $\alpha = 20^\circ$ is caused by particles of charge Z from Cen A that is distant $D_S = 4$ Mpc. Then, the intensity of the extragalactic magnetic field (B_{EG}) that would produce this distortion of events from the direction of Cen A can be constrained.

From the schematic drawing in Fig. 3.21, the Larmor radius R_L can be derived as

$$R_L = \frac{D_S}{\sqrt{2\,(1 - \cos(2\alpha))}}. \tag{3.4}$$

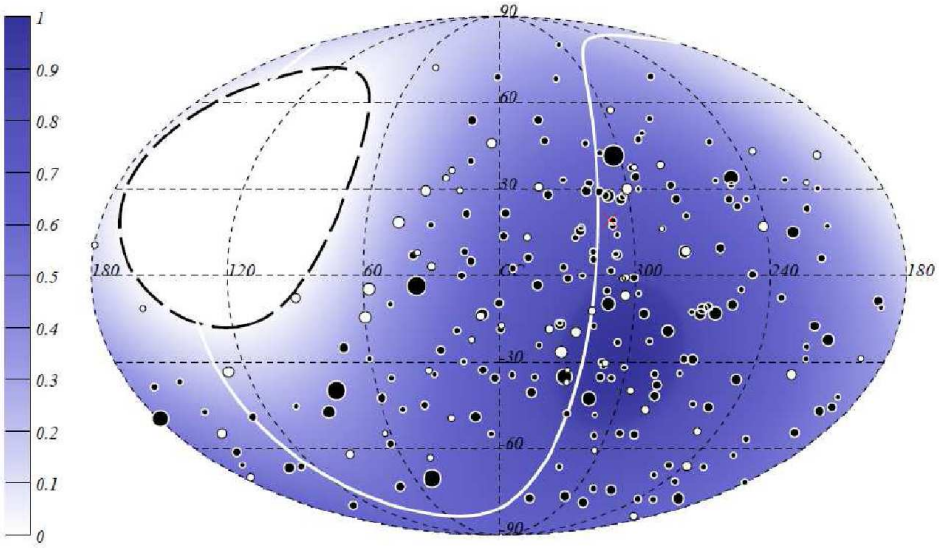

Figure 3.19: Sky map in galactic coordinates (longitude $l_{\rm gal}$, latitude $b_{\rm gal}$) of the arrival directions of events with energy above 52 EeV detected by the Pierre Auger Observatory. The black (white) points correspond to vertical (inclined) events. The size of each point scales with energy. The bluish color describes the relative exposure. The position of Cen A ($l_{\rm gal} = 309.5°$, $b_{\rm gal} = 19.5°$) is marked by the red cross. The white line corresponds to the position of the so–called Super-galactic plane. The map comes from [84].

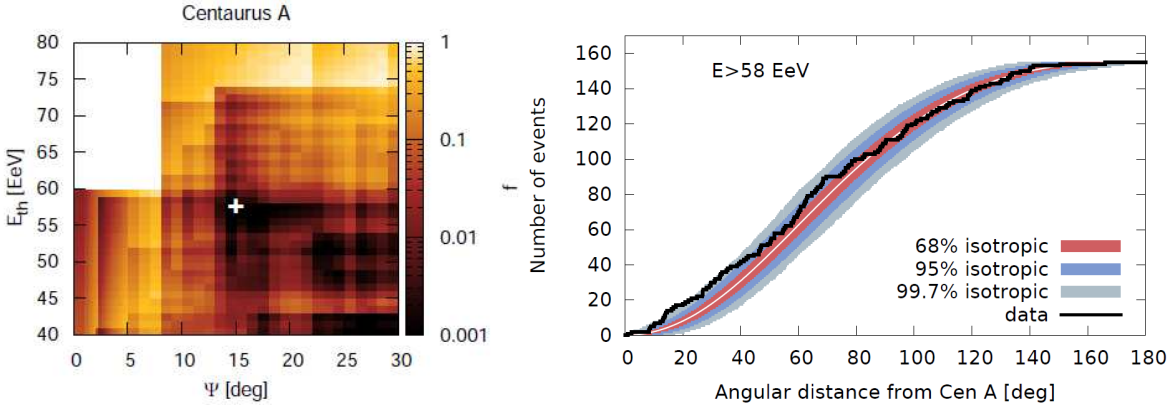

Figure 3.20: **Left panel:** Fraction of isotropic simulations (f) with an equal or higher number of events than the measured data distributed around the position of Cen A. This fraction is plotted as a function of the minimum energy ($E_{\rm th}$) and the angular distance from the position of Cen A (Ψ). **Right panel:** The integral number of events as a function of the angular distance from the position of Cen A compared with the isotropic hypothesis. The energy threshold $E_{\rm th} = 58$ EeV corresponding to the minimum value of f (marked by the white cross in the left panel) was applied. Pictures come from [84].

Using $R_{\rm L}$ from Eq. (2.1) the intensity of the extragalactic magnetic field is estimated to be

$$B_{\rm EG}[\mu{\rm G}] = \frac{E[{\rm EeV}] \cdot \sqrt{2\,(1-\cos(2\alpha))}}{Z \cdot D_{\rm S}[{\rm kpc}]}. \tag{3.5}$$

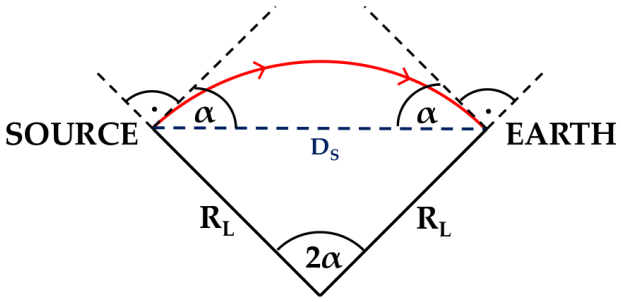

Figure 3.21: Schematic drawing of the propagation of particle along the path (in red) curved with the Larmor radius R_L in the extragalactic magnetic field. The distance of the source from the Earth is denoted as D_S and the observed angular separation between the position of the source in the sky and the arrival direction of the particle is α.

The excess of events was observed in the energy range $\langle 50,\ 70 \rangle$ EeV which gives $B_{EG} = 9 - 12$ nG assuming protons to be responsible for this excess. Note that helium nuclei or heavier nuclei that would evoke the observed excess would give lower values of B_{EG} and a more distant source (e.g. Centaurus cluster distant ~50 Mpc) as well. Therefore the estimated values of B_{EG} are actually the the upper limits. This can have a crucial impact on our possibilities to search for anisotropy at the highest energies. With the intensity of the extragalactic magnetic field in order of ~10 nG the Larmor radius is $R_L = 5$ Mpc / Z at energy 50 EeV and $R_L = 10$ Mpc / Z at energy 100 EeV. This would make it almost impossible to find anisotropic signals of sources more distant than the closest AGNs.

However, the observed 20° excess around Cen A could be caused by completely different source with different position in the sky and with a different distance or just by a statistical fluctuation and also the extragalactic magnetic field can be inhomogeneous. A more profound study [87] of the excess around the direction of Cen A obtained a limit $B_{EG} \geq 20$ nG assuming the primary proton composition.

Large–scale Anisotropy – Dipole

The search for a large–scale anisotropy with the Pierre Auger Observatory data was performed in [88]. The SD data of vertical and horizontal events were combined to cover 85 % of the exposed sky. The flux of UHECR in equatorial coordinates is shown in Fig. 3.22 for energies between 4 and 8 EeV and for energies above 8 EeV. Whereas for the lower energy bin no significant departure from isotropy was found, for energies above 8 EeV a dipole structure is evident. The amplitude for the first harmonic in right ascension was set to 4.4 ± 1.0 % with a chance probability $6.4 \cdot 10^{-5}$.

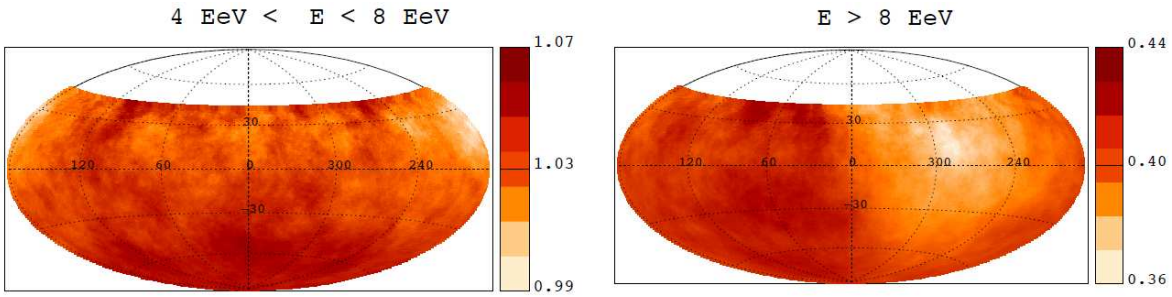

Figure 3.22: The flux [$\mathrm{km^2 sr^{-1} yr^{-1}}$] of UHECR measured by the Pierre Auger Observatory at energy 4 EeV $< E <$ 8 EeV (**left**) and $E >$ 8 EeV (**right**). The sky maps are plotted in equatorial coordinates. They were smoothed in angular windows of 45°. Plots come from [88].

3.4.4 Discussion of Measurements

Following properties of UHECR and atmospheric showers were observed with the data of the Pierre Auger Observatory.

- **Energy Spectrum:** The ankle at energy $\sim 10^{18.7}$ eV (~5 EeV) and the steep suppression beyond $\sim 10^{19.5}$ eV (~30 EeV) in the UHECR flux are established with a high statistical significance.

- **Mass Composition:** The mean mass number of UHECR decreases slightly at energies from $10^{17.8}$ eV up to $10^{18.3}$ eV (~2 EeV) where a proton dominance (>50%) is indicated by MC predictions. At higher energies, the mean mass number increases steadily up to $\sim 10^{19.6}$ eV (~40 EeV). A pure proton composition of UHECR was excluded at energies $10^{18.5-19.0}$ eV (3–10 EeV).

- **Hadronic Interactions:** The excess of muons in the measured data wrt. MC predictions and also the interpretations of X_{max} and X^{μ}_{max} measurements indicate a lack of understanding of the hadronic interactions beyond the LHC energies.

- **Neutral Particles:** No observation of a clear shower candidate induced by a neutral particle has been identified yet. Limits on fluxes of photons exclude the Top–down models. There is no excess of neutrons from the Galactic plane or Galactic center.

- **Anisotropy:** The anisotropic signal at the highest energies (>50 EeV) that is stable in time is observed in the 20° vicinity of the closest AGN: Cen A. The correlation of arrival directions with the nearby AGNs fainted with time and does not improve with energy. There is a dipole structure with a small amplitude in the distribution of arrival directions of UHECR above 8 EeV.

The origin of the ankle based on the pair production of protons on the cosmic microwave background ("dip" model) is in tension with the measurement of the Pierre Auger Observatory that excludes the pure proton composition around the ankle energy. The ankle can be explained by a transition between the two types of sources of UHECR with different spectral indices as in the case of

the transition from the Galactic to the extragalactic component. According to the Peter's cycle [9], the end of the energy spectrum of the Galactic component should be formed with particles of higher charges (easier to accelerate). However, the transition to the extragalactic component could take place at energies where the contribution of Galactic protons is still dominant and then it would not be in a tension with the quite light mass composition of primaries around the ankle energy. The alternative explanation [65] of the ankle by the photo-disintegration of nuclei directly at the extragalactic sources is also a viable option. It predicts a light composition around the ankle energies and an increasing mass of primaries towards the higher energies. The spectrum of the Galactic component is then predicted to end at lower energies than the ankle energy.

The observed few % dipole in the arrival directions of UHECR above 8 EeV can be an indication of diffusive propagation of extragalactic UHECR in the extragalactic magnetic field. This could be realized when the amplitude of the extragalactic magnetic field is large and/or UHECR are of higher charge (see e.g. [89]). However, this dipole might also be the consequence of an inhomogeneous distribution of sources in the sky in case of small deflections of UHECR in the extragalactic magnetic field.

The steep decrease of the cosmic–ray flux at the highest energies could be caused by the GZK effect of protons, or by the maximal energy to which the particles can be accelerated in the sources. In the latter case, the end of the spectrum would be likely dominated by heavier nuclei as they are easier to be confined in the region with a magnetic field. Although the X_{max} measurement suggests an increase of $\langle \ln A \rangle$ with energy, there is still no statistically significant measurement of the primary composition at energies at the end of the spectrum.

The largest experiment located in the northern hemisphere, the Telescope Array, published a bit different interpretation of the results about the mass composition [90] and the energy spectrum [91] than the Pierre Auger Observatory. They claimed that their data are compatible with a light composition of primaries. However it needs to be stressed that the Telescope Array has about 4–times smaller aperture and therefore smaller statistical significance of their results, especially at the highest energies. Moreover, the Telescope Array interpreted its measurement of the depth of shower maximum using models of hadronic interactions that were not tuned to the LHC data. Recently it was shown [92] that its measurement of $\langle X_{\mathrm{max}} \rangle$ is consistent with the $\langle X_{\mathrm{max}} \rangle$ measurement of the Pierre Auger Observatory. The energy of the ankle measured with the Telescope Array data is very similar to the ankle energy observed by the Pierre Auger Observatory. On the other hand, the Telescope Array measured a bit less steep decrease at the end of the energy spectrum. The only anisotropy signature which this experiment observes is about 3 σ excess in the region 20° around a position ($l_{\mathrm{gal}} = 177°$, $b_{\mathrm{gal}} = 51°$) where no astrophysical object capable of UHECR acceleration is known [93]. It needs to be also noted that the Telescope Array and the Pierre Auger Observatory observe different regions in the sky and therefore different results about UHECR at the highest energies could be in principle possible.

A reliable determination of the mass composition of primaries, especially at the highest energies, with large event statistics seems to be an important step forward in further studies of UHECR to

answer the still–opened questions. Measurement of the muon component with a large surface array (full duty cycle) could be one way how to accomplish that. However, on the other hand, the observed inconsistency of the MC predictions and the measured data for the muon component is an issue that needs to be fixed simultaneously. Therefore, accompanying measurements with more detectors of different energy thresholds for muons combined with a measurement of the EM component would not be only beneficial, but also necessary. From these reasons, an upgrade of the Pierre Auger Observatory focused on the detection of muons is planned to be build in the near future [94].

With decreased systematic uncertainty of the muon measurement and with a large exposure, the precise measurement of the mass composition of UHECR could be performed also at the highest energies. Importance of such a measurement can be drawn from the Fig. 3.23. A much more precise measurement of $\langle \ln A \rangle$ than the current measurements provide (gray band) could distinguish even between the individual source scenarios. Beyond that, a direct search for UHECR sources could be performed at the highest energies using the selection of protons or light nuclei that are less distorted due to the magnetic fields providing the desired "proton astronomy".

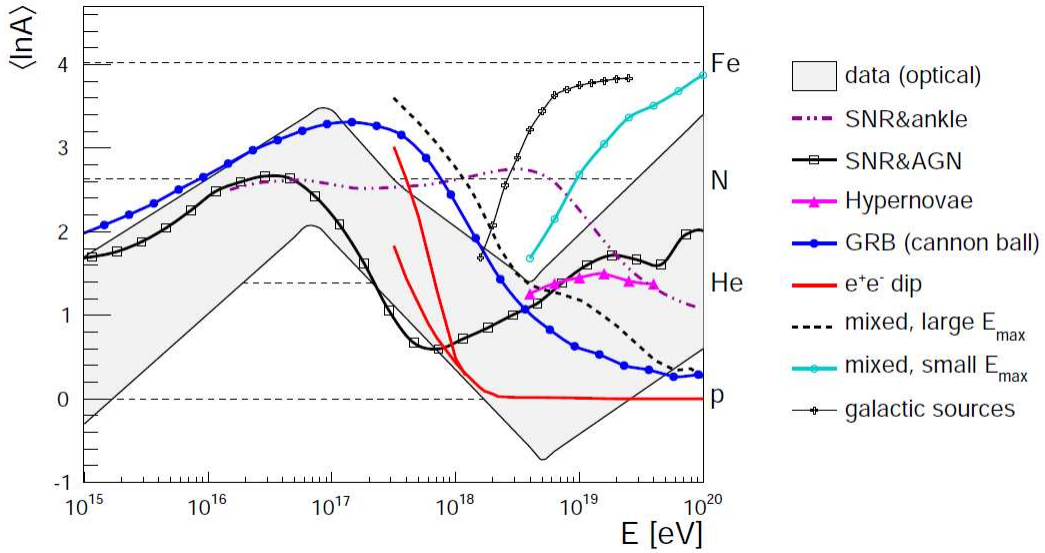

Figure 3.23: Energy evolution of $\langle \ln A \rangle$ predicted for various types of UHECR sources is shown together with the results combined from all available optical measurements. Plot comes from [31].

Chapter 4

Sensitivity of Attenuated Signals in Surface Detectors to Primary Masses

The chapter is focused on the attenuation of signals measured in surface detectors due to the different amount of atmospheric depth that is passed by showers before they reach the ground level. Especially, the bias of the reconstructed shower energy with respect to the mass composition of UHECR is studied. On the other hand, this bias is utilized to introduce a method sensitive to the type of primary particles. The chapter contains the author's original research.

The chapter includes two sectional topics. In the first section, the CIC method (see Section 3.3.2) and the "MC–approach" are compared. This comparison is motivated by the fact that these two different methods are applied by the analysis teams of the two largest surface arrays ever built, the Pierre Auger Observatory and the Telescope Array. The CIC method is also tested for the presence of a prominent source that would violate the assumption of constant intensity. These studies were published in conference proceedings [95]. In the second section, a parameter sensitive to the dispersion of primary masses is introduced for an observatory composed of independent muon and electromagnetic detectors. The CIC approach applied separately to signals of both types of detectors is combined in this case. The method was indicated in conference proceedings [96] and finally published as journal paper in [97].

4.1 Attenuation Curves obtained with Different Observatories

At any cosmic ray observatory of UHECR such as the largest ground arrays that are currently operating, the Telescope Array and the Pierre Auger Observatory, the energy reconstruction requires a correction of the measured signal to account for the zenith angle of an incoming primary particle initiating the air shower. This correction reflects different amounts of air masses penetrated by the air showers that reach the detector with different zenith angles. It can be obtained using the data–driven CIC method or using the MC–based estimation.

As mentioned at the end of the previous chapter, the mean of the X_{max} distribution measured by

the two largest experiments as a function of energy is compatible within experimental uncertainties as well as the spectral slopes around the ankle and the ankle energy itself. However, there are several discrepancies in the measured energy spectrum at the highest energies that might become significant when larger statistics is collected and/or the systematic uncertainties are decreased. The possible differences of the data measured by these two observatories were a motivation to probe their different approaches to correct the signal in the surface detector for the attenuation with zenith angle Θ.

In this section, it is studied how the reconstructed energies are affected when the primary particles are of a mixed composition of protons and iron nuclei. Both possibilities, the application of the CIC method and the approach with the attenuation curve obtained from MC, are investigated separately for the EM type as well as for the EM+μ type of surface detectors. The EM type of observatory is analogical to the surface detectors of the Telescope Array that are predominantly sensitive to the EM component. The EM+μ type of observatory represents a type of observatory analogical to the surface detectors of the Pierre Auger Observatory that are sensitive to the EM component and to the muon component as well. Since the CIC method is based on the assumption of the uniform distribution of events in $\cos^2(\Theta)$, the estimation of the influence of a possible source at the highest energies was also performed. Presence of such a source violates to some extend the assumption of the uniform distribution in $\cos^2(\Theta)$.

To address these questions, a Toy MC in combination with outputs of shower simulations produced by CORSIKA ver. 7.37 at energy 10^{19} eV were used. At first, the attenuation curves of the ground signal were calculated based on rough assumptions of the detector responses to the CORSIKA showers induced by protons and iron nuclei. Both EM and EM+μ types of ground detectors were considered. These curves together with the size of signal fluctuations then served as the input for the Toy MC to generate a large number of events over a wide range of energies. Both, MC–like and CIC–like, approaches were then applied to the generated data in the last step.

The two currently largest UHECR experiments use scintillator detectors (the Telescope Array) or water Cherenkov detectors (the Pierre Auger Observatory). Both experiments are located at the approximately same altitude (around 1400 m a.s.l. equivalent to ~880 g/cm^2 of the vertical atmospheric depth). The signals of thin scintillator detectors are dominantly induced by EM particles, while the signal in the water Cherenkov detectors is produced by EM particles and muons as well. In both cases, the signal (S) of the surface detector array has to be corrected for different attenuation of the shower size with respect to the amount of air penetrated before reaching the detector.

The Telescope Array uses the so–called look–up table from MC simulations providing the relation between the signal size, zenith angle and the shower energy [91]. Only the protons are considered as the primary particles. The reconstructed energies are then rescaled to match the energies measured in the fluorescence detector. This procedure is an extension of the energy independent application of the signal attenuation curve. This method is denoted as the MC–approach in the following.

The CIC method is applied to the data measured by the Pierre Auger Observatory providing a relationship (attenuation curve) between the signal size and the $\cos^2(\Theta)$ at a given intensity (energy)

cut. In this approach, it is assumed that the flux of incoming particles is isotropic above a given energy. This implies a flat distribution of events in $\cos^2\Theta$. In the next step, for each shower the signal at the reference angle 38° (S_{38}) is calculated using the normalized attenuation curve (CIC curve). The S_{38} value is then related to the shower energy calibrated by the fluorescence detector (as described in Section 3.3.2). The CIC curve is studied as a function of energy (intensity cut). Since no substantial deviations in the shape of the CIC curve were found, just one curve is finally used for showers of all energies.

4.1.1 CORSIKA simulations

The showers generated by the Prague group of the Pierre Auger Collaboration were used in the following. Primary protons and iron nuclei of energy 10^{19} eV were chosen to induce simulated showers in 10 steps of fixed zenith angles from 0° up to 60°, equidistant in $\cos^2(\Theta)$. The most recent model QGSJet II–04 was used to simulate hadronic interactions at high energies (above 80 GeV). The second model tuned with LHC data, EPOS–LHC, was used for comparison. The FLUKA model [98] was used for low energy interactions (below 80 GeV). Energy thresholds of 50 MeV and 1 MeV were chosen for muons and EM particles, respectively. In total, 2400 air showers were generated.

The signal of the EM detector (assuming thin scintillators at 1400 m a.s.l. with the array density similar to the Telescope Array) was supposed to be proportional to the ground density of EM particles at 800 m from the shower core in the plane perpendicular to the shower axis. For the EM+μ type of observatory (assuming water Cherenkov detectors at 1400 m a.s.l. with the array configuration similar to the Pierre Auger Observatory), the EM part of the signals was assumed to be proportional to the energy density of EM particles and the muon part of the signals to the muon density in 1000 m from the shower core in the plane perpendicular to the shower axis. The absolute strengths of signals induced by muons and EM particles were normalized to be equal for vertical proton showers. These rough assumptions are far from the detailed understanding of the detector responses at current observatories and shall be taken just as two illustrative examples of observatories with EM and EM+μ types of detectors.

The normalized attenuation curves are shown in the left panel of Fig. 4.1 for the array of EM detectors and in the left panel of Fig. 4.2 for the EM+μ observatory. The curves were normalized at the reference zenith angle 38°. In left panel of Fig. 4.2, the attenuation curve used at the Pierre Auger Observatory [61] derived by the CIC method is presented for completeness. In the right panels of Figs. 4.1, 4.2, the ratio of the signals induced by iron nuclei to the signals induced by protons are plotted as a function of the zenith angle for the EM and EM+μ observatory, respectively.

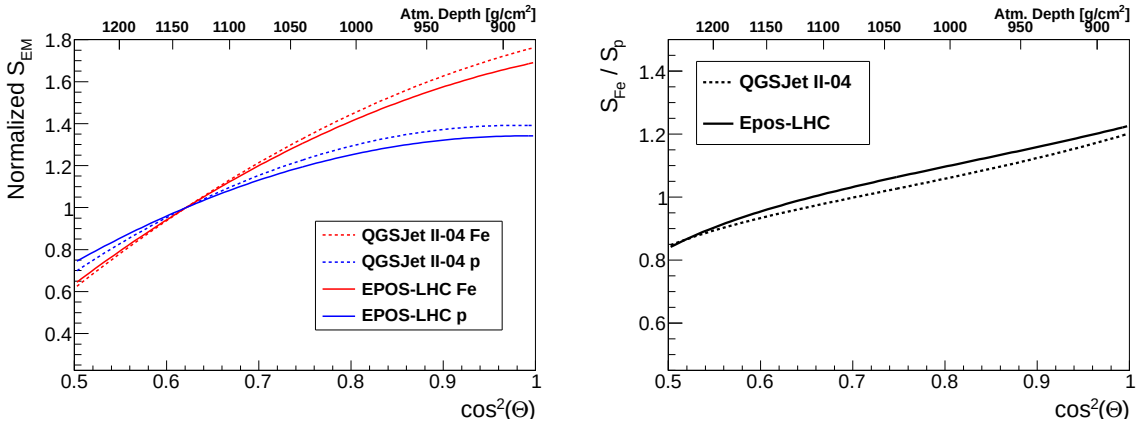

Figure 4.1: Reference signals (S_{EM}) for the array of **EM** detectors. Attenuation of the signal normalized at 38° is shown in the **left panel** for showers initiated by protons (blue) and iron nuclei (red) of energy 10^{19} eV. Ratio of the absolute signal induced by iron nuclei (S_{Fe}) to the absolute signal induced by protons (S_{p}) is illustrated in the **right panel** as a function of the zenith angle. Corresponding atmospheric depth is indicated on the upper horizontal axis. Note the smaller range of horizontal axis ($\cos^2(0°)$ – $\cos^2(45°)$) wrt. Fig. 4.2. The models of hadronic interactions are distinguished by types of lines.

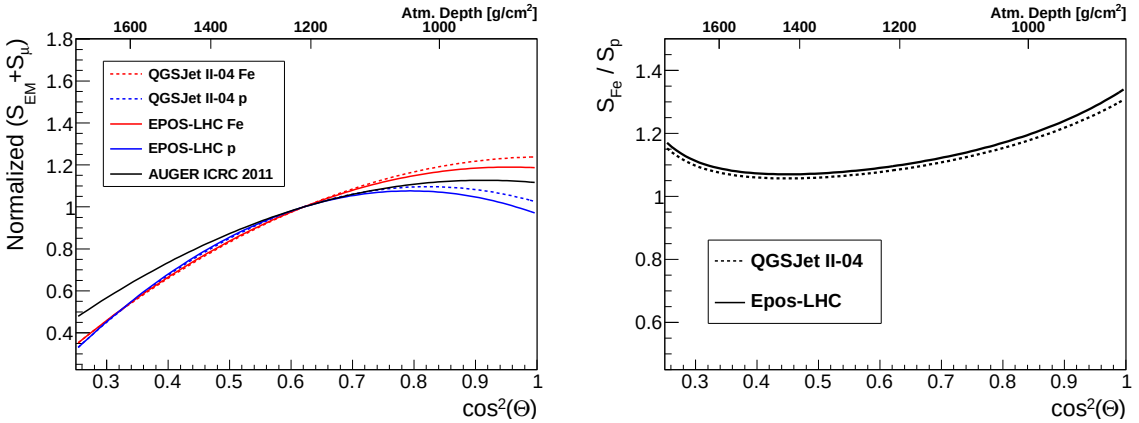

Figure 4.2: The same description as for Fig. 4.1, but for the array of **EM+μ** detectors. Normalized CIC curve from ICRC 2011 of the Pierre Auger Observatory is depicted in black for illustration in the left panel.

4.1.2 Toy MC

The primary energies (E_{MC}) were simulated in the range $\langle 10^{18.5},\ 10^{20} \rangle$ eV according to the energy spectrum in a form

$$J(E_{\mathrm{MC}}) = \frac{\mathrm{d}N}{\mathrm{d}E_{\mathrm{MC}}} = E_{\mathrm{MC}}^{-\gamma} \frac{1}{1 + \mathrm{e}^{\frac{\log(E_{\mathrm{MC}}) - \log(E_{1/2})}{\log(W_{\mathrm{E}})}}}, \tag{4.1}$$

i.e. by a smooth function with a steep decrease at the end of the spectrum. The value of $\log(E_{1/2})$ was set to 19.6, $\log(W_{\mathrm{E}})$ to 0.15 and the spectral index γ was taken as 2.7. The arrival directions were

simulated isotropically (uniformly distributed in $\cos^2(\Theta)$ for Θ of $\langle 0°, 60°\rangle$). The time of the cosmic–ray detection was uniformly distributed within a long time period to cover all possible sky coordinates observable by an array placed at the location of the Pierre Auger Observatory (necessary for studies of the sensitivity of CIC curve to the presence of a source in Section 4.1.4). It was further assumed that the shower energy $E_{\rm MC}$ and the shower signal at 38°, S_{38}, are related by (see also Section 3.3.2)

$$E_{\rm MC} = a \cdot S_{38}^{b}. \tag{4.2}$$

Here an arbitrary normalization constant $a = 10^{16}$ eV was chosen. For the sake of simplicity the exponent $b = 1$ was taken. It is not far from the value estimated at the Pierre Auger Observatory (see again Section 3.3.2). It is worth noting that this relationship also reflects approximately the look–up table used at the Telescope Array experiment.

The value of S_{38} was corrected according to the corresponding zenith angle and particle type using the QGSJet II–04 attenuation curves shown in the left panels of Figs. 4.1, 4.2 to get the signal S for a given shower. Ratios of signals induced by iron nuclei to signals induced by protons (right panels of Figs. 4.1 and 4.2) were accounted for. Resulting signal values were then smeared with a Gaussian of variance equal to 10% (5%) of the signals for protons (iron nuclei)[1]. This way the detector responses to 10^7 showers initiated by protons and iron nuclei were simulated in a wide range of energies and zenith angles.

4.1.3 Energy reconstruction

After all the ground signals were generated, either the CIC method or the MC–based approach were applied to obtain the reference signal S_{38} for each simulated shower. This signal was then transformed using Eq. (4.2) to get the reconstructed energy ($E_{\rm SD}$). The comparison of the two different methods is demonstrated in Fig. 4.3 for the array of EM detectors (left) and of EM+μ detectors (right). The average ratio of the reconstructed energy to the MC true energy is plotted as a function of the zenith angle. Samples of pure protons, pure iron nuclei and of a mixed composition of 50% p + 50% Fe were analyzed. The cut value (N) for the CIC method was chosen to correspond to the flux around 10 EeV of the MC energy.

What should be read out from the Fig. 4.3 are not the absolute positions of the average energy ratios, since their value is in fact always re-normalizable to unity averaging over the whole $\cos^2(\Theta)$ range when the energy calibration with the fluorescence detectors is applied. The important behaviors are the relative changes of the plotted ratio with zenith angle.

For the array of EM detectors (left panel of Fig. 4.3), about a 30% difference in size of $\langle E_{\rm SD}/E_{\rm MC}\rangle$ between 0° and 45° is observed, when the attenuation curve of protons is applied to the sample including only iron nuclei (red line). For the mixed composition (blue solid line), the difference is still

[1]Different values of variances were used to smear the signals in Section 4.2 where the treatment of shower–to–shower fluctuations and detector resolutions was more important.

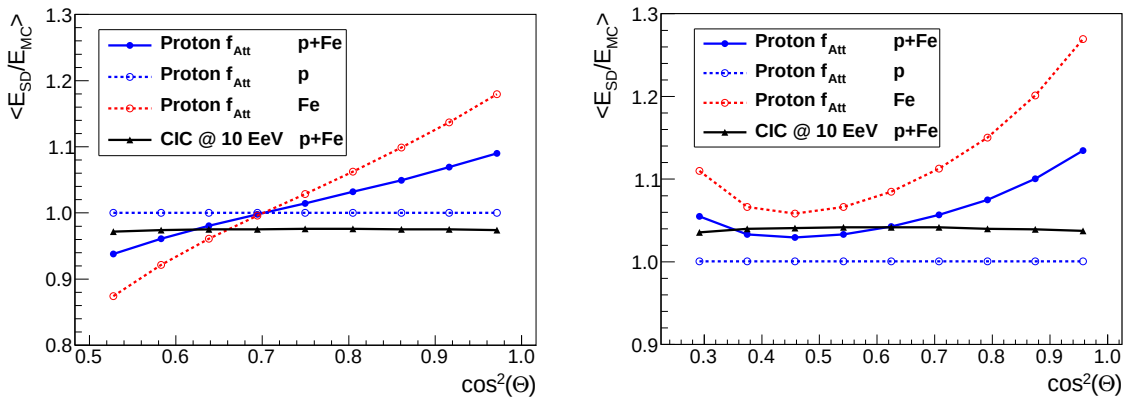

Figure 4.3: Average ratio of the reconstructed energy (E_{SD}) to the MC energy (E_{MC}) depending on the zenith angle for the array of **EM** detectors (**left**) and of **EM+μ** detectors (**right**). The attenuation curve (f_{Att}) for protons is used for the mixed composition of 50% p + 50% Fe (full blue line), pure protons (dashed blue line) and pure iron nuclei (dashed red line). Results obtained using the CIC approach at 10 EeV are plotted for the mixed composition (full black line).

about 15%. On the contrary, the CIC approach applied to the mixed composition of primaries (black line) would eliminate this zenith angle dependence to a percent level from its definition.

Analogous conclusion can be derived also for the EM+μ observatory (right panel of Fig. 4.3). About 20% difference in the size of $\langle E_{\mathrm{SD}}/E_{\mathrm{MC}}\rangle$ between 0° and 60° is visible for the sample including only iron nuclei using the attenuation curve for protons (red line). In case of the mixed composition, the difference of $\langle E_{\mathrm{SD}}/E_{\mathrm{MC}}\rangle$ yields about 10% for showers with Θ between 0° and 60° (blue solid line). However, the application of the CIC method (black line) shows almost no zenith angle dependence.

Altogether, the CIC method eliminates the zenith angle bias of the reconstructed energies and it does not need any assumption on the mass composition of cosmic rays. Being based on the measured data only, it also does not need to rely on MC simulations as in the case of the MC–based approach. On the other hand, when the MC attenuation curve is used to convert the registered signals to energies (in case of the Telescope Array only protons are assumed as primaries in the large range of energies), a nonuniform zenith angle dependence of $\langle E_{\mathrm{SD}}/E_{\mathrm{FD}}\rangle \approx \langle E_{\mathrm{SD}}/E_{\mathrm{MC}}\rangle$ could indicate an observation of a mixed composition of primary particles. However, it can also indicate that the MC simulations do not reproduce the attenuation curves well.

Another interesting question is: How well the CIC method reproduces the MC attenuation curves inserted into the Toy MC? For pure protons or pure iron nuclei almost a perfect match is expected. For a mixed composition, the reconstructed CIC curve should lie in between the MC attenuation curves (f_{Att}) for protons and iron nuclei. This is demonstrated in the left panel of Fig. 4.4 for the EM+μ observatory and mass composition of 50% p + 50% Fe. Taking the normalization at 38°, the largest difference between the reconstructed CIC and MC attenuation curves of protons and iron nuclei is at $\Theta = 0°$. At this zenith angle, the parameter $\Delta_{\mathrm{Fe-p}} = D1/D2$ is defined, where $D1$ is

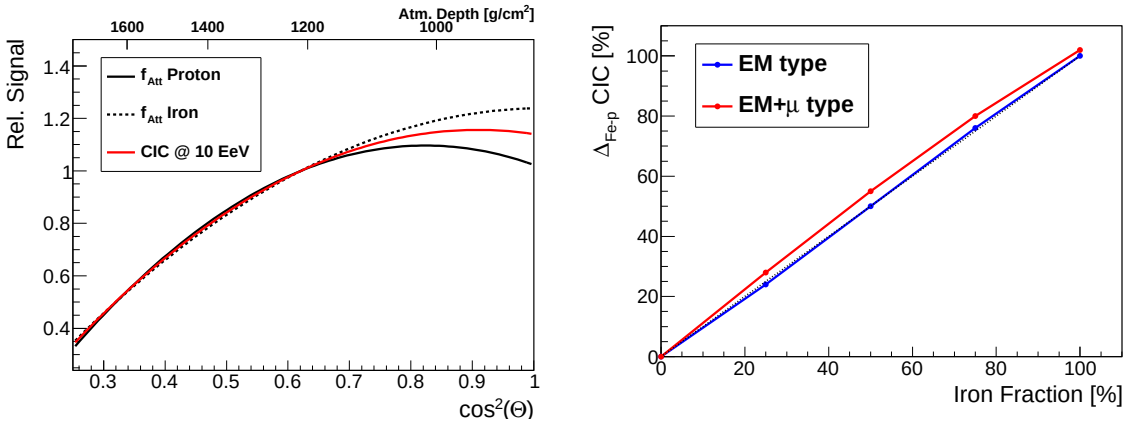

Figure 4.4: **Left panel:** CIC curve derived at ∼10 EeV (red) calculated for the mixed composition of 50% protons and 50% iron nuclei is shown together with the MC attenuation curves (f_{Att}) for the **EM+μ** detector. Curves are normalized to 38°. **Right panel:** The relative size of the CIC curve difference from the MC attenuation curves is plotted vs. the iron fraction in the cosmic–ray beam of protons and iron nuclei. Direct proportion is shown for illustration by black dash–dotted line.

the difference between the reconstructed CIC curve and the attenuation curve of protons and $D2$ is the difference between the attenuation curves of protons and iron nuclei. The parameter $\Delta_{\mathrm{Fe-p}}$ then defines the position of the reconstructed CIC curve in between the attenuation curve of protons and the attenuation curve of iron nuclei ($\Delta_{\mathrm{Fe-p}} = 0$: CIC is in agreement with the f_{Att} of protons, $\Delta_{\mathrm{Fe-p}} = 0.5$: CIC is just in the middle between the f_{Att} of protons and iron nuclei, $\Delta_{\mathrm{Fe-p}} = 1$: CIC matches the f_{Att} of iron nuclei). In the right panel of Fig. 4.4, the evolution of $\Delta_{\mathrm{Fe-p}}$ is plotted as a function of the fraction of iron nuclei in a set of showers induced by protons and iron nuclei for the EM and the EM+μ observatory as well.

A perfect match between the CIC curve and the corresponding f_{Att} is observed for showers induced only by protons and for showers induced only by iron nuclei as well. While $\Delta_{\mathrm{Fe-p}}$ obtained for the EM observatory just follow the fraction of iron nuclei and can be, in principle, used to address the mass composition of primaries, for the EM+μ observatory $\Delta_{\mathrm{Fe-p}}$ always shows a little bit higher values than the fraction of iron nuclei (CIC curve is closer to the attenuation curve of iron nuclei). This can be explained by the fact that the showers induced by heavier primaries produce higher ground signals (more muons) than the showers induced by lighter primaries. The CIC method selects the N^{th} highest value of signal in a given bin of $\cos^2(\Theta)$. Therefore, in case of mixed compositions of primaries, the method finds in average a bit higher signal in every bin of $\cos^2(\Theta)$ (than the overall average signal induced by protons and iron nuclei) as there are more signals induced by heavier primaries that are selected in the set of N events. This effect is actually also illustrated by the ratio of signals induced by iron nuclei and protons which is larger for the EM+μ detector than for the EM detector (right panels of Figs. 4.1, 4.2).

4.1.4 CIC Method with a Source

In case of the presence of a localized source at the highest energies, the assumption of the CIC method about the isotropic distribution of arrival directions would be violated. This effect was tested by adding events with arrival directions from the 20° vicinity of Cen A (as an example) to the isotropic background of mixed composition of 50% protons and 50% iron nuclei. The violation of the constant intensity is illustrated in the left panel of Fig. 4.5 where the distribution in $\cos^2(\Theta)$ is plotted only for events originating in the 20° vicinity of Cen A. The direction of Cen A was chosen as it is a region where an event excess of UHECR was found (see Section 3.4.3). The threshold energy above which the signal of the source contributes to the isotropic background was set to 50 EeV. The spectral index of the source $\gamma = 2.7$ was applied without the GZK–like suppression at the end of the energy spectrum. Events were simulated up to the energy of 100 EeV. The CIC method was tested with the EM+μ detector located in the same coordinates as the Pierre Auger Observatory. The source of protons was simulated with various strengths defined as the ratio of the number of added events to the number of isotropic events coming from the same region on the sky.

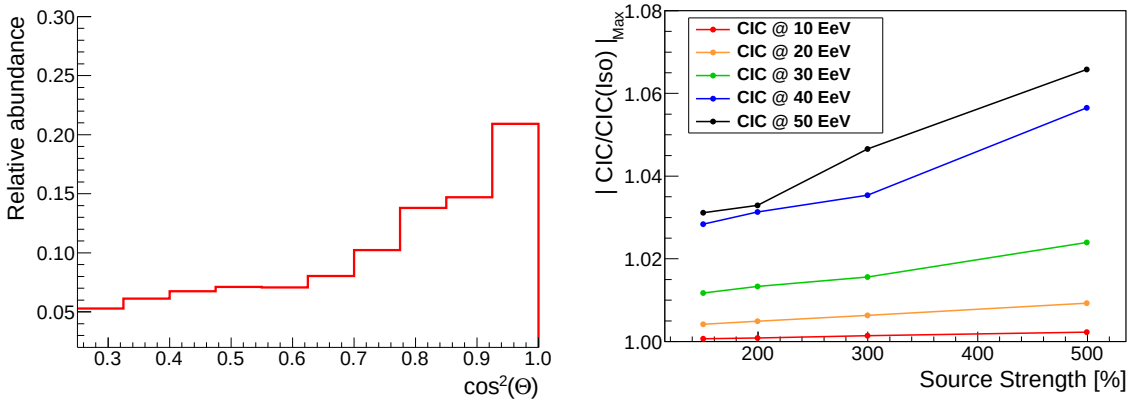

Figure 4.5: **Left panel:** Distribution of $\cos^2(\Theta)$ normalized to 1 of events arriving from the 20° vicinity of Cen A. The location of the EM+μ detector was considered to be the same as the location of the Pierre Auger Observatory. **Right panel:** Maximal relative deviations of the CIC curves reconstructed from the sample of isotropic events combined with the source events with respect to the CIC @ 10 EeV estimated from the sample of isotropic events only are plotted as a function of the source strength. Results are shown for the CIC curves inferred at different energy cuts that are indicated in the legend of the plot.

In the right panel of Fig. 4.5, the maximal deviation of the ratio of the CIC curve reconstructed at different energies for samples of events with anisotropic distribution on the sky to the CIC curve estimated at the energy 10 EeV for a sample of events with isotropic distribution on the sky is plotted as a function of the source strength. Deviations are observed to increase with the intensity cut value approaching the threshold energy of the source. Naturally, it also increases with the source strength. However, the deviations are at a few percent level and the CIC method remains reliable even in case of the presence of a strong source. Thus the reconstructed energies are also affected by less than few

percent at most. Note that the excess of events in the 20° vicinity of Cen A measured by the Pierre Auger Observatory for energies above 52 EeV corresponds roughly to the Source strength of 300% and that the intensity cut is performed at the Pierre Auger Observatory slightly below 10 EeV.

4.2 Dispersion of Primary Masses applying CIC Approach

Findings presented in Section 4.1 and especially the proportion between the parameter $\Delta_{\mathrm{Fe-p}}$ and the size of the primary beam mixture (right panel of Fig. 4.4) led to further studies of the sensitivity of CIC method to the mass composition of primary particles. The following studies are performed for a hypothetical observatory with the surface array consisting of independent EM and μ detectors (i.e. not EM and EM+μ detectors as in Section 4.1).

In general, the ground arrays used for the detection of UHECR showers are sensitive to secondary muons, to the EM component of an air shower or to their combinations. There are several previous works, e.g. [99, 100], studying the primary mass composition and its influence on the CIC method and vice versa. Usually, the detected muon and EM signals are utilized to separate primary mass groups, see e.g. [10], or to determine the average mass number of a set of air showers, see e.g. [101]. The dispersion of the distribution of the primary mass is more difficult to obtain. The precise fluorescence measurement of the distributions of the depth of shower maximum is used, see e.g [67, 90, 102], albeit with a low duty cycle. The combination of measurements of the mean value and the dispersion of the distribution of the primary mass is discussed in [31, 40]. However, these analyses suffer from a strong dependence on models of hadronic interactions. Recently, a new method estimating the spread of masses in the UHECR primary beams has been presented [74] and applied [75]. Unlike the following analysis, this method is based on the simultaneous measurements of the depth of shower maximum and the muon shower size.

A hypothetical observatory of ultra–high energy cosmic rays is considered in the following text. It consists of two surface detector arrays (full duty cycles) that measure independently electromagnetic and muon signals induced by the same air showers. The CIC approach applied simultaneously to both types of signals is used to calculate the number of events with the highest energies matched in both detectors in each bin of $\cos^2(\Theta)$. The zenith angle behavior of this number provides the information regarding the spread of primary masses. The results obtained using two models of hadronic interactions tuned to the LHC data (run I) are very similar and indicate a weak dependence on details of these interactions.

This section presents a method to obtain information about the spread of primary masses from the data collected simultaneously by different types of surface detectors. The average features of CORSIKA showers simulated at an energy of 10^{19} eV are used as inputs to a fast and simplified simulation (similarly as in Section 4.1) of signals in both detectors caused by showers over a wide range of primary energies. The application to the measured data would require a precise knowledge

of the detection process. In this analysis the detailed detector responses are not included. Instead, detector imperfections are represented by a simple Gaussian smearing of signals.

4.2.1 Simulated Detector Signals Corresponding to UHECR Showers

To address the details of the CIC method a large simulated data sample is necessary, ideally $\sim 10^6$ simulated showers, that is comparable with the achievable statistics of the largest UHECR experiment ever built. To avoid excessive computational requirements, a set of showers induced by proton (p), helium (He), nitrogen (N) and iron (Fe) primaries was generated with an energy of 10^{19} eV as in Section 4.1. These showers were produced with CORSIKA ver. 7.37 by the Prague group of the Pierre Auger Collaboration. The shower–to–shower fluctuations and the correlations between the muon and EM components were then derived from the signals that they produce in both hypothetical arrays. Finally, attenuation curves for both types of signals were constructed. These curves were utilized in the simplified simulation of the muon and EM signals induced by showers over a wide range of energies.

A hypothetical observatory with independent muon and EM detectors was considered at the ground level, 1400 m a.s.l. (880 g/cm^2 of vertical atmospheric depth). The signal of the muon detector was assumed to be proportional to the ground density of muons with a threshold energy $E_{\rm Th}$ = 500 MeV. The signal of the EM detector was modeled to be proportional to the ground density of EM particles with $E_{\rm Th}$ = 1 MeV. These detector responses were motivated by responses of thin scintillators shielded by 250 g/cm^2 of mass overburden (muon detector) and thin unshielded scintillators (EM detector).

Reference Shower Signals

The reference CORSIKA showers were simulated at a fixed energy of 10^{19} eV. Although the signal fluctuations and the shapes of the attenuation curve depend slightly on the shower energy, the final results are not affected by such variations. To describe low energy interactions, the FLUKA model was used. The high energy interactions were simulated using the two most up–to–date models tuned to the LHC data (run I): QGSJet II–04 and EPOS–LHC. About 60 showers were produced for each primary, each model of high energy interactions and for each of seven zenith angles between 0° and 45° maintaining equal steps in $\cos^2(\Theta)$.

The reference muon and EM signals, S_μ^{19} and $S_{\rm EM}^{19}$, were determined for each model, primary and zenith angle as the densities of corresponding particles averaged over these 60 showers at a distance of 1000 m from the shower core. Both these reference signals were fitted by quadratic functions of $\cos^2(\Theta)$ (attenuation curves) with precisions at the level of a few percent. The muon and EM attenuation curves are depicted in Fig. 4.6. They depend on the type of the primary particle. The EM signal obeys a stronger dependence on the zenith angle than the muon signal.

In Fig. 4.7, the ratios of ground signals induced by primary He, N and Fe nuclei to the proton–induced signal are depicted for the array of muon (left panel) and EM (right panel) detectors. Whereas

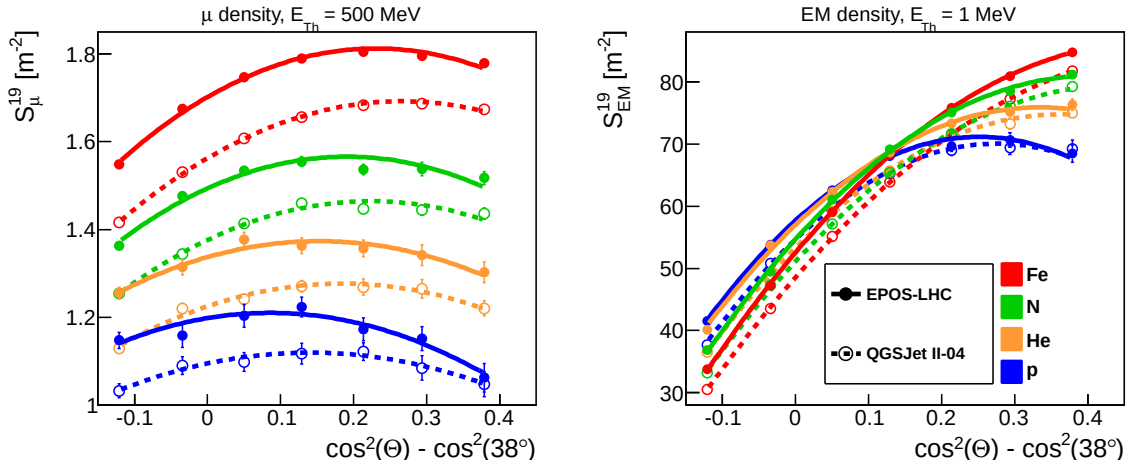

Figure 4.6: Attenuation curves. Reference signals of CORSIKA showers of energy 10^{19} eV are fitted with quadratic functions of $\cos^2(\Theta)$ for the array of muon detectors (**left panel**) and EM detectors (**right panel**) in the range $\Theta \in \langle 0°, 45° \rangle$. Two models of hadronic interactions and four primary species are distinguished by types of lines and colors, respectively.

the ratio for S_μ^{19} is greater than one for all zenith angles and increases with the mass number of the primary particle, the ratio for S_{EM}^{19} decreases more steeply with zenith angle than in the case of S_μ^{19}; and is even smaller than unity beyond $\Theta \simeq 30°$. This different behavior of S_μ^{19} and S_{EM}^{19} with the zenith angle for different primary particles plays the main role in the considerations described in what follows.

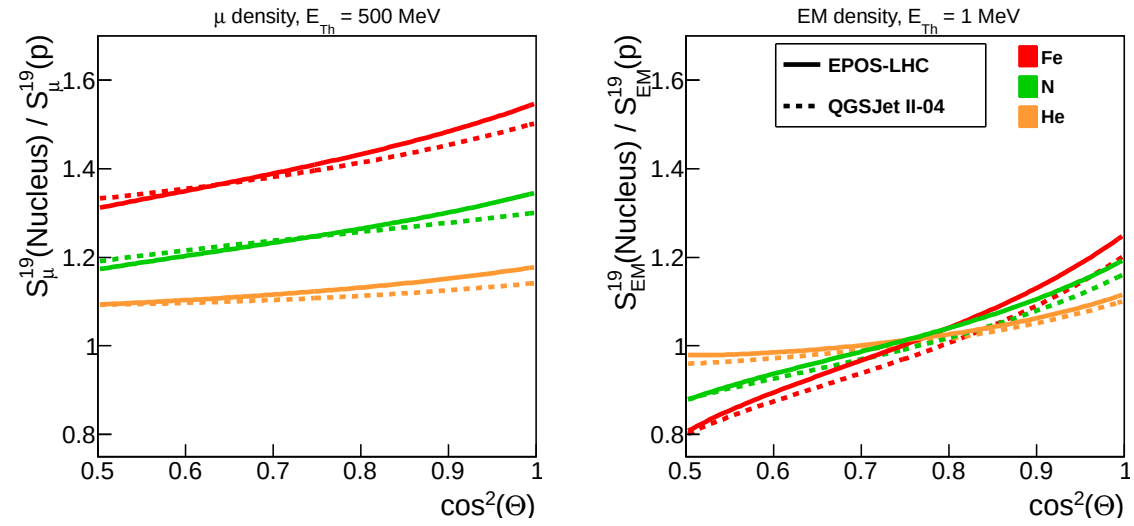

Figure 4.7: Ratios of shower signals. Nucleus to proton ratios for the muon (**left panel**) and EM (**right panel**) signals are plotted as a function of $\cos^2(\Theta)$. CORSIKA simulations at energy 10^{19} eV were used. Two models of hadronic interactions and three primary nuclei are distinguished by types of lines and colors, respectively.

Important aspects to be explored are the fluctuations of the muon and EM signals and their respective correlations. To include these effects in the simplified simulations of shower signals, the correlations of S_{μ}^{19} and S_{EM}^{19} and their fluctuations were studied in detail for each zenith angle, for both models of hadronic interactions and for all four primary particles. Relative fluctuations in the muon signal were estimated to be about 3% for primary iron nuclei increasing up to 20% for primary protons. It turned out that they change a little in the whole range of zenith angles; the largest change was observed for protons (20% at 0° and 15% at 45°). Somewhat smaller relative fluctuations in the EM signal occurred, in a way that they are reasonably well correlated with the relative muon fluctuations. However, the roughly linear relationship between the muon and EM signal depends on the zenith angle. An example of the properties of the signal fluctuations and their relationship is shown in Fig. 4.8.

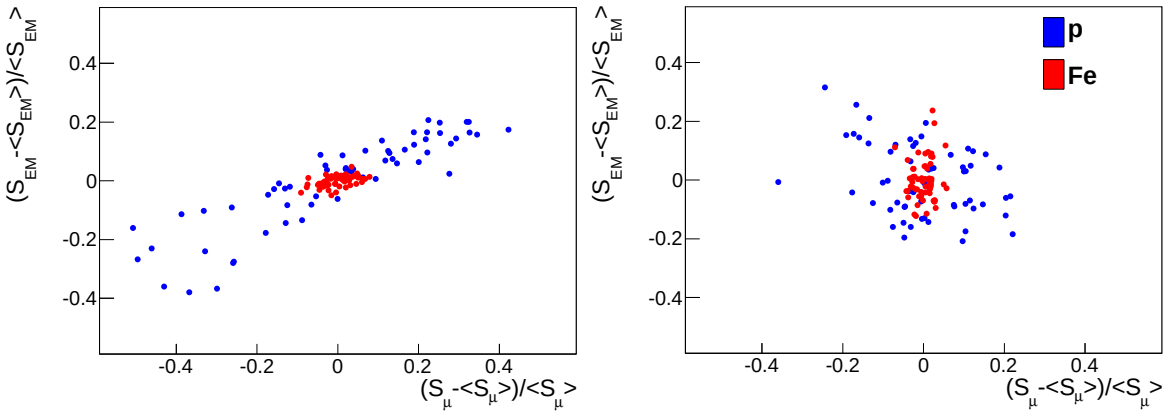

Figure 4.8: Spread of the EM signal plotted as a function of spread of the muon signal. Sixty showers induced by protons (blue) and 60 showers induced by iron nuclei (red) were simulated with the QGSJet II–04 model at energy 10^{19} eV and with zenith angles 0° (**left**) and 45° (**right**).

Simplified Simulation of Shower Signals

Utilizing characteristics of the reference signals, simplified simulations of shower signals that are induced simultaneously in two idealized detector arrays responding to the muon and EM components, respectively, were performed. A number of air showers for various mass composition scenarios preserving the basic properties of CORSIKA showers were produced. These sets of air showers were characterized by their realistic energy spectrum. The arrival directions of the primary particles were assumed to be isotropic (uniform in $\cos^2(\Theta)$). Besides the zenith angle of its arrival, each shower was identified by the muon and EM signal that triggered simultaneous responses of the two arrays of detectors. The latter two quantities were obtained from the shower energy assuming the attenuation of secondary particles in the atmosphere and shower fluctuations supplemented by detector resolutions as described in the following.

To be more specific, 286 four–component primary beams with protons and He, N and Fe nuclei were used. This way all possible mass compositions of primaries were covered differing in the relative abundance of each of these four primaries in steps of 10%. The shower energies were generated in the range $\langle 10^{18.5}, 10^{20} \rangle$ eV using a spectral index 2.7 and including the GZK–like feature at the end of the spectrum according to Eq. (4.1). The shower zenith angles were generated randomly between 0° and 45° assuming they are distributed uniformly in $\cos^2(\Theta)$. The maximal value of the zenith angle corresponds to the upper bound for the full trigger efficiency of the EM detectors deployed in current arrays, see e.g. [91].

In order to describe the detector response, it was assumed that the shower energy is directly linked with a single signal that would be recorded when a shower of the same energy hits the detector array at a zenith angle of 38°. It was further assumed that the shower energy E_{MC} and this shower signal, S_{38}, are related according to Eq. (4.2). An arbitrary normalization constant $a = 10^{16}$ eV was chosen. For the sake of simplicity the exponent $b = 1$ was taken. As mentioned in the previous section, it is not far from the value estimated at the Pierre Auger Observatory and at the Telescope Array experiment.

In the subsequent analysis, the muon and EM signals were determined for a shower induced by a given primary particle with a given primary energy that is incident at a given zenith angle. In the first step, the type of the primary particle was generated according to a chosen mass composition scenario. The generated shower energy E_{MC} was transformed to the shower signal S_{38} using Eq. (4.2). Then, muon and EM responses for the shower incident at the generated zenith angle were obtained. For this purpose, corresponding reference shapes of the attenuation curves (Fig. 4.6) and their ratios (Fig. 4.7) were applied to the shower signal S_{38}. In the next step, the fluctuations of the shower signals of both muon and EM components and their respective correlations were included into the analysis. The results from the CORSIKA simulations were used for this purpose. Finally, another smearing of the muon and EM signals was additionally applied in order to model the effect of detector resolutions. For both signals the Gaussian smearing with a relative variances of 20% was used. Note that these detector resolutions were set to be worse than those resolutions quoted by the current detector arrays [91, 55]. This way, the simulated muon and EM signals were produced, S_{EM} and S_μ, that each air shower induces in the two idealized arrays of the muon and EM detectors at a wide range of primary energy preserving the basic properties of CORSIKA showers. In particular, 7×10^5 air showers were simulated for each of different mass compositions of the beam of the primary particles.

Combined Signal Approach

In order to get sufficient information about the properties of the combined responses of the two arrays of detectors sensitive to the muon and EM secondaries, different mass compositions of the primary beams were studied. It turned out that the dispersion of the primary mass can be assessed by relying upon different shapes of the attenuation curves for the muon and EM signal, see also Fig. 4.7. To quantify this finding, a parameter was introduced that is sensitive to the dispersion of the mass of

a beam of primary particles causing air showers that generate the muon and EM signals in the two idealized arrays of detectors.

Following the procedure of inferring the CIC curve, the sets of MC data for each of the composition scenarios were each divided into 7 equidistant bins in $\cos^2(\Theta)$, where $0 \leq \Theta \leq 45°$, containing ~100 000 events per bin. In each such bin, $N_{\rm Cut}$ = 12 000 events with the highest signals induced in both the muon and EM detectors were selected. This choice corresponds roughly to the selection of events with a primary energy higher than about 10^{19} eV. Specifically, for each bin of $\cos^2(\Theta)$, a set $\mathbb{M}^{\mu}$ of 12 000 events with the highest signal in the muon detector was selected and another set $\mathbb{M}^{\rm EM}$ of 12 000 events with the highest signal in the EM detector. Finally, the number of identical events, $N_{\rm m} = |\mathbb{M}^{\mu} \cap \mathbb{M}^{\rm EM}| \leq N_{\rm Cut}$, that are present in both these event sets was counted.

Dependencies of the fraction of the number of events that matched in both detectors, $N_{\rm m}/N_{\rm Cut}$, are shown in Fig. 4.9 as a function of zenith angle for four different primary beams. For any one–component scenario only a small mass–dependent decrease of the number $N_{\rm m}$ is expected with increasing zenith angle. It is due to combined effects given by shower–to–shower fluctuations of the muon and EM signals, their correlations and the resolutions of both detectors (see results in Fig. 4.9 for pure proton beams in blue and for iron nuclei in red). On the other hand, as the primary particles become mixed, the orderings of events according to sizes of their signals in the two detectors diverge, resulting in an additional decrease of the number of matched events $N_{\rm m}$ with increasing zenith angle (see results in Fig. 4.9 for mixed compositions in orange and green). This effect is mainly caused by a very different ordering of the sizes of EM signal with respect to a primary particle type at different zenith angle bins.

Let us consider, for example, that iron nuclei and proton primaries of similar energies incident at zenith angles of about 40° cause air showers that induce signals in the muon detector that are slightly larger than the signal $S^{\mu}_{\rm Cut}$. This signal corresponds to the chosen threshold number $N_{\rm Cut}$, i.e. these events still belong to the set $\mathbb{M}^{\mu}$. Consideration of these events was motivated by the fact that there is a higher chance for primary iron nuclei compared to primary protons to induce air showers that end up in the set of events $\mathbb{M}^{\mu}$, see left panel of Fig. 4.7 ($S^{19}_{\mu}({\rm Fe}) > S^{19}_{\mu}({\rm p})$ for $\Theta \simeq 40°$). On the other hand, since the EM signal induced by primary iron nuclei in the EM detector is smaller on average than the EM signal caused by protons for considered events, see right panel of Fig. 4.7 ($S^{19}_{\rm EM}({\rm Fe}) < S^{19}_{\rm EM}({\rm p})$ for $\Theta \simeq 40°$), there is a higher chance that the signal of protons is larger than the threshold value $S^{\rm EM}_{\rm Cut}$ than it is for the signal of iron nuclei. Here, the threshold signal $S^{\rm EM}_{\rm Cut}$ is determined by the threshold number $N_{\rm Cut}$ in the EM detector. Therefore, most of the events under consideration that are caused by primary iron nuclei are not included in the set $\mathbb{M}^{\rm EM}$. As a result, the number of matched events $N_{\rm m}$ decreases more steeply with the increasing zenith angle of incident particles for primary beams consisting of a mixture of particles than for pure primary beams, as demonstrated in Fig. 4.9.

To a first approximation, the number of matched events $N_{\rm m}$ is well described by a quadratic function of $\cos^2(\Theta)$ for any primary composition. The fitted quadratic curves of the fraction of matched events are also shown in Fig. 4.9. They were mostly found as decreasing functions of the increasing

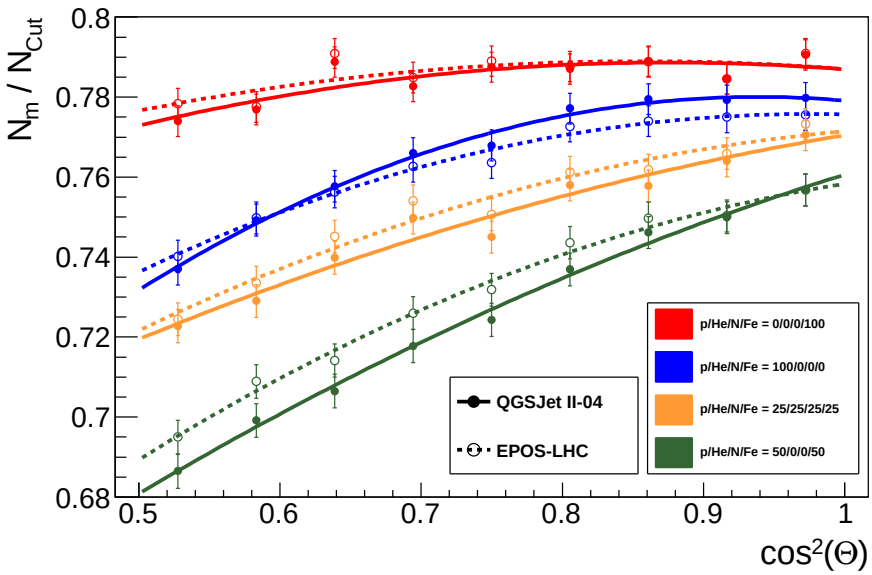

Figure 4.9: Attenuation of the matched fraction. Fractions of simulated events that are matched in both detectors, N_m/N_{Cut}, are plotted as a function of $\cos^2(\Theta)$. Results of four examples of the primary mass composition (different colors) and for the two models of hadronic interactions (full and empty markers) are shown. Depicted curves are quadratic fits to these fractions.

zenith angle. Inferred from these curves, a descriptive parameter that simply quantifies this dependence was defined

$$\Phi = 1 - \frac{N_m(\Theta = 45^\circ)}{N_m(\Theta = 0^\circ)}. \tag{4.3}$$

It expresses the decrease of the number of events N_m matched in both muon and EM detectors with zenith angle from 0° to 45° as displayed in Fig. 4.9. For the pure primary beams, the parameter Φ acquires larger values for lighter primaries. Even larger values are expected for the non–zero variance of the mass of incident primaries.

4.2.2 Sensitivity to Mass Composition

In what follows, several sets of four–component primary beams were examined. These beams were characterized by the mean and the variance of the logarithmic mass of primary nuclei. Specifically, it was assumed that the primary cosmic rays consist of four nuclei with A_i nucleons, i = p, He, N, Fe, contributing with relative abundances $f_i \in \langle 0,\ 1\rangle$, where $\sum_{i=1}^{4} f_i = 1$. The mean logarithmic mass, $\langle \ln A\rangle$, and the dispersion of the logarithmic mass in the primary beam, $\sigma^2(\ln A)$, are given by Eq. (2.31).

Dispersion of Primary Masses

Using the two models of hadronic interactions, the muon and EM signals were simulated as they occur in the idealized arrays of detectors for each of the 286 arbitrarily chosen four–component primary

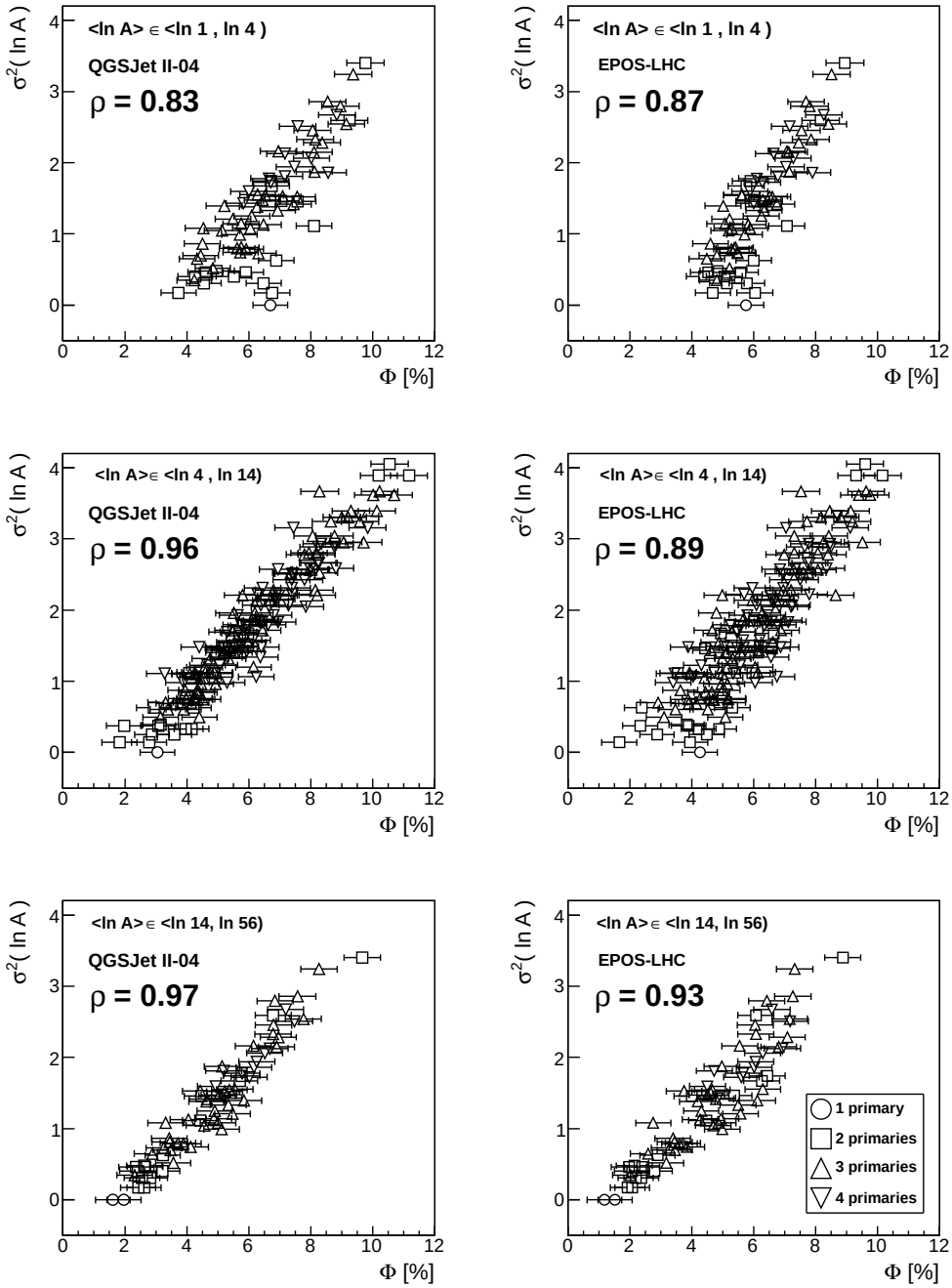

Figure 4.10: Sensitivity to the dispersion of primary masses. The variance of the logarithmic mass of the primary beam, $\sigma^2(\ln A)$, is plotted as a function of the parameter Φ defined in Eq. (4.3) for QGSJet II–04 (**left panels**) and EPOS–LHC (**right panels**). Three regions of the mean logarithmic mass, $\langle \ln A \rangle$, are selected (**rows of panels**) from 286 different mass compositions of the primary beam. The Pearson's correlation coefficient ρ is calculated for each of 6 plots. Markers indicate the number of primaries present in the beam.

beams within the simplified treatment described in the previous text. Corresponding matched fractions of the muon and EM events were determined as functions of the zenith angle. Finally, for each of the chosen primary composition the descriptive parameter Φ given in Eq. (4.3) was derived, and this parameter was related with the given dispersion of the logarithmic mass in the primary beam.

The results for three regions of $\langle \ln A \rangle$ are summarized in Fig. 4.10. In this figure, the dispersion of the primary beam is depicted as a function of the parameter Φ for QGSJet II–04 (left panels) and EPOS–LHC (right panels). The incident beams with a single primary up to four primary components were analyzed. Good agreement is observed between the results obtained with both examined models of hadronic interactions. In this analysis, the spread of the primary beam masses increases with the difference of the number of matched events N_{m} between the zenith angles of 0° and 45° (see Fig. 4.9), as described by the parameter Φ introduced in Eq. (4.3). The Pearson's correlation coefficient (ρ) of $\sigma^2(\ln A)$ and Φ is calculated for each region of $\langle \ln A \rangle$ and each model of hadronic interactions and it is displayed in the left upper corner of every plot in Fig. 4.10.

It turns out that the parameter Φ correlates well with the dispersion of logarithmic mass of the primary beam constituents. Obviously, the knowledge of the mean logarithmic mass increases its explanatory power. To demonstrate this feature, different bins of $\langle \ln A \rangle$ of a width of $w \approx 1.3$ were used. It is equivalent to the information that $\langle \ln A \rangle$ can be obtained from an independent measurement at the same energy. The choice of w is realistic since, for example, the uncertainty derived from the measurements performed at 10^{19} eV is typically $\delta(\langle \ln A \rangle) = 0.4 < w/2$, see bottom panels of Fig. 3.10.

On average, the parameter Φ decreases with the increasing mean logarithmic mass. Also, the correlation between Φ and $\sigma^2(\ln A)$ is improving with the increasing mean logarithmic mass.

It is worth emphasizing that the parameter Φ behaves similarly with the dispersion of the primary mass for a wide range of the selected thresholds N_{Cut}. In the presented examples, $N_{\mathrm{Cut}} = 12\,000$ is only a matter of an arbitrary choice reflecting the total number of events that was simulated and the width of the $\cos^2(\Theta)$ bin that was chosen. Also the numbers of matched events, N_{m}, are not of crucial importance in this treatment; only their relative changes with the zenith angle play any roles.

In this procedure, the size of the number of matched events is primarily given by the shower–to–shower fluctuations and by the resolutions of both detectors. On the other hand, the evolution of the number of matched events with the zenith angle is mainly caused by corresponding reference responses of the muon and EM detectors as obtained for different primary nuclei in Section 4.2.1.

Discussion

The presented relationship between the variance of the logarithmic mass of the primary beam, $\sigma^2(\ln A)$, and the parameter Φ derived from different responses of the two arrays of different detectors is rather general. It stems from the basic properties of available shower observables as well as from the adopted CIC approach. Somewhat different detector responses that might be various functions of the zenith angle, while proportional to the muon or EM density, would not change this result significantly.

For example, the muons were not considered in the response of the EM detector (thin scintillator)

since their inclusion cannot change the results substantially. The reason is that the ground density of the total number of muons is about 15–50 times smaller than the ground density of EM particles. Moreover, the zenith angle behavior of the muon component is rather moderate.

Nonetheless, it needs to be stressed that a specific application of the parameter Φ to quantify the spread of mass in the primary cosmic ray beam for the measured UHECR data would require a detailed knowledge of the detectors' responses. Taking into account the specificity of their observables, this technique could also be generalized for observatories studying cosmic rays of lower energies.

In a sense, the effects of shower–to–shower fluctuations on the zenith–angle dependence of the number of matched events are not substantial in this treatment. It was verified numerically that the results presented in Fig. 4.10 will change only marginally for several times stronger correlations between the muon and EM signals. Less significant fluctuations and correlations incorporated in simulated signals leave the results almost unaffected. The studied relationship between $\sigma^2(\ln A)$ and Φ remains valid also in cases where the shower signals are taken at various distances from the shower core. The same holds for different threshold energies of detected secondary particles in both types of detectors.

The crucial ingredient of the presented method is that the two most up–to–date models of hadronic interactions do not show any substantial deviations in terms of shapes of reference attenuation curves and their ratios. For a given primary composition, the relationship between the two types of signals, as expressed by the parameter Φ, does not depend strongly on the actual values of the muon and EM signals. Therefore, the details of the models of hadronic interactions are rather suppressed in this treatment. One needs to keep in mind, however, that the properties of the reference showers could still be different from the properties of the real showers detected in the current detector arrays.

In comparison with the statistical uncertainty of the currently most precise method based on the depth of shower maximum measured at 10^{19} eV shown in bottom panels of Fig. 3.10, the spread of the mass $\sigma^2(\ln A)$ can be determined with a similar uncertainty $\delta(\sigma^2(\ln A)) \simeq 0.5$. This uncertainty was estimated as the variance of the distribution of $r = \sigma^2_{\rm meas}(\ln A) - \sigma^2(\ln A)$, where $\sigma^2_{\rm meas}$ was calculated using a linear fit of $\sigma^2(\ln A)$ depending on Φ for different regions of $\langle \ln A \rangle$ and various models of hadronic interactions. The variance of r is decreasing with increasing $\langle \ln A \rangle$, see also correlation coefficients in Fig. 4.10. Similar or even better precision, when compared to other methods, and weak dependence on the model assumption make the presented method well suitable to complement frequently conducted studies of the mass composition of primary particles that are based on the analysis of the mean logarithmic mass of primary species.

4.3 Summary

In both parts of the chapter, the basic properties of CORSIKA showers modeled with two post–LHC models of hadronic interactions were used for simplified simulations of the detector responses to UHECR showers.

In the first section, two primaries were considered to initiate showers detected in EM detectors and in detectors of a combined response to the EM and muon shower component. These rough responses were motivated by responses of surface detectors deployed at the Telescope Array and at the Pierre Auger Observatory, respectively. In the second section, four different primaries were considered to initiate showers that induce signals in a hypothetical observatory with two different types of arrays sensitive to the EM and to the muon component.

In the first part of the chapter, it was demonstrated that for a pure composition the CIC method and the investigated MC–based approach are equivalent to correct the signals for attenuation with zenith angle. For a mixed composition, the CIC method eliminates the zenith angle bias in the reconstruction of the shower energy, whereas the zenith angle bias is present in the investigated MC–based approach both for EM and EM+μ detectors. Once the models of hadronic interactions truthfully predict the shape of attenuation curves, the relative deviation of the reconstructed CIC curve from the MC predictions could be used to address the mass composition of primary particles. The studied example of a source signal at the highest energies (above 50 EeV) shows almost no impact on the CIC shape for intensity cuts at lower energy ($\lesssim$ 30 EeV) and small deviations (few %) of the CIC shape were observed for intensity cuts at energies $\gtrsim$ 40 EeV.

In the second part of the chapter, the CIC approach was applied to both signals that were reconstructed in coincident arrays of EM and muon detectors of a hypothetical observatory. It was demonstrated that the dispersion of the mass in the primary beam of the UHECR particles can be addressed and even measured using the zenith angle behavior of the number of matched events in both types of arrays. Very similar results for the two models of hadronic interactions tuned to the LHC data were obtained. The developed method could be applied to the data of an observatory with independent muon and EM detectors of some future observatory when a detailed response of the detectors is incorporated in the simulations. Even the existing observatories probing lower energies of cosmic rays can benefit from this method (e.g. KASCADE–Grande with its muon and EM detectors).

Chapter 5

Combined Analysis of Ground Signal and Depth of Shower Maximum

The parameter that is most often used to study the mass composition of UHECR is the depth of shower maximum (X_{max}). As it was discussed in Section 2.3, the number of muons on ground (N_μ) measured with surface detectors is another quantity that could be used to study the mass composition of UHECR. In this chapter, a combined analysis of simulated showers is performed in the (N_μ, X_{max}) plane and the measured data of the Pierre Auger Observatory are analyzed in the (ground signal, X_{max}) plane where the ground signal is the signal induced in the water Cherenkov detectors. As in the previous chapter, also this chapter contains the author's original research.

At first, a method to obtain simultaneously the primary fractions and the rescaling of the muon signal (see Section 3.4.2) is introduced and demonstrated on a set of simulated showers in Section 5.1. The method was presented in the conference proceedings [103]. Secondly, the method is applied to the data of the Pierre Auger Observatory in Section 5.2. Note that the application of the method shall be taken as very preliminary. It is not set as a part of the official results of the Pierre Auger Observatory. Nevertheless the author takes the opportunity to preliminarily demonstrate the method using the real data.

5.1 Combined Analysis of Muon Shower Size and Depth of Shower Maximum

As it was already presented in Section 3.4.2, the mass composition of UHECR can be inferred on an average basis from the measurement with fluorescence detectors when the central moments of X_{max} distribution are compared with MC predictions. The fluorescence technique provides a precise measurement of X_{max} with a resolution around 20 g/cm^2, but a large systematic uncertainty remains in the interpretation of the mass composition of UHECR. The obstacle comes predominantly from different predictions of hadronic interaction models that are extrapolated from accelerator energies

to interaction energies of UHECR particles. These energies can be larger even by a few orders of magnitude in the center of mass system than the energies of collisions at accelerators. The mass composition of UHECR remains uncertain, and even unknown at the highest energies where a steep decrease of the flux is observed. Moreover, the number of events collected by fluorescence telescopes wrt. the number of events identified by ground detectors is smaller by a factor of 10 due to their low duty cycle.

Assuming a small number of types of primary particles in the UHECR beam, the most probable fractions of these primaries were inferred in [71] by the Pierre Auger Collaboration using the fluorescence measurement (see also Fig. 3.12). The measured distributions of X_{max} were compared with the X_{max} distributions of simulated showers that were initiated by a combination of assumed primaries. Large differences in the results were found among the models of hadronic interactions. Also, a degeneracy of solutions with similar probability can be expected as, generally, there are more combinations of MC distributions of the individual primaries which describe the measured distributions similarly well.

A measurement of the number of muons with ground detectors can provide an independent way to infer the mass composition of UHECR. Muon detectors have almost 100% duty cycle and, when a good resolution of N_μ is achieved ($\lesssim$10%), even better separability of the individual primaries can be achieved than in the case of the X_{max} measurement using the fluorescence technique. However, there is a lack of produced muons in MC simulations when compared with the measured data as it was pointed out in Section 3.4.2. The underestimation of the muon production is usually characterized in terms of the muon rescaling factor R_μ. This factor reflects how much the number of muons produced in the MC simulations needs to be increased to fit the measured data. Moreover, a steeper dependence (almost linear) of N_μ on the shower energy, see e.g. Eq. (2.21), than the dependence (logarithmic) of X_{max} on the shower energy, see e.g. Eq. (2.24), makes the study of mass composition using only the N_μ measurement more difficult than in case of the X_{max} measurement. Therefore a simple comparison of the measured distributions of N_μ with MC predictions would be very complicated and a simultaneous measurement of the shower energy is necessary to study the mass composition of UHECR using the measurement of N_μ.

A combined measurement of UHECR showers with the fluorescence technique (X_{max} and shower energy) and muon detectors (N_μ) could be a more successful way to address the mass composition of UHECR. In the previous studies, the detected muon and electromagnetic signals were utilized to determine the average mass number of a set of air showers, see e.g. [101]. There are also methods estimating the spread of masses in the UHECR primary beams via correlation of N_μ and X_{max} [74], or from signals in muon and electromagnetic detectors presented in Section 4.2. However, it needs to be mentioned that the two currently operating experiments (the Pierre Auger Observatory and the Telescope Array) do not yet directly measure the muon component of showers with zenith angles below 60°.

This section introduces another method to determine the fractions of the assumed primaries in

which the rescaling of N_μ can be achieved simultaneously with a single fit of a combined measurement of $X_{\max}$ and N_μ. In order to investigate potential of this method, MC showers were generated with two models of hadronic interactions tuned to the LHC data (run I).

5.1.1 Simulated Showers

Around 10^5 showers were simulated with the CONEX 4.37 generator for p, He, N and Fe primaries with a fixed energy $10^{18.5}$ eV and for each of the two models of hadronic interactions (QGSJet II–04 and EPOS–LHC). The zenith angles (Θ) of showers were distributed uniformly in $\cos^2\Theta$ for Θ in $\langle 0,\ 60°\rangle$.

For each shower, muons with threshold energy 1 GeV at ~1400 m a.s.l. were counted to calculate N_μ. Electromagnetic particles of energies above 1 MeV formed the longitudinal profile (dependence of the deposited energy on the atmospheric depth) that was fitted with the Gaisser–Hillas function (see Eq. (3.1)) to obtain $X_{\max}$.

The Gaussian smearing of $X_{\max}$ and N_μ with a variance equal to $\delta(X_{\max})$ and $\delta(N_\mu)$, respectively, was applied to each simulated shower. These smearings ($\delta(X_{\max}) = 20$ g/cm^2 and $\delta(N_\mu)/N_\mu = 10\%$) imitate the detector resolutions. A correction for the attenuation of N_μ with zenith angle was adopted due to the different amount of atmosphere penetrated by the air shower before it reaches the ground. The correction was made using a cubic function in $\cos^2(\Theta)$ for each model of hadronic interactions. An equally mixed composition of p, He, N and Fe was considered to obtain an average attenuation of N_μ.

5.1.2 Method

For both hadronic interaction models, the $X_{\max}$ distributions were parametrized with Gumbel functions [104] g_i (see Fig. 5.2) for all of the four primaries i = p, He, N, Fe. Also, the dependence of the mean N_μ, $\langle N_\mu\rangle$, on $X_{\max}$ was parametrized with quadratic functions in $X_{\max}$ that were denoted as $\langle N_\mu^i\rangle$ (see Fig. 5.1); again for each of the four primaries. The single rescaling factor R_μ of $\langle N_\mu^i\rangle$ was introduced[1] to incorporate into the method the case when a rescaling of $\langle N_\mu^i\rangle$ obtained from MC is needed to fit the measured $\langle N_\mu\rangle$. Then, for a combination of four primaries with relative fractions f_i, $\sum f_i = 1$, the resulting dependence of $\langle N_\mu\rangle$ on $X_{\max}$ is given by

$$\langle N_\mu\rangle = \sum_i \left(w_i \cdot \langle N_\mu^i\rangle\right) R_\mu \tag{5.1}$$

where the weights w_i are expressed as

$$w_i = \frac{f_i \cdot g_i}{\sum_j \left(f_j \cdot g_j\right)}. \tag{5.2}$$

[1] In principle R_μ can be different for showers induced by different primaries, but within the superposition model the usage of single R_μ for all four primaries is fair approximation. The dependence of R_μ on $X_{\max}$ is also neglected.

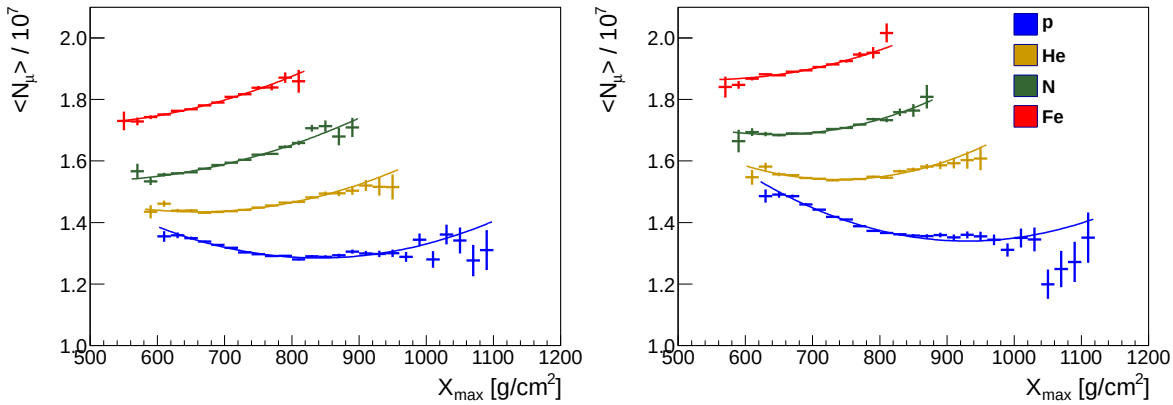

Figure 5.1: Dependence of the mean N_μ on $X_{\max}$ parametrized with quadratic functions $\langle N_\mu^i \rangle$. Showers initiated by four primaries (see colors in the legend) were simulated with QGSJet II–04 (**left**) and EPOS–LHC (**right**) for $\delta(X_{\max}) = 20$ g/cm^2 and $\delta(N_\mu)/N_\mu = 10\%$. Only bins of $X_{\max}$ with more than 30 showers were considered in the quadratic fits.

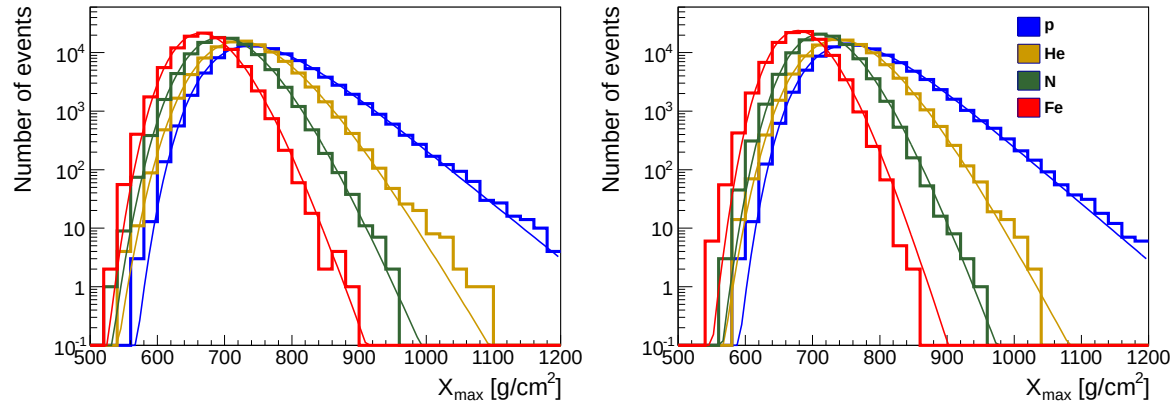

Figure 5.2: Distributions of $X_{\max}$ parametrized with Gumbel functions g_i. Showers initiated by four primaries (see colors in the legend) were simulated with QGSJet II–04 (**left**) and EPOS–LHC (**right**) for $\delta(X_{\max}) = 20$ g/cm^2.

For each bin of $X_{\max}$ with width 20 g/cm^2, $\langle N_\mu \rangle \equiv \langle N_\mu \rangle (X_{\max})$ is calculated as the weighted average of $\langle N_\mu^i \rangle \equiv \langle N_\mu^i \rangle (X_{\max})$ rescaling all $\langle N_\mu^i \rangle$ with the same factor R_μ. The weights $w_i \equiv w_i(X_{\max})$ reflect the relative contribution of each individual primary with a relative fraction f_i to each bin of $X_{\max}$ according to $g_i \equiv g_i(X_{\max})$.

Thus, any given dependence of $\langle N_\mu \rangle$ on $X_{\max}$, which is similar to the dependence of showers initiated with a combination of proton, helium, nitrogen and iron nuclei, can be fitted with the four–parameter ($f_{\rm p}$, $f_{\rm He}$, $f_{\rm N}$ and R_μ) fit. The Fe fraction is obtained afterwards as $f_{\rm Fe} = 1 - f_{\rm p} - f_{\rm He} - f_{\rm N}$.

An example of application of the method to the mixed composition of showers initiated with 50% p and 50% Fe is shown in Fig. 5.3. The fitted dependence of $\langle N_\mu \rangle$ on $X_{\max}$ (black points) is shown with

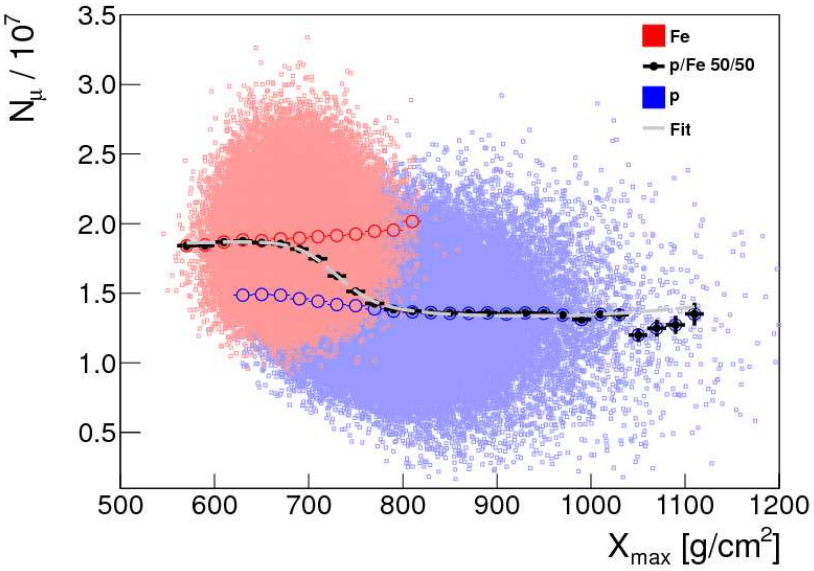

Figure 5.3: Example of a fit (gray dashed line) for a set of showers composed of 50% p and 50% Fe (black points). Showers were generated with EPOS–LHC for $\delta(X_{\rm max}) = 20$ g/cm^2 and $\delta(N_\mu)/N_\mu = 10\%$. The individual p and Fe showers are shown with light blue and light red points, respectively. $\langle N_\mu^{\rm p}\rangle$ is depicted with blue open points and $\langle N_\mu^{\rm Fe}\rangle$ with red open points. The parametrized g_i and $\langle N_\mu^i\rangle$ for EPOS–LHC were considered in the fit.

the gray dashed line. The hadronic interaction model EPOS–LHC was used in this example for the generation of showers as well as for the parameterization of g_i and $\langle N_\mu^i\rangle$. Starting from the lowest values of $X_{\rm max}$, $\langle N_\mu\rangle$ matches $\langle N_\mu^{\rm Fe}\rangle$ for $X_{\rm max} \lesssim 650$ g/cm^2 where a transition towards $\langle N_\mu^{\rm p}\rangle$ begins. The transition continues up to $X_{\rm max} \approx 800$ g/cm^2. For higher values of $X_{\rm max}$, $\langle N_\mu\rangle$ matches $\langle N_\mu^{\rm p}\rangle$.

5.1.3 Tests of Method

In this subsection, basic examples of the presented method are shown together with estimates of how accurately the primary fractions and the muon rescaling factor can be determined. In the following, the detector resolutions are assumed to be $\delta(X_{\rm max}) = 20$ g/cm^2 and $\delta(N_\mu)/N_\mu = 10\%$. In total, 286 combinations of mixed compositions of p, He, N and Fe with fractions in steps of 10% were considered for both models of hadronic interactions. Each of these compositions was reconstructed with each of the two parameterizations obtained for the two models of hadronic interactions. Additionally, an example dataset was reconstructed with parameterizations of each of the two models to have another assessment of the method with respect to the two models of hadronic interactions.

The difference between the fitted ($f_{\rm FIT}$) and the true ($f_{\rm MC}$) primary fractions is shown in Fig. 5.4 for QGSJet II–04 (blue) and EPOS–LHC (red) considering all 286 possible compositions of the four primaries. The reconstructed primary fractions of showers generated with a different model than that was used for the parameterization with g_i and $\langle N_\mu^i\rangle$ are depicted in green and black. Scenario 1 (2) cor-

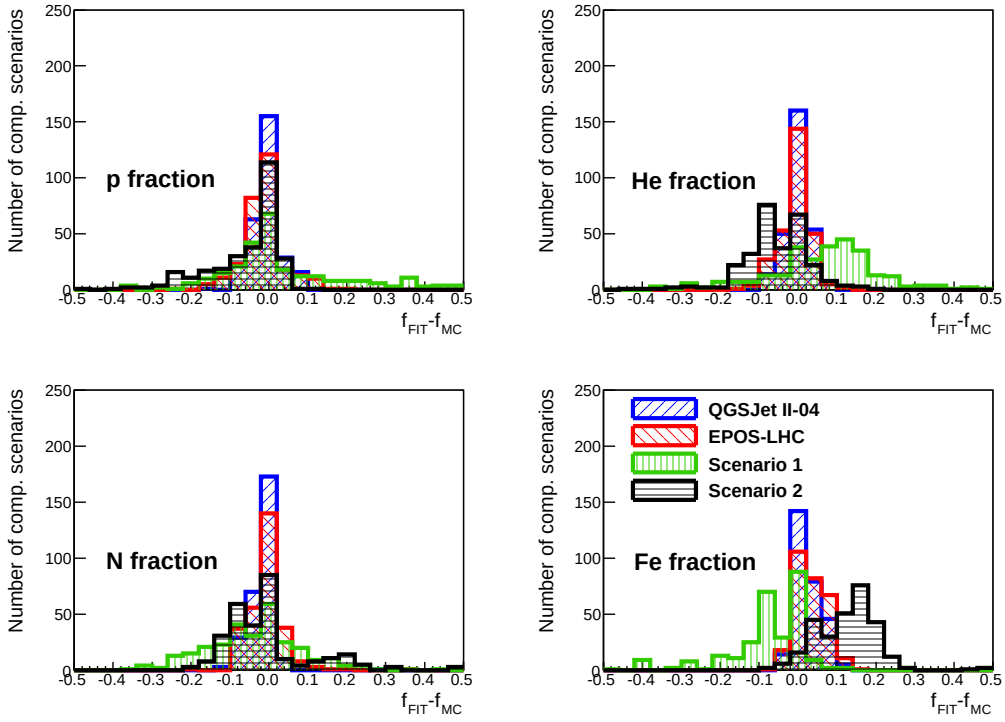

Figure 5.4: The difference between the fitted (f_{FIT}) and the true (f_{MC}) primary fractions. All 286 possible compositions of the four primaries in steps of 10% were considered. Scenario 1 (2) corresponds to QGSJet II–04 (EPOS–LHC) showers fitted with parameterizations of g_i and $\langle N_\mu^i \rangle$ from EPOS–LHC (QGSJet II–04).

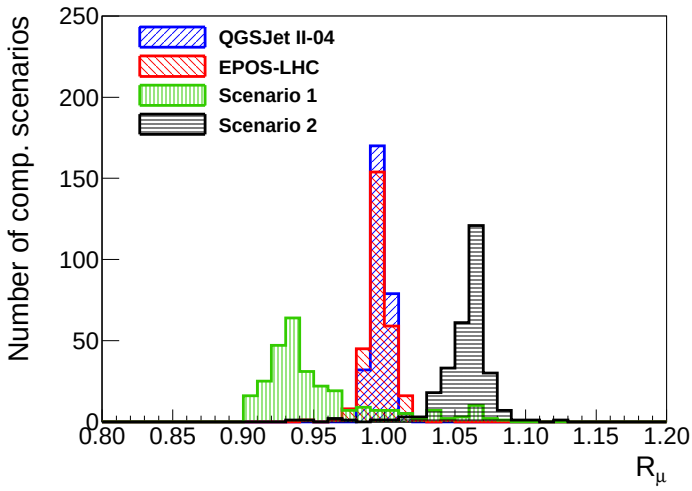

Figure 5.5: Rescaling of the number of muons. All 286 possible compositions of the four primaries in steps of 10% were considered. Scenario 1 (2) corresponds to QGSJet II–04 (EPOS–LHC) showers fitted with parameterization of g_i and $\langle N_\mu^i \rangle$ from EPOS–LHC (QGSJet II–04).

responds to showers produced with QGSJet II–04 (EPOS–LHC) and fitted with the parameterizations obtained from EPOS–LHC (QGSJet II–04) showers.

When the same model of hadronic interactions is used for the generation of showers and the parameterization with g_i and $\langle N_\mu^i \rangle$, the primary fractions are reconstructed within ∼5% of the true values. This defines the precision of the method in case of primary fractions. However, in cases of Scenario 1 and 2 (when the true g_i and $\langle N_\mu^i \rangle$ are not precisely known), the primary fractions can be inferred with a deviation of the order even ∼25%.

The muon rescaling factor is plotted for the 286 possible compositions of the four primaries in Fig. 5.5. The muon rescaling factor was found to be within a few % from unity, when the same models were used for the parameterization and the generation of showers (red and blue). This defines the precision of the method in case of R_μ. Black and green histograms correspond to the relative difference of N_μ for showers generated with QGSJet II–04 and EPOS–LHC, which is about 6%.

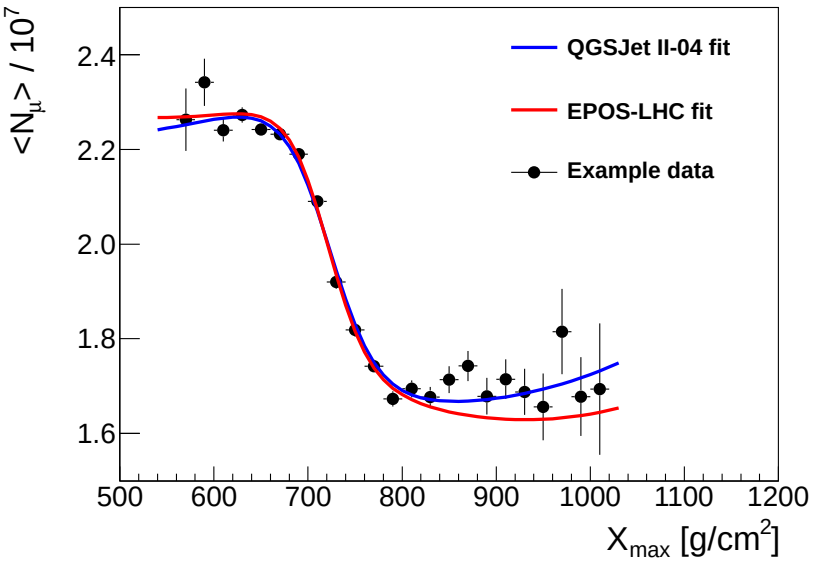

Figure 5.6: An example of data (black points) fitted with QGSJet II–04 (blue) and EPOS–LHC (red) parameterizations.

As another check, an example data composed of 5000 p and 5000 Fe showers were produced with QGSJet II–04. For each shower, N_μ was scaled by a factor 1.3 and $X_{\max}$ was increased by 7 g/cm^2. Note that EPOS–LHC generates showers with $X_{\max}$ deeper by about 14 g/cm^2 than QGSJet II–04 on average. These example data were fitted with parameterizations for both models of hadronic interactions (see Fig. 5.6). Both fits describe the example data similarly well giving somewhat different primary fractions and muon rescaling factors that are shown in Tab. 5.1. The deviation of f_p is about 10% when different parameterizations (Figs. 5.2, 5.1) based on the two most recent models of hadronic interactions were used. The ratio of R_μ for the two models reflects again that EPOS–LHC produces by about 6% more muons than QGSJet II–04 on average.

Table 5.1: Fitted parameters for the example data from Fig. 5.6.

Model	f_{p} [%]	f_{He} [%]	f_{N} [%]	R_μ
QGSJet II–04	41 ± 2	0 ± 1	0 ± 1	1.297 ± 0.004
EPOS–LHC	52 ± 3	4 ± 3	0 ± 1	1.214 ± 0.004

5.2 Application to the Data of the Pierre Auger Observatory

In this section a method presented in the previous section is applied to the data of the Pierre Auger Observatory. The number of muons is not directly measured at the Pierre Auger Observatory for zenith angles below 60°. However, the ground signal is sensitive to the EM component and to muons as well and therefore it is used instead of N_μ in the combination with the depth of shower maximum.

At first, the parameters used in the combined analysis are specified. Then, the features observed in the dependence of the mean ground signal on the depth of shower maximum of measured data are probed for reconstruction issues. Finally, this dependence is discussed and interpreted using detailed MC simulations.

The same data of the Pierre Auger Observatory that were selected in the study of X_{max} distributions [67] are analyzed in this section. These data were reconstructed with the software Offline [105] v2r9p5. The response of surface and fluorescence detectors to CORSIKA showers was simulated also with the Offline v2r9p5. These simulated showers [106] produced by the Pierre Auger Collaboration were reconstructed and selected with the same cuts as the measured data.

5.2.1 Ground Signal and Depth of Shower Maximum

In the first approximation, the responses of the water Cherenkov detector (the signal $S(1000)$) to the muon and EM component of shower are equal at small zenith angles ($DX \lesssim 200$ g/cm^2), see left panel of Fig. 5.7. The signals induced by the EM component have very similar size for showers induced by protons and iron nuclei of the same energy for almost all distances of X_{max} to the ground (and also for all zenith angles). On the other hand, the signals induced by the muon component differ substantially for p and Fe primary particles. Therefore, the SD signal is sensitive to the mass composition of UHECR (after the attenuation of the EM component with zenith angle is accounted for).

Not only the dependence of the SD signal on zenith angle, but also its dependence on energy has to be taken into account. The correction of $S(1000)$ for the different amount of atmosphere that is passed by shower of a given zenith angle is performed using the CIC approach (the signal S_{38}, see Section 3.3.2). The energy evolution of the ground signal is corrected using the FD energy. The ratio of reconstructed energies

$$\frac{E_{\mathrm{SD}}}{E_{\mathrm{FD}}} = \frac{a \cdot S_{38}^{b}}{E_{\mathrm{FD}}} \tag{5.3}$$

actually provides an estimate of the relative change of the SD signal independently on energy and

zenith angle. This ratio will be used in the following as the ground signal that is sensitive to the number of muons on ground (shown in an internal note [108]). The same calibration constants a, b from Eq. (3.3) were used as for the data of the Pierre Auger Observatory as for the simulated showers induced by all primaries.

The sensitivity of the ground signal to the mass composition of UHECR (or the mass composition bias in the reconstructed SD energy) is indicated for MC simulations in the right panel of Fig. 5.7. About 20% difference between the average S_{38} for showers induced by protons and iron nuclei is expressed with the corresponding calibration curves.

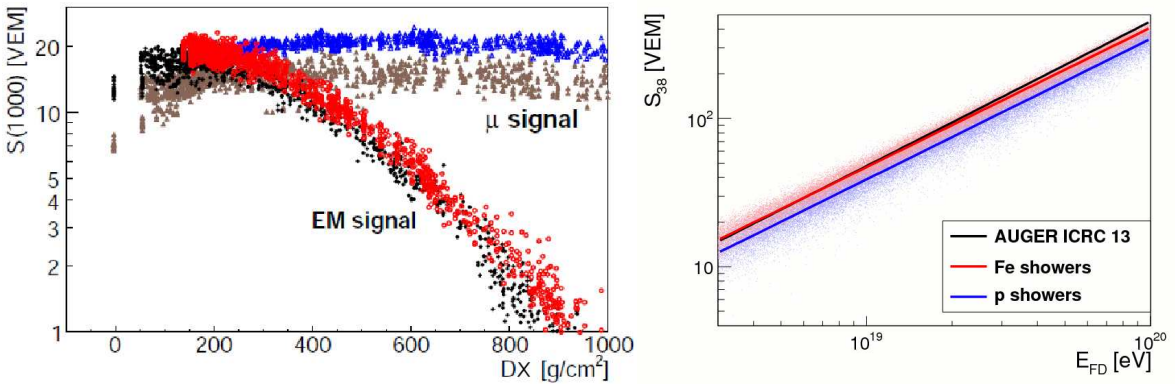

Figure 5.7: **Left panel:** Dependence of the SD signal on the distance of $X_{\max}$ to the ground (DX). Showers initiated by protons (black and brown) and iron nuclei (red and blue) are shown for signals induced by EM particles and muons. Picture comes from [107]. **Right panel:** Calibration curves inferred from the Golden events of the Pierre Auger Observatory (black line) [44] and of the simulated showers that were induced by protons (blue line) and iron nuclei (red line). The generated showers were produced with EPOS–LHC.

As it was previously described in Section 3.3.1, the reconstructed E_{FD} is very little sensitive to the primary mass. It is due to the fact that the measured calorimetric energy nicely scales with the energy of the primary particle. The remaining part (~10%) of the shower energy, the missing energy, needs to be added to the calorimetric energy to obtain the total shower energy. The reconstructed shower energy differs within few percent for showers induced by protons and iron nuclei. Therefore the reconstructed FD energy is considered to have only very small mass composition bias (few %).

The correlation between the ground signal and the number of muons on the ground level from CORSIKA simulations is shown in Fig. 5.8. The ground signal of simulated showers was reconstructed using the same CIC curve and the same SD calibration curve used for the reconstruction of data of the Pierre Auger Observatory. Therefore the reconstructed E_{SD} is systematically smaller than the reconstructed E_{FD} as a consequence of the known lack of muons in MC simulations wrt. to the measured data (as discussed in Section 3.4.2 and as visible in the right panel of Fig. 5.7). The total number of muons at the ground level $N_{\mu}^{\mathrm{CORSIKA}}(E_{\mathrm{MC}}, \Theta)$ was obtained directly from the CORSIKA program without the detector reconstruction. It was scaled with energy of the primary particle E_{MC}

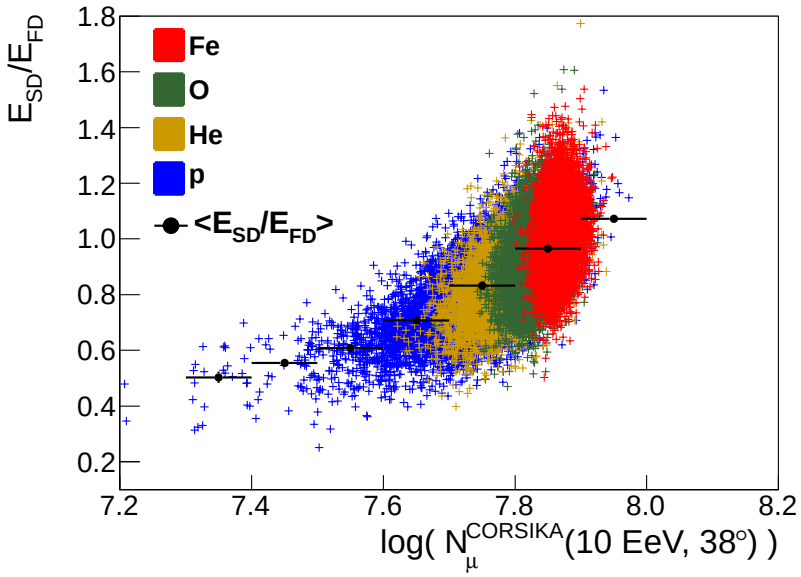

Figure 5.8: The ground signal ($E_{\mathrm{SD}}/E_{\mathrm{FD}}$) plotted as a function of the total number of muons on ground. This number was obtained from CORSIKA and is equivalent to the total number of muons of a shower with energy 10^{19} eV and zenith angle 38°. The showers induced by four primaries (colors) of energy $10^{18.5-19.0}$ eV were produced with the model EPOS–LHC. The average values of the ground signal over all primaries are shown by black points.

and $\beta = 0.9$ for every shower according to Eq. (2.21) as

$$N_{\mu}^{\mathrm{CORSIKA}}(10\ \mathrm{EeV}, \Theta) = N_{\mu}^{\mathrm{CORSIKA}}(E_{\mathrm{MC}}, \Theta) \cdot \left(\frac{10^{19}\ \mathrm{eV}}{E_{\mathrm{MC}}}\right)^{\beta} \tag{5.4}$$

to correspond to the total number of muons produced by a shower of energy 10^{19} eV. It was also corrected for the attenuation with zenith angle using the CIC approach obtaining $N_{\mu}^{\mathrm{CORSIKA}}(E_{\mathrm{MC}}, 38°)$.

The parameter $E_{\mathrm{SD}}/E_{\mathrm{FD}}$ in fact represents the same information as $S^*(1000)$ used in [75], see Section 3.4.2. It holds:

$$S^*(1000) = S_{38} \cdot \left(\frac{10^{19}\ \mathrm{eV}}{E_{\mathrm{FD}}[\mathrm{eV}]}\right)^{1/b} = \left(\frac{E_{\mathrm{SD}}}{E_{\mathrm{FD}}}\right)^{1/b} \cdot \left(\frac{10^{19}\ \mathrm{eV}}{a}\right)^{1/b} \tag{5.5}$$

where a, b are the calibration constants from Eq. (3.3). As b is very close to one,

$$S^*(1000) \cong \frac{E_{\mathrm{SD}}}{E_{\mathrm{FD}}} \cdot 47.8\ \mathrm{VEM}. \tag{5.6}$$

Note also that the ground signal defined as the ratio of reconstructed energies is in fact invariant to the changes in the energy scale.

The depth of shower maximum increases with energy, see Eq. (2.24). Therefore, a correction for this energy evolution was incorporated, although the dependence is weak (linear in logarithm

of energy). The elongation rate D is very similar for three models of hadronic interactions (Sibyll, QGSJet II–04 and EPOS–LHC) and for 4 primaries and hence the value $D = 56$ g/cm^2 is taken as their average from [109] where $D \in \langle 54,\ 58 \rangle$ g/cm^2. The quantity X^{19}_{max} is defined as

$$X^{19}_{\mathrm{max}} = X_{\mathrm{max}} + D \cdot (19 - \log(E_{\mathrm{FD}}\ [\mathrm{eV}])) \tag{5.7}$$

and it corresponds to the X_{max} measured at energy 10^{19} eV. Note that this correction is in fact relevant only for wide energy bins. It also enables to compare the X_{max} of measured data, or simulations, for different energy bins with a single variable. The depth of shower maximum does not depend on the zenith angle with a fair approximation as the interaction processes responsible for the shower development depend on the penetrated atmospheric depth.

5.2.2 Breaks in Dependence of Mean Ground Signal on X_{max}

To draw any conclusion about the mass composition of primary particles from the measured data, it is necessary to apply a wide range of selections related to the SD and FD data. For the SD selection, only events with zenith angle $\leq 60^\circ$ satisfying the physics trigger T4 and the quality trigger T5 [45] (standard SD reconstruction cuts) were accepted. Events detected during the so–called bad periods, when the proper SD reconstruction was not assured, were removed from the analysis. For the FD selection, the detector effects (limited viewing angles of telescopes) were removed using the so–called Field–Of–View (FOV) cuts and the quality cuts provided a reliable reconstruction of X_{max} according to the standard X_{max} analysis [67]. These FD cuts provide not only a reliable reconstruction of the longitudinal profile, but also an unbiased selection of events with respect to the mass composition of primary particles.

Three samples of the data of the Pierre Auger Observatory with FD energy above $10^{17.8}$ eV are discussed in this section. The sample of 19759 hybrid events used in the study of X_{max} distributions [67], including all the mentioned FD cuts, is in the following plots depicted with black lines ("Hybrid with FOV"). A subset of 9003 events of this sample with a successful reconstruction of the shower in the SD is denoted as "Golden with FOV" in blue. Finally, the Golden data with 19943 events satisfying all the FD cuts but with the released FOV cuts are depicted in red ("Golden, no FOV"). The hybrid data set is used as the unbiased benchmark in some of the following plots. The Golden data without the FOV cuts provide a cross–check of features of the Golden data with the FOV cuts that are used in the subsequent section to interpret the measured data with MC.

The energy spectra of these three samples of measured data are shown in Fig. 5.9. The Golden data with the FOV cuts contain approximately half of the number of events in the hybrid data set, whereas the sample of Golden data with released FOV cuts is of the similar size as the hybrid data set.

Regarding the zenith angle distributions (Fig. 5.10), the FOV cuts (black and blue) restrict the zenith angles towards somewhat higher values compared to the case when the FOV cuts are not in-

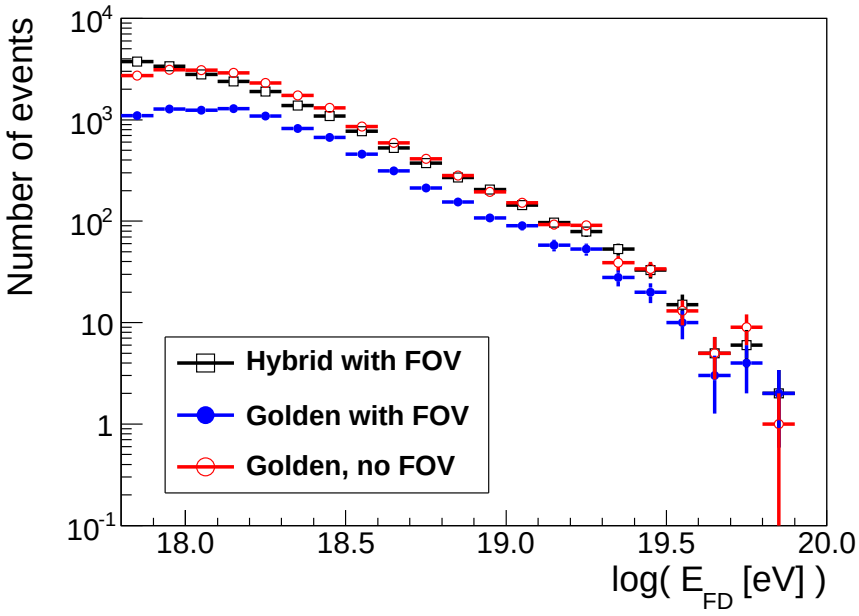

Figure 5.9: Energy spectra of three samples of data measured at the Pierre Auger Observatory that are described in the text. The hybrid data were selected for $\Theta < 90°$, whereas the Golden data for $\Theta < 60°$.

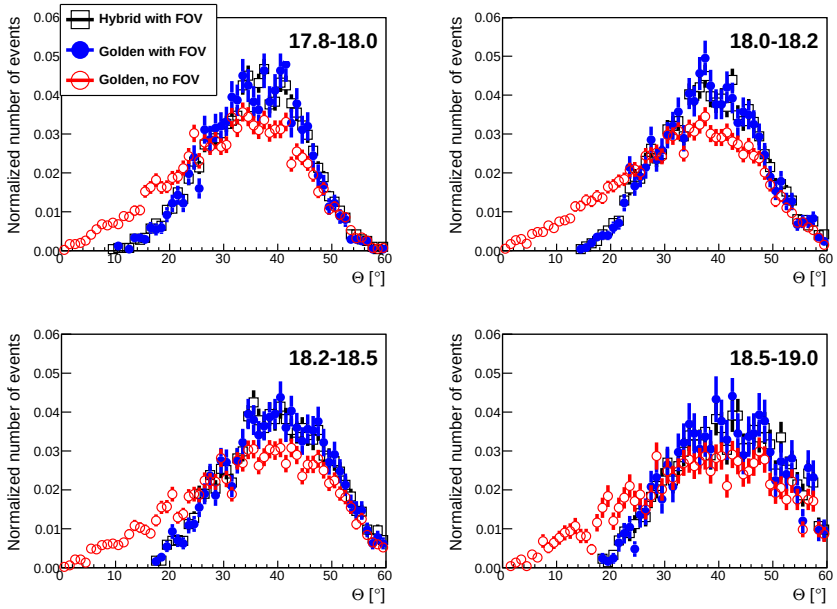

Figure 5.10: Normalized distributions of the zenith angle for the three samples of the measured data. The respective intervals of $\log(E_{\mathrm{FD}}\ [\mathrm{eV}])$ are shown in up-right corners of the plots.

cluded (red). The requirement of a successful SD reconstruction does not influence the zenith angle distribution at all energies (black and blue histograms are on top of each other).

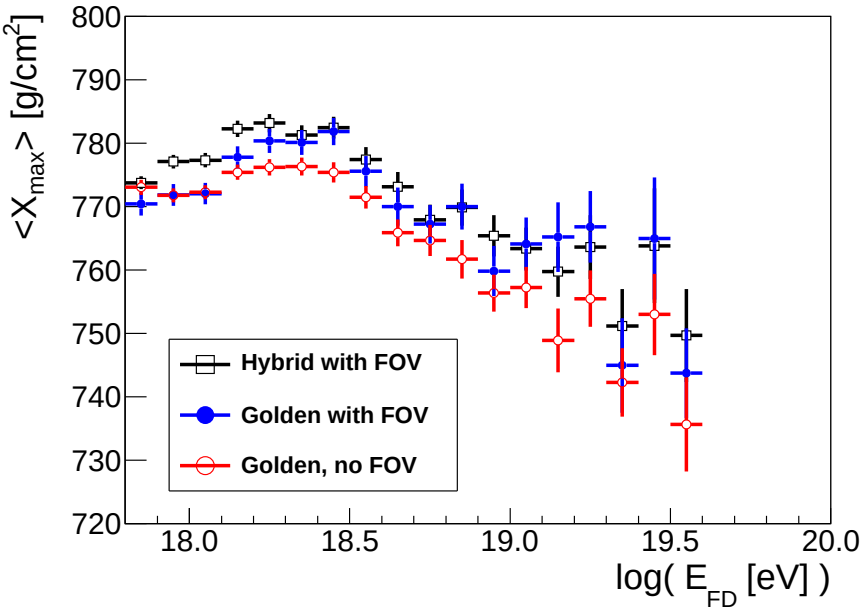

Figure 5.11: Dependence of the mean of the X_{max} distribution on FD energy for three samples of data measured at the Pierre Auger Observatory.

Fig. 5.11 shows the dependence of the mean of the X_{max} distribution on FD energy for three samples of the measured data. When no FOV cuts were used (red), a systematic shift of $\langle X_{\mathrm{max}} \rangle$ towards shallower showers compared to the hybrid data (black) is evident for all energies. It is a consequence of the geometric aperture of the FD that is on average favorable for shallower showers. Whereas $\langle X_{\mathrm{max}} \rangle$ of the Golden data with the FOV cuts (blue) is consistent with $\langle X_{\mathrm{max}} \rangle$ of the hybrid data with the FOV cuts (black) for energies above $10^{18.2}$ eV, below this energy a difference between these two $\langle X_{\mathrm{max}} \rangle$ values is visible. This difference is a combination of two effects. At first, the X_{max} acceptance can be in principle different (different selection of events) for golden and hybrid showers. Secondly, this observed difference can be an indication of a presence of heavier nuclei (shallower X_{max}) that are more probable to trigger in the SD for these energies since the showers induced by heavier nuclei contain higher amount of muons. As it was indicated in Fig. 5.1 for different primaries, the dependence of N_{μ} on X_{max} is moderate for protons and the correlation between N_{μ} and X_{max} is even positive in case of heavier nuclei. Therefore, a selection of showers with higher N_{μ} of single primary should not decrease $\langle X_{\mathrm{max}} \rangle$ much. Thus the observed difference of $\langle X_{\mathrm{max}} \rangle$ between the hybrid data with the FOV cuts and the Golden data with the FOV cuts can be also a real indication of a mixed composition below $10^{18.2}$ eV.

Fig. 5.12 contains the dependence of the mean ground signal on X^{19}_{max} for two samples of Golden data (with and without the FOV cuts) for 4 energy bins ($10^{17.8-18.0}$, $10^{18.0-18.2}$, $10^{18.2-18.5}$, $10^{18.5-19.0}$ eV). For energies below $10^{18.5}$ eV, abrupt changes ("breaks") can be seen around X^{19}_{max} = 700–740 g/cm^2 and X^{19}_{max} = 800–860 g/cm^2 for both data samples. Therefore, these breaks can not be a consequence of the FOV cuts. For the energy bin $10^{18.5-19.0}$ eV a steadily decreasing trend of the mean ground

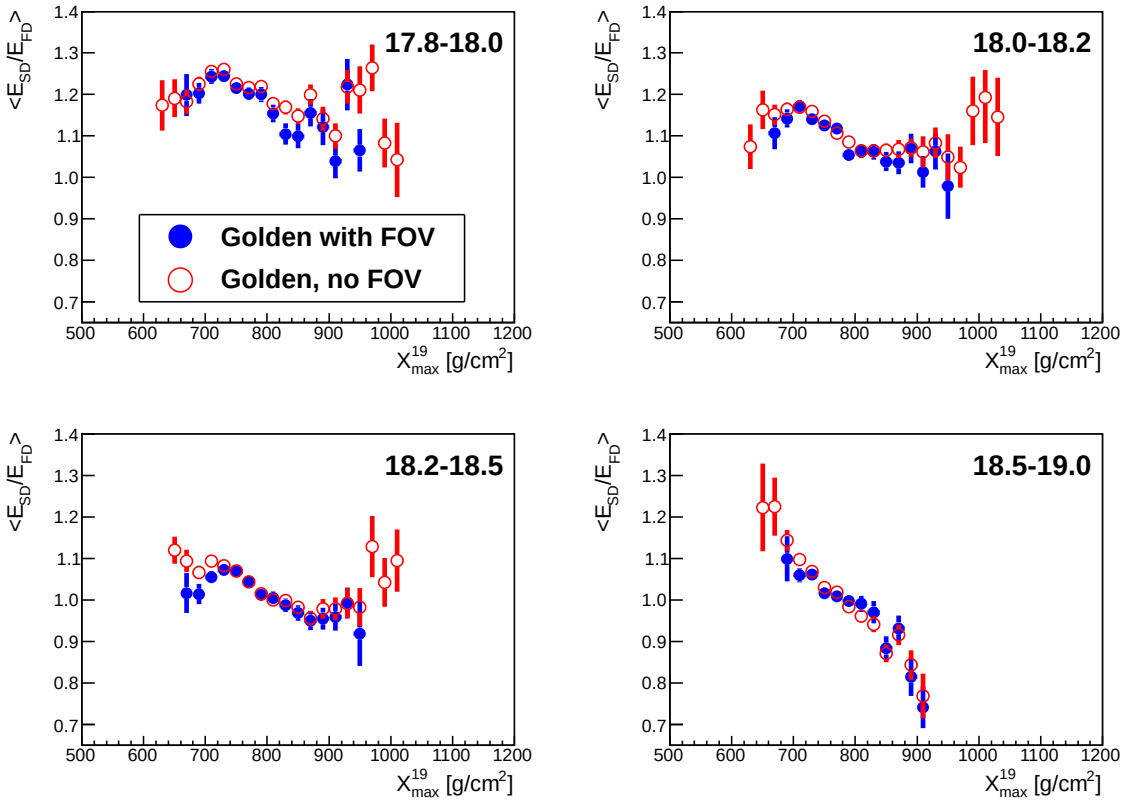

Figure 5.12: Dependence of the mean ground signal on X^{19}_{max} for two samples of the measured data. The respective intervals of $\log(E_{\mathrm{FD}}\ [\mathrm{eV}])$ are shown in up-right corners of the plots.

signal is observed in both data samples.

Various checks for reconstruction issues that could cause these breaks were performed. The dependence of the mean ground signal on $\cos^2(\Theta)$ is not constant below the energy threshold $10^{18.5}$ eV (see Fig. 5.13). Note that above this energy threshold the showers induced by protons and iron nuclei have the same trigger efficiency ≥ 0.95, whereas below this energy their trigger efficiencies are different and depend also on the zenith angle. Showers of $\Theta \lesssim 20°$ as well as showers of $\Theta \gtrsim 45°$ containing a higher amount of muons are more probable to trigger below $10^{18.5}$ eV (higher number of triggered stations). Fig. 5.14 shows that the observed breaks do not vanish when the data are divided into two sets (4 left and 4 right panels) according to the zenith angle (below and above 40°). The breaks are less significant (with taking the statistical errors into account) due to the fact that the number of events is approximately twice smaller than in Fig. 5.12, but they occur at the approximately same values of X^{19}_{max} as in Fig. 5.12. For various ranges of the zenith angle the breaks did not disappear.

In Fig. 5.15, the dependence of the mean ground signal on the stage of shower evolution after reaching X_{max} (DX) is plotted. Knowing X_{max}, zenith angle and actual atmospheric pressure[2] p the

[2]The air pressure and the air temperature are measured at the Pierre Auger Observatory every five minutes [110].

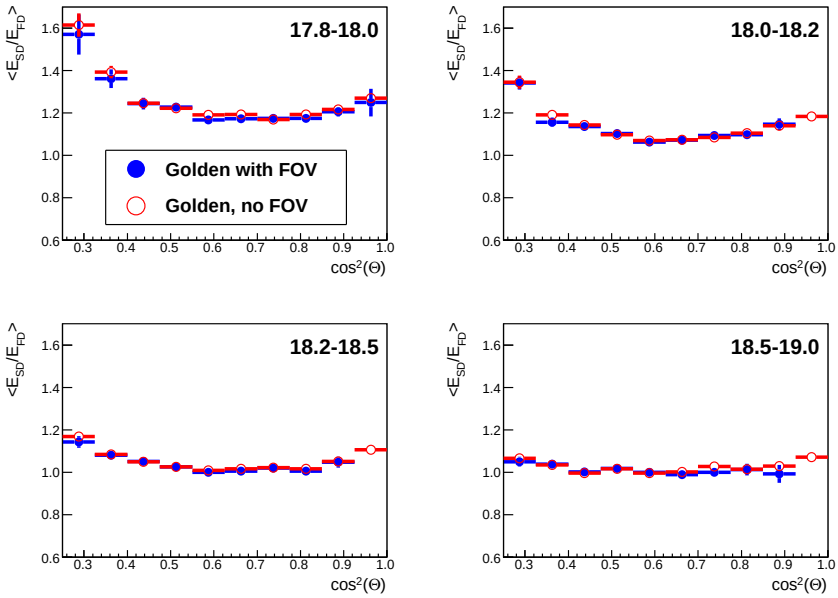

Figure 5.13: Dependence of the mean ground signal on the zenith angle for data sets with and without the FOV cuts. The respective intervals of $\log(E_{\mathrm{FD}}\ [\mathrm{eV}])$ are shown in up-right corners of the plots.

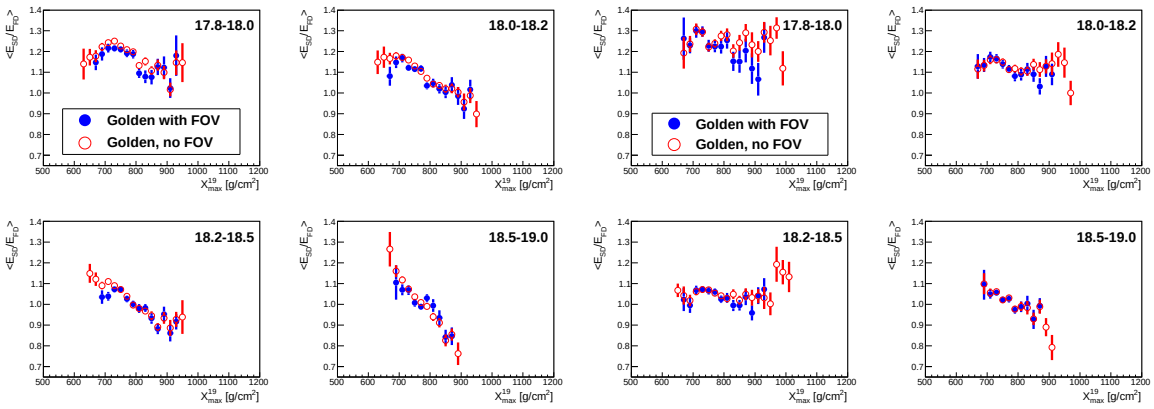

Figure 5.14: Dependence of the mean ground signal on X^{19}_{max} for zenith angles 0–40° (**four left panels**) and 40–60° (**four right panels**). The respective intervals of $\log(E_{\mathrm{FD}}\ [\mathrm{eV}])$ are shown in up-right corners of the plots.

distance of X_{max} to the ground was calculated as

$$DX[\mathrm{g/cm^2}] = p[\mathrm{Pa}]/g[\mathrm{m/s^2}]/10/\cos(\Theta) - X_{\mathrm{max}} \tag{5.8}$$

where g is the acceleration due to gravity of the Earth. The dependence of the mean ground signal on DX is not constant below $10^{18.5}$ eV from the same reasons as in the case of the dependence of the ground signal on $\cos^2(\Theta)$. As an example of a check for origin of the observed breaks due to a

combination of events of a wide range of DX, the dependence of the mean ground signal on X^{19}_{max} is plotted for showers with $DX \in \langle 200,\ 400 \rangle$ g/cm^2 in Fig. 5.16. In this range of DX, the dependence of the mean ground signal on DX is roughly flat for all energies (see Fig 5.15). If the breaks in Fig. 5.12 were caused by breaks in DX, they would disappear in Fig. 5.16. The breaks remained at the approximately same values of X^{19}_{max} as in the Fig. 5.12. The breaks did not disappear even for various selections of the range in the stage of shower evolution.

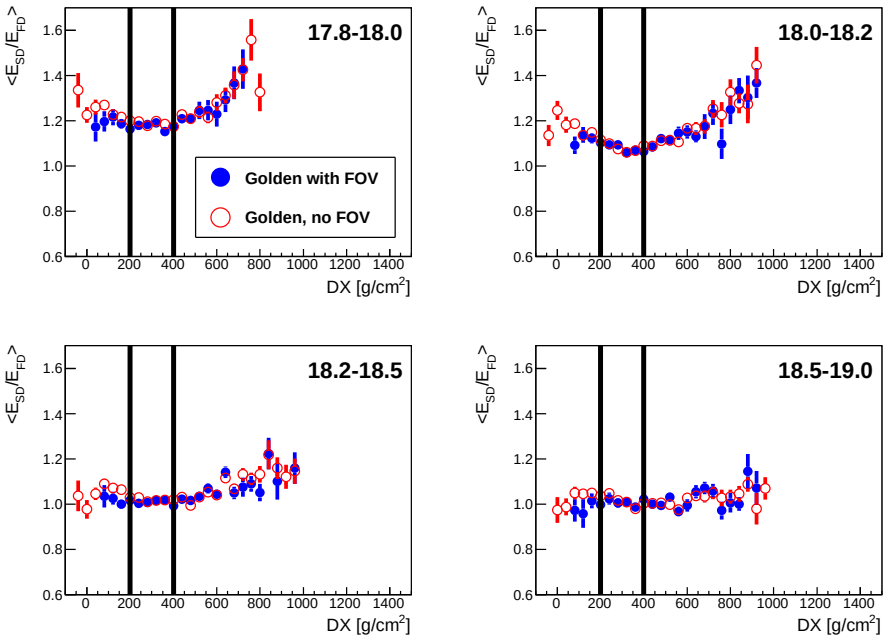

Figure 5.15: Dependence of the mean ground signal on the distance of X_{max} to the ground for data sets with and without the FOV cuts. The respective intervals of $\log(E_{\mathrm{FD}}$ [eV]) are shown in up-right corners of the plots. The black vertical lines illustrate the selected range of DX that was used for the check of the two–breaks origin in Fig. 5.16.

Another check that was performed is the stability of the ground signal with time. The temporal dependence of the ground signal can be caused by the aging of the SD and of the FD (steady long–term effect) or by atmospheric conditions (mainly air pressure and air temperature) that are changing during the year (annual fluctuations). No significant time dependence of $\langle X_{\mathrm{max}} \rangle$ vs. E_{FD} was found.

In Fig. 5.17, the dependence of the mean ground signal on the GPS time[3] of shower detection (T_{GPS}) is shown for four energy bins. The Golden data without the FOV cuts (in red) are shown only for a cross–check. The ground signal exhibits the long–term effect and the annual fluctuations as well in all four energy bins. The linear fits of the Golden data with the FOV cuts are depicted with blue lines expressing the average steady increase of the ground signal with time. From these fits, the ground signal is estimated to increase by 1.6-3.0% per year.

[3]The GPS time is the time of detection measured by the GPS receiver. It counts the number of seconds from 00:00 a.m. on 6$^{\mathrm{th}}$ January 1980. One year takes then about 31.5 Ms.

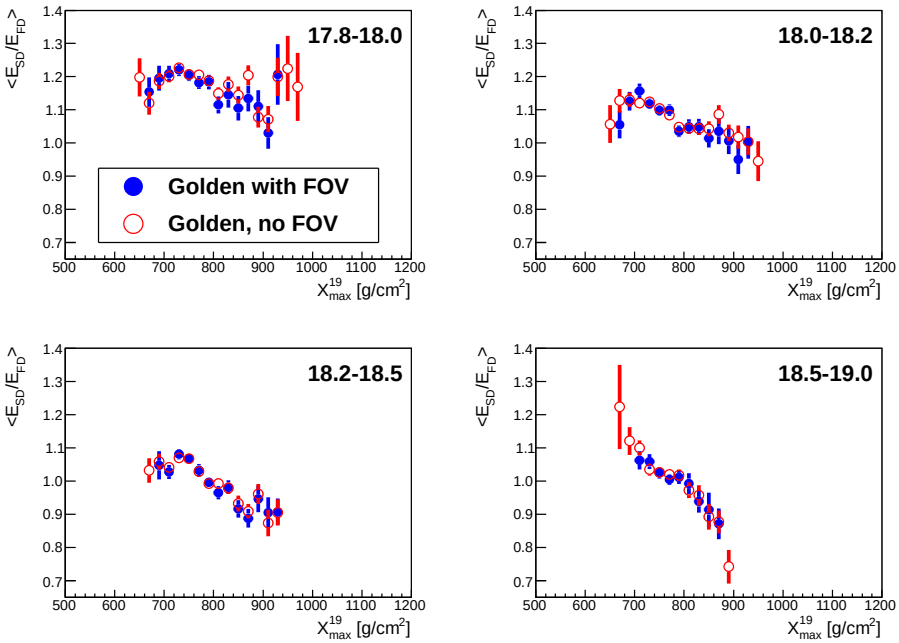

Figure 5.16: Dependence of the mean ground signal on X^{19}_{max} for DX $\in \langle 200,\ 400 \rangle$ g/cm^2 for data sets with and without the FOV cuts. The respective intervals of $\log(E_{\mathrm{FD}}\ [\mathrm{eV}])$ are shown in up-right corners of the plots.

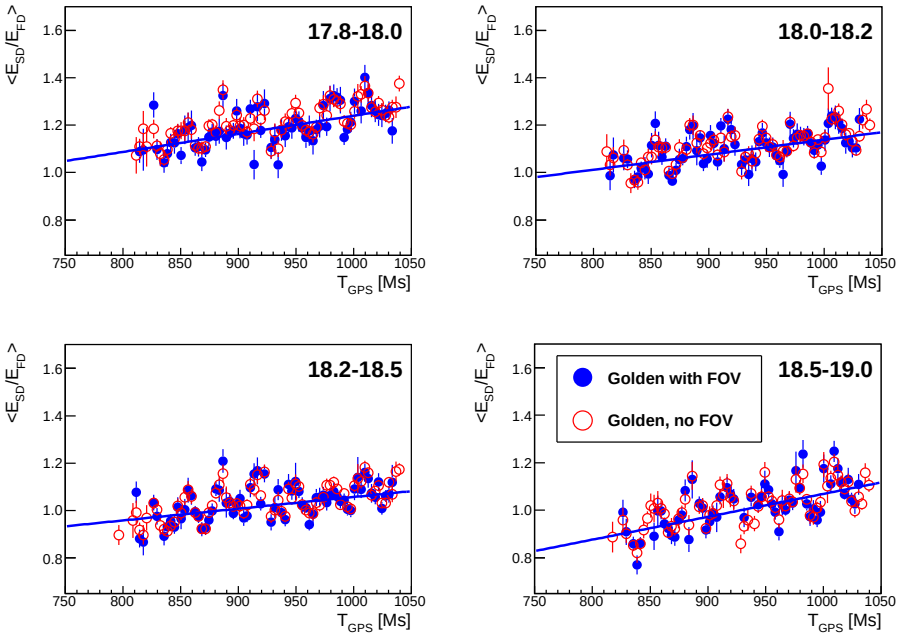

Figure 5.17: Dependence of the mean ground signal on the GPS time. The respective intervals of $\log(E_{\mathrm{FD}}\ [\mathrm{eV}])$ are shown in up-right corners of the plots.

The annual fluctuations of the mean ground signal are visible in Fig. 5.17 at ~30 Ms time scale. These fluctuations are shown in Fig. 5.18 as a function of the month of detection (M). The ground signal of each event in these plots was corrected for the steady increase with time ~2.3%/year as

$$(E_{\rm SD}/E_{\rm FD})(T_{\rm Ref},\ M) \equiv E_{\rm SD}/E_{\rm FD}(T_{\rm Ref},\ M) = E_{\rm SD}/E_{\rm FD}(T_{\rm GPS},\ M) + 2.3\%/{\rm year}\cdot(T_{\rm Ref} - T_{\rm GPS}) \quad (5.9)$$

where $T_{\rm Ref} = 900$ Ms was chosen as the reference GPS time. The mean of the ground signal corrected for the long–term effect according to Eq. (5.9) was then fitted in each energy bin with a general cosine function of the month M when the event was detected:

$$C(M) = C_{\rm max}\cdot\cos(P\cdot(M - S)) + O \quad (5.10)$$

where $C_{\rm max}$ is the amplitude of the annual fluctuations, P was fixed to reflect the annual period of 12 months ($P = 2\pi/12$), $S > 1$ is the shift of the maximum and O is the offset parameter. The four fits (shown in Fig. 5.18) for different energy intervals provided similar values of $C_{\rm max} \simeq 5.5\%$ and $S \simeq 1.1$ with the minimum of $\langle E_{\rm SD}/E_{\rm FD}(T_{\rm Ref})\rangle$ around July and with the maximum around January.

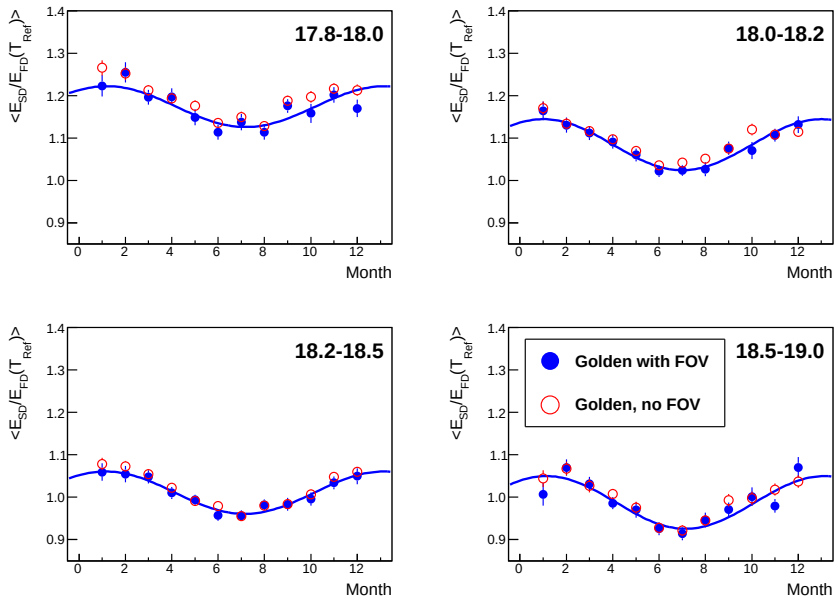

Figure 5.18: Dependence of the mean ground signal on the month of detection during a year. The ground signal was corrected for a long–term effect according to Eq. (5.9). The respective intervals of $\log(E_{\rm FD}$ [eV]) are shown in up-right corners of the plots.

In fact, this is in accordance with [110] where the effect of the average air density on the signal in water Cherenkov detectors was studied. The air density peaks around the middle of the year (austral winter) and reaches its minimum around the beginning of the year (austral summer). Generally, the higher the air density, the lower the Moliere radius (transverse spread of 90% of the EM energy) and

therefore also the smaller lateral spread of EM showers. Consequently, somewhat lower reconstructed ground signals can be expected for seasons with higher air density in the middle of the year compared to seasons in the beginning of the year.

A correction for these annual fluctuations of the ground signal was adopted for each event detected in month M as

$$E_{\mathrm{SD}}/E_{\mathrm{FD}}(T_{\mathrm{Ref}},\, M_{\mathrm{Ref}}) = E_{\mathrm{SD}}/E_{\mathrm{FD}}(T_{\mathrm{Ref}},\, M) + C_{\max}\cdot(\cos(P\cdot(M_{\mathrm{Ref}}-S)) - \cos(P\cdot(M-S))) \quad (5.11)$$

where the reference month was chosen to be April ($M_{\mathrm{Ref}} = 4$). Combining the two time corrections in Eqs. (5.9), (5.11) the corrected ground signal is plotted in Fig. 5.19 together with the uncorrected ground signal. The absolute value of $\langle E_{\mathrm{SD}}/E_{\mathrm{FD}}(T_{\mathrm{Ref}},\, M_{\mathrm{Ref}})\rangle$ (gray points) depends naturally on the choice of T_{Ref} and M_{Ref}. The two breaks in the dependence of $\langle E_{\mathrm{SD}}/E_{\mathrm{FD}}(T_{\mathrm{Ref}},\, M_{\mathrm{Ref}})\rangle$ on $X^{19}_{\max}$ remained at the same positions with very similar significances.

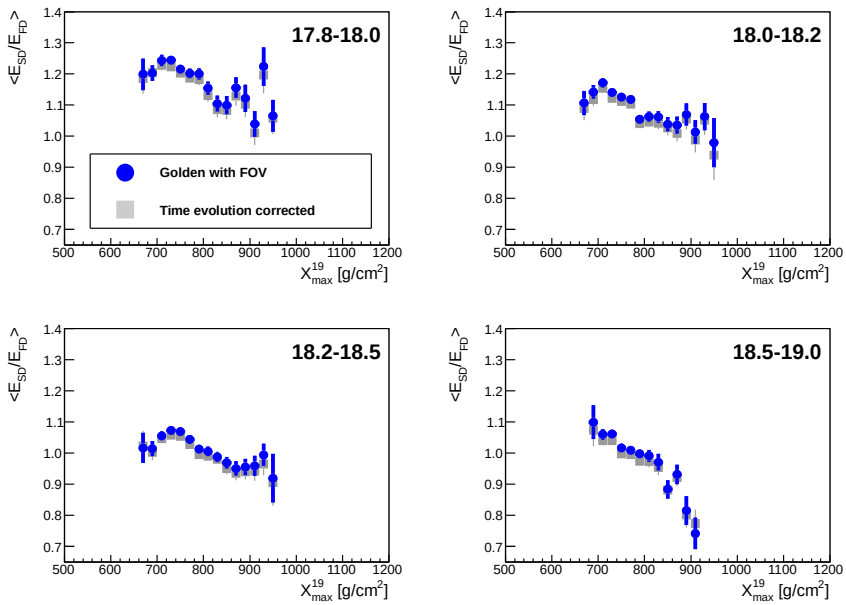

Figure 5.19: Dependence of the mean ground signal on $X^{19}_{\max}$ for the Golden data with the FOV cuts with (gray) and without (blue) the correction for the time evolution of the ground signal. The respective intervals of $\log(E_{\mathrm{FD}}\ [\mathrm{eV}])$ are shown in up-right corners of the plots.

In Fig. 5.20, the Golden data with the FOV cuts are compared to the same data with the energy scale shifted by ±14%. Note that these shifts in energies correspond to the systematic uncertainty in the energy scale of the Pierre Auger Observatory. The little sensitivity of the observed breaks to the energy scale comes from the definition of the ground signal as the ratio of reconstructed energies. The small deviations come from the correction of $X_{\max}$ for the energy evolution, see Eq. (5.7).

Altogether, the breaks observed in Fig. 5.12 can not be a consequence of the usage of the FOV cuts, wrong correction for the attenuation of the ground signal with zenith angle, elongation rate correction

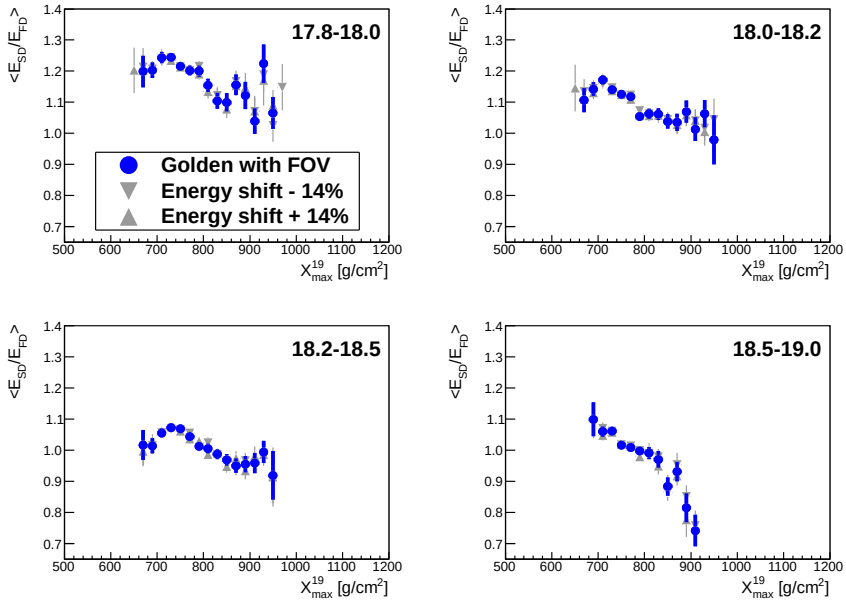

Figure 5.20: The comparison of the Golden data with the FOV cuts with the same data shifted in the energy scale by ±14%. The respective intervals of $\log(E_{\mathrm{FD}}\ [\mathrm{eV}])$ are shown in up-right corners of the plots.

of X_{max} or due to the selection of events with different stage of shower evolution. These breaks can not be also caused by the time evolution of the ground signal and there is a negligible effect of the energy scale. As no reconstruction issue inducing the breaks in the dependence of the mean ground signal on the depth of shower maximum was found, these breaks are in the following considered as the manifestation of the mass composition bias in the reconstructed SD energy measured by the Pierre Auger Observatory. In the following, the Golden data with the FOV cuts are interpreted using detailed MC simulations that were treated in the exactly same way as the measured data including all the applied cuts, the SD calibration curve and the CIC curve.

5.2.3 Interpretation of Measured Data based on Simulated Showers

MC simulations with full SD and FD reconstructions obtained from the MC shower library [106] were used for the interpretation of the Golden data with the FOV cuts. The MC showers induced by p, He, O and Fe were generated with CORSIKA in the range of energy $\langle 18.5, 19.0\rangle$ and zenith angle $\langle 0°, 60°\rangle$ for three models of hadronic interactions (QGSJet II–04, EPOS–LHC and Sibyll 2.1). The simulation of the detector responses together with the SD and FD reconstructions was performed with the same Offline version v2r9p5 that was used for the reconstruction of measured data. The same cuts, including the FOV cuts, as were used for the measured data were applied to the generated showers.

An example of the dependence of the ground signal on X^{19}_{max} for a mixed composition of primaries 50% p + 50% Fe is shown in Fig. 5.21. The mean values of the ground signal for the mixed set of

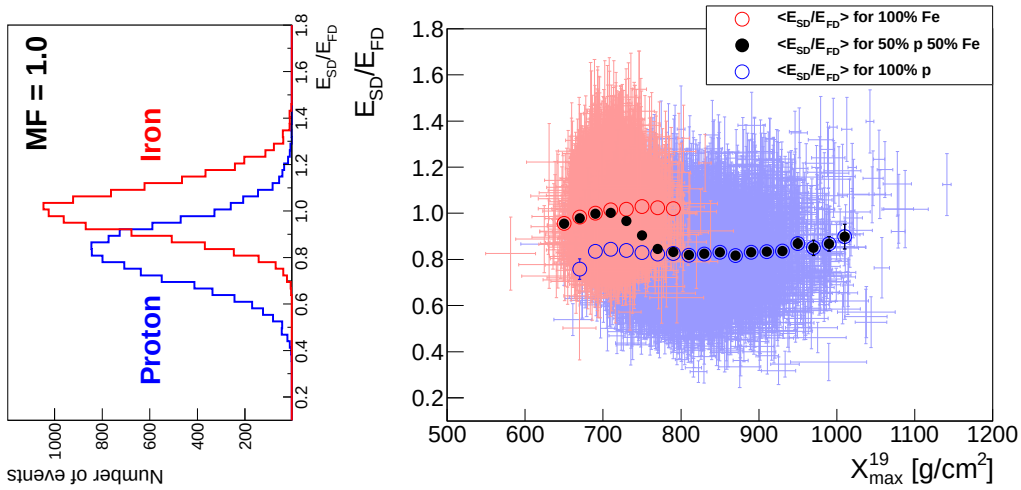

(a) (b)

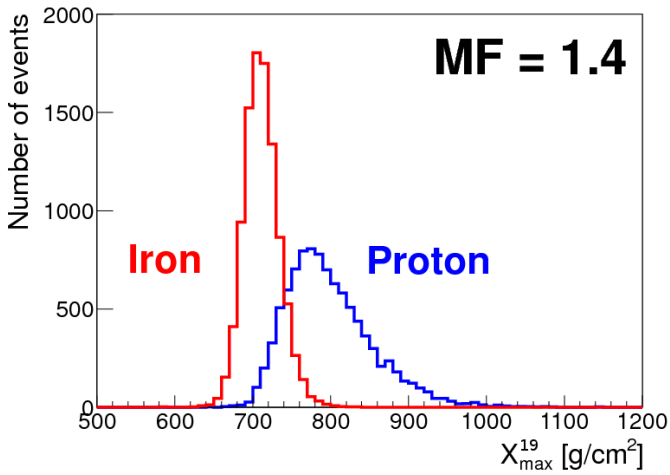

(c)

Figure 5.21: **(a):** Projected distribution of the ground signal for showers induced by protons and iron nuclei. **(b):** Dependence of the ground signal on $X_{\max}$ for showers induced by protons and iron nuclei. The showers were produced with model EPOS–LHC. The mean values of the ground signal are plotted with open blue and open red markers for showers induced by protons and iron nuclei, respectively. The mean ground signal of the mixed composition of 50% p + 50% Fe is depicted with black full markers. **(c):** Projected distribution of $X^{19}_{\max}$ for showers induced by protons and iron nuclei. The merit factors (MF) of the projected distributions, calculated according to Eq. (2.29), are depicted in right upper corners of the plots.

showers are depicted by black full points. Note that the "two–breaks dependence" of the mean ground signal on $X^{19}_{\max}$ is very similar to those observed in Fig. 5.12; including the positions of the breaks. The two–breaks structure in the dependence of the mean ground signal on $X^{19}_{\max}$ comes from the fact

that two observables sensitive to the primary type are combined together. To illustrate this effect, the projected distributions of the two observables are shown next to each axis. The merit factors of distributions of $E_{\mathrm{SD}}/E_{\mathrm{FD}}$ and X^{19}_{max}, calculated according to Eq. (2.29), are $MF(\mathrm{p},\mathrm{Fe}) \simeq 1.0$ and $MF(\mathrm{p},\mathrm{Fe}) \simeq 1.4$, respectively.

The following analysis is analogous to the method presented in the Section 5.1 for N_μ and X_{max} at a fixed energy. Instead of these two observables, the energy independent $E_{\mathrm{SD}}/E_{\mathrm{FD}}$ and X^{19}_{max} are used for different energy bins.

The parametrized dependencies of the mean ground signal on X^{19}_{max} with quadratic functions $\langle E_{\mathrm{SD}}/E_{\mathrm{FD}}\rangle_i \equiv \langle E_{\mathrm{SD}}/E_{\mathrm{FD}}\rangle_i(X^{19}_{\mathrm{max}})$ are shown in the upper panels of Fig. 5.22 for showers induced by each of 4 primaries (i = p, He, O, Fe) for 3 models of hadronic interactions. Note that there are no negative correlations nor significant features (two breaks) observed for any of the four primary particles and three models of hadronic interactions. The normalized X^{19}_{max} distributions are depicted in the bottom panels of Fig. 5.22. These distributions were parametrized with Gumbel functions $g_i \equiv g_i(X^{19}_{\mathrm{max}})$.

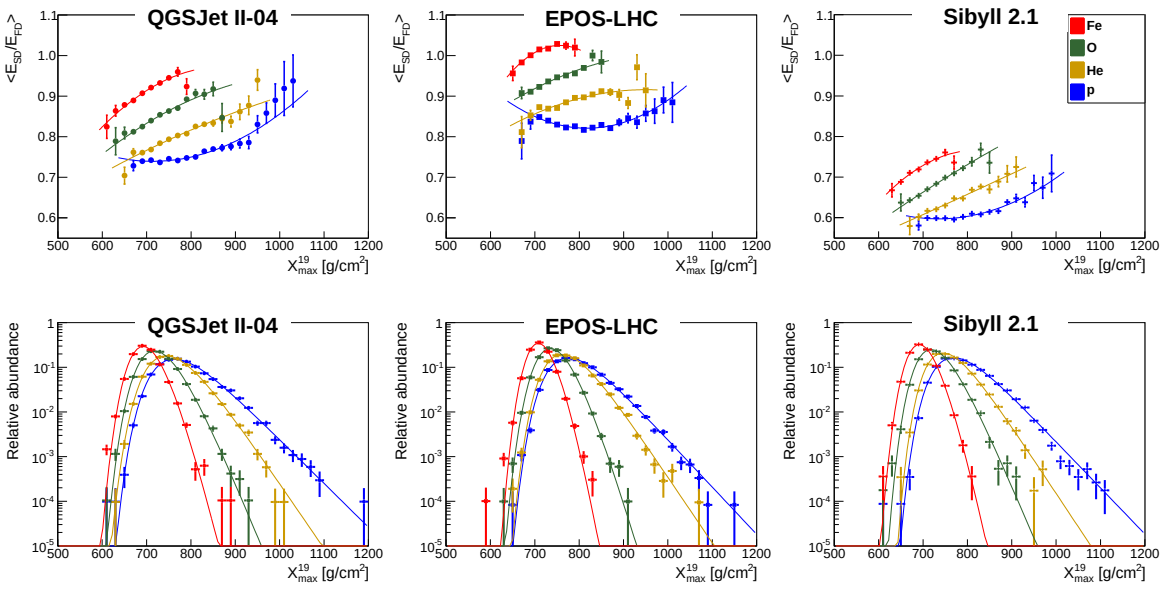

Figure 5.22: Parametrization of MC showers produced with QGSJet II–04 (**left**), EPOS–LHC (**middle**) and Sibyll 2.1 (**right**). In the **upper plots**, the dependence of the mean ground signal on X^{19}_{max} is parametrized with quadratic function $\langle E_{\mathrm{SD}}/E_{\mathrm{FD}}\rangle_i$ for each of four primaries (i = p, He, O, Fe). In the **bottom plots**, the normalized distributions of X^{19}_{max} are parametrized with Gumbel functions g_i for each of the four primaries.

Analogously to the method presented in Section 5.1 for $\langle N_\mu\rangle \equiv \langle N_\mu\rangle(X_{\mathrm{max}})$, the dependence of $\langle E_{\mathrm{SD}}/E_{\mathrm{FD}}\rangle \equiv \langle E_{\mathrm{SD}}/E_{\mathrm{FD}}\rangle(X^{19}_{\mathrm{max}})$ on X^{19}_{max} is fitted with a combination of MC predictions for 4 primaries (p, He, O and Fe) with relative fractions f_i, $\sum f_i = 1$, in the UHECR beam according to

$$\langle E_{\mathrm{SD}}/E_{\mathrm{FD}}\rangle = \sum_i \left(w_i \cdot \langle E_{\mathrm{SD}}/E_{\mathrm{FD}}\rangle_i\right) f_{\mathrm{SD}} \tag{5.12}$$

where the weights w_i are expressed as

$$w_i = \frac{f_i \cdot g_i}{\sum_j \left(f_j \cdot g_j \right)} \tag{5.13}$$

with $j = \mathrm{p}, \mathrm{He}, \mathrm{O}, \mathrm{Fe}$. The rescaling factor of the ground signal, f_{SD}, is introduced to rescale each of the functions $\langle E_{\mathrm{SD}}/E_{\mathrm{FD}} \rangle_i$ with the same value in order to incorporate the lack of muons in MC simulations wrt. the measured data.

Thus, the dependence of $\langle E_{\mathrm{SD}}/E_{\mathrm{FD}} \rangle$ on X^{19}_{max} can be in principle fitted with the four–parameter (f_{p}, f_{He}, f_{O} and f_{SD}) fit using the χ^2 method. The Fe fraction is obtained afterwards as $f_{\mathrm{Fe}} = 1 - f_{\mathrm{p}} - f_{\mathrm{He}} - f_{\mathrm{O}}$. Since the discrepancies between the models of hadronic interactions are still too high, the primary fractions are problematic to be unambiguously fitted together with f_{SD}; as it is described in the following. However, when the primary fractions are fixed, the rescaling parameter remains the only parameter that is fitted.

For the following interpretation of the data measured at the Pierre Auger Observatory, the showers simulated in the energy range $10^{18.5-19.0}$ eV were used. This energy range is narrower than the energy range of the measured data ($10^{17.8-19.0}$ eV). The shapes of $\langle E_{\mathrm{SD}}/E_{\mathrm{FD}} \rangle_i$ and g_i were checked with other showers from the MC shower library that were simulated in energy ranges $10^{18.0-18.5}$ eV, $10^{19.0-19.5}$ eV and $10^{19.5-20.0}$ eV. The number of these showers was much smaller than the number of showers in the energy range $10^{18.5-19.0}$ eV. Nevertheless no obvious dependence of the shapes of parametrized functions ($\langle E_{\mathrm{SD}}/E_{\mathrm{FD}} \rangle_i$ and g_i) on energy was found.

Mass Composition

Four left panels of Fig. 5.23 contain the reduced χ^2 values of the best fits for 286 tested mass compositions of all possible primary fractions of p, He, O and Fe in steps of 10% that were fixed in the fit when f_{SD} was the only free parameter. These different mass compositions of primaries are denoted as *comp #*. The primary fractions corresponding to *comp #* are plotted in the right panel of Fig. 5.23. Note that the proton fraction decreases with *comp #* and that the helium fraction increases with *comp #* for a given proton fraction.

The reduced χ^2 values are very similar for QGSJet II-04 and for Sibyll 2.1. It is a consequence of very similar shapes of dependencies of $\langle E_{\mathrm{SD}}/E_{\mathrm{FD}} \rangle_i$ on X^{19}_{max} for these two models (see the up-left and up-right panel of Fig. 5.22). The degeneracy of solutions that describe the dependence of $\langle E_{\mathrm{SD}}/E_{\mathrm{FD}} \rangle$ on X^{19}_{max} similarly well (see also Fig. 5.24) is obvious for all three models (no distinctive minimum of χ^2/NDF among *comp #*). Therefore the unambiguous derivation of the primary fractions from the data of the Pierre Auger Observatory is complicated within the presented method. Thus the fits with the primary fractions set free are not performed in the following. Instead, the one–parameter fits with all possible combinations of the four primaries were applied.

Fig. 5.24 shows the solutions with all possible primary fractions fixed in steps of 10% that describe the measured data with χ^2/NDF smaller than 4. The plots indicate that the "two–breaks trend" of the

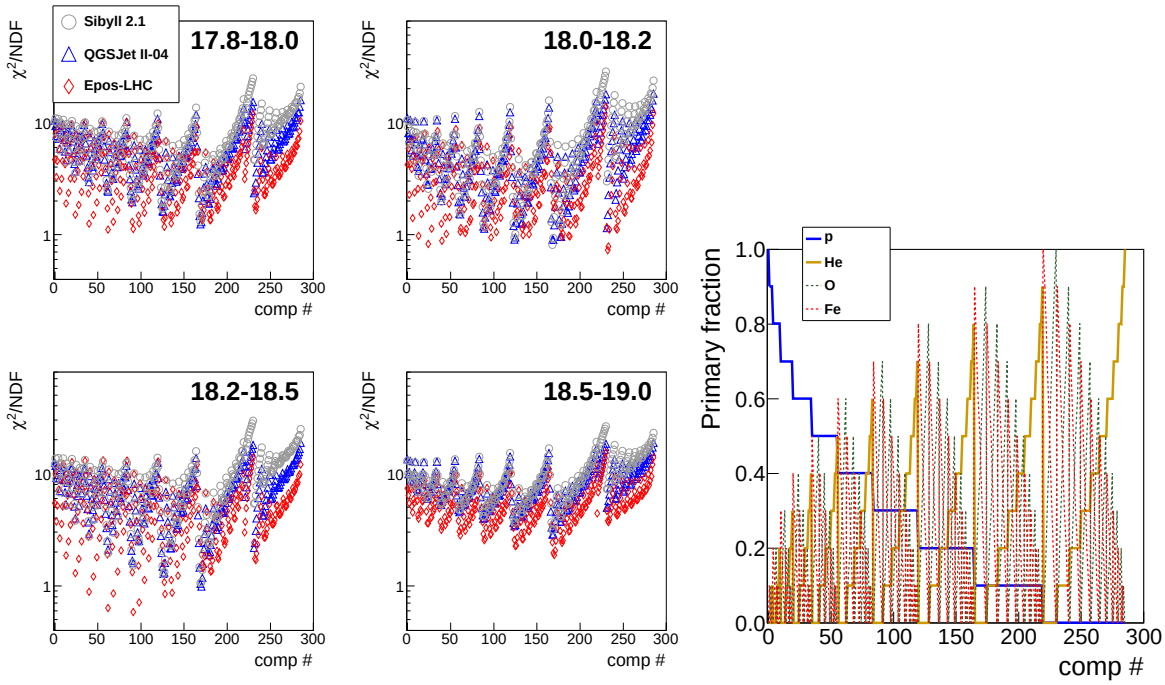

Figure 5.23: **Four left panels:** Reduced χ^2 values for 286 mass compositions of all possible combinations of p, He, O and Fe in steps of 10% that were fixed in the fit of the data of the Pierre Auger Observatory. **Right panel:** Primary fractions corresponding to each of these 286 combinations of primaries denoted as *comp #*.

measured data in the three lower energy bins and the decreasing trend in the highest energy bin can be described using all three models of hadronic interactions. Important conclusion is that the dependence of the ground signal on $X^{19}_{\rm max}$ can be satisfactorily explained only with a mixed composition of the primary beam. In case of pure beams of primary particles, no "two–breaks structure" nor the negative correlation in this dependence is observed (see again upper plots in Fig. 5.22).

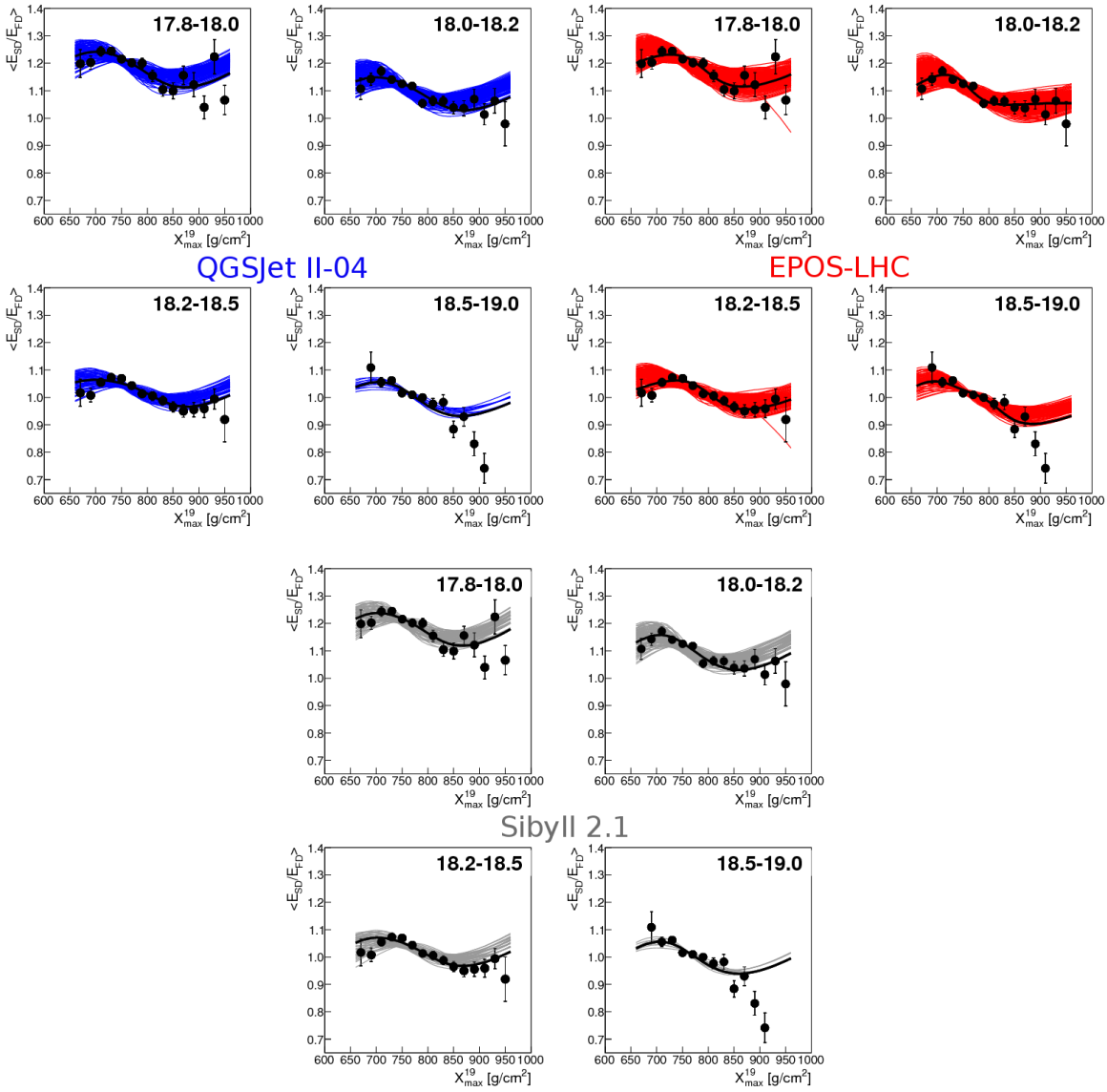

Figure 5.24: The data of the Pierre Auger Observatory (black points) fitted with parameterization obtained with QGSJet II–04 (**four up-left panels**), EPOS–LHC (**four up-right panels**) and Sibyll 2.1 (**four bottom panels**). The primary fractions were fixed to all 286 possible combinations of p, He, O and Fe. Only the solutions that described the data with $\chi^2/\mathrm{NDF} < 4$ are shown. The fits with the smallest χ^2/NDF are depicted with thick black lines. The respective intervals of $\log(E_{\mathrm{FD}}\ [\mathrm{eV}])$ are shown in up-right corners of the plots.

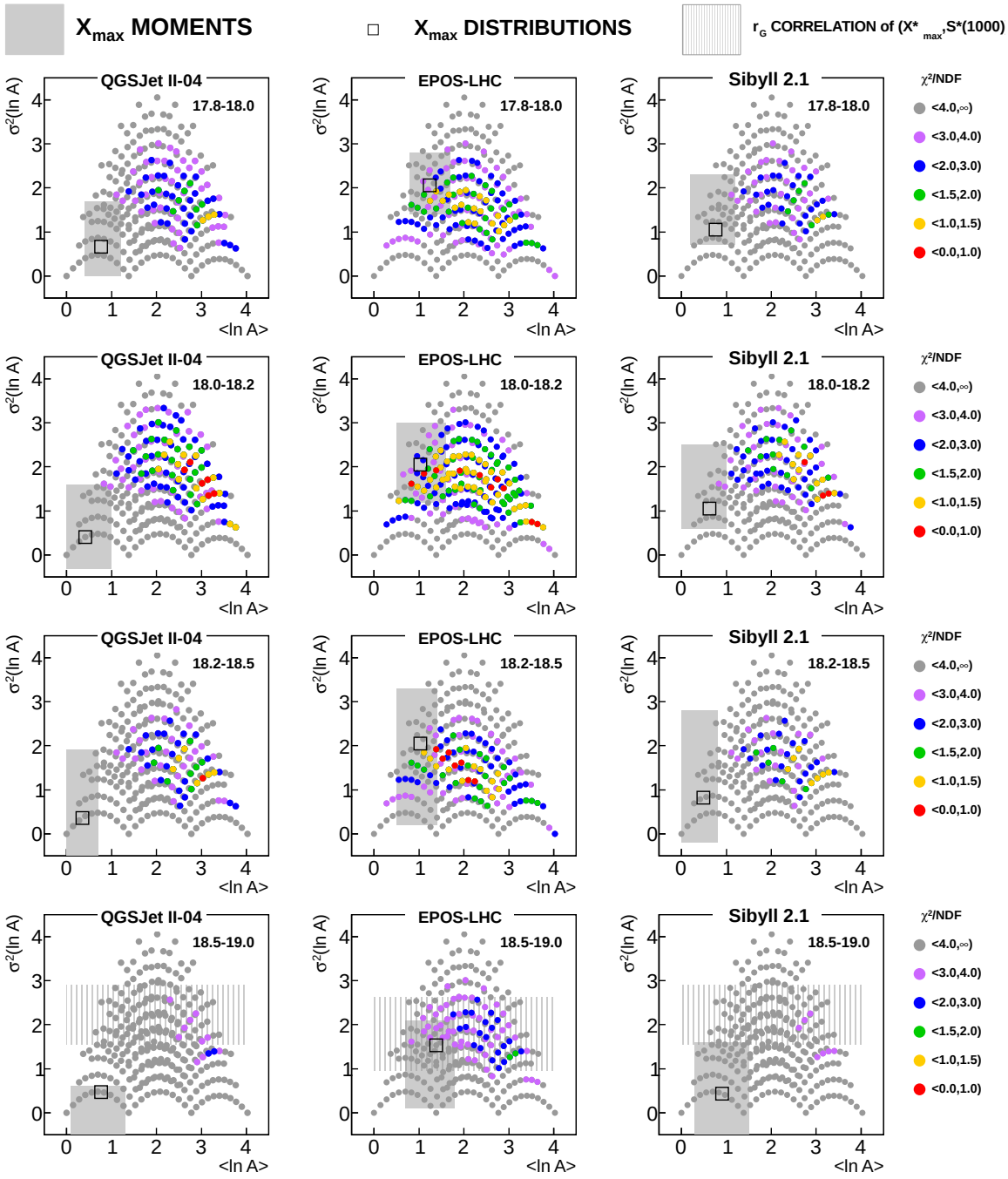

Figure 5.25: The umbrella plots for the fits of the dependence of $\langle E_{\rm SD}/E_{\rm FD}\rangle$ on $X^{19}_{\rm max}$ for QGSJet II–04 (**left panels**), EPOS–LHC (**middle panels**) and Sibyll 2.1 (**right panels**). The panels are ordered **from top to bottom** according to intervals of increasing $\log(E_{\rm FD}$ [eV]) that are shown in up-right corners of the plots. The points correspond to all possible combinations of p, He, O and Fe with relative fractions in steps of 10%. Their color reflects the reduced χ^2 of the fit with Eq. (5.12) to the data of the Pierre Auger Observatory. The shaded boxes include the estimated solutions from the analysis of the $X_{\rm max}$ moments in Fig. 3.10. The black open squares correspond to the moments of $\ln A$ calculated from the estimated primary fractions in Fig. 3.12 obtained by fitting the $X_{\rm max}$ distributions. The spread of masses inferred from the correlation between $S^*(1000)$ and $X^*_{\rm max}$ (Fig. 3.15) is depicted with dashed boxes.

The mean and the variance of $\ln A$ can be calculated for each combination of the four primaries that were fixed in the fit while $f_{\rm SD}$ was free. Fig. 5.25 contains the points in the plane ($\ln A$, $\sigma^2(\ln A)$) corresponding to each such a combination of primaries with colors of points assessed according to the reduced χ^2 of the fit. The plots are shown for three models of hadronic interactions (from left to right) and for four energy bins (from top to bottom). The corresponding moments of $\ln A$ derived from the moments of $X_{\rm max}$ distributions in Fig. 3.10 are indicated by gray boxes. The black open squares correspond to the moments of $\ln A$ calculated from the estimated primary fractions in Fig. 3.12 where the $X_{\rm max}$ distributions were fitted with combinations of $X_{\rm max}$ distributions of simulated showers induced by four primaries. For the highest energy bin (bottom panels), the spread of masses inferred from the correlation between $S^*(1000)$ and $X^*_{\rm max}$ (Fig. 3.15) is depicted with dashed boxes.

The plots in Fig. 5.25 can be used to test the consistency between the $X_{\rm max}$ measurement and the combined measurement of the ground signal and $X_{\rm max}$. For QGSJet II-04, the combined measurement is better described (smaller χ^2/NDF) with primary beams of larger $\langle \ln A \rangle$ and larger $\sigma^2(\ln A)$ than in case of the $X_{\rm max}$ measurement for all four energy bins. Remember that the nonphysically negative $\sigma^2(\ln A)$ derived from the moments of $\ln A$ at higher energies was already discussed in Section 3.4.2.

The model EPOS–LHC gives the most consistent results between the $X_{\rm max}$ measurement and the combined measurement of the ground signal and $X_{\rm max}$ among the three models of hadronic interactions. There are always some combinations of the four primaries that are compatible with the $X_{\rm max}$ measurement and simultaneously describe the dependence of $\langle E_{\rm SD}/E_{\rm FD} \rangle$ on $X^{19}_{\rm max}$ quite well.

The parameterization inferred from showers produced with Sibyll 2.1 describe the dependence of $\langle E_{\rm SD}/E_{\rm FD} \rangle$ on $X^{19}_{\rm max}$ similarly well for the same combinations of primaries as for QGSJet II–04. The main difference in the description of the measured data by these two models lies in the rescaling factor that is different for these two models as it is discussed in the following.

As it was already mentioned in the previous text, the trigger efficiency in the SD is different for different primaries below $10^{18.5}$ eV. The dependence of the trigger efficiency on energy is shown in right panel of Fig. 5.26 for protons (red) and iron nuclei (black). The zenith angle was integrated up to 60°. The maximal difference of the trigger efficiency between protons (∼0.55) and iron nuclei (∼0.7) is at energy around 10^{18} eV. The trigger efficiency is in the first approximation predominantly dependent on the number of muons on ground. In Fig. 5.1, or in upper panels of Fig 5.22, roughly the same difference of N_μ, or of the ground signal, is observed between p and He, He and N(O), N(O) and Fe. Therefore, the trigger efficiencies 0.55, 0.60, 0.65 and 0.70 for p, He, O and Fe, respectively, were chosen to check the maximal effect of the SD trigger on the mean and the variance of $\ln A$ of the primary particles. In the left and middle panel of Fig. 5.26, the differences of the mean and of the variance of $\ln A$, respectively, between the case with and without considering the trigger efficiency effect are shown for all 286 possible combinations of p, He, O and Fe with relative fractions in steps of 10%. The mean of $\ln A$ of the UHECR beam is overestimated by 0.3 at most due to the trigger effect. The variance of $\ln A$ is influenced by the SD trigger up to 0.5. Therefore the effect of trigger efficiency below $10^{18.5}$ eV can not change the conclusion that the primary beam is of mixed composition in

the studied interval of energies. Also the observed incompatibility for QGSJet II–04 and Sibyll 2.1 remains unaffected by the effect of trigger efficiency.

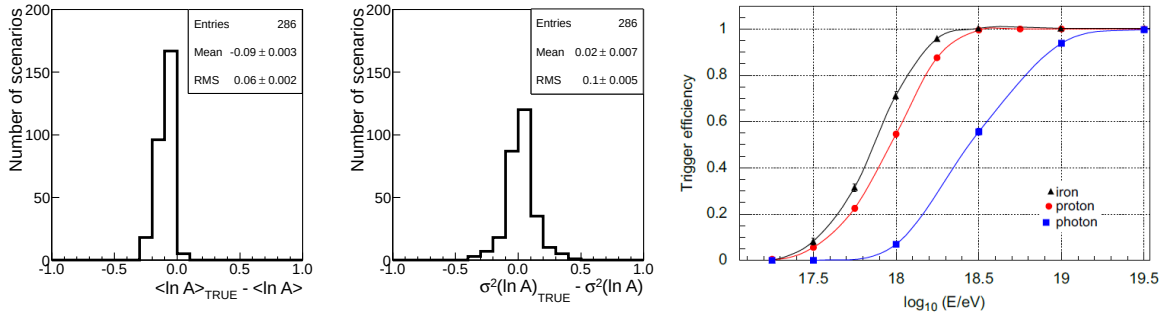

Figure 5.26: Comparison of true UHECR moments of $\ln A$, the mean (**left**) and the variance (**middle**), with those moments of $\ln A$ that include the effect of different trigger efficiencies for different primaries. The trigger efficiency was estimated at energy 10^{18} eV from the plot in the right panel. All possible combinations of p, He, O and Fe with relative fractions in steps of 10% were considered. The **right** plot describes the trigger efficiency of the SD at the Pierre Auger Observatory as a function of energy for different primaries. The showers with zenith angles up to 60° were included. Picture comes from [45].

Lack of Muons in MC Simulations

The rescaling factor of the ground signal that was fitted with Eq. (5.12) is plotted vs. *comp* # in Fig. 5.27. Comparing with the plot in the right panel of Fig. 5.23, f_{SD} depends mainly on the proton and helium fraction. In both cases, f_{SD} increases with the fraction of proton and helium in the UHECR beam. That is reasonable since protons and helium nuclei are the lightest primaries that were considered.

The rescaling factor for a given model of hadronic interactions depends also on energy, which comes mainly from the fact that the mean ground signal of the measured data ($\langle E_{\mathrm{SD}}/E_{\mathrm{FD}}\rangle^{\mathrm{DATA}}$), averaged over all X^{19}_{max} values, increases with decreasing energy below $10^{18.5}$ eV (see Fig. 5.12). Below this energy, showers with a higher content of muons are more probable to trigger (approximately uniformly in X_{max}). Therefore the reconstructed SD signal and consequently $\langle E_{\mathrm{SD}}/E_{\mathrm{FD}}\rangle$ is larger towards lower energies below $10^{18.5}$ eV. Since this is a reconstruction feature (trigger effect) of the measured data that is not present in the MC simulations of energies $10^{18.5-19.0}$ eV, f_{SD} needs to be corrected for this effect for each energy bin as

$$\bar{f}_{\mathrm{SD}} = f_{\mathrm{SD}} - (\langle E_{\mathrm{SD}}/E_{\mathrm{FD}}\rangle^{\mathrm{DATA}} - 1). \tag{5.14}$$

The rescaling factor corrected for the trigger effect ($\bar{f}_{\mathrm{SD}}$) is plotted in Fig. 5.28 as a function of proton plus helium fraction ($f_{\mathrm{p}} + f_{\mathrm{He}}$). The energy dependence is then very moderate. A weakly increasing trend of $\bar{f}_{\mathrm{SD}}$ with $f_{\mathrm{p}} + f_{\mathrm{He}}$ is observed for all three models of hadronic interactions.

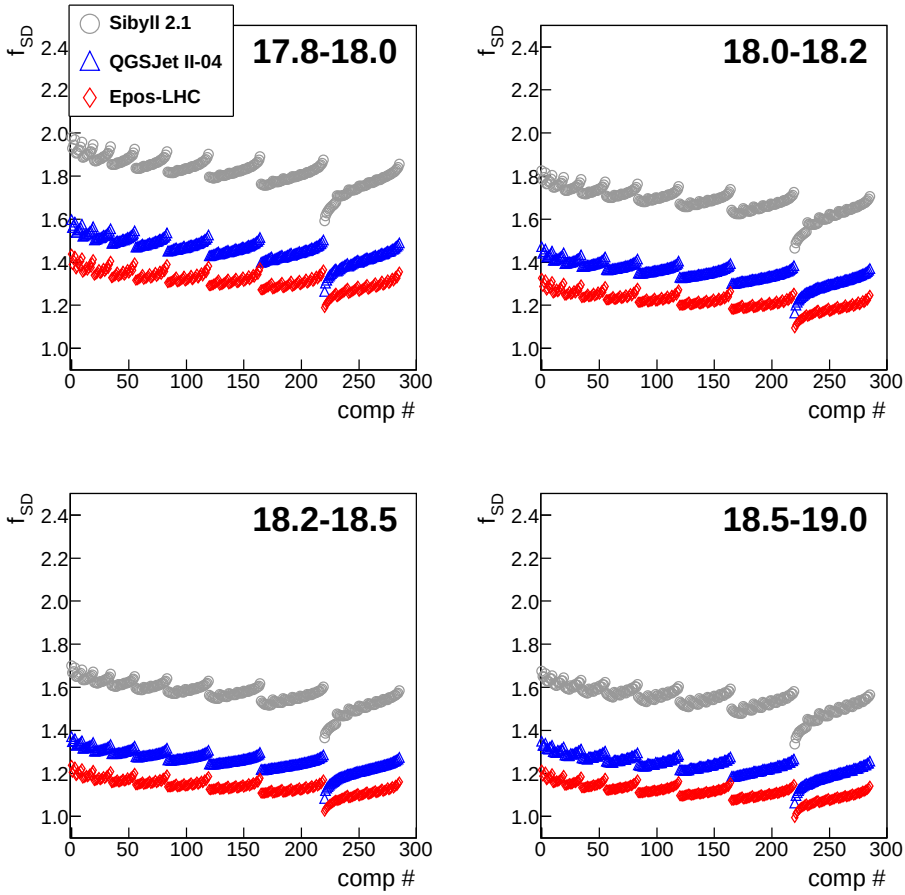

Figure 5.27: Dependence of the rescaling factor of the SD signal fitted with Eq. (5.12) to the data of the Pierre Auger Observatory with fixed primary fractions of all possible combinations of p, He, O and Fe (denoted with *comp #*) with relative fractions in steps of 10%. The respective intervals of $\log(E_{\mathrm{FD}}\ [\mathrm{eV}])$ are shown in up-right corners of the plots. The models of hadronic interactions are distinguished according to types and colors of markers.

According to the interpretation of the measured distributions of X_{max} in Fig. 3.12, $f_{\mathrm{p}} + f_{\mathrm{He}}$ is above ~0.5 for all three models of hadronic interactions in the energy range $10^{17.8-19.0}$ eV. Therefore, the most realistic estimation of the discrepancy between the MC predictions and the measured data for the SD signal (predominantly in the number of muons) was performed for combinations of primaries fulfilling two conditions: $f_{\mathrm{p}} + f_{\mathrm{He}} \geq 0.5$ and $\chi^2/\mathrm{NDF} < 4$ of the fit. The resulting range of the rescaling factor of the SD signal is shown in Fig. 5.29 as a function of energy for all three models of hadronic interactions. The range of $\bar{f}_{\mathrm{SD}}$ for $f_{\mathrm{p}} + f_{\mathrm{He}} \geq 0.5$ is depicted with dashed boxes. The range of $\bar{f}_{\mathrm{SD}}$ applying the additional condition on the reduced χ^2 of the fit is illustrated with full boxes.

To conclude, the models of hadronic interactions EPOS–LHC, QGSJet II–04 and Sibyll 2.1 produce of ~10-20%, ~25-35% and ~55-70%, respectively, smaller signal in the SD than it is observed at the Pierre Auger Observatory for showers with energies $10^{17.8-19.0}$ eV.

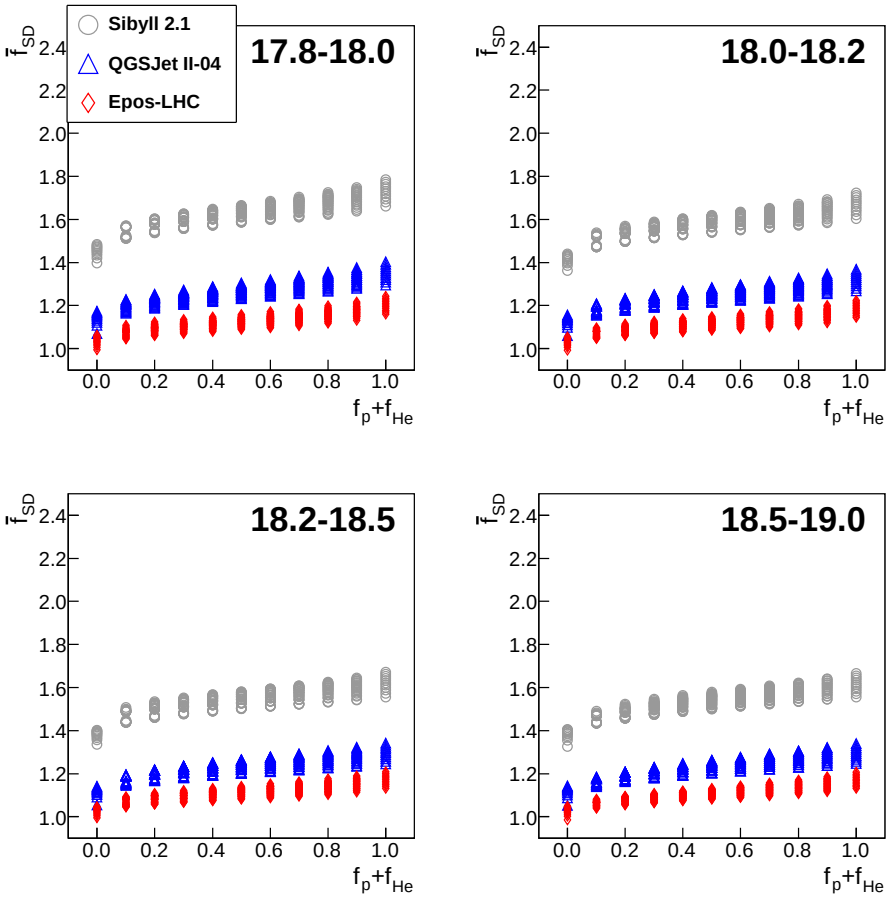

Figure 5.28: Dependence of the rescaling factor of the SD signal (corrected for the trigger effect) on proton plus helium fraction (f_p + f_{He}) corresponding to Fig. 5.27. The respective intervals of log(E_{FD} [eV]) are shown in up-right corners of the plots. The models of hadronic interactions are distinguished according to type and color of markers.

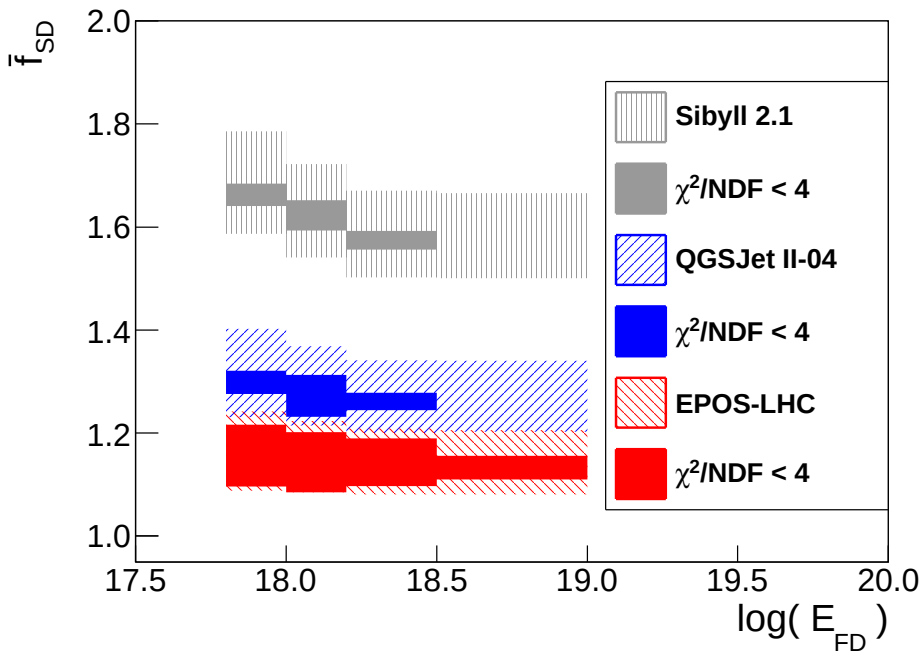

Figure 5.29: Dependence of the rescaling factor of the SD signal (corrected for trigger effect) on energy. The dashed bands include results for all combinations of primaries with $f_{\mathrm{p}} + f_{\mathrm{He}} \geq 0.5$ from Fig. 5.28. The full bands correspond to the subset of results with $\chi^2/\mathrm{NDF} < 4$ of the fit. Three models of hadronic interactions are distinguished by different colors.

5.3 Summary

A method to obtain simultaneously the primary fractions of UHECR and the muon rescaling factor from a combined measurement of N_μ and $X_{\max}$ was presented in Section 5.1. Simulated showers with two models of hadronic interactions tuned to the LHC data (run I) were used to test the method. Its precision was tested with different combinations of primaries and with example data. The primary fractions and the muon rescaling factor can be determined within a few % when the proper parameterization of $\langle N_\mu \rangle(X_{\max})$ and of $X_{\max}$ distributions are known. The difference of the primary fractions from the true values reconstructed with the two parameterizations based on the two models of hadronic interactions was observed to be about 25%. The muon rescaling factor reflected the relative difference (around 6%) in the average muon shower size of the two models of hadronic interactions.

In Section 5.2, the presented method was preliminarily applied to the data of the Pierre Auger Observatory for a combination of $E_{\mathrm{SD}}/E_{\mathrm{FD}}$ and $X^{19}_{\max}$ in four energy intervals between $10^{17.8}$ eV and $10^{19.0}$ eV. The measured data can be reliably described with MC showers only when a mixed composition of primaries with $\sigma^2(\ln A) \in \langle 1, 3 \rangle$ is considered. The model of hadronic interactions EPOS–LHC showed consistent results with $X_{\max}$ analyses, whereas a tension was observed in case of QGSJet II–04 and Sibyll 2.1. In case of the comparison with the study of the correlation between the ground signal and $X_{\max}$ at $10^{18.5-19.0}$ eV, the results are compatible for all the models. The results suggest that the ground signal in simulated showers needs to be increased by 25-35% for QGSJet II–04, by 10-20% for EPOS–LHC and by 55-70% for Sibyll 2.1 to match the measured data. These findings are consistent (see Tab. 5.2) with observations of R_μ shown in the left and right panel of Fig. 3.16 for the official analysis of vertical and inclined events, respectively.

Table 5.2: Rescaling of the SD signal ($\bar{f}_{\mathrm{SD}}$) compared with published analyses of the Pierre Auger Observatory data regarding the rescaling of the number of muons (R_μ). The latter results on R_μ for vertical ($0^\circ \leq \Theta \leq 60^\circ$) and inclined ($62^\circ \leq \Theta \leq 80^\circ$) showers were estimated from the left and right panel of Fig. 3.16, respectively, including the systematic uncertainty.

Model	$\bar{f}_{\mathrm{SD}}$ from $\langle E_{\mathrm{SD}}/E_{\mathrm{FD}} \rangle$ vs. $X^{19}_{\max}$	R_μ for $0^\circ \leq \Theta \leq 60^\circ$	R_μ for $62^\circ \leq \Theta \leq 80^\circ$
QGSJet II–04	25-35%	30-80%	15-65%
EPOS–LHC	10-20%	10-50%	5-50%
Sibyll 2.1	55-70%	-	-

Chapter 6

Number of Muons with Resistive Plate Chambers

It was indicated in Section 2.3 that the number of muons measured by surface detectors has a potential to discriminate between the primaries (taking the benefit of full duty cycle). Moreover, the Pierre Auger Observatory data showed that the crucial point of the correspondence between the observed data and hadronic interactions taking place in the UHECR showers is probably hidden in proper understanding of the muon component (production of muons, muon spectra, total number of muons). Current models of hadronic interactions still produce less muons than it is observed with the data of the Pierre Auger Observatory (see discussion in Section 3.4.2). Therefore the Pierre Auger Observatory upgraded with detectors providing additional measurement focused on the muon component would be of a high scientific importance.

Also other scientific outputs of the Pierre Auger Observatory could be more decisive with a better discrimination of the primary mass using the SD measurement, which operates with full duty cycle. Such enhancement would improve or extend also the conclusions on UHECR at the highest energies regarding anisotropy searches or deviations in the magnetic fields. Above that, stronger considerations about the properties of UHECR sources from the spectra of different primaries could be derived, as e.g. in [111]. Many more specific branches of UHECR studies depending on the mass composition of primaries would be improved.

The Pierre Auger Observatory proposed several options of the SD upgrade and characterized their properties. Although the final selection favored different solution (using scintillators placed on top of the water Cherenkov stations [94]) this chapter is focused on the author's original contribution to the possible upgrade of the observatory using Resistive Plate Chambers (RPCs) placed under the water Cherenkov stations to directly measure the muon component of UHECR shower. Properties of this proposed upgrade solution are studied using detailed MC simulations with the models of hadronic interactions tuned to the LHC data (run I). The proposed array of RPCs placed under the water Cherenkov stations was named as the Muon Auger RPC Tank Array (MARTA) [112]. In particular, the

separability of primaries is evaluated considering only a measurement of the muon component with RPCs.

In the following, the design of the proposed SD array upgraded with RPC detectors will be briefly discussed. Then a parametrization of the LDF slope of particle density measured with MARTA is presented for the purpose of reliable calculation of the number of muons on event–by–event basis. Finally, the estimated performance of considered enhancement for separation of primaries according to the measured number of muons is presented and discussed.

6.1 Description of Surface Array Equipped with RPC Detectors

In general, the RPC is a gaseous particle detector consisting of two parallel high resistivity plates connected to a high voltage, two medium resistive electrodes (transparent to the induced signal) and a gap filled with a gas (see Fig. 6.1). When an ionizing particle propagates through the chamber, an avalanche of electrons is produced in the gas near the location of particle penetration in the upper plate. The appropriate read–out electronics (pickup cells) collect the induced signals with a very good time resolution (~ns). The number of plates and gaps can be naturally increased as well as the material, read–out electronics and the type of gas can be adjusted to match the required detector performance (detection efficiency, time and space resolution, dead time etc.).

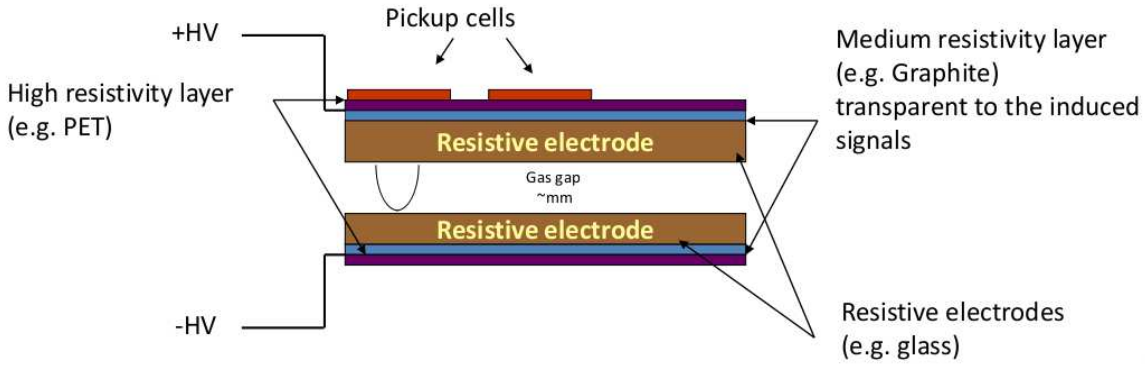

Figure 6.1: Schematic description of one Resistive Plate Chamber (RPC) with read–out cells. Picture is taken from [113].

One RPC unit considered in the developed Geant4 [114] simulation of MARTA response includes 3 parallel soda–lime glass layers (electrodes) of 1.9 mm thickness. Two 1.0 mm gaps between the glass layers are filled with $C_2F_4H_4$ (R134a). The high voltage is applied by means of a layer of resistive acrylic paint on the outer glass electrodes. The chamber of dimensions 1.2×1.6 m^2 is read out by 64 rectangular 15×20 cm^2 pads arranged in the 8×8 matrix and the chamber is enclosed in a 3 mm thick aluminium box. Four such chambers are placed inside a precast concrete placed under the water Cherenkov station (see Fig. 6.2). The concrete walls provide an additional shielding of the EM component wrt. the atmospheric depth by ~50 g/cm^2 (20 cm of concrete). The responses of such

a design to shower particles were adopted in the MARTA branch of the Auger simulation software Offline v2r9p0.

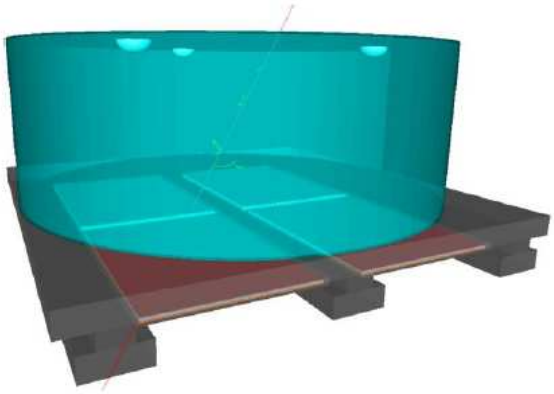

Figure 6.2: Illustration of 4 RPCs (brown) installed below the water Cherenkov station (blue) inside the precast concrete (dark gray). Picture is taken from [113].

The segmented (position sensitive) design of the read–out electronics allows to count the number of pads that collect a signal induced by at least one ionizing particle. Each pad corresponds to a different shielding of the EM component with respect to the direction of the shower axis due to a different amount of material (water + concrete) traversed by a particle in the detector system. The average EM contamination (ratio of the signal induced by the EM component to the signal induced by all particles) across the RPC surface obtained from 500 showers induced by protons of energy $10^{19.5}$ eV and $\Theta = 40^{\circ}$ is shown in Fig. 6.3 for illustration. It is clearly visible that due to the segmented read–out area it is possible to select pads with a lower EM contamination compared to the rest of the pads. For the purpose of following analysis, the pads with additional mass overburden of 167 g/cm^2 to the atmospheric depth were selected individually for each station based on the shower geometry. Such pads (~2/3 of the total number of pads for $\Theta = 40^{\circ}$) then create the so–called fiducial area suitable for the measurement of muons. In this fiducial area, the EM contamination in this RPC signal is at most at a level of ~25% [115] when showers induced by protons with $\Theta \simeq 40^{\circ}$ are detected with stations distant ~500 m from the shower core. Since only the information, if the pad was hit by at least one particle can be obtained, the pile–up occurs for higher muon densities closer to the shower core. This effect was accounted for according to [116].

In this chapter, the direct detection of muons is probed using 4 RPCs of total area 7.68 m^2 installed just under the water Cherenkov station (one SD station covers an area of 10 m^2 on ground) in a precast concrete. Two deployment schemes of MARTA stations were considered (see Fig. 6.4). In the first case, the installation of RPCs under all 1600 stations of the main SD (spacing 1.5 km) is considered. In the second case, the installation of RPCs under ~1/3 of stations was assumed. The latter configuration of stations equipped with RPCs forms a regular triangular array with spacing ~2.6 km. Such configuration eases the financial requirements, however for the price of a decreased number of muons measured per event.

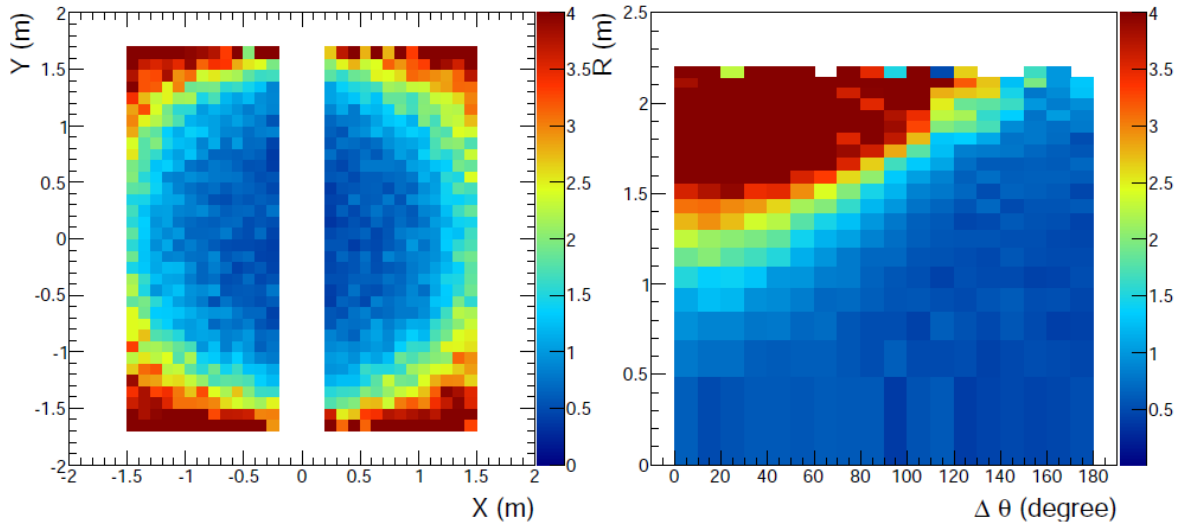

Figure 6.3: Average EM contamination in the Cartesian coordinate system (**left**) and in the Polar coordinate system (**right**) centered in the middle of the water Cherenkov station on the ground. Five hundred showers induced by protons of energy $10^{19.5}$ eV and $\Theta = 40°$ were used. Pictures come from [115].

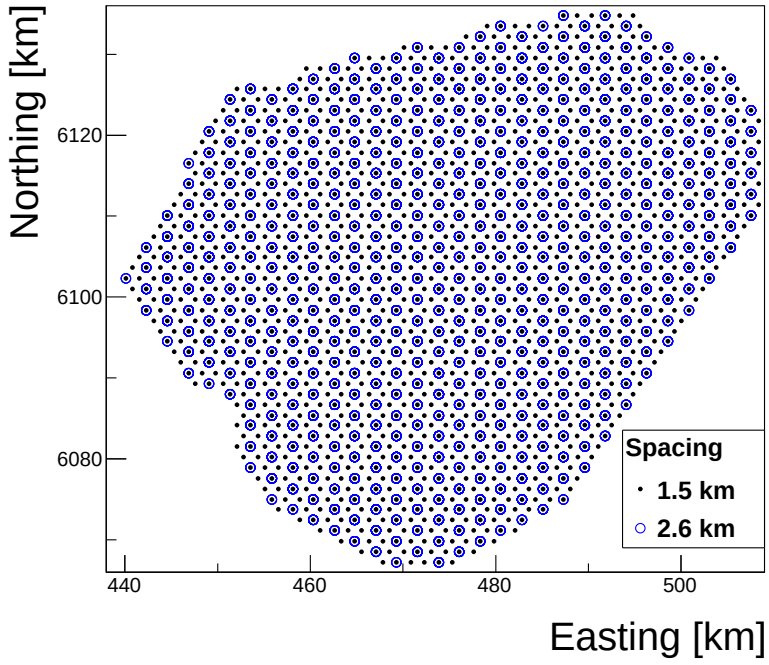

Figure 6.4: Positions of stations considered for MARTA with the 1.5 km spacing (black dots) and with the 2.6 km spacing (blue circles) in the MC simulations.

6.2 Simulated Showers and Detector Responses

Two libraries of CORSIKA showers reconstructed with the MARTA branch of Auger Offline v2r9p0 were used in the following analysis. The showers from the first library were produced with pre–LHC models of hadronic interactions, whereas the second library with models tuned to the LHC data.

The first library [117] contains showers induced by primary particles of energy in the range $\langle 10^{19.0}, 10^{19.5} \rangle$ eV and of zenith angle in the range $\langle 0°,\ 60° \rangle$. The primary protons and iron nuclei were considered to produce showers using the hadronic interaction model EPOS 1.99, whereas for the model QGSJet II–03 only showers induced by protons were generated. The showers from this library were used for the parametrization of the LDF slope, described in Section 6.3, taking the benefit of a large number of generated showers with a wide range of energies and zenith angles.

The showers from the second library [118] were analyzed to estimate the separability of primaries in Section 6.4. The showers induced by 4 primaries (p, He, N, Fe) were produced with QGSJet II–04 and EPOS–LHC for fixed primary energies (10^{19}, $10^{19.8}$ eV) and fixed zenith angles ($\Theta = 21°,\ 38°,\ 52°$). For each model, primary particle and zenith angle 500 showers at 10^{19} eV and 200 showers at $10^{19.8}$ eV were produced. The effect of the energy resolution $\delta(E)$ on the reconstruction of the number of muons was studied with the sets of showers generated in a continuous range of energies $\langle 10^{18.85},\ 10^{19.1} \rangle$ eV (2000 showers), $\langle 10^{19.6},\ 10^{19.8} \rangle$ eV (500 showers) of spectral index $\gamma = -1$ and in a continuous zenith angle Θ of $\langle 0°,\ 60° \rangle$. The fact that N_μ depends almost linearly on the shower energy, see Eq. (2.21), implies the importance of a precise measurement of the shower energy. The showers can then be selected according to the energy from an energy bin $\langle E_1, E_2 \rangle$ where $E_{1,2} = \langle E \rangle (1 \mp \delta(E))$. Shower cores were distributed randomly over the whole area of the observatory.

6.3 Parametrization of LDF Slope

The number of muons in a certain range of distances from the shower core is obtained integrating the LDF of particle densities measured by the MARTA stations. The LDF function can be fitted for each MARTA event with the slope set free, or with the slope fixed to the average value obtained from the whole set of events. For certain shower–array configurations, when a lot of MARTA stations are available in the considered range of distances from the shower core, a precise fit can be obtained with the free slope of the LDF. However, for most of the events the shower–array configurations are not that convenient. In the following, the fixed LDF slope was applied in the event–by–event procedure and therefore a parametrization of the LDF slope on energy and zenith angle was performed. Finally, the slope parametrized using the pre–LHC models was applied to showers simulated with models tuned to the LHC data to estimate the potential of MARTA to separate primaries in Section 6.4. As it will be shown in the following, the difference of the parametrized slope between the pre–LHC models and models tuned to the LHC data is within few %.

The value of LDF in 1000 m ($\rho_{1000}^{\mathrm{MARTA}}$) was chosen in this study as the quantity proportional to

the overall number of muons on ground[1]. It was obtained from an event–by–event fit of the LDF of particle density in the limited range of distances $\langle 500,\ 2000\rangle$ m from the shower core. These distances were selected to be larger than 500 m because of the increasing EM contamination towards the shower core even in the fiducial area. For distances of stations from the shower core greater than ~2000 m the flux of particles is getting so low that the average number of hits in stations starts to be around 1 only. The Maximum Likelihood fit of LDF would be needed to treat correctly also the stations with no signal triggered. This is relevant for stations distant farther than ~2000 m from the shower core. The total number of muons detected by MARTA for a single shower is however dominated by a contribution of stations located closer to the shower core (higher muon density) and the Maximum Likelihood fit would change $\rho_{1000}^{\mathrm{MARTA}}$ wrt. χ^2 fit by ~1% at most for the limited range of distances considered. Therefore a χ^2 fit of the LDF with distances between 500 m and 2000 m was sufficiently applied on event–by–event basis to estimate the potential to separate primary particles according to the number of muons using the presented design of MARTA detectors.

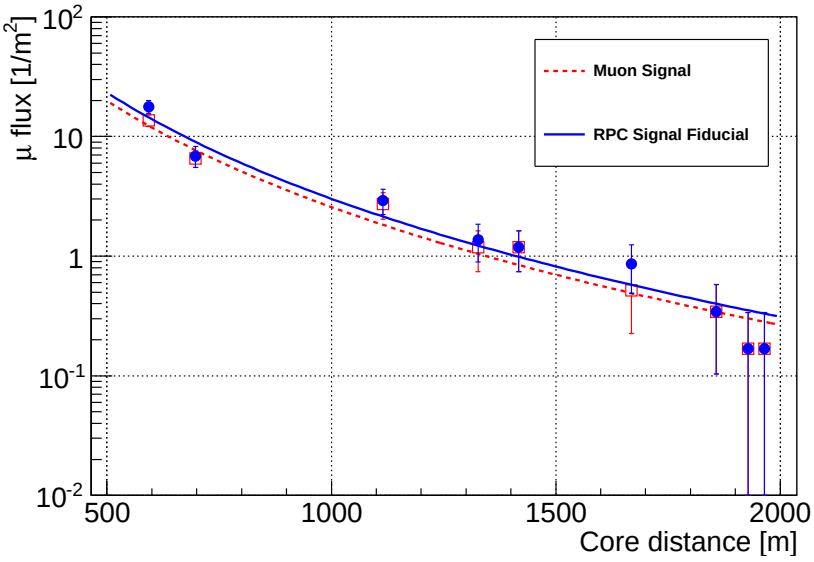

Figure 6.5: Example of LDF reconstruction for the Ideal Signal (red) and for the RPC Signal (blue).

Two fluxes measured with RPC detectors placed under the water Cherenkov stations of the Pierre Auger Observatory were considered: the flux of muons arriving to RPCs (Ideal Signal) with core distance (r) in the range $\langle 500,\ 2000\rangle$ m and the flux of all particles hitting RPCs (RPC Signal) in the fiducial area for r in the range $\langle 500,\ 1000\rangle$ m combined with the flux of all particles in the whole RPC area for r in the range $\langle 1000,\ 2000\rangle$ m. Beyond the core distance ~1000 m the EM component is already heavily absorbed in the atmosphere with respect to the muon component that the whole RPC area can be used without substantially increasing the EM contamination in the RPC signal. An

[1]The slope of the LDF was fixed, and therefore $\rho_{1000}^{\mathrm{MARTA}}$ possess the same information as the integrated LDF.

example of reconstructed LDF for the RPC Signal and for the Ideal Signal is illustrated in Fig. 6.5 for a typical MARTA event.

Five bins of SD energy (E_{SD}) and 10 bins of sec(Θ) were chosen to parametrize the slope of LDF. The reconstructed E_{SD} and sec(Θ) were used to exploit quantities that are measurable in reality by the SD. As mentioned above, only the non–zero fluxes of hits (ρ) measured by RPC stations with r of $\langle 500,\ 2000\rangle$ m were included to obtain the average LDF for each bin of E_{SD} and sec(Θ). The χ^2 minimalization of the modified NKG function:

$$\langle\rho(r)\rangle = \rho_{1000}\left(\frac{r}{1000}\right)^{\beta}\left(\frac{r+700}{1000+700}\right)^{\beta+\gamma} \tag{6.1}$$

was used, where γ was fixed to 0 to decrease the number of free parameters[2], and ρ_{1000}, β were the fitted parameters.

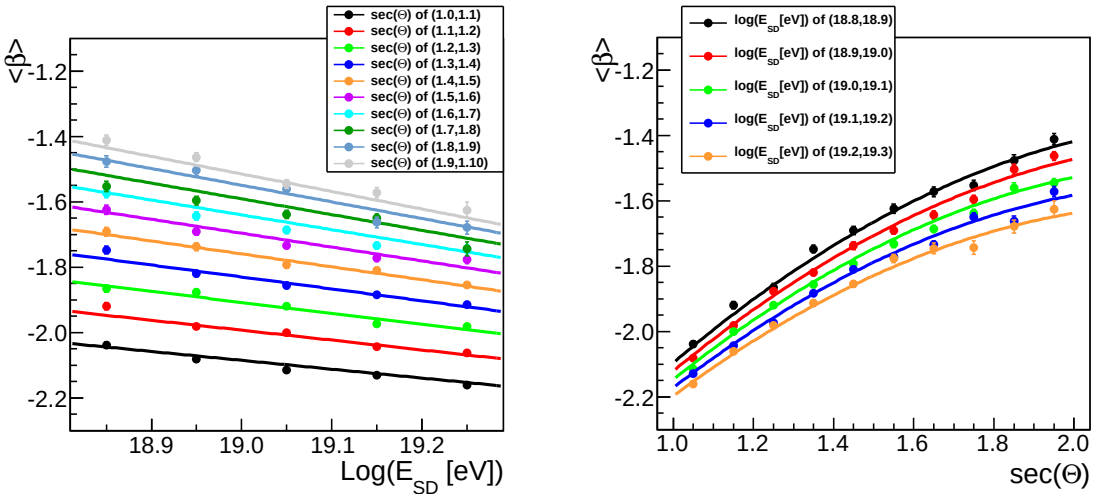

Figure 6.6: Parametrized LDF slope of the RPC Signal for proton showers produced with QGSJet II–03. Fitting range of the LDF was $\langle 500,\ 2000\rangle$ m. Curves correspond to the fitted function in Eq. (6.2).

The average LDF slope $\langle\beta\rangle \equiv \beta$ obtained for the RPC Signal of showers induced by protons that were produced with the hadronic interaction model QGSJet II–03 is shown in Fig. 6.6 for illustration. $\langle\beta\rangle$ was fitted with a function assumed to be linear in the SD energy and quadratic in sec(Θ):

$$\langle\beta\rangle = (a_0 + a_1\cdot E_{SD}) + (b_0 + b_1\cdot E_{SD})\cdot \sec(\Theta) + (c_0 + c_1\cdot E_{SD})\cdot \sec^2(\Theta). \tag{6.2}$$

For the parametrization of showers induced by protons and iron nuclei (~50/50) the appropriate intersected region of reconstructed E_{SD} for protons and iron nuclei was chosen[3]. Fitted parameters for the

[2] In fact, the non–zero parameter γ makes the slope of LDF steeper for distances beyond 1700 m (near the limit 2000 m). As the range of LDF fitting is always restricted to be within 2000 m, no significant impact on ρ_{1000}^{MARTA} was observed.

[3] The difference of E_{SD} for protons and iron nuclei comes from the bias caused by different number of muons, discussed in Section 3.4.2 and Chapter 5.

Ideal Signal are shown in Tab. 6.1 and for the RPC Signal in Tab. 6.2 for different mass compositions of primaries and different models of hadronic interactions.

Table 6.1: Parameters of the average LDF slope $\langle\beta\rangle$ fitted with Eq. (6.2) for the **Ideal Signal**.

Primaries	Model	LDF Range	a_0	a_1	b_0	b_1	c_0	c_1
p	QGSJet II–03	[500,2000]m	-2.815	-0.005	8.832	-0.409	-1.475	0.0681
p	EPOS 1.99	[500,2000]m	-5.409	0.118	8.532	-0.382	-0.944	0.0374
Fe	EPOS 1.99	[500,2000]m	-6.219	0.162	7.915	-0.351	-1.338	0.0582
p+Fe	EPOS 1.99	[500,2000]m	-6.033	0.154	8.037	-0.360	-1.207	0.0526

Table 6.2: Parameters of the average LDF slope $\langle\beta\rangle$ fitted with Eq. (6.2) for the **RPC Signal**.

Primaries	Model	LDF Range	a_0	a_1	b_0	b_1	c_0	c_1
p	QGSJet II–03	[500,2000]m	-5.314	0.096	8.927	-0.380	-0.897	0.0282
p	EPOS 1.99	[500,2000]m	-6.978	0.176	8.506	-0.350	-0.773	0.0198
Fe	EPOS 1.99	[500,2000]m	-7.006	0.182	7.769	-0.315	-1.691	0.0681
p+Fe	EPOS 1.99	[500,2000]m	-6.791	0.170	7.957	-0.325	-1.537	0.0606

6.3.1 Stability of Parametrized LDF Slope

The parametrization of $\langle\beta\rangle$ was found very stable wrt. various aspects, nevertheless the differences of the LDF slope that are always within 5% are discussed in this subsection in more detail. The relative difference of $\langle\beta\rangle$ between the Ideal Signal and the RPC Signal using the corresponding parameterization is plotted in the left panel of Fig. 6.7 for proton showers produced with QGSJet II–03. The comparison between QGSJet II–03 and EPOS 1.99 for the RPC Signal of proton showers is shown in the right panel of Fig. 6.7. In the left panel of Fig. 6.8, the relative difference of parametrized $\langle\beta\rangle$ using showers induced by protons and iron nuclei is depicted for the model EPOS 1.99. In the right panel of Fig. 6.8, the relative difference of parametrized $\langle\beta\rangle$ using the models of hadronic interactions tuned to the LHC data and the parametrization of $\langle\beta\rangle$ for EPOS 1.99 p+Fe is plotted.

The stations with non–zero fluxes were included to find the parametrization of $\langle\beta\rangle$. The ignorance of the so–called silent stations, stations with no signal triggered, has a consequence that a flattening of the reconstructed LDF occurs at distances beyond ∼2000 m for hadron–induced showers where the particle flux (≃ muon flux) is smaller than ∼1 per the RPC area. Naturally this effect overestimates a bit also the fitted flux below 2000 m. This means that the fitted slope is a bit less steeper than the true muon LDF and therefore the absolute value of the fitted $\langle\beta\rangle$ is a bit smaller. This difference was found to be well within 5%.

The energy dependence of $\langle\beta\rangle$ obtained in the LDF range $\langle 500,\ 2000\rangle$ m seems to be a consequence of the fact that the silent stations were not incorporated in the average LDF. As the shower

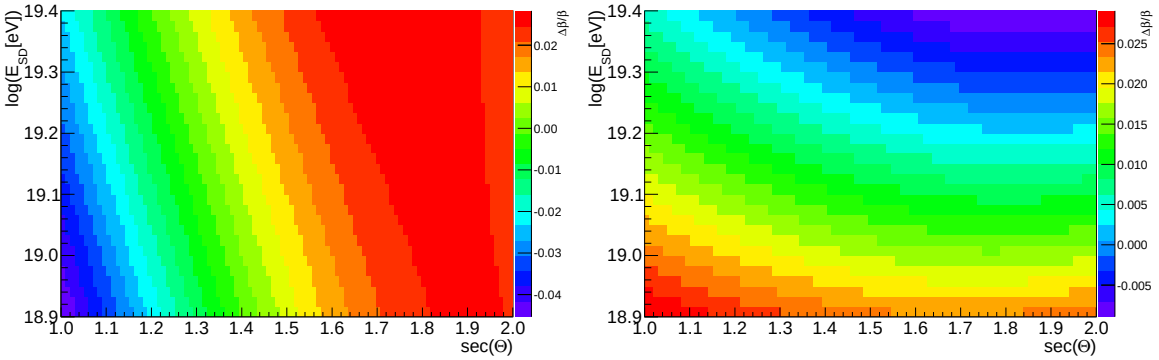

Figure 6.7: **Left panel:** Relative differences of parametrized $\langle\beta\rangle$ for the Ideal Signal and the RPC Signal, "(Ideal Signal–RPC Signal)/RPC Signal", using proton showers produced with QGSJet II–03. **Right panel:** Relative differences of parametrized $\langle\beta\rangle$ inferred using different models, "(EPOS 1.99–QGSJet II–03)/QGSJet II–03", for the RPC Signal of proton showers.

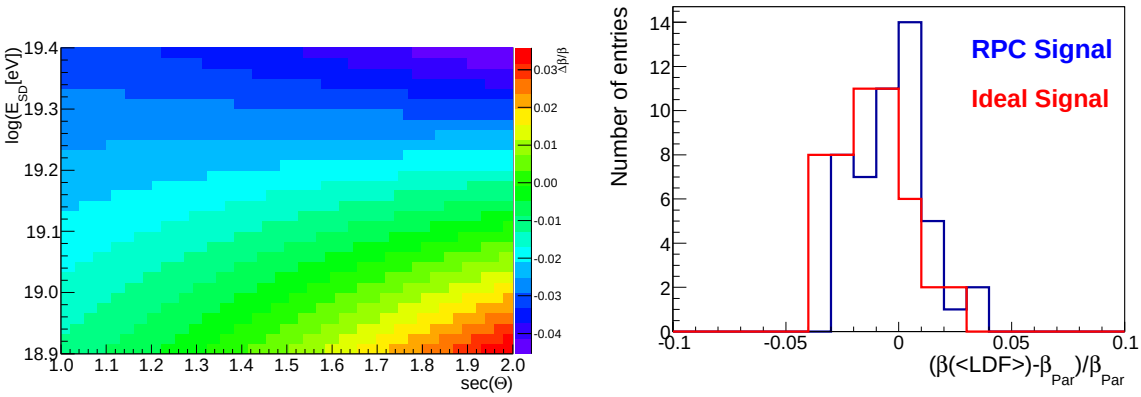

Figure 6.8: **Left panel:** Relative differences of parametrized $\langle\beta\rangle$ inferred using showers produced with EPOS 1.99 induced by different primaries, "(Fe–p)/p", for the RPC Signal. **Right panel:** Comparison of relative differences of parametrized $\langle\beta\rangle$ obtained using the models of hadronic interactions tuned to the LHC data, $\beta(<\text{LDF}>)$, and the parametrization of $\langle\beta\rangle$ for EPOS 1.99 p+Fe (β_{Par}). For the two models of hadronic interactions tuned to the LHC data (QGSJet II–04, EPOS–LHC) there were used showers induced by four primaries (p, He, N, Fe) of two fixed energies (10^{19} eV, $10^{19.8}$ eV) and three fixed zenith angles ($21°, 38°, 52°$).

energy increases, the lateral size of shower increases as well and the artificial flattening of the LDF then starts farther from the shower core (steeper LDF slope). Analogously, the LDF slope of the RPC Signal is steeper than the LDF slope of the Ideal Signal almost for all energies as the density of the RPC Signal is always higher than the density of the Ideal Signal.

The relative differences of $\langle\beta\rangle$ between the ideal and measurable case (left panel of Fig. 6.7) are dependent on sec(Θ) and slightly on the SD energy. At smaller zenith angles the EM contamination in the RPC Signal is larger and therefore the effect of flattening is smaller and the LDF slope is steeper. As EPOS 1.99 produces more muons in average than QGSJet II–03, the effect of flattening is weaker

in case of EPOS 1.99 and therefore the LDF slope for EPOS 1.99 is steeper than for QGSJet II–03. On the other hand, the relative differences of $\langle\beta\rangle$ between showers induced by protons and iron nuclei (left panel of Fig. 6.8) are dependent on energy and almost independent on sec(Θ). The parametrized LDF slope for protons is steeper than for iron nuclei at higher energies, which could be explained by fading of the flattening effect (true LDF of proton showers is steeper than the true LDF of showers induced by iron nuclei).

In summary, the obtained parameterization of the dependence of $\langle\beta\rangle$ on energy and zenith angle show deviations only within ~5% with respect to different mass compositions of primaries, types of signals and most importantly on models of hadronic interactions. This uncertainty of the LDF slope affects the fitted $\rho_{1000}^{\mathrm{MARTA}}$ by less than 1%. Therefore the parametrization obtained by EPOS 1.99 for 50% p + 50% Fe was chosen to be used in the following analysis of showers generated with models already tuned to the LHC data.

6.4 Separability of Primaries using MARTA

In this section the performance of two MARTA arrays with respect to the separation power of the primary mass is studied at the event–reconstruction level using detailed simulation library produced by the MARTA team. Two types of array configurations covering the whole area of the SD array are considered as indicated in Fig. 6.4. Comparing the reconstructed value of $\rho_{1000}^{\mathrm{MARTA}}$ with the true value $\rho_{1000}^{\mathrm{MC}}$ the EM bias and the resolution of the measurement of the number of muons with MARTA is estimated. The separation power to distinguish protons from other primaries is assessed with Merit factor (see Eq. (2.29)) values calculated from the distributions of $\rho_{1000}^{\mathrm{MARTA}}$ for different primaries.

6.4.1 Selection Efficiency

In order to reconstruct $\rho_{1000}^{\mathrm{MARTA}}$ with a certain minimal precision, a requirement was applied to the total number of hits in MARTA stations $N_{\mathrm{hits}}^{\mathrm{Total}}$ in the region $\langle 500,\ 2000\rangle$ m and to the number of stations N_{st} with non–zero signal in the same region. Such requirements have a consequence on the selection efficiency, which needs to be maintained sufficiently high, especially at the highest energies. When $N_{\mathrm{st}} = 1$, only events with $N_{\mathrm{hits}}^{\mathrm{Total}} \geq 20$ were accepted. In case of $N_{\mathrm{st}} \geq 2$, the total number of hits $N_{\mathrm{hits}}^{\mathrm{Total}} \geq 10$ was requested. In Fig. 6.9 the selection efficiency is plotted as a function of energy using the requirements mentioned above. Whereas for the array with 1.5 km spacing (full markers) almost full efficiency is observed, for the 2.6 km array (open markers) the selection efficiency spans between 65% and 85% at 10^{19} eV and at energy $10^{19.8}$ eV it becomes 85% increasing up to almost 100% for more inclined showers.

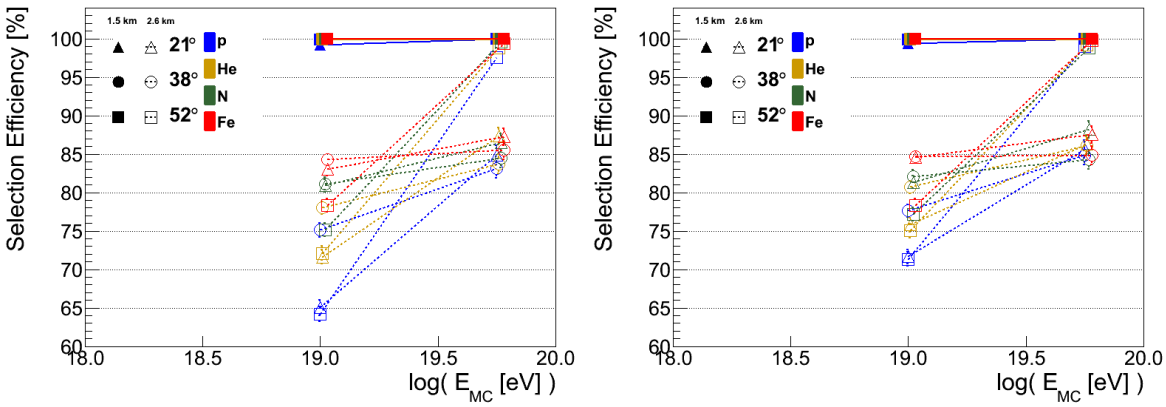

Figure 6.9: Dependence of the selection efficiency on MC energy for QGSJet II–04 (**left panel**) and EPOS–LHC (**right panel**). The primaries are distinguished by colors. Different markers correspond to different types of arrays and different zenith angles.

6.4.2 Resolution

The detector resolution of the measured number of muons on ground has a crucial impact on the separation of primaries as it was already indicated in Fig. 2.7 when the detector resolution of 20% was considered. Therefore it is important to estimate it as precisely as possible. For this purpose, a comparison of the measured $\rho_{1000}^{\mathrm{MARTA}}$ with MC true value $\rho_{1000}^{\mathrm{MC}}$ is used. The resolution is inferred as the variance of the Gaussian fit to the histogram of $(\rho_{1000}^{\mathrm{MARTA}} - \rho_{1000}^{\mathrm{MC}})/\rho_{1000}^{\mathrm{MC}}$.

However, $\rho_{1000}^{\mathrm{MC}}$ (at the RPC level) is not so easy to obtain at the stage of simulation production. $\rho_{1000}^{\mathrm{MC}}$ represents the true muon density at the level of the RPC detector below the water Cherenkov station. Calculating the muon density from the total number of muons on ground obtained directly from CORSIKA showers would underestimate the value of the resolution, because the muon density at the RPC level is affected by the absorption of muons in the additional material (water + concrete). In the Offline simulation of the detector response to the CORSIKA shower the reconstructed data of 12 additional imaginary stations (so–called dense stations) are also saved. These dense stations are not used to obtain $\rho_{1000}^{\mathrm{MARTA}}$. They are located 1000 m from the shower core and placed equidistantly in azimuth, besides the stations of the regular array. From the number of muons injected into each of the 12 MARTA stations (N_{μ}^{Dense}) under these dense stations the average muon density at 1000 m from the shower core, $\rho_{1000}^{\mathrm{MC}} \equiv \langle \rho_{1000}^{\mathrm{Dense}} \rangle$, was estimated.

Nevertheless, the statistical error of calculating $\rho_{1000}^{\mathrm{MC}}$ needs to be considered. Therefore the Poissonian fluctuations of the signal in dense stations (see the black line in Fig. 6.10) are quadratically subtracted from the the variance of $(\rho_{1000}^{\mathrm{MARTA}} - \rho_{1000}^{\mathrm{MC}})/\rho_{1000}^{\mathrm{MC}}$ to estimate the value of the true MARTA resolution. Note that the fluctuations of the muon density at energy 10^{19} eV are dominated by Poissonian fluctuations, whereas at energy $10^{19.8}$ eV the Poissonian fluctuations are comparable to shower–to–shower fluctuations (quadratically added to Poissonian fluctuations).

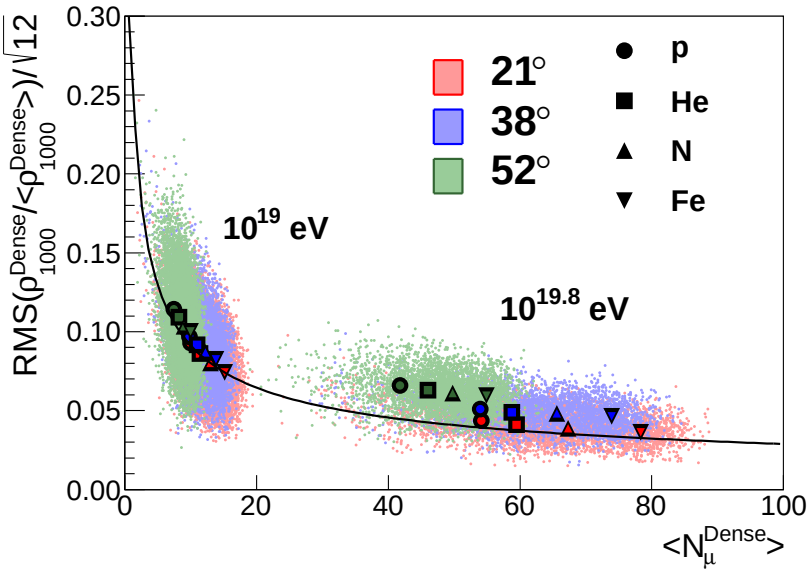

Figure 6.10: Relative fluctuations of the muon density in 12 dense stations depending on the average number of muons $\langle N_\mu^{\text{Dense}} \rangle$ collected by a single dense station. For the average values, the types of primaries are distinguished by different shapes of markers and the different colors correspond to different zenith angles. Showers with $\langle N_\mu^{\text{Dense}} \rangle \lesssim 15$ were induced by primaries with energy 10^{19} eV and showers with $\langle N_\mu^{\text{Dense}} \rangle \gtrsim 20$ were induced by primaries of energy $10^{19.8}$ eV. The showers were produced with QGSJet II–04. The predicted Poissonian fluctuations $\sqrt{\langle N_\mu^{\text{Dense}} \rangle}/\langle N_\mu^{\text{Dense}} \rangle / \sqrt{12}$ are shown by the black line.

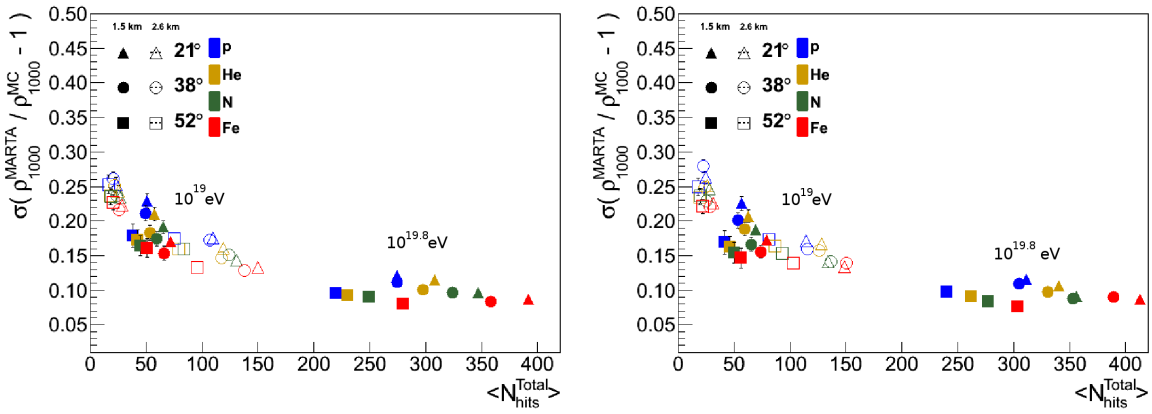

Figure 6.11: The resolution of MARTA detector depending on the number of total hits in the range [500, 2000] m. Different primaries and zenith angles are distinguished for QGSJet II–04 (**left panel**) and EPOS–LHC (**right panel**) by colors and shapes of markers, respectively. The resolutions for the array with spacing 1.5 km and 2.6 km are plotted with full and open markers, respectively. Showers of energy 10^{19} eV collected $\langle N_{\text{hits}}^{\text{Total}} \rangle$ below ~70 (30) and events of energy $10^{19.8}$ eV produced $\langle N_{\text{hits}}^{\text{Total}} \rangle$ above ~200 (60) in the array with spacing 1.5 km (2.6 km).

The resulting resolutions obtained individually for two energies, three zenith angles and four primaries are plotted in Fig. 6.11 as a function of the average number of total hits in RPCs $\langle N_{\rm hits}^{\rm Total}\rangle$ detected in the range [500, 2000] m. The resulting resolution is a combination of Poissonian fluctuations of $\langle N_{\rm hits}^{\rm Total}\rangle$ and shower–to–shower fluctuations. For $\langle N_{\rm hits}^{\rm Total}\rangle \simeq 50$ the resolution is estimated to be about 20% and for events with $\langle N_{\rm hits}^{\rm Total}\rangle > 200$ the resolution decreases to about 10%. The results are similar for both models of hadronic interactions.

6.4.3 EM Bias

Although the selection of pads in the fiducial area provides an additional mass overburden to the atmospheric depth at the ground level by more than ~170 g/cm^2, there are still some secondary EM particles with enough energy to penetrate into the RPCs. Therefore it is necessary to estimate also the contribution of such EM punch–through particles that artificially increase the reconstructed muon signal. This bias is defined as the mean of the Gaussian fit to the histogram of $(\rho_{1000}^{\rm MARTA} - \rho_{1000}^{\rm MC})/\rho_{1000}^{\rm MC}$ and it is plotted as a function of energy in Fig. 6.12 for QGSJet II–04 and in Fig. 6.13 for EPOS–LHC showers initiated by protons and iron nuclei.

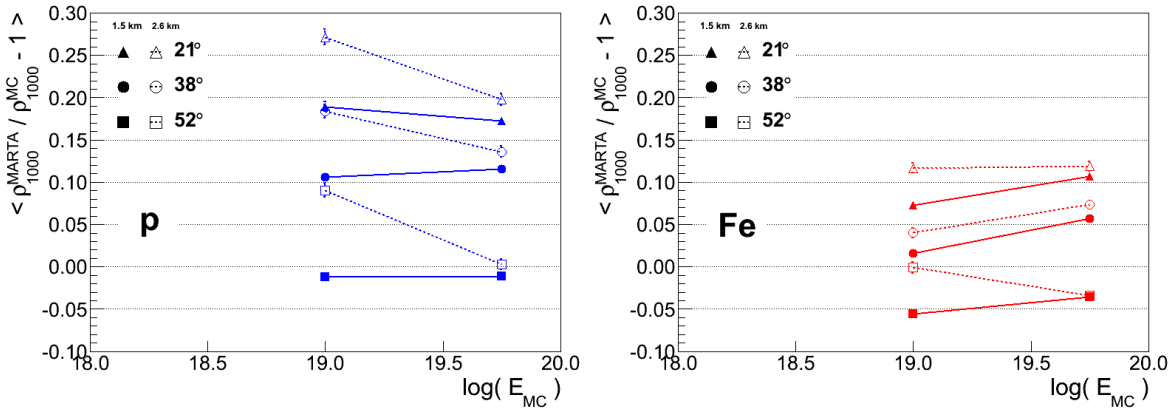

Figure 6.12: Bias of the reconstructed muon signal of showers induced by protons (**left panel**) and iron nuclei (**right panel**) using MARTA stations for three zenith angles. Showers were produced with **QGSJet II–04**. The zenith angles and types of arrays are distinguished by types of markers. Lines connect points only for better visualization.

As expected, the EM bias decreases with zenith angle (absorption of the EM component) and it decreases also with increasing mass of the primary particle (larger distance of $\langle X_{\rm max}\rangle$ to the ground). The value of the EM bias includes also the detection efficiency of RPC, which is about 95%. Therefore, the EM bias is estimated to be about 25% (15%) for vertical ($\Theta \simeq 20°$) showers induced by protons (iron nuclei), ~15% (5%) for showers induced by protons (iron nuclei) with $\Theta \simeq 40°$ and it almost vanishes for zenith angles $\Theta \simeq 50°$ for primary protons as well as for iron nuclei since the EM component is already absorbed in these inclined showers. The EM bias is similar for both models of hadronic interactions. Whereas for the energy $10^{19.8}$ eV the bias for both types of array is similar,

at the energy 10^{19} eV the bias for the array with 2.6 km spacing is systematically larger wrt. to the 1.5 km array.

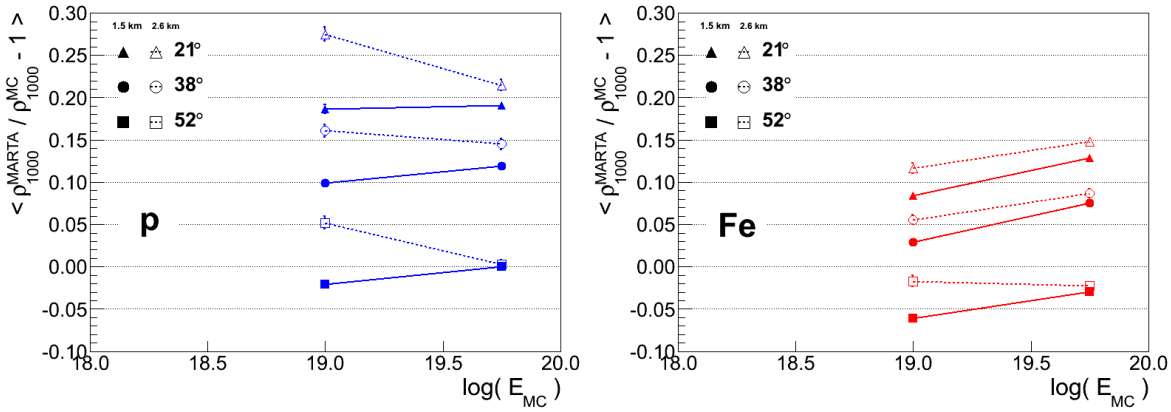

Figure 6.13: The same description as for Fig. 6.12. Showers were produced with **EPOS–LHC**.

6.4.4 Merit Factor

The most important aspect of MARTA is the possibility to separate between the individual types of primaries. To quantify the potential of MARTA to separate between two primaries the Merit Factor defined in Eq. (2.29) was calculated in the following for the distributions of $\rho_{1000}^{\mathrm{MARTA}}$ of showers induced by different primaries.

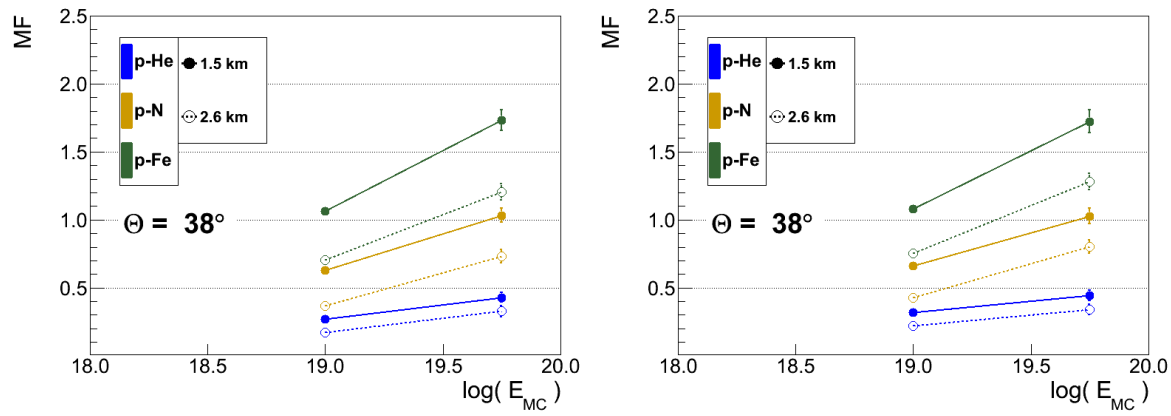

Figure 6.14: Merit factor of proton–nucleus (see colors in the legend) depending on the generated energy using QGSJet II–04 (**left panel**) and EPOS–LHC (**right panel**). Showers with fixed E_{MC} and fixed $\Theta = 38°$ were reconstructed with two types of arrays (full and open markers). Lines connect points only for better visualization.

In Fig. 6.14, MF(p, A) for showers induced by protons (p) and nuclei (A) of fixed zenith angle 38° is plotted as a function of MC energy for QGSJet II–04 (left) and EPOS–LHC (right). Separations

between proton and He, N, Fe primaries were considered since the prime goal of MARTA would be to select proton showers at the highest energies for anisotropy studies. A general increase of $MF(\mathrm{p,A})$ with energy is in accordance with the fact that, at higher energies, $\rho_{1000}^{\mathrm{MARTA}}$ is calculated from more muons collected in the MARTA stations and therefore with better resolutions and consequently narrower distributions of $\rho_{1000}^{\mathrm{MARTA}}$.

The dependence of $MF(\mathrm{p,Fe})$ on MC energy is shown in Fig. 6.15 for different fixed zenith angles and models of hadronic interactions. A slight improvement of the mass separability with decreasing zenith angle is visible. Although the resolution is slightly improving with decreasing zenith angle and there is ∼2–10 % difference between the EM bias of showers induced by protons and iron nuclei (mean values of the distributions of $\rho_{1000}^{\mathrm{MARTA}}$ are closer to each other than in case of $\rho_{1000}^{\mathrm{MC}}$), the zenith angle behavior of $MF(\mathrm{p,Fe})$ seems to be influenced mostly by the effect visible in Fig. 6.16. In this figure, about 20% decrease of the Fe/p ratio of the muon signal estimated from current SD data between 10° and 60° is shown for both models, which implies better mass separation at smaller zenith angles.

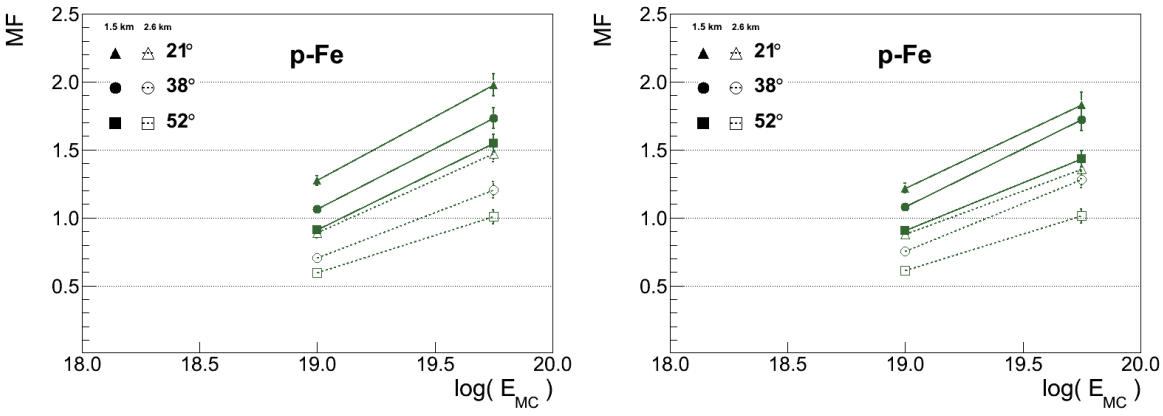

Figure 6.15: Merit factor for separation between primary protons and iron nuclei depending on the generated energy using QGSJet II–04 (left panel) and EPOS–LHC (right panel) for different zenith angles. Fixed E_{MC} was considered. Lines connect points only for better visualization.

The previous calculations of $MF(\mathrm{p,A})$ were performed for fixed MC energies only, assuming perfect energy resolution and no mass composition bias in the reconstructed energy. The energy resolution needs to be accounted for to obtain a realistic estimation of the separation power between the primaries. The mass composition bias is hard to remove from the current SD energy reconstruction, as it was already shown in Chapter 5, because the SD signal is sensitive also to muons. However, in principle the energy can be reconstructed using the EM component only, when from the total SD signal the muon component is subtracted using the MARTA measurement. And, as it was shown in Eq. (2.27), the EM component at a certain shower age should be, in the first approximation, unbiased wrt. the mass composition of primary particles. Therefore the mass composition bias in the SD energy reconstruction is not considered in the evaluation of the potential of MARTA to separate different primary species in this study.

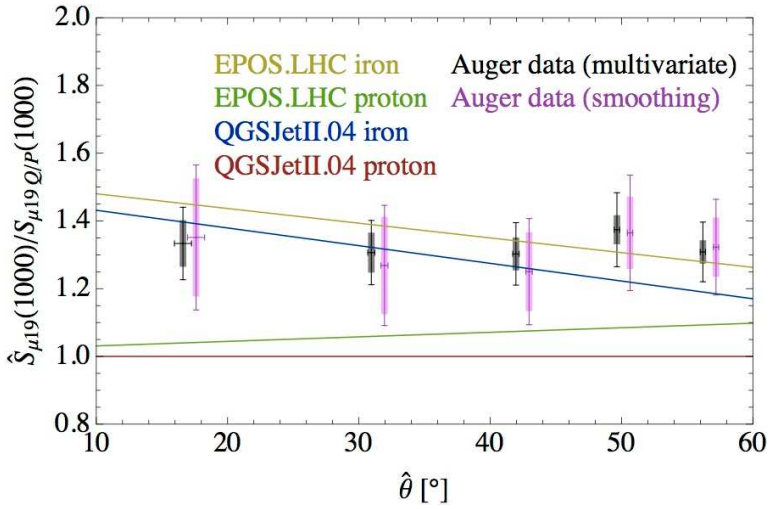

Figure 6.16: Zenith angle dependence of the measured muon signal relatively to the predictions of hadronic interaction model QGSJet II–04 at energy 10^{19} eV. The points of the data of the Pierre Auger Observatory for the two adopted methods were artificially shifted by ±0.5° for better visibility. Picture comes from [119] where detailed description is given.

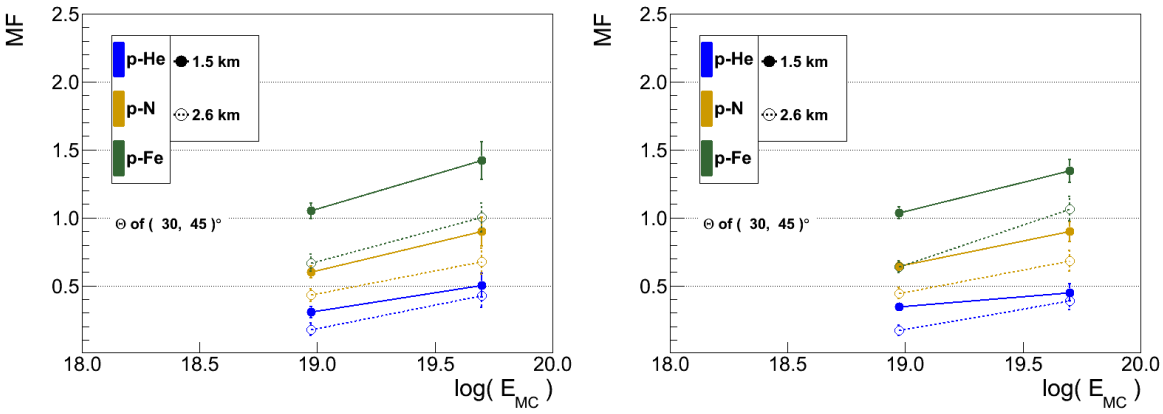

Figure 6.17: Merit factor for continuous simulations depending on the generated energy using QGSJet II–04 assuming the energy resolution of 7% (**left panel**) and of 12% (**right panel**). Lines connect points only for better visualization.

In Fig. 6.17, MC showers of continuous energy and zenith angle were used to calculate $MF(\mathrm{p,A})$ and thus to estimate the separability of protons from heavier nuclei. MC energies were selected to be included in the range $\langle E_1,\ E_2\rangle$ where $E_{1,2} = \langle E\rangle(1 \mp \delta(E))$. The centers of bins were chosen as $\langle E\rangle = 10^{18.975}$ eV and $\langle E\rangle = 10^{19.7}$ eV. The energy resolution $\delta(E) = 7\%$ (left panel) and $\delta(E) = 12\%$ (right panel) corresponds to the current energy resolution of the hybrid and SD reconstruction, respectively. The bin in zenith angle was chosen to keep the results comparable to Fig. 6.14 where |*theta* was fixed to 38° and the energy resolution was not considered. Although the set of showers generated with continuous zenith angles and energy was significantly smaller than in the case of showers with fixed

zenith angles and energy, a weak trend of decreasing $MF(\mathrm{p,A})$ with increasing value of the energy resolution can be seen.

6.5 Discussion of MARTA Potential

Since 2008 when the base–line project of the Pierre Auger Observatory was completed, the subproject Auger Muon and Infill Ground Array (AMIGA) is being built [120]. Whereas the Infill part (water Cherenkov stations in denser grid) was completed in 2011, the system of buried scintillators devoted to the detection of pure muon component is still under construction. Plastic scintillators with size of 30 m^2 are buried 2.3 m under the ground (vertical mass overburden gives $E_{\mathrm{Th}} \approx 1$ GeV for muons) at the Infill site to detect only the muon part of the shower. In such case, the EM component is sufficiently shielded with more than ∼500 g/cm^2 (increases with the zenith angle) additionally to the atmospheric depth. In an ideal case, these large muon detectors would be installed near all SD stations of the Pierre Auger Observatory and a large event statistics at the highest energies would be collected including the information about the number of muons. However, such an upgrade would be too much cost demanding and even technically impossible at some places of swampy or rock terrain with inappropriate conditions for digging. Therefore, an upgrade of the observatory using RPCs could be the cost–efficient alternative.

According to the analysis of detailed MC simulations, the MARTA array with spacing 2.6 km would collect such a small number of muons in average between 500 m and 2000 m from the shower core that the separability of protons from the heavier primaries would be very hard even at the highest energies. In case of the MARTA array with spacing 1.5 km, the separability at energy 10^{19} eV is similar to the separability of the sparser array at the highest energies, but it is improving towards the highest energies. At the highest energies, the separation power between showers induced by protons and iron nuclei is at a similar level ($MF(\mathrm{p,Fe}) \simeq 1.4$) as for the quantity X_{max} that is observed with fluorescence detectors. As in the case of the X_{max} measurement, the event–by–event separability of primaries seems to be impossible ($MF(\mathrm{p,Fe}) < 2$) with both suggested MARTA designs.

It needs to be noted that the information about the EM component was not used in the previous considerations on the separability between primary masses. The size of the EM component could be obtained via subtraction of the muon signal from the total signal in the water Cherenkov stations to improve the separability of primaries using a multivariate analysis.

The EM bias in $\rho_{1000}^{\mathrm{MARTA}}$ is quite large (up to 25%). Therefore, its size, evolution with zenith angle and energy is dependent on MC simulations, which would make more difficult to interpret the measured data.

The final selection of the proposal to upgrade the surface detectors at the Pierre Auger Observatory favored the solution with plastic scintillators mounted on top of the water Cherenkov stations. However, the idea of placing RPC units under the water Cherenkov detectors would be beneficial for stations of larger volume at some future UHECR observatory. In such a case, there would be a smaller

punch through of the EM component and also a larger area with sufficient EM shielding to collect more muons and to achieve a higher power to separate between different types of primaries.

It needs to be also noted that the segmentation of RPC units can provide further possibilities of enhanced measurements [121]. The track-length of single muon in the water Cherenkov station can be calculated using the "MPD approach" (see Section 3.4.2) and test the response of the water Cherenkov detector [122], the saturation can be suppressed towards closer distances to the shower core when smaller readout areas were applied or if an analog readout was added.

Chapter 7

Conclusions

The mass composition of cosmic–ray particles of ultra–high energies (UHECR) is of crucial importance to understand the phenomenon of these elusive particles. The thesis was devoted to the problem of resolving the mass composition of UHECR using the detection of induced extensive air showers (EAS). The potential of new methods was investigated using Monte Carlo (MC) simulations and, when possible, the methods were preliminarily applied to the data of the Pierre Auger Observatory. The author's original research with emphasis on the mass composition of UHECR showers was described in three chapters divided according to three general objectives:

- attenuation of the signal in surface detectors wrt. mass composition of UHECR for current and future observatories (Chapter 4),
- combined analysis of the muon shower size and X_{max} with the aim to strengthen the information about the cosmic–ray composition (Chapter 5),
- possible detection of muons with RPCs placed under the water Cherenkov detectors and its impact on the separation between primary–mass species (Chapter 6).

In **Chapter 4**, the basic properties of CORSIKA showers produced with two models of hadronic interactions tuned to the LHC data were used to simulate modeled responses of ground detectors to UHECR showers.

The responses of surface detectors to EAS that are similar to the responses of surface detectors deployed at the two largest experiments of UHECR were considered in Section 4.1. It was found that the Constant Intensity Cut (CIC) method (used at the Pierre Auger Observatory) and the MC–based approach (used at the Telescope Array) are equivalent for beams consisting of only one type of primary particle. For a mixed composition of primary particles, the CIC method eliminates the zenith angle bias in the energy reconstruction, whereas this bias is present in the MC–based approach. Therefore, an observation of varying dependence of $\langle E_{\mathrm{SD}}/E_{\mathrm{FD}}\rangle$ on $\cos^2(\Theta)$ (at energies with full trigger efficiency) with an observatory applying the MC–based approach (such as Telescope Array) would indicate that the mass composition of UHECR is different from that assumed in the MC–based

approach or that the predicted zenith angle dependence inferred from MC is different from reality. On the other hand it was also shown that, if the models of hadronic interactions reach the state when they reflect reality, a comparison between the measured CIC curve and the attenuation curves predicted by the models for different primary species can be used to constrain the mass composition of UHECR. Since the CIC approach assumes isotropy in incoming directions of arriving primary particles, the influence of presence of strong sources on the CIC method was addressed in detail. The studied example of an anisotropic signal from a prominent source at the highest energies shows almost no impact on the CIC shape for intensity cuts at lower energies. Small deviations were observed for intensity cuts close to the energy where the anisotropic signal of the source starts to be significant. It also means that in case of the excess of events observed in the Cen A region by the Pierre Auger Observatory, the CIC curve derived at lower energy (~7 EeV) than the excess is observed (above ~52 EeV) is not affected by such a violation of the isotropy assumption at the highest energies. These results were published in conference proceedings [95].

In Section 4.2, the CIC approach was applied simultaneously to two signals that were induced in an array of coincident muon and electromagnetic (EM) detectors at a hypothetical observatory. It was demonstrated that the dispersion of the mass in the primary beam of UHECR particles can be addressed and even measured using the zenith angle behavior of the number of events matched in both types of arrays above a given intensity cut. Very similar results were obtained for the two models of hadronic interactions tuned to the LHC data. Therefore this method that addresses the spread of primary masses can complement information on the mean logarithmic mass that is usually obtained from EM and muon size of showers. The developed method could be applied to the data of an observatory with independent muon and EM detectors when a detailed response of the detectors is incorporated into the simulations. The method was indicated in the conference proceedings [96] and published as the journal paper [97].

In **Chapter 5**, the original method to simultaneously infer the relative fractions of primary particles (f_i, $i = \mathrm{p, He, N, Fe}$) and the rescaling of the number of muons (R_μ) was introduced. It is based on the decomposition of the dependence of $\langle N_\mu \rangle$ on X_{max} to the individual contributions $\langle N_\mu^i \rangle$ of the assumed primaries with relative fractions f_i in the UHECR beam for each bin of X_{max}. The method was published in the conference proceedings [103].

The potential of this approach was demonstrated in Section 5.1 on simulated showers assuming realistic resolutions of the measurements of N_μ and X_{max}. When the proper dependencies of $\langle N_\mu^i \rangle$ on X_{max} and the distributions of X_{max} are known for each primary particle i, f_i and R_μ can be inferred within few–percent accuracy. However, different models of hadronic interactions predict different dependencies of $\langle N_\mu^i \rangle$ on X_{max} and different distributions of X_{max}. Therefore a typical systematic uncertainty at a level of 25% was found for the fitted f_i in further analysis. With our current knowledge of hadronic interactions, this method can hardly find unambiguously the primary fractions in the UHECR beam. On the other hand, the method estimates R_μ precisely (within few %).

In Section 5.2, the method was preliminarily applied to the data of the Pierre Auger Observatory. The number of muons is not directly measured at the observatory for zenith angles within 60°, but the signal in water Cherenkov detectors is induced by EM particles and muons as well. Therefore the ground signal corrected for zenith angle and energy (the ratio of reconstructed energies E_{SD}/E_{FD}) was used instead of N_μ. For each shower, X_{max} was corrected for its energy evolution (X^{19}_{max}). Then $\langle E_{SD}/E_{FD}\rangle$ and X^{19}_{max} that are both independent on energy and zenith angle were used within the method for four energy bins between $10^{17.8}$ eV and $10^{19.0}$ eV.

At first, the dependence of $\langle E_{SD}/E_{FD}\rangle$ on X^{19}_{max} observed with the data of the Pierre Auger Observatory was checked for reconstruction issues. Then, due to the similarity of the structure in this dependence (presence of "two breaks") to the one observed in MC simulations for mixed compositions of primaries, the measured data were interpreted to be of a mixed composition of primary particles. The showers generated with three models of hadronic interactions were treated in the exactly same way as the measured data. The exact unambiguous determination of the primary fractions was found not feasible within the method. All the possible primary fractions of the four components (p, He, O, Fe) fixed in steps of 10% were tested for consistency with the measured data leaving only the rescaling factor of the ground signal to be single free parameter. The results indicate that the mixed composition of primary particles with $\sigma^2(\ln A) \in \langle 1,\ 3\rangle$ is present at energies $10^{17.8-19.0}$ eV. This finding questions the dip–model of ankle observed in the UHECR spectrum. The dip–model predicts the fraction of protons at the acceleration site more than 85%.

Another comparison with two methods based on the X_{max} distributions only and with a method studying correlation between the ground signal and X_{max} was performed (using umbrella plots) for three models of hadronic interactions and for the four energy bins. The model EPOS–LHC provided the most consistent interpretation of the measured data with mass composition of primary particles among all the different analyses. For QGSJet II–04 and Sibyll 2.1 significant inconsistencies were observed.

The rescaling factor of the ground signal was found to be ~10-20%, ~25-35% and ~55-70% for EPOS–LHC, QGSJet II–04 and Sibyll 2.1, respectively, with negligible energy dependence in $10^{17.8-19.0}$ eV. This rescaling factor reflects predominantly the lack of muons in simulated showers wrt. to the measured data. The results are compatible with other analyses published by the Pierre Auger Observatory regarding the lack of muons in simulated showers.

The **Chapter 6** was focused on the evaluation of a potential upgrade of the Pierre Auger Observatory with Resistive Plate Chambers (RPCs) placed under the water Cherenkov stations using detailed MC simulations. These segmented RPCs with additional shielding of the EM component wrt. atmospheric depth could be used as direct muon detectors. Two deployment schemes of RPCs in the SD of the Pierre Auger Observatory were considered (1.5 km and 2.6 km grids).

The detailed simulations of UHECR showers and detector responses were analyzed to parametrize the LDF of the RPC signal. The value of LDF in 1000 m (ρ^{MARTA}_{1000}) was then fitted on event-by-event basis and treated as an observable sensitive to the mass composition of UHECR. The resolution and

the electromagnetic bias of $\rho_{1000}^{\mathrm{MARTA}}$ were estimated for different primaries, energies and zenith angles using two models of hadronic interactions tuned to the LHC data. Finally, the separability of protons from He, N and Fe nuclei was evaluated. The separability of primaries was found insufficient to distinguish between protons and iron nuclei on the event-by-event basis for both considered grids of RPC stations. For the 1.5 km grid, a separability comparable with the X_{max} measurement could be achieved at the highest energies where a steep suppression of the cosmic–ray spectrum is observed. At these energies, almost all events can be selected with a resolution of $\delta(N_\mu)/N_\mu \simeq 10\%$. However, the EM bias in $\rho_{1000}^{\mathrm{MARTA}}$ was found relatively large (up to even ~25%). Therefore, its size, evolution with zenith angle and energy is dependent on MC simulations, which would make more difficult to interpret the measured data. Generally, muon detectors of a larger collecting area and with a larger mass overburden than the considered MARTA design would be more appropriate to study UHECR at the highest energies; considering an array of similar size, detector spacing and altitude as the Pierre Auger Observatory.

To summarize, the results obtained with the studies described in the thesis indicate that for the future research of UHECR and high energy interactions taking place in EAS it would be beneficial, if the future observatories of UHECR

- are composed of giant arrays of coincident surface detectors sensitive to different shower components (e.g. EM detectors and muon detectors of large enough size),
- are complemented by denser arrays of particle detectors to study the individual shower components in a wide range of energies of primary particles to decrease the systematic uncertainties in the mass composition measurements,
- contain the fluorescence detectors for precise energy calibrations of the surface arrays and to remove the strong correlation between the number of muons and the shower energy,
- apply the CIC method (or other method providing an unbiased energy estimator wrt. the primary composition) to deal with the correction of the signal in the surface detectors due to the different amount of atmosphere passed by showers before reaching the ground.

Then the crucial ingredient of UHECR studies, the mass composition of primary particles, could be inferred from the measured data with better precision and statistics. Also the size of systematics due to the different predictions of models of hadronic interactions could be decreased due to the measurements at lower energies. And, eventually, the origin of UHECR particles that has been hidden for more than 50 years could be revealed; may be even with the help of methods presented in this thesis.

References

[1] J. Linsley, "Evidence for a primary cosmic-ray particle with energy 10^{20} eV", Phys. Rev. Lett. **10** (1963) 146.

[2] K. Greisen, "End to the cosmic ray spectrum?", Phys. Rev. Lett. **16** (1966) 748.

[3] G. T. Zatsepin and V. A. Kuz'min, "Upper limit of the spectrum of cosmic rays", JETP Lett. **4** (1966) 78.

[4] K.-H. Kampert & A. A. Watson, "Extensive air showers and ultra high-energy cosmic rays: a historical review", EPJ H **37** (2012) 359.

[5] M. Nagano & A. A. Watson, "Observations and implications of the ultrahigh-energy cosmic rays", Rev. Mod. Phys. **72** (2000) 689.

[6] C. Grupen, "Astroparticle Physics", Springer Science & Business Media, 2005.

[7] D. H. Perkins, "Particle Astrophysics, Second Edition", Oxford Master Series in Physics 10, 2008.

[8] M. S. Longair, "High Energy Astrophysics, Third Edition", Cambridge University Press, 2011.

[9] B. Peters, "Primary cosmic radiation and extensive air showers", Il Nuov. Cim. **22** (1961) 800.

[10] KASCADE-Grande Collaboration, "KASCADE-Grande measurements of energy spectra for elemental groups of cosmic rays", Astropart. Phys. **47** (2013) 54.

[11] Y. A. Gallant & A. Achterberg, "Ultra-high-energy cosmic ray acceleration by relativistic blast waves", MNRAS **305** (1999) L6.

[12] A. M. Hillas, "The Origin of Ultra-High-Energy Cosmic Rays", Annu. Rev. Astron. Astrophys. **22** (1984) 425.

[13] E. Waxman, "Cosmological Gamma-Ray Bursts and the Highest Energy Cosmic Rays", Phys. Rev. Lett. **75** (1995) 386.

[14] P. Blasi, R. Epstein, A. V. Olinto, "Ultra-High-Energy Cosmic Rays from Young Neutron Star Winds", ApJ **533** (2000) L123.

[15] G. R. Farrar, A. A. Berlind, D. V. Hogg, "Foreground and Source of a Cluster of Ultra-High-Energy Cosmic Rays", ApJ **642** (2006) L89.

[16] M. Kachelriess, "The rise and fall of top-down models as main UHECR sources", Proc. of the XXth Recontres de Blois, Blois, France, arXiv:0810.3017 [astro-ph].

[17] The IceCube Collaboration, IceCube (IceCube Neutrino Observatory) webpage `http://icecube.wisc.edu/`.

[18] The KM3NeT Collaboration, KM3NeT (A multi-km3 sized Neutrino Telescope) webpage `http://www.km3net.org/home.php/`.

[19] The H.E.S.S. Collaboration, H.E.S.S. (High Energy Stereoscopic System) webpage `http://www.mpi-hd.mpg.de/hfm/HESS/`.

[20] The HAWC Collaboration, HAWC (The High-Altitude Water Cherenkov Observatory) webpage `http://www.hawc-observatory.org/`.

[21] The CTA Collaboration, CTA (Cherenkov Telescope Array) webpage `https://www.cta-observatory.org/`.

[22] The Pierre Auger Collaboration, "The Pierre Auger Cosmic Ray Observatory", NIM A **798** (2015) 172.

[23] Telescope Array Collaboration, TA webpage `http://www.telescopearray.org/`.

[24] S. Lee, A. Olinto, G. Sigl, "Extragalactic magnetic field and the highest energy CR", ApJ **455** (1995) L21.

[25] L. A. Anchordoqui & H. Goldberg, "A lower bound on the local extragalactic magnetic field", Phys. Rev. D **65** (2002) 021302.

[26] M. Lemoine & E. Waxman, "Anisotropy vs chemical composition at ultra-high energies", JCAP **11** (2009) 9.

[27] D. Allard, "Propagation of extragalactic ultra-high energy cosmic-ray nuclei : implications for the observed spectrum and composition", Proc. of the Rencontres de Moriond 2009, La Thuile, Italy, arXiv:0906.3156 [astro-ph.HE].

[28] R. Ruffini, G.V. Vereshchagin, S.-S. Xue, "Cosmic absorption of ultra high energy particles", submited to JCAP (2015), arXiv:1503.07749 [astro-ph.HE].

[29] W. Heitler, "The Quantum Theory of Radiation, 3rd edition", Oxford University Press, London, 1954.

[30] J. Mathews, "A Heitler model of extensive air showers", Astropart. Phys. **22** (2005) 387.

[31] K.-H. Kampert & M. Unger, "Measurements of the cosmic ray composition with air shower experiments", Astropart. Phys. **35** (2012) 660.

[32] T. Bergmann et al., "One-dimensional Hybrid Approach to Extensive Air Shower Simulation", Astropart. Phys. **26** (2007) 420.

[33] T. Pierog *et al.*, "First results of fast one-dimensional hybrid simulation of EAS using CONEX", Nucl. Phys. Proc. Suppl. **151** (2006) 159.

[34] T. Erber, "High-Energy Electromagnetic Conversion Processes in Intense Magnetic Fields", Rev. Mod. Phys. **38** (1966) 626.

[35] B. McBreen and C. J. Lambert, "Interactions of high-energy ($E > 5 \times 10^{19}$ eV) photons in the Earth's magnetic field", Phys. Rev. D **24** (1981) 2536.

[36] S. Ostapchenko, "Monte Carlo treatment of hadronic interactions in enhanced Pomeron scheme: QGSJET-II model", Phys. Rev. D **83** (2011) 014018.

[37] T. K. Gaisser, "Cosmic Rays and Particle Physics", Cambridge University Press, Cambridge, 1990.

[38] D. Heck *et al.*, "Upgrade of the Monte Carlo code CORSIKA to simulate extensive air showers with energies > 10^{20} eV", FZKA 6019 (1998).

[39] F. Catalani *et al.*, "Statistical methods applied to composition studies of ultrahigh energy cosmic rays", Astropart. Phys. **28** (2007) 357.

[40] The Pierre Auger Collaboration, "Interpretation of the Depths of Maximum of Extensive Air Showers Measured by the Pierre Auger Observatory", JCAP **02** (2013) 26.

[41] The Pierre Auger Collaboration, website of the Publications Committee of the Pierre Auger Observatory, `http://augerpc.in2p3.fr/` [downloaded 1. 8. 2015].

[42] The Pierre Auger Collaboration, "Properties and performance of the prototype instrument for the Pierre Auger Observatory", NIM A **523** (2004) 50.

[43] K. Shinozaki & M. Teshima, "AGASA Results", Nucl. Phys. B (Proc. Suppl.) **136** (2004) 18.

[44] A. Schulz for the Pierre Auger Collaboration, "Observation of the suppression of the flux of cosmic rays above 4×10^{19}eV", Proc. of the 33rd ICRC 2013, Rio de Janeiro, Brasil, arXiv:1307.5059 [astro-ph.HE].

[45] The Pierre Auger Collaboration, "Trigger and Aperture of the Surface Detector Array of the Pierre Auger Observatory", NIM A **613** (2010) 29.

[46] The Pierre Auger Collaboration, "Reconstruction of inclined air showers detected with the Pierre Auger Observatory", JCAP **08** (2014) 019.

[47] The Pierre Auger Collaboration, "The fluorescence detector of the Pierre Auger Observatory", NIM A **620** (2010) 227.

[48] C. Meurer, N. Scharf for the Pierre Auger Collaboration, "HEAT – a low energy enhancement of the Pierre Auger Observatory", Astrophys. Space Sci. Trans. **7** (2011) 183.

[49] The Pierre Auger Collaboration, "The Rapid Atmospheric Monitoring System of the Pierre Auger Observatory", JINST **7** (2012) P09001.

[50] The AIRFLY Collaboration, "Precise measurement of the absolute fluorescence yield of the 337 nm band in atmospheric gases", Astropart. Phys. **42** (2013) 90.

[51] T. K. Gaisser, A. M. Hillas, "Reliability of the method of constant intensity cuts for reconstructing the average development of vertical showers", Proc. of the 15th ICRC 1977, Plovdiv, Bulgaria.

[52] Observer Team, "The Auger Observer", webpage `http://augerobserver.fzk.de`.

[53] M. Nyklicek, P. Travnicek, "On the size of missing energy of cosmic ray showers", Proc. of the 31st ICRC 2009, Lodz, Poland.

[54] M. J. Tueros for the Pierre Auger Collaboration, "Estimate of the non-calorimetric energy of showers observed with the fluorescence and surface detectors of the Pierre Auger Observatory", Proc. of the 33rd ICRC 2013, Rio de Janeiro, Brasil, arXiv:1307.5059 [astro-ph.HE].

[55] V. Verzi for the Pierre Auger Collaboration, "The Energy Scale of the Pierre Auger Observatory", Proc. of the 33rd ICRC 2013, Rio de Janeiro, Brasil, arXiv:1307.5059 [astro-ph.HE].

[56] J. G. Wilson, K. Greisen *et al.*, "Progress in Cosmic Ray Physics, Vol. 3", North-Holland, Amsterdam, 1956.

[57] K. Kamata and J. Nishimura, "The Lateral and the Angular Structure Functions of Electron Showers", Prog. Theoret. Phys. Suppl. **6** (1958) 93.

[58] D. Newton, J. Knapp, A. A. Watson, "The Optimum Distance at which to Determine the Size of a Giant Air Shower", Astropart. Phys. **26** (2007) 414.

[59] J. Hersil et al., "Observations of Extensive Air Showers near the Maximum of Their Longitudinal Development", Phys. Rev. Lett. **6** (1961) 22.

[60] J. Vícha, "Aspects of energy calibration of cosmic ray showers detected by surface detector at the Pierre Auger Observatory", Diploma thesis, Czech Technical University, 2010, `http://physics.fjfi.cvut.cz/publications/ejcf/DP_Jakub_Vicha.pdf`.

[61] R. Pesce for the Pierre Auger Collaboration, "Update of the energy calibration of data recorded with the surface detector of the Pierre Auger Observatory", Proc. of the 32nd ICRC 2011, Beijing, China, arXiv[astro-ph]:1107.4809.

[62] J. Vícha & J. Chudoba for the Pierre Auger Colaboration, "Data Processing at the Pierre Auger Observatory", J. Phys.: Conf. Ser. **608** (2015) 012077.

[63] V. Berezinsky *et al.*, "Dip in UHECR spectrum as signature of proton interaction with CMB", Phys. Lett. B **612** (2005) 147.

[64] D. Allard *et al.*, "On the transition from galactic to extragalactic cosmic-rays: spectral and composition features from two opposite scenarios", Astropart. Phys. **27** (2007) 61.

[65] M. Unger *et al.*, "Origin of the ankle in the ultra-high energy cosmic ray spectrum and of the extragalactic protons below it", arXiv:1505.02153 [astro-ph.HE].

[66] A. Letessier-Selvon for the Pierre Auger Observatory, "Highlights from the Pierre Auger Observatory", Proc. of the 33rd ICRC 2013, Rio de Janeiro, Brasil, arXiv:1310.4620 [astro-ph.HE].

[67] The Pierre Auger Collaboration, "Depth of Maximum of Air-Shower Profiles at the Auger Observatory: Measurements at Energies above $10^{17.8}$ eV", Phys. Rev. D **90** (2014) 122005.

[68] K. Werner, F. M. Liu and T. Pierog, "Parton ladder splitting and the rapidity dependence of transverse momentum spectra in deuteron-gold collisions at the BNL Relativistic Heavy Ion Collider", Phys. Rev. C **74** (2006) 044902.

[69] T. Pierog and K. Werner, "EPOS Model and Ultra High Energy Cosmic Rays", Nucl. Phys. Proc. Suppl. **196** (2009) 102.

[70] E. J. Ahn *et al.*, "Cosmic ray interaction event generator SIBYLL 2.1", Phys. Rev. D **80** (2009) 094003.

[71] The Pierre Auger Collaboration, "Depth of Maximum of Air-Shower Profiles at the Pierre Auger Observatory: Composition Implications", Phys. Rev. D **90** (2014) 122006.

[72] The Pierre Auger Collaboration, "Erratum: Muons in air showers at the Pierre Auger Observatory: Measurement of atmospheric production depth", Phys. Rev. D **92** (2015) 019903(E).

[73] T. Pierog *et al.*, "Air Shower Development, Pion Interactions and Modified EPOS Model", Proc. of the 34th ICRC 2015, The Hague, Netherlands, PoS(ICRC2015)337.

[74] P. Younk & M. Risse, "Sensitivity of the correlation between the depth of shower maximum and the muon shower size to the cosmic ray composition", Astropart. Phys. **35** (2012) 807.

[75] A. Yushkov for the Pierre Auger Collaboration, "Composition at the "ankle" measured by the Pierre Auger Observatory: pure or mixed?", Proc. of the 34th ICRC 2015, The Hague, Netherlands, PoS(ICRC2015)335, arXiv:1509.03732 [astro-ph.HE].

[76] F. Diogo for the Pierre Auger Collaboration, "Measurement of the average electromagnetic longitudinal shower profile at the Pierre Auger Observatory", Proc. of the 34th ICRC 2015, The Hague, Netherlands, PoS(ICRC2015)413, arXiv:1509.03732 [astro-ph.HE].

[77] G. R. Farrar for the Pierre Auger Collaboration, Proc. of the 33rd ICRC 2013, Rio de Janeiro, Brasil, arXiv:1307.5059 [astro-ph.HE].

[78] The Pierre Auger Collaboration, "Muons in air showers at the Pierre Auger Observatory: Mean number in highly inclined events", Phys. Rev. D **91** (2015) 032003.

[79] C. Bleve for the Pierre Auger Collaboration, "Updates on the neutrino and photon limits from the Pierre Auger Observatory", Proc. of the 34th ICRC 2015, The Hague, Netherlands, PoS(ICRC2015)1103, arXiv:1509.03732 [astro-ph.HE].

[80] The Pierre Auger Collaboration, "A search for point sources of EeV photons", ApJ **789** (2014) 160.

[81] The Pierre Auger Collaboration, "An improved limit to the diffuse flux of ultra-high energy neutrinos from the Pierre Auger Observatory", Phys. Rev. D **91** (2015) 092008.

[82] The Pierre Auger Collaboration, "A Search for Point Sources of EeV Neutrons", ApJ **760** (2012) 148.

[83] The Pierre Auger Collaboration, "Correlation of the Highest-Energy Cosmic Rays with Nearby Extragalactic Objects", Science **318** (2007) 938.

[84] The Pierre Auger Collaboration, "Searches for Anisotropies in the Arrival Directions of the Highest Energy Cosmic Rays Detected by the Pierre Auger Observatory", ApJ **804** (2015) 15.

[85] R. Liu *et al.*, "On the excess of ultra-high energy cosmic rays in the direction of Centaurus A", ApJ **755** (2012) 139.

[86] G. R. Farrar *et al.*, "Galactic magnetic deflections and Centaurus A as a UHECR source", JCAP **01** (2013) 023.

[87] H. Yuksel *et al.*, "The Centaurus A Ultrahigh-Energy Cosmic Ray Excess and the Local Extragalactic Magnetic Field", ApJ **758** (2012) 16.

[88] The Pierre Auger Collaboration, "Large scale distribution of ultra high energy cosmic rays detected at the Pierre Auger Observatory with zenith angles up to 80 degrees", ApJ **802** (2015) 111.

[89] D. Harari *et al.*, "Anisotropies of ultrahigh energy cosmic rays diffusing from extragalactic sources", Phys. Rev. D **89** (2014) 123001.

[90] The Telescope Array Collaboration, "Study of Ultra-High Energy Cosmic Ray composition using Telescope Array's Middle Drum detector and surface array in hybrid mode", Astropart. Phys. **64** (2014) 49.

[91] The Telescope Array Collaboration, "The Cosmic Ray Energy Spectrum Observed with the Surface Detector of the Telescope Array Experiment", ApJ **768** (2013) L1.

[92] R. Abbasi *et al.* for the Pierre Auger Collaboration and the Telescope Array Collaboration, "Report of the Working Group on the Composition of Ultra High Energy Cosmic Rays", Proc. of the UHECR 2014 workshop, Springdale, USA, arXiv:1503.07540 [astro-ph.HE].

[93] R. Abbasi *et al.*, "Study of Ultra-High Energy Cosmic Ray Composition Using Telescope Array's Middle Drum Detector and Surface Array in Hybrid Mode", ApJ **790** (2014) L21.

[94] R. Engel for the Pierre Auger Collaboration, "Upgrade of the Pierre Auger Observatory (AugerPrime)", Proc. of the 34th ICRC 2015, The Hague, The Netherlands, PoS(ICRC2015)686.

[95] J. Vícha *et al.*, "On the methods to determine signal attenuation curve for different surface arrays", Proc. of the 33rd ICRC 2013, Rio de Janeiro, Brasil, ISBN: 978-85-89064-29-3, arXiv:1310.0330 [astro-ph.HE].

[96] J. Vícha *et al.*, "Signal Attenuation Curve for Different Surface Detector Arrays", Astropart., Part., Space Phys. and Det. for Phys. App. (2014) 162.

[97] J. Vícha *et al.*, "Study of Dispersion of Mass Distribution of Ultra-High Energy Cosmic Rays using a Surface Array of Muon and Electromagnetic Detectors", Astropart. Phys. **69** (2015) 11.

[98] A. Ferrari *et al.*, "FLUKA: A multi-particle transport code (Program version 2005)", CERN report CERN-2005-010 (2005).

[99] J. Alvarez-Muniz *et al.*, "Atmospheric shower fluctuations and the constant intensity cut method", Phys. Rev. D **66** (2002) 123004.

[100] J. C. Arteaga-Velazquez *et al.*, "The Constant Intensity Cut Method applied to the KASCADE-Grande muon data", Nucl. Phys. B Proc. Suppl. **196** (2009) 183.

[101] P. Luczak *et al.*, "The $< \ln A >$ study in the primary energy range $10^{16} - 10^{17}$ eV with the Muon Tracking Detector in the KASCADE-Grande experiment", Proc. of the 33rd ICRC 2013, Rio de Janeiro, Brasil, arXiv:1308.2059 [astro-ph.HE].

[102] E. Barcikowski *et al.* for the HiRes, Pierre Auger, Telescope Array and Yakutsk Collaborations, "Mass composition working group report", EPJ Web of Conferences **53** (2013) 01006.

[103] J. Vícha *et al.*, "On the Combined Analysis of Muon Shower Size and Depth of Shower Maximum", Proc. of the 34th ICRC 2015, the Hague, Netherlands, PoS(ICRC2015)433, arXiv:1509.06320 [astro-ph.IM].

[104] E. J. Gumbel, "Statistics of extremes", Dover Publications, 2004.

[105] S. Argiro *et al.*, "The Offline Software Framework of the Pierre Auger Observatory", NIM A **580** (2007) 1485.

[106] Naples Auger Group, Hybrid Offline simulation of Corsika files, `http://natter.na.infn.it:18501/` [downloaded 5.11. 2015].

[107] F. Schmidt *et al.*, "Applying Extensive Air Shower Universality to Ground Detector Data", Proc. of the 30th ICRC 2007, Merida, Mexico, arXiv:0706.1990 [astro-ph].

[108] J. Vicha *et al.*, "SD to FD Energy Ratio as Parameter Sensitive to Muon Content", Auger internal note, GAP-2011-042.

[109] S. Petrera, "Update of the parameterisations given in “Interpretation of the Depths of Maximum...” in the energy range 10^{17} – 10^{20} eV", Auger internal note, GAP-2014-083.

[110] The Pierre Auger Collaboration, "Atmospheric effects on extensive air showers observed with the surface detector of the Pierre Auger observatory", Astropart. Phys. **32** (2009) 89.

[111] R. Liu *et al.*, "Constraints on the source of ultra-high energy cosmic rays using anisotropy vs chemical composition", ApJ **776**, (2013) 88.

[112] MARTA Collaboration, "MARTA Muon Auger RPC for the Tank Array Design Report", Auger internal note, GAP-2013-020.

[113] B. Tomé, "Towards a proposal for the installation of RPC’s @ Auger", presentation at Particle Physics @ Auger, Lisboa, Portugal, 16-20 January 2012.

[114] S. Agostinelli *et al.*, "Geant4 - A Simulation Toolkit", NIM A **506** (2003) 250.

[115] L. Cazon *et al.*, "Expected performance of MARTA in the measurement of muons", Auger internal note, GAP-2013-018.

[116] A. Supanitsky *et al.*, "Underground Muon Counters as a Tool for Composition Analyses", Astropart. Phys. **29** (2008) 461.

[117] Naples Auger Group, MARTA Offline simulation of Corsika files, `http://natter.na.infn.it:18501/protected/MARTA/Marta.html` [downloaded 20.10. 2013].

[118] KIT server, internal server for the Pierre Auger Collaboration [downloaded 1.6. 2014].

[119] B. Kegl for the Pierre Auger Collaboration, Proc. of the 33rd ICRC 2013, Rio de Janeiro, Brasil, arXiv:1307.5059 [astro-ph.HE].

[120] A. Etchegoyen *et al.*, Proc. of the 30th ICRC 2007, Merida, Mexico, arXiv:0710.1646 [astro-ph].

[121] P. Abreu *et al.*, "Muon Array with RPCs for Tagging Air showers", Proc. of the 34th ICRC 2015, The Hague, Netherlands, PoS(ICRC2015)629.

[122] P. Assis for the Pierre Auger Collaboration, "Measurement of the water-Cherenkov detector response to inclined muons using an RPC hodoscope", Proc. of the 34th ICRC 2015, The Hague, Netherlands, PoS(ICRC2015)620, arXiv:1509.03732 [astro-ph.HE].